DAMAGE DETECTION AND DAMAGE EVOLUTION MONITORING OF COMPOSITE MATERIALS FOR NAVAL APPLICATIONS USING ACOUSTIC EMISSION TESTING

by

Nikolaos Angelopoulos

A thesis submitted to
The University of Birmingham
For the degree of
DOCTOR OF PHILISOPHY

School of Metallurgy and Materials

College of Engineering and Physical Sciences

University of Birmingham

June 2017

Synopsis

Maritime transport has profound importance for the world economy. Vessels of all sizes constantly transport large numbers of passengers and goods across the sea, often under adverse operational conditions. Vessels need to exhibit high levels of reliability, availability, maintainability and safety (RAMS). However, at the same time their performance needs to be optimised ensuring the lowest possible fuel consumption with the maximum operational capacity and range without compromising RAMS. Sweating of naval assets and profitability should be maximised for the operator ensuring investment in future projects and supporting the growth of maritime transport and world economy as a whole.

Vessels have been traditionally manufactured using naval steel grades such AH, DH and EH. Smaller leisure and specialised purpose vessels such as patrol boats, etc. have been built using fibre-reinforced composite (FRC) materials. This trend is gradually penetrating the market of larger commercial vessels including freight and cruise ships. However, these are still the early days and further investigation of the optimum FRC manufacturing techniques and mechanical properties together with an in-depth understanding of the damage mechanics are required before such materials can become more commonplace.

This project has investigated different glass FRCs using different manufacturing techniques. Glass fibres are preferred due to their lower cost in comparison with carbon fibres. The use of carbon FRCs in maritime applications is limited to the fabrication of racing and high performance speedboat vessels. Samples manufactured under laboratory conditions have been compared with those manufactured by a shipyard. It has been seen that the in-house samples had generally superior performance. Steel-to-composite joints have also been assessed including different designs. The effect of different features in the design such as drilled holes

and bolts on the mechanical performance of the manufactured samples has also been evaluated.

The damage mechanisms involved during damage propagation and features causing damage initiation have been considered. Damage initiation and subsequent evolution have been monitored using acoustic emission (AE). Various signal processing approaches have been employed (manual and automatic) for optimum evaluation of the AE data obtained in a semi-quantitative manner. It has been shown that AE could be applied effectively for structural health monitoring of naval structures in the field. Several factors and parameters that need to be considered during acquisition and analysis have been successfully determined. The key results of the study together with mechanical testing and characterisation of samples employed are presented in summarised form within the present thesis.

Dedication

To my adoring wife Lina, for her being a perpetual source of unconditional love, support and encouragement.

To our son Giorgos who was born during the write-up period of this work and offered lots of pleasant breaks.

Without them my life would be empty and meaningless.

Acknowledgements

During the time working on my Doctoral research project at the School of Metallurgy and Materials of the University of Birmingham, several people have contributed towards my success. Without their support and assistance the successful completion of this work would not be possible.

I wish to take this opportunity to express my sincere gratitude to my supervisor Dr. Mayorkinos Papaelias for offering the opportunity for research under supervision. His deep knowledge, support, encouragement, patience, and precious guidance and suggestions were a significant contribution towards the successful completion of this research work, and enabled me to develop a strong knowledge and understanding on the subject. It was a great pleasure and honour to work with him.

I wish to thank Professor Gerard Fernando for his assistance, support, scientific guidance and constructive criticism which helped me to obtain vital knowledge and complete my research work.

I would also like to express my gratitude to Dr. Surya Pandita for his invaluable contribution on manufacturing the test pieces and for his cooperation during the mechanical tests. I also gratefully acknowledge the technical support provided by Mr Frank Biddlestone, Mr Mark Paget, Mr David Price and Mr David Cope.

I wish to gratefully acknowledge the financial support received from the European Commission through the FP7 project MOSAIC (grant agreement 314037).

I also wish to especially thank my family for their continuous support and encouragement during the past four years that allowed me to complete my research work.

Last but not least, many thanks to my fellow researchers Samuel Olukunle Ojo, Francisco Nieves Bogonez and Richard Murray for their assistance and cooperation in several experimental tasks, as well as maintaining a friendly environment in our work space.

Table of Contents

LIST OF ABBREVIATIONS

ABM	Autoclave Bag Moulding
AE	Acoustic Emission
AEM/S	Advanced Enclosed Mast/Sensor
AFP	Automated Fibre tow Placement
CM	Compression Moulding
CFRP	Carbon Fibre Reinforced Plastics
DAQ	Data Aquisition
DPI	Dye Penetrant Inspection
ECT	Eddy Current Testing
FBGs	Fibre-Bragg Gratings
FFT	Fourier Transform
FRC	Fibre-Reinforced Composite
GFRP	Glass Fibre Reinforced Plastics
HDT	Hit Definition Time
HLT	Hit-Lockout Time
ILSS	Interlaminar Shear Strength
IR	Infrared
ISODATA	Iterative Self-Organising Data Analysis Technique
LVDT	Linear variable differential transformer
LVQ	Learning Vector Quantization
MCMV	Mine-countermeasure vessels
NDE	Non Destructive Evaluation
NDT	Non-Destructive Testing

PAC	Physical Acoustics Corporation
PDT	Peak Definition Time
PZT	Lead-Zirconate-Titanate
RAMS	Reliability, Availability, Maintainability Safety
RI	Resin Infusion
RTM	Resin Transfer Moulding
SHM	Structural Health Monitoring
SOM	Self-Organising Map
SMC	Sheet Moulding Compound
UT	Ultrasonic Testing
UV	Ultra-Violet

LIST OF FIGURES

LIST OF TABLES

CHAPTER 1

INTRODUCTION

1.1 Introduction

1.1.1 Composite materials

Composite materials consist of at least two distinct constituents; a stiff reinforcement, commonly fibres, and a softer constituent that surrounds and binds the reinforcement, forming a continuous matrix. Fibre-reinforced composites (FRCs) comprise an array of stiff fibres embedded in a continuous polymer matrix that binds the fibres into certain orientations. The fibrous phase of a composite material is typically much stiffer than the matrix phase resulting in the FRCs exhibiting high strength and stiffness [1-5].

There various types of FRCs commercially available. The most common types are based on glass, carbon and aramid fibres with diameters ranging from 7μm to 15μm. The fibres are embedded in a thermosetting or thermoplastic polymer matrix. The resulting material exhibits excellent strength to weight ratio [1-4]. High strength and low weight materials are highly desirable particularly for transport, defence and sports structural applications, where high performance and increased corrosion resistance are essential.

The continuously increasing demand for energy efficiency and performance optimisation has driven the transport industry to make widespread use of lightweight materials such as aluminium, magnesium and titanium alloys, and FRCs, for manufacturing of critical structural and engine components.

1.1.2 Composite materials in transport industry, aerospace and automotive

In recent years Airbus and Boeing, have increased substantially the use of FRCs in manufacturing large parts of aircraft, such as the fuselage and wings. The jetliner A310, which entered commercial service in 1983, made use of less than 5% in weight FRCs. The utilisation of FRCs was significantly increased in the construction of A380, which is made of 25% in weight from FRCs. The use of FRCs increased further in the Airbus A350XWB design [6]. The A350XWB entered commercial use in 2015 and it is manufactured in weight from 53% FRCs, 19% aluminium alloys, 14% titanium alloys, 6% steel and 8% miscellaneous materials [7]. Boeing has also increased substantially the use of FRCs, particularly in the B787 Dreamliner aircraft design, which is manufactured in weight from 50% FRCs, 20% aluminium alloys, 15% titanium alloys, 10% steel and 5% miscellaneous materials [8] (Figure 1.1).

FRCs permit a lower overall weight structure resulting in considerably reduced fuel consumption and increased aircraft operational efficiency. Furthermore, improved corrosion and fatigue resistance characteristics contribute to significantly reduce maintenance intervals, resulting in lower repair costs and higher aircraft availability throughout its lifetime [8].

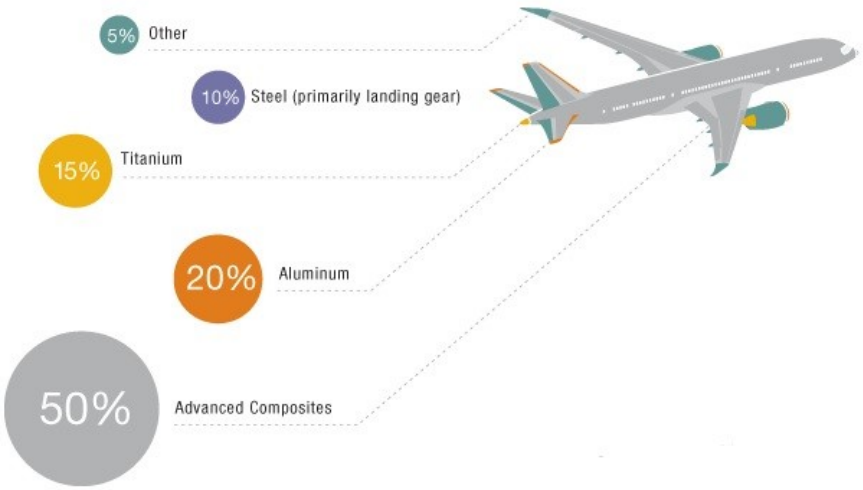

Figure 1.1: Utilisation of FRC materials on the Boeing 787 Dreamliner [8], Copyright © Boeing Company

The need for low-weight and high performance has also led the motorsports industry to make extensive use of carbon fibre-reinforced plastics (CFRP), such as the car body of Formula One racing cars. The use of CFRPs by the automotive industry has so far been limited for the construction of high-speed automobiles, were high performance is favoured over high manufacturing costs. FRCs have been extensively used in the design of the Lamborghini Aventador. Its body panels and monocoque chassis are entirely made of CFRPs [9] (Figure 1.2).

The use of FRCs in the automotive industry is not a novelty. For instance, the body of the 1953 Chevrolet Corvette was made of glass fibre reinforced plastic (GFRP) [3, 5]. The use of FRCs for manufacturing of general production automobiles has strong potential since low weight structures lead to improved fuel efficiency, better performance and reduced greenhouse gas footprint. Moreover, structural components manufactured from FRCs have

excellent crash energy absorption properties which significantly enhance the protection of driver and passengers thanks to the better crashworthiness achieved [10-13].

Figure 1.2: a) Lamborghini Aventador and b) CFRP monocoque chassis,

1.1.3 Composite materials in maritime sector

Ferritic naval steel grades, such as the AH, DH and EH grades, are commonly used in naval construction [14]. FRCs have been increasingly used for the fabrication of leisure, specialised, high performance and warfare vessels. However, the use of FRCs for the construction of larger commercial vessels has been limited. FRCs offer significant advantages over conventional steel structures due to their lower weight, high strength and toughness, improved fatigue properties, and superior corrosion resistance [14-17].

FRCs are non-magnetic and hence exhibit high radar-wave absorption properties, rendering them suitable for military applications [14, 17]. Patrol boats, mine-hunter vessels, corvettes, submarine and warship structural components and superstructures are increasingly constructed using FRCs based on glass and carbon fibres [18, 19]. The photograph in Figure 1.3 shows a Visby class corvette built of FRCs. The Visby class corvette is made of a poly-

vinyl chloride core sandwich structure with carbon and glass fibre reinforced polymer skin [18].

A disadvantage of using FRCs in maritime applications is the higher material and manufacturing cost. However, the initial high cost can be offset by the lower fuel consumption due to the weight reduction of the structure, and lower operational and maintenance cost due to the superior resistance of these materials to sea water corrosion and better fatigue performance [14, 17-20].

Hybrid composite-to-metal joints, are gaining popularity for the construction of maritime components leading to stiffer and lighter structures [21-23]. Hybrid composite-to-steel joints can be utilised for the construction of several structural maritime components including superstructures and decks [21, 24]. Boyd et al. [24, 25] analysed a type of joint that was developed for the helicopter hangar attachment of the La Fayette class frigate. The joint consists of a steel insert within a GFRC sandwich with a balsawood core (Figure 1.4) [24]. The steel end of the hybrid joint can be welded to the steel structure of the ship.

Figure 1.3: Visby Class corvette,

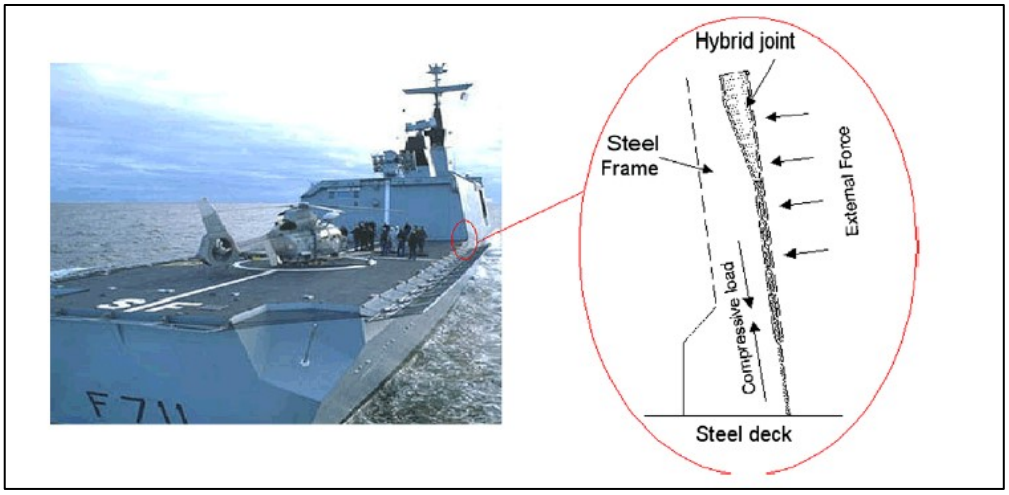

Figure 1.4: Hybrid composite to steel joint on the La Fayette class frigate [24]

Reprinted from Composites: Part B, Vol.39/5, S.W. Boyd, J.I.R. Blake, R.A. Shenoi, J. Mawella, Optimisation of steel–composite connections for structural marine applications, 891–906, Copyright 2008, with permission from Elsevier.

The failure rate and performance evaluation of maritime structures and components manufactured from FRCs is subject to future statistical analysis on the long run. Statistical data presented in previous studies has primarily focused on collisions and accidents due to human error [26-28]. Post-accident activity will require the repair or the replacement of damaged components, and it cannot represent the actual performance and life span of the material. Furthermore, due to the limited use of FRCs in the construction of commercial vessels, no official record of failures on maritime FRC structures is kept.

During the manufacturing process various defects can arise in a composite structure affecting its quality and hence future performance. Manufacturing defects such as voids, fibre waviness, inclusions, errors in the laminate stacking sequence, uncured matrix regions [29], missing fibre tows and fibre overlaps [30] can significantly degrade the strength and the stiffness of FRCs.

Voids are among the most frequently occurring defects during the manufacturing process. Void formation is caused by trapped air and volatile compounds in the composite structure [31], trapped air in the liquid resin [32] or increased moisture content during the manufacturing process [33]. The void content is also affected by the applied autoclave pressure during the curing process. Application of high pressure leads to reduced void content within a composite structure [34]. The presence of voids has a detrimental effect on the mechanical properties of FRCs. For a void content level of 0-5%, each 1% increase in void content leads to a decrease of 9.7% in interlaminar shear strength (ILSS) and 10.3% in flexural strength of FRCs [35]. The flexural modulus is further decreased by 5%. An increase of 2% in void content will cause a further 20% decrease in ILSS and flexural strength, while the flexural modulus decreases by 10% [35]. An increase of 11% in void content causes a drop of 41% in ILSS [36]. High void content is a major quality concern during manufacturing of FRC components. In critical and high performance applications like aerospace structures, low void content levels below 1% are essential for meeting the safety and performance requirements. Components with void content above 1% are not tolerable [34]. In less critical applications, including maritime transport related structures, higher void levels up to 5% are acceptable [35]. Unfortunately the lack of sufficient detail in the current industrial standards concerning maritime vessel construction using FRCs can lead to void contents in excess of 5% and up to 11% [37].

FRCs are becoming increasingly popular for several structural applications. The aerospace sector is already making extensive use of CFRPs. The use of FRC is expanding on the automotive and maritime industry. The production cost of FRC components gradually becomes more affordable. The need for increased fuel efficiency has profound importance increasing the applicability of FRCs in future transport systems on land, in air and at sea.

As the use of FRCs increases it is evident that due care must be taken to control the defects and monitor the structural health of components manufactured from such materials. This is required in order to evaluate the condition of the component in real time and estimate its remaining service lifetime. Since catastrophic failure can have serious implications for any transport system, ensuring structural integrity during operation is a primary concern at all times.

1.2 Importance of Non-Destructive Evaluation of Fibre Reinforced Composite components

FRCs can develop flaws during manufacturing and while in-service. The presence of flaws results in decreased structural integrity adversely influencing future performance and posing a serious safety risk. The increasing use of FRCs by the industry calls for techniques which are able to effectively evaluate the structural health of components manufactured from such materials. To detect manufacturing defects and in-service damage, various Non-Destructive Testing (NDT) methods can be applied. The most common NDT methods include, Ultrasonic Testing (UT), radiography, shearography, infrared thermography and Eddy Current Testing (ECT) [38, 39]. The latter technique is only applicable for CFRCs due to the electrical conductivity of carbon fibres.

The anisotropic and complex nature of FRCs means that different types of defects can initiate and evolve. Taking into account the limitations of each NDE technique in terms of sensitivity and detectability, certain defects and damage modes can be very challenging to identify or

fully characterise [38, 39]. Inspection of FRCs is normally performed during scheduled maintenance intervals.

The application of Structural Health Monitoring (SHM) methods can offer significant advantages over conventional NDT methods. SHM includes methods that can be used while the component is in-service, monitoring damage propagation within the material in real time [40-42]. Instead of inspecting the whole structure to detect the faulty or failed areas, the maintenance engineers can gather the damage related data recorded from the SHM methods and focus their attention directly to the location where the fault or failure are present. Therefore, SHM methods can reduce the inspection time and maintenance cost. SHM can be carried out using a variety of techniques including the analysis of Lamb waves, strain measurements, vibration measurements [40, 41], Fibre Bragg Gratings (FBGs) and distributed optical fibre sensing [43], and Acoustic Emission (AE) [38, 40-42].

AE is a widely applied SHM technique in which piezoelectric transducers are attached on the component during normal service or testing. The AE method is based on the detection of elastic transient stress waves emitted from localised damage sources under load causing damage to evolve in the component being assessed [38, 44-46].

The main limitation of AE is that it is not capable of detecting any defects unless load is applied and further damage growth occurs. Therefore, any damage which is not active will not be detectable. In addition, mechanical and ambient background noise can have a negative impact on the sensitivity of the AE measurements [38]. Damage quantification in composite materials using AE monitoring can be quite complicated due to the anisotropic characteristics of FRCs, and the different damage mechanisms active during structural degradation.

Different damage modes in FRCs can give rise to different AE signal features required to be analysed in order to assess damage severity and monitor the overall structural health of the component effectively. Undesirable AE activity due to echoes and background noise not related to actual damage within the material can be present during monitoring. The presence of echoes and background noise has an adverse effect on the quality of AE results since they can mask signals arising from the sources of actual damage. Although AE is an SHM technique with considerable capabilities and potential, detailed and extensive research is required towards the successful application of the technique for quantifying damage in FRCs.

1.3 Aims and objectives

This project investigated the applicability of AE testing in monitoring damage initiation and evolution in GFRPs. The knowledge obtained in this work can be further developed and applied for the continuous monitoring of structural degradation of naval structures and components under in-service conditions. In-service loading conditions and accidental impacts can result in damage initiation and growth causing AE to be generated. The operational environment involves numerous mechanical noise sources generating high amounts of ambient noise that need to be filtered out. The ambient noise can be eliminated by obtaining the key AE noise signal features, such as duration, rise-time and energy, in order to apply the necessary filters. However, during the development stage of an on-board maritime AE system detailed preliminary research is required in order to obtain the ambient AE noise signals characteristics. In addition the positioning of the AE transducers in the vessel can affect the noise pick-up. As a result for the application of AE in the field, the optimum positioning of

the AE sensors on the vessel to further limit the noise effect and allow effective monitoring of damage would need to be determined.

FRCs are a suitable alternative to conventional steel grade naval construction. During failure FRCs can generate AE signals with different signal features. Therefore the characteristics of AE signals produced during damage propagation in FRCs must be determined and analysed in detail.

FRC single skin or sandwich structures have been widely used until now in many small and medium size high-speed crafts. FRCs have recently begun being introduced in the construction of larger ship structures, such as parts of the superstructure, balconies, hatches, etc. Reduction of vessel deadweight is essential for minimising fuel consumption and increasing speed. The application of general hybrid steel-to-composite structures has been gaining momentum in recent years.

Different manufacturing techniques for FRC plates and steel-to-composite joints have been investigated. The samples evaluated in this study have been manufactured both in-house and by a shipyard enabling the quality between the industrial produced components to be compared. The samples have been characterised with respect to the microstructural characteristics, void content and fabric quality. Furthermore, the flexural and tensile properties have been assessed and damage mechanisms studied. Additional features in the design such as drilled holes and bolts have been evaluated.

The applicability of AE in monitoring structural degradation in GFRPs and composite-to-steel joints is evaluated in this work. Within this study, a signal processing approach based on

the use of data clustering algorithms is proposed for distinguishing and monitoring the evolution of the different types of failure that are active in FRCs under load. The potential for developing further the proposed AE signal analysis for monitoring structural degradation of FRC maritime components and vessels is also discussed.

The main objectives of this study are summarised next.

- Initial testing on E-glass fibre bundle samples to evaluate the capability of the AE sensors in detecting each failing filament during loading and secondly to assess the factors that influence the AE activity recorded.
- Signal processing to obtain the main characteristics of fibre fracture AE signals and AE noise.
- Characterisation of GFRP plates made with different manufacturing methods.
- Mechanical testing on GFRP samples and identification of damage initiation and damage growth by examining the AE graphs.
- Data clustering using the K-means, Forgy ISODATA and LVQ algorithms.
- Comparison of the clustering results from each algorithm.
- Identification of AE signals associated with damage related events and noise.
- Determination of the key features of AE signals associated with the different damage modes.
- Monitoring of the evolution of each damage mode during testing.
- Comparison of the results obtained after the noise cluster is removed and after the manual filtering methods have been applied.
- Bending tests on steel-to-composite hybrid joints and analysis of the AE recorded signals.

- Discussion on the applicability of the AE testing in monitoring structural degradation in FRP components under in-service conditions.

The key results from this work are presented in the following chapters together with the overall experimental methodology employed. The results are also compared and evaluated with those reported in previous published studies.

CHAPTER 2

COMPOSITE MATERIALS AND MANUFACTURING METHODS

2.1 Introduction

Composite materials can be classified in three main categories; particulate, laminated and fibre reinforced composites.

- Particulate composite materials consist of stiff particles evenly distributed in a continuous matrix [4].
- Laminated composites consist of layers of at least two different materials stacked together in a laminate. The resulting material exhibits high strength and stiffness [4].
- FRCs consist of stiff fibres embedded in a continuous and softer matrix. The resulting composites exhibit high strength and stiffness [2, 4, 47].

The key role of the matrix is to bind together and transfer the load to the embedded fibres, while the stiff fibres reinforce the structure and offer high stiffness and strength. The resulting materials have properties such as, toughness, strength, and stiffness that are superior to either fibres and matrix alone [2, 4, 47].

A variety of fibre reinforcement arrangements are commercially available. Continuous fibre tows and rovings, chopped fibres, chopped fibre strands, and a wide range of fibre fabrics are extensively used in manufacturing FRCs [1, 2]. The arrangement and orientation of reinforcement fibres within the composite material can determine the mechanical properties and level of anisotropy exhibited [1].

FRCs with fibres arranged in favoured orientations, are anisotropic and their mechanical properties vary with the direction of loading. Figure 2.1 illustrates the effect of fibre

orientation on the tensile strength of a unidirectional FRC laminate [1, 47]. Higher strength is achieved if the load is applied to the direction of the fibres, while the low strength is obtained if the load is applied perpendicular to the fibres. The tensile strength is gradually decreasing as the angle between the fibre orientation and the applied load increases. It can be seen that the tensile strength does not decrease linearly with the angle between the fibres and the load. This behaviour of unidirectional FRCs is described by the following expression [48]:

$$\frac{1}{{\sigma_{ts}}^2} = \frac{cos^4\theta}{{\sigma_x}^2} + \left(\frac{1}{{\tau_{1,2}}^2} - \frac{1}{{\sigma_x}^2}\right) cos^2\theta sin^2\theta + \frac{sin^4\theta}{{\sigma_y}^2} \qquad \text{(Equation 2.1)}$$

Where:

- σ_{ts}^2 is the maximum tensile strength.
- σ_x is the axial strength in tension.
- σ_y is the transverse strength in tension.
- $\tau_{1,2}$ is the shear strength.
- θ is the angle between the fibres and the applied load.

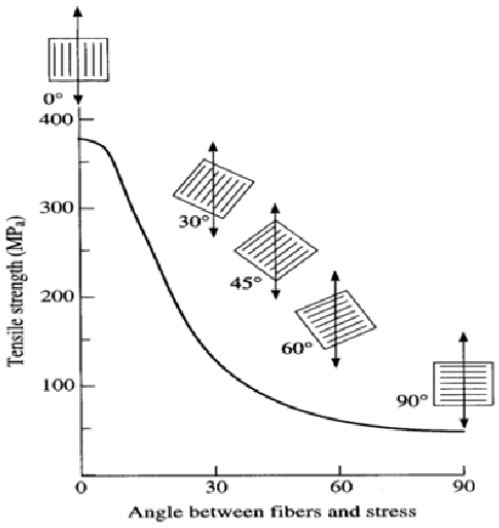

Figure 2.1: Effect of fibre orientation on the tensile strength [47].

2.2 Reinforcing fibres

A wide range of reinforcing fibres and polymer matrices are utilised for manufacturing of FRCs. The most commonly used fibre types are E-glass, S-glass, Carbon, and Aramid. A variety of polymeric, ceramic, and natural fibres are also commercially available.

2.2.1 Carbon fibres:

In graphite carbon atoms are arranged in hexagonal arrays. The atoms in the basal planes are held together with strong covalent bonds. The hexagonal planes are held together with weak van der Waals bonds. Therefore, the crustal structure of carbon is highly anisotropic. The crystal structure of graphite is shown in Figure 2 a). The Young modulus normal to the basal planes is approximately 1000GPa, while parallel to the basal planes just 35GPa [1]. Carbon fibres are typically 8µm in diameter and consist of a turbostatic carbon crystal structure. Turbostatic carbon closely resembles the graphite's crystal structure, except that the graphite layers are not regularly packed in the fibre's axis. The crystal structure of carbon fibres is shown in Figure 2.2 b) [1]. It can be seen that to obtain high Young's modulus and strength, the basal graphite levels must be oriented in the fibre's axis.

Carbon fibres are commonly produced by using poly-acrylonitrile (PAN) fibres. PAN fibres are initially stretched to align the polymer chains within the fibres. Under tension the PAN fibres are then heated in a hot air atmosphere at a temperature range of 200-300^{o}C. At this stage crosslinking of the polymer chain takes place. The ultimate turbostatic graphite structure is produced in the subsequent carbonisation step, while fibre tension is being

retained. Carbonisation often starts in a low temperature furnace at 700-800°C, and ends in a high temperature furnace ranging at 1200-1500°C. Further crystallisation of the graphite structure is achieved by carbonising at temperatures up to 2480°C [49].

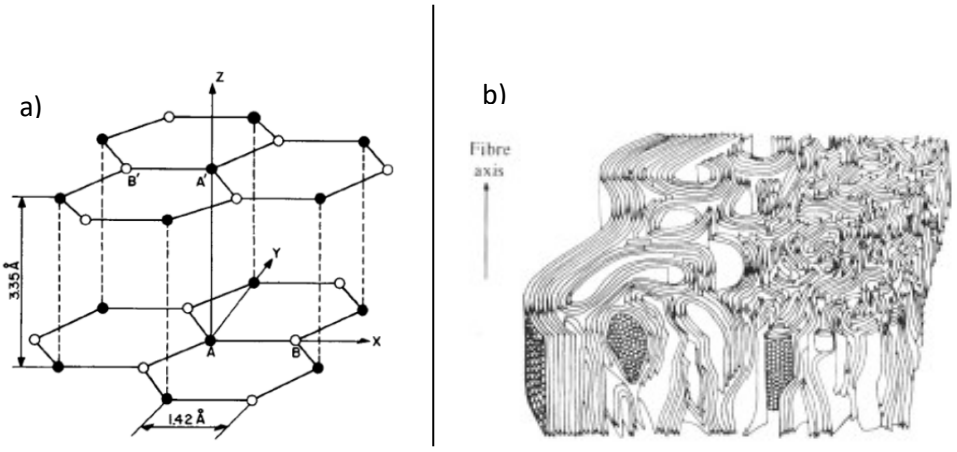

Figure 2.2: a) Graphite structure [47] and b) Carbon fibre structure [1].

2.2.2 Aramid fibres

Aramid fibres have been developed from polyamide polymers and exhibit high modulus of elasticity. Aramid fibres were first developed by DuPont under the trade name Kevlar™ [1]. The use of Aramid fibres was initially intended for reinforcing tiles and plastics. The light weight, high strength and high toughness of these fibres have led to the development of applications in structural components, sails, armours, tyres, and high performance personal protective equipment [2]. Aramid fibres are derived from aromatic polymer molecules. These polymer molecules act as rigid rods in solution and align parallel to each other to form

ordered and aligned domains. A solution of aromatic polymer is passed through a spinneret to develop a high orientation of the ordered aromatic polymer chains to the flow direction. The solvent is then removed and further alignment of the molecules takes place during suitable heat treatment. The polymer chain molecules are aligned to the fibre axis resulting in high axial strength. However, due to the weak inter-chain hydrogene bonding, aramid fibres are highly anisotropic. Kevlar^{TM} 49 fibres exhibit an axial Young's modulus of 130GPa, while the radial modulus is only 10GPa. Due to the weak inter-chain bonding, aramid fibres tend to split into finer fibrils during failure. This is commonly seen during failure of Kevlar^{TM} FRCs [1].

2.2.3 Glass fibres

Glass fibres are the most widely used in manufacturing of structural FRCs. They exhibit high strength and stiffness, and resistance to chemical attack [2]. Glass fibres are mainly composed of Silicon oxide (SiO_2) with further additions of Boron, Calcium, Sodium and Aluminium oxides. The types of glass fibres that are commercially available are E-glass, S-glass and C-glass [1].

E-glass (where E stands for electrical), is the most commonly used type of glass fibres and exhibits high strength and stiffness, good electrical and weathering properties. C-glass (where C stands for corrosion), has improved corrosion resistance compared to E-glass, but exhibits lower strength. S-glass (where S stands for strength), exhibit higher strength, modulus and temperature resistance compared to E-glass, but they are more expensive [1].

Glass fibres are produced by extruding melted glass through a series of metal bushings, each of which has hundreds of holes in its base. Under the influence of gravity the melted glass flows through the bushings and fine filaments are mechanically drawn. The fibres are wound on drums at several thousand meters per minute. The diameter of E-glass fibres ranges between 8-15μm. During the manufacturing process a thin emulsified polymer binder is sprayed on the fibres. The key role of the binder is to protect the fibres from surface damage during processing, to bind the fibres together, and increase the interfacial strength between the fibre surface and matrix [1].

Glass is a macroscopic amorphous material. Therefore, the strength and elasticity modulus of the different types of glass fibres are determined by the atomic structure. Glass fibres based on SiO_2 have a tetrahedral atomic network with a silicon atom at the centre forming covalent bonds with oxygen atoms at the four corners. The resulting structure is a rigid tetrahedral covalently bonded network. The network can be disrupted by the presence of non-covalent elements (e.g. Ca, Na and K) which in turn form ionic bonds with the oxygen atoms and result in decreased strength. However, the presence of Ca, Na and K can improve the flexibility of glass fibres. Unlike carbon and aramid, glass fibres are isotropic and have the same transverse and axial Young's moduli of 76GPa [1].

The properties of different types of reinforcement fibres are shown in Table 2.1. It can be seen that the strain at failure for the fibres used for FRC manufacturing ranges from 0.6% to 3%. In contrast, the maritime steel grades are able to sustain strains up to 20%. FRCs are not capable of sustaining such high strain levels due to the low failure strain of their reinforcing fibres. As a result, the maritime design standards need to be revised for FRCs.

Table 2.1: Properties of several fibre types [1]

Fibre	Density P (Mg/m)	Young Modulus E (GPa)	Poisson's ratio ν	Tensile strength σ_{uts} (MPa)	Strain at failure ε_f (%)	Thermal expansivity α (10^{-6} / K)	Thermal conductivity κ (W/(mk))
SiC monofilament	3.0	400	0.2	2.4	0.6	4.0	10
Boron Monofilament	2.6	400	0.2	4.0	1.0	5.0	38
High Modulus Carbon	1.95	axial 380 radial 12	0.2	2.4	0.6	axial -0.7 radial 10	105
High Strength Carbon	1.75	axial 230 radial 20	0.2	3.4	1.1	axial -0.4 radial 10	24
E-Glass	2.56	76	0.22	2	2.6	4.9	13
Nicalon™	2.6	190	0.2	2	1.0	6.5	10
Kevlar 49™	1.45	axial 130 radial 10	0.35	3	2.3	axial -6 Radial 54	0.04
FP™ fibre	3.9	380	0.26	2.0	0.5	8.5	8
Saffil™ fibre	3.4	300	0.26	2.0	0.7	7.0	5
Sic Whisker	3.2	450	0.17	5.5	1.2	4.0	100
Cellulose (flax)	1.0	80	3.0	2.0	3.0	-	-

2.3 Reinforcement types

The mechanical properties of FRCs are strongly dependent on the fibre arrangement and distribution within the structure. All reinforcing fibres exist over a wide variety of arrangement types. During the production process continuous tows of fibres are wound in rotating drums and form continuous fibre rovings. Several types of rovings are available and fibre tows consist of just few hundreds up to several thousands of individual filaments [3].

FRCs can also consist of chopped fibres randomly distributed within the polymer matrix. The resulting material exhibits isotropic mechanical properties due to the random distribution and orientation of the fibres [1, 3].

Continuous fibres can be arranged into stitched or woven fabrics. Fibre textiles can be unidirectional or biaxial. Unidirectional fibre fabrics consist of several continuous fibre tows orientated at the same direction, which are bound together by continuous stiches [2]. Biaxial fibre fabrics consist of continuous fibre tows orientated along two perpendicular directions. Woven fabrics are constructed of fibre tows which are bi-directionally interlacing with over-under placement during the weaving process. To satisfy the requirements of specific applications, different weave patterns such as plain, twill-weave and satin weave are available [5]. In bi-axial stitched fabrics individual layers of oriented fibre tows in the transverse and longitudinal directions are stitched in place using continuous threads. Stitched fabrics are available in a wide range of multi-ply orientations [50]. The directions of the fabric are called wrap and fill (or weft) respectively. Wrap is the direction in which the fibres run along the continuous length of the fabric roll, while fill is the transverse direction in which the fibre tows run along the width of the fabric. Another commonly used type of fibre arrangement form is the chopped fibre mat. Chopped fibres are arranged in random plane orientations. Hence, the resulting FRC exhibits isotropic mechanical properties [1].

A widely utilised fibre preform for manufacturing FRCs is the fibre prepreg. Prepregs consist of a uni-directional array of fibres or fibre fabrics, pre-impregnated with uncured resin [2, 5]. During the manufacturing process layers of prepregs are laid-up to develop the desired structure. The uncured lay-up of prepregs is then cured to a rigid and stiff composite structure.

2.4 Matrices

The other important constituent of FRCs is the matrix material. The matrix apart from protecting and binding together the reinforcing fibres transfers and distributes the applied load to them. The matrix is usually a thermosetting polymer but thermoplastics can be used also.

2.4.1 Thermosetting resins

Thermosetting resins are the most extensively used matrix materials in manufacturing of FRCs. Epoxy, polyester and vinyl-ester resins are the most commonly used [1, 19, 47, 51]. Liquid resin is formed into a hard and rigid network by cross-linking during the curing process. Curing can be achieved at room temperature, but it is common to use heating for a specific time in order to achieve optimum mechanical properties. Shrinkage during curing and cooling after the cure cycle can lead to residual stresses in the FRC. Thermoset materials are stiff and rigid and fail in brittle manner [1]. A main disadvantage of thermosetting polymers is that the cross-linking process cannot be reversed. Thus, thermoset matrices cannot be re-moulded or reused.

2.4.1.1 Polyester resins

Unsaturated polyester offers an effective combination of moderate cost and good mechanical performance. Liquid polyester resin is a solution in which the styrene solvent reacts with the

polymer under the presence of a peroxide catalyst and a cobalt octoate-based accelerator to form a rigid cross-linked network. The curing reaction is exothermic and provides the necessary heat to aid the curing process. However, the thickness of the laminate must be limited, as excessive thickness can cause heat build-up sufficient to damage the material during manufacturing. Resin shrinkage between 5-8% occurs during the curing process [19].

The main types of polyesters are [19]:

- Orthopthalic polyesters containing maleic and phthalic anydrites with an addition of propylene glycol. They are the cheapest and most widely used matrices for the construction of small boats.
- Isophthalic polyester consists of isophthalic acid instead of phthalic anhydrite. It is more expensive but has better mechanical properties and water resistance compared with orthophtalics. The improved water resistance can be advantageous for the construction of high performance boats and marine gel coats.
- Bisphenol polyesters, where the phthalic acid and phthalic anhydrite are replaced by bisphenol A, offer improved water and chemical resistance, but at higher cost.

2.4.1.2 Vinyl ester resins

Vinyl ester resins are chemically similar to epoxies, but the curing process is similar to that of polyester resins. Similarly to polyesters, the liquid resin is a solution in which the styrene solvent reacts with the polymer under the presence of a peroxide catalyst and a cobalt-based accelerator, to form the rigid cross-linked network. Vinyl ester resins are cold cured and curing reaction is exothermic [19].

Vinyl ester has significantly higher cost compared to the isophthalic polyester (estimated cost of $5180.00/tonne for the vinyl ester resin, against $4070.00/tonne for the isophtalic polyester resin [52]) but exhibits superior resistance to water and chemical attack, better strength and stiffness at elevated temperatures, and greater failure strain compared with polyesters.

2.4.1.3 Epoxy resins

Epoxy resins are used for the construction of high performance FRC laminates. Epoxy resin shrinkage of 3% occurs during cure. This is lower compared with the shrinkage of polyesters. Epoxies offer improved mechanical properties compared with polyesters. Although the cost of epoxy resins is generally high, they are often preferred in high performance applications

Curing of epoxy resins requires the addition of hardener as a reactive for the cross-linking process. Epoxies cured at elevated temperatures of 60–150°C are used in pultrusion, filament winding and compression moulding processes. Cold-curing in the range (20-25°C) is suitable for contact moulding processes. Cold-cured resins have slightly inferior mechanical properties compared with those obtained from hot cured epoxies [19].

2.4.2 Thermoplastic resins

Thermoplastic polymers derive their strength from the inherent properties of the polymer chains and high molecular weight. In amorphous thermoplastics the high concentration of molecular entanglements between polymer chains lead to a rigid network. In semi-crystalline thermoplastics, a high degree of molecular order is present within the molecular structure. Heating of amorphous materials leads to a disentanglement of the polymer chains and the material softens and becomes a viscous liquid. In semi-crystalline materials heat causes the crystalline phase to melt and result in an amorphous and viscous liquid [1].

Thermoplastic materials can develop anisotropic behaviour during the solidification. In amorphous materials the polymer chains can be aligned during the melt flow or under plastic deformation. In crystalline polymers the crystalline phase can develop dominant orientation because of the non-uniform nucleation at the surface of the fibres, or during the melt flow. Temperature gradients in the melt can also cause dominant orientation and lead to anisotropic behaviour [1].

Thermoplastics show high strains before failure, high resistance to chemical attack good thermal stability and resistance to water absorption. However, nylons do not show good resistance to water absorption due to the high degree of crystallinity in their structure. The properties of common thermosetting and thermoplastic polymers are shown in Table 2.2 [1]. Thermoplastics can undergo high amounts of deformation and sustain high strains. However, the molecular weight, the structure of the polymer chains, the crystallisation degree and inter-chain interactions affect the Young's modulus and the strength of the polymer.

Processing of thermoplastic FRCs can be more difficult compared with thermosets. This happens because thermoplastics are already formed polymers and their melts are highly viscous which cannot be easily impregnated in an array of fibres [1]. Thermoplastic FRCs are primarily manufactured by chopped fibres with length in the range of 3-12mm with the resin in a melt condition [53]. The use of continuous long fibres can be difficult and complicated from the melt condition due to the poor impregnation of the high viscous melt.

Table 2.2: Properties of thermosetting and thermoplastic resins [1]

Matrix	Density ρ ($Mg\,m^{-3}$)	Youngs's modulus E (GPa)	Poisson's Ratio ν	Tensile strength σ_{max} (MPa)	Failure strain ε_f (%)	Thermal expansivity α ($10^{-6}\,K^{-1}$)	Thermal conductivity κ ($W\,m^{-1}\,K^{-1}$)
Thermosetts							
Epoxy	1.10 - 1.4	3 - 6	0.38 – 0.4	35 - 100	1 - 6	60	0.1
Polyestsers	1.2 - 1.5	2 – 4.5	0.37 – 0.39	40 - 90	2	100 - 200	0.2
Thermoplastics							
Nylon 6,6	1.14	1.4 - 2.8	0.3	60 - 70	40 - 80	90	0.2
Polypropylene	0.90	1.0 – 1.4	0.3	20 - 40	300	110	0.2
PEEK	1.26 -1.32	3.6	0.3	17	50	47	0.2

2.5 Fibre-Matrix interface

The fibre-matrix interface is the boundary between a fibre and matrix. The role of the interface is critical as applied loads are transferred from the matrix to the fibres through the interface. Therefore, the characteristics of the interface have a crucial role on the final mechanical properties of the FRC [1].

Absorption and wetting plays an important role on the interfacial adhesion between the fibres and matrix. If the contact angle of the liquid resin to the fibre is small, sufficient wetting of the fibres takes place and a strong interfacial bond can form. Adhesion is primary caused by van der Waals bonding. Other types of bonding have positive impact on interfacial adhesion.

Other fibre-matrix interfacial bonding types are chemical bonding, interdiffusion processes, electrostatic attraction, and mechanical keying [1]. The features and strength of the interface are strongly dependent on the fibre-matrix system.

Fibres are often coated with special coupling agents in order to improve interfacial bonding. Glass fibres are treated with silane coupling agent. Silane agents are complex molecules which react and bond at one end with the glass and at the other with the polymer matrix. The silane coating is water-resistant and forms a strong bond with polymer matrices. In a thermosetting matrix, silane reacts with the liquid resin during curing and forms a permanent link. For a thermoplastic matrix the covalent links of the polymer are chemically connected to the silane and form a strong interfacial bond [1].

2.6 Manufacturing methods

FRCs can be manufactured through various routes. The most widely utilised manufacturing methods are:

- Hand Lay-up
- Spray-up
- Resin Transfer Moulding
- Vacuum Bag Moulding
- Resin Infusion
- Autoclave Bag Moulding
- Compression Moulding
- Automated Fibre Tow Placement

- Filament Winding
- Pultrusion
- Sheet Moulding Compound

2.6.1 Hand Lay-up

Hand lay-up is one of the most common manufacturing routes for the construction of FRC components. In hand lay-up an open stiff and rigid mould is used. Prior to the lay-up process the mould can be coated with an appropriate release agent that will ease the de-moulding of the finished part after the curing. Furthermore, the mould can be optionally coated with a gel coat finish layer when a high quality surface finish is required for the final component. After the mould surface preparation is complete, layers of dry fibre reinforcements are placed on the mould by hand. The reinforcement fibres are arranged along the direction of the design loading conditions. Additional layers can be added to further reinforce the cured part along a specific direction. The layers of the dry fibres are impregnated with resin. A hand roller is then used to consolidate the laminate and squeeze the air pockets out of the structure. After lay-up the laminate is cured. The finished part is de-moulded after curing has been completed [2, 5, 19]. Hand lay-up is used in manufacturing of boat hulls and decks, tanks and vessels, and other components for the transport industry [2]. The hand lay-up route is shown in Figure 2.3.

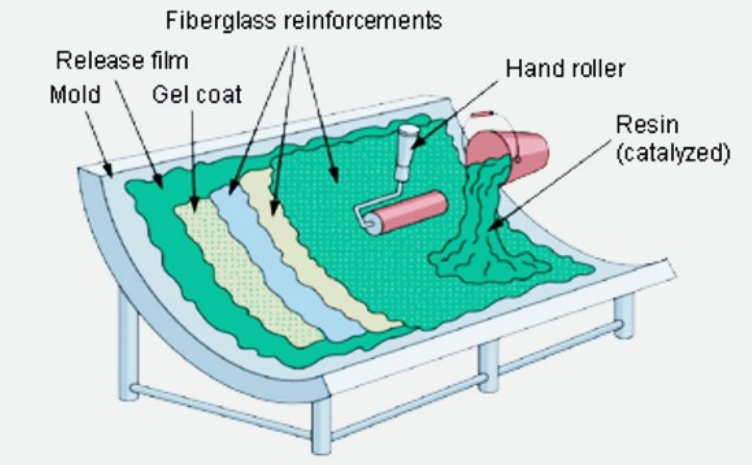

Figure 2.3: Hand lay-up process [54].

2.6.2 Spray -up

Spray-up is a common manufacturing route similar to the hand lay-up used for the same applications. Reinforcing fibres are chopped and sprayed simultaneously with the resin system onto the mould using a spray gun. The fibre-resin mixture is manually consolidated on the mould with hand rollers [2, 4, 19]. The length of the chopped fibres ranges from 12-50mm [4, 19]. After curing the cured part is removed from the mould. The spray-up process is shown in Figure 2.4.

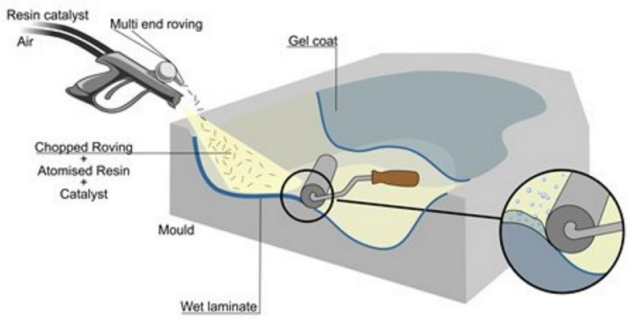

Figure 2.4: Spray-up process [55].

2.6.3 Resin Transfer Moulding

Resin Transfer Moulding (RTM) is a manufacturing route where dry reinforcing fibres are enclosed in a die cavity, and the resin-catalyst mixture is injected under low pressure in the mould. The curing process is often heat-assisted and carried out in the mould. RTM is used for the construction of automotive body parts [1, 2, 4, 5]. The principle components of RTM are shown in Figure 2.5

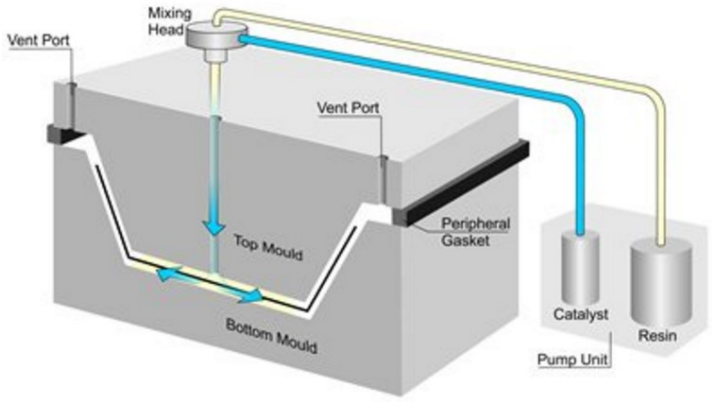

Figure 2.5: RTM process [56].

2.6.4 Vacuum Bag Moulding

In Vacuum Bag Moulding (VBM) or Vacuum Bagging the impregnated fibre lay-up is placed in a sealed flexible plastic sheet. The lay-up is cured under pressure by applying vacuum in the space between the plastic sheets which contains the fibre lay-up. Under atmospheric pressure the resin-impregnated fibres are consolidated and trapped air pockets are squeezed out of the laminate [5]. After curing, the sealed bag is opened and the cured part is removed

from the mould. VBM is used in the construction of a wide variety of components including large boats [19].

The key characteristics of VBM are shown in Figure 2.6. A plastic film is placed on the mould to ease the removal of the cured laminate. A piece of release film or peel ply fabric is placed on the plastic film, and impregnated fibres are placed on the release film/peel ply. Another piece of peel ply or release film is placed on the impregnated fibres. A piece of breather fabric is then placed on the release film or peel ply. The vacuum hoses are placed on top of the breather, through which the air is driven out of the lay-up. The system is then cover with a piece of plastic film and sealed with appropriate sealant tape.

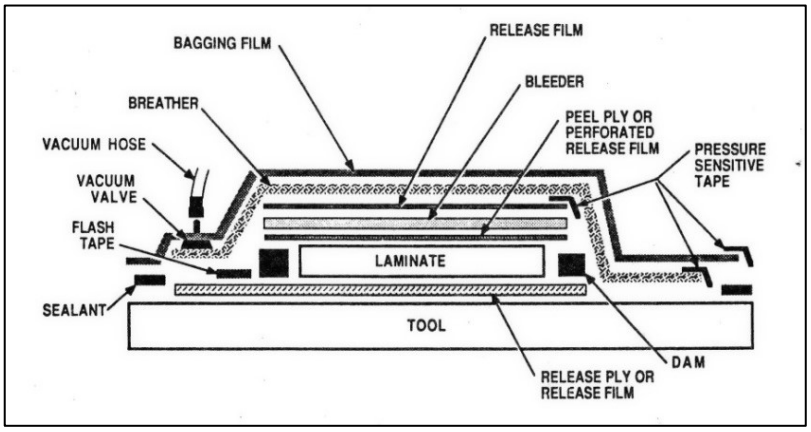

Figure 2.6: Vacuum bagging lay-up [57].

2.6.5 Resin Infusion

Resin Infusion (RI) is a manufacturing route where curing and consolidation takes place under pressure. The lay-up of dry reinforcing fibres is placed in a mould which is closed in plastic bag system. Under vacuum the resin is sucked in the sealed bagging system,

impregnating the fibres. The atmospheric pressure consolidates the laminates. After curing the sealed bag is opened and the cured part is removed from the mould. RI is widely used in manufacturing of decks and hulls for recreational boats, military vessels, other transport applications and wind turbine blades [2].

The RI characteristics are shown in Figure 2.7. Similarly to the VBM, a plastic film is placed on the mould to ease the removal of the cured laminate. A piece of release film or peel ply fabric is placed on the plastic film, and impregnated fibres are placed on the release film/peel ply. Another piece of peel ply or release film is placed on the impregnated fibres. A piece of resin flow medium is then placed onto the peel ply or release film. The resin inlet tube is placed on the resin flow media, whereas the resin outlet and vacuum lines are placed on the peel plies that surround the reinforcement fibres. The system is then covered with a piece of plastic film and the RI lay-up is it is sealed with appropriate sealant tape. Under vacuum the resin is sucked through the resin inlet impregnating the fibres. After the impregnation is complete, the resin inlet is clamped and the laminate is cured under vacuum.

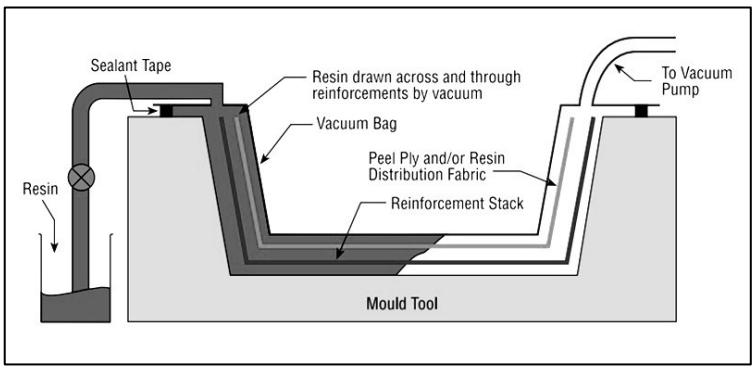

Figure 2.7: Resin Infusion manufacturing route [4].

2.6.6 Autoclave Bag Moulding of pre-impregnated fibre forms

High performance FRC components are often constructed using lay-ups of fibre prepregs, which are consolidated and cured in an autoclave oven under pressure at elevated temperatures. Aircraft wings and fuselage components, and high performance automotive parts are manufactured using the Autoclave Bag Moulding (ABM) Route [2].

Fibre prepreg layers are stacked in predetermined fibre orientations placed in an open mould. The prepreg laminate is placed between two layers of release film, while a further layer of plastic film is placed over the laminate and sealed against the mould with appropriate sealant tape. The lay-up is then placed in the autoclave and vacuum is applied between the bagging material and the laminates, so that the plies of prepregs are consolidated and compressed through the thickness against the mould. The autoclave applies high pressure at elevated temperatures to improve the consolidation and cure the resin. As the temperature in the autoclave is raised, the viscosity of the resin is lowered. Under high pressure the gases within prepreg layers are removed from the lay-up, reducing the void content in the cured laminate to <1%. A layer of release film and a layer of breather fabric is placed under the bagging sheet to enable the evacuation process and removal of gases [50]. The characteristics of the bagging lay-up for the autoclave processing are shown in Figure 2.8.

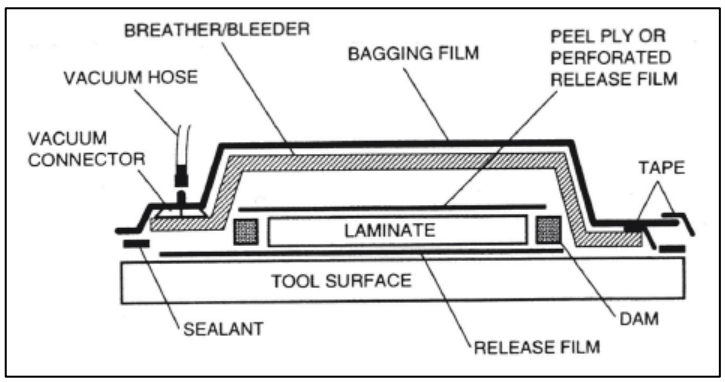

Figure 2.8: Autoclave vacuum bagging lay-up [57].

2.6.7 Compression Moulding

In Compression Moulding (CM) a closed mould is used to form and cure a composite structure. CM is used for the construction of automotive and aerospace components. Impregnated reinforcements or fibre preforms are initially placed on the open lower counterpart of the mould. The upper counterpart of the mould closes the mould, and under the action of the applied pressure it forms the pre-impregnated reinforcement into the final shape. Furthermore, the mould is usually heated to cure the resin [2, 5]. After curing the mould is opened and the cured component is removed. The compression moulding route and the spreading of the moulding material into the mould cavity are shown in Figure 2.9.

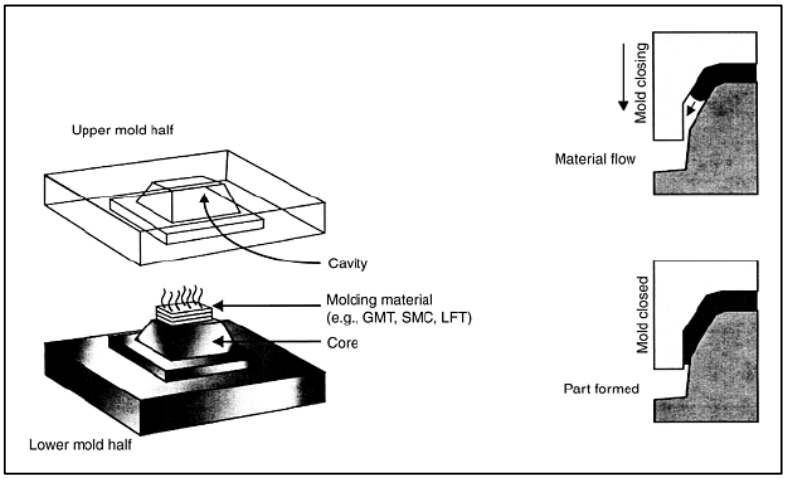

Figure 2.9: Compression moulding process [2].

2.6.8 Automated Fibre Tow Placement

In Automated Fibre tow Placement (AFP) individual resin impregnated fibre tows are fed through a computer-controlled head. The automated head places the fibre tows onto a work surface. The width of the fibre tow can be adjusted to eliminate the gaps and overlaps. During placement the dispensing speed varies, allowing the tows to conform to the mould, or part geometry. The placement head is often equipped with a rolling device to compact and consolidate the placed fibre tows on the lay-up. AFP has the unique capability of maintaining a true fibre orientation on a complex contour surface. AFP is primarily used for the construction of commercial and military aircraft components [2, 50]. The head of the automated fibre placement is shown in Figure 2.10.

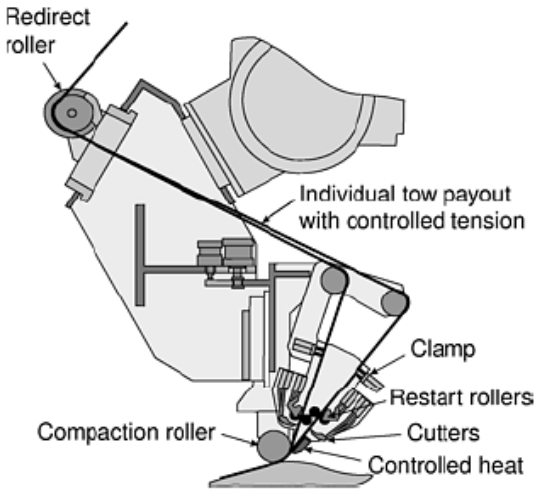

Figure 2.10: Automated fibre tow placement head [2].

2.6.9 Filament winding

Filament winding is an automated process in which continuous fibre tows impregnated with liquid resin are wrapped round a rotating mandrel [2, 5, 19]. Filament winding is used for manufacturing pressure vessels, gas storage tanks, rocket motor components, aircraft fuselages [2] piping systems, oil and water storage tanks, radar domes and torpedo hulls [19]. The filament winding process is shown in Figure 2.11.

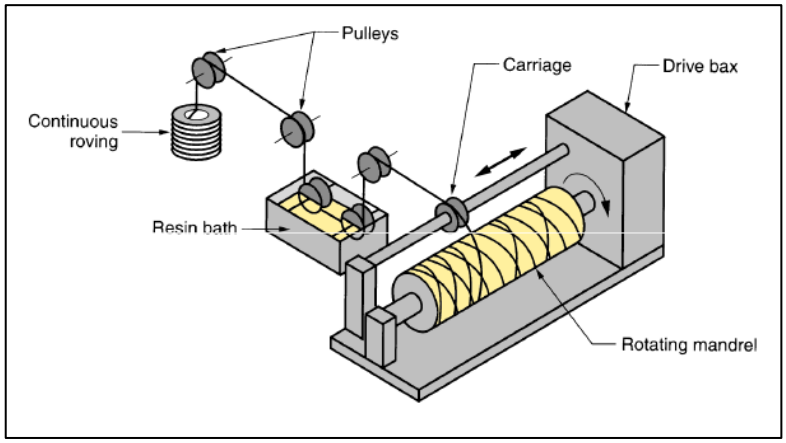

Figure 2.11: Filament winding manufacturing process [57].

2.6.10 Pultrusion

Pultrusion is a process for the manufacturing of continuous composite profiles with constant cross section. In pultrusion dry fibre tows are pulled from their creels into a resin bath. The resin impregnated fibres are then passed through a die which shapes the fibres into the desired profile. At this point the pre-shaped resin impregnated fibres are drawn into a heated metal die which cures the resin to its final shape. The cured profile exits the mould as it is continuously pulled by a clamping mechanism. The product cools down as it emerges from

the puller mechanism and is cut to the desired length [2]. The pultrusion process is illustrated in Figure 2.12.

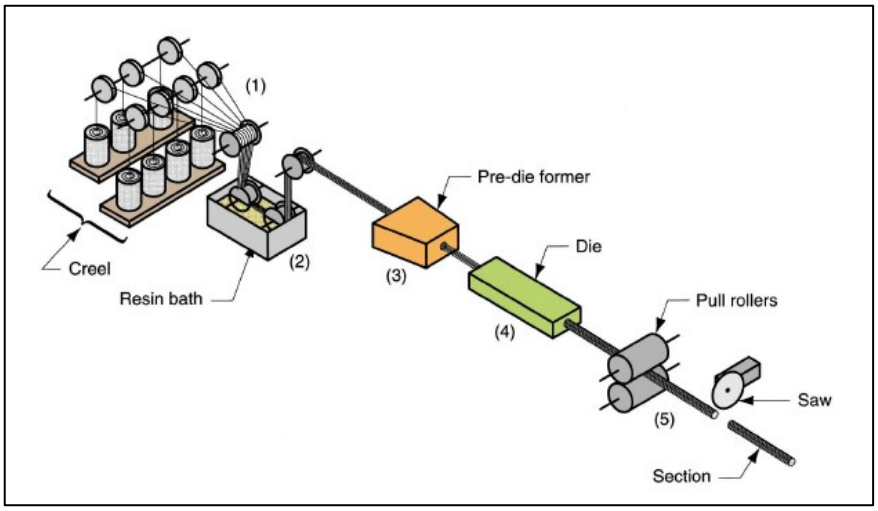

Figure 2.12: Pultrusion manufacturing process [57].

2.6.11 Sheet Moulding Compound

In Sheet Moulding Compound (SMC) a thermosetting resin is mixed with thickening agents, particulate fillers such as $CaCO_3$, and chopped fibres to form a slurry. The slurry is then placed between two thermoplastic films and passed over a series of rolls to impregnate the reinforcement fibres and consolidate the structure. After the consolidation step the fibres lie in the plane of the sheet. The thermoplastic films are subsequently removed. The consolidated sheet is then passed through a hot press mould which cures the resin and produces the final product [1].

CHAPTER 3

COMPOSITE MATERIALS AND STRUCTURES FOR MARITIME APPLICATIONS

3.1Introduction

FRCs are increasingly used in the place of conventional naval steel grades, primarily due to the requirements for lightweight, high-strength and corrosion resistant structures. The superior fatigue cracking and corrosion resistance of FRCs can increase design lifetime whilst contributing to reduced maintenance costs. A lightweight FRC structure can help minimise fuel consumption and enable higher operational speeds [14-18]. The paramagnetic nature and high absorptivity of radar waves that FRCs exhibit, has led the defence industry to gradually increase their use in the construction of high speed military vessels with increased payload capabilities and low radar signatures [18].

The use of hybrid composite-to-metal joints is gradually increasing. FRC-to-steel joints are used for the construction of less critical load bearing applications like superstructure components and decks. Reduced superstructure weight increases the payload capability and helps increase the maximum speed of the vessel [24, 25]. Hybrid joints generally consist of a steel insert within an FRC component. The FRC component is connected to the vessel's main structure by welding the steel end of the joint to the steel structures of the ship.

A key consideration in constructing maritime components and vessels using FRCs is the manufacturing cost. However, the high initial cost is offset by reduced running and maintenance expenditure due to lower weight, superior fatigue and corrosion resistance [14-18].

3.2 Performance of FRC materials in the marine industry

FRCs are used over a wide spectrum of applications ranging from pleasure boats and military vessels to helicopter decks and superstructure components [58].

3.2.1 Weight reduction

Conventional steel maritime structures are heavy. The increased weight of the structures leads to lower operational speeds increasing significantly fuel consumption. Heavyweight vessels can have an adverse effect on the ship's payload carrying capacity and hydrodynamic performance [14]. Increased use of FRCs in construction of structural components can overcome these problems as the reduced structural weight can increase the payload capability, improve operational range and maximum operational speed while lowering fuel consumption considerably.

3.2.2 Stiffness and strength of FRC structures

The weakness of steel structures lies on the local stress concentration points which are prone to fatigue cracking. Cyclic loading occurs in maritime structures due to variations of loading conditions during vessel operation and machinery-induced vibrations. These variable loading conditions induce fully reversed tensile to compressive stresses causing fatigue damage initiation and propagation [19]. The low stiffness issues arise usually around superstructure components. Over the years the need for stiffer structures has been a key priority for the

maritime industry [14]. The use of GFRPs for the construction of superstructure components can overcome the low-stiffness problems [59], thanks to the improved strength and fatigue cracking resistance [14-17, 19, 60].

Steels exhibit a Young's Modulus of 250GPa, while AH36 grade steels exhibit a Yield Stress (YS) of 365Mpa and Ultimate Tensile Strength (UTS) of 490MPa [61]. Typical GFRPs reinforced with E-glass fabric and with a fibre fraction of 50% exhibit a Young's modulus of 25GPa, and a UTS of 440MPa. In addition, CFRPs reinforced with carbon fibre fabric have a Young's modulus of 70GPa, and a UTS of 600MPa [62]. FRPs exhibit greater strength-to-weight ratio compared to steel due to their low density (ρ_{GFRPs} =1.9 g/cm^3 and ρ_{steels}=7.8 g/cm^3).

High fibre content improves the fatigue cracking resistance of FRCs and results in reduced matrix strains [63-65]. Brunbauer et al. [65] reported that an increase in the fibre fraction from 30% to 55% in a unidirectional CFRP, increases the fatigue limit from 267MPa to 435MPa.

The use of GFRPs is not limited to superstructures, but can also be used to hull fabrication. Therefore, the further assessment of the strength and stiffness of load bearing components has been an important task for assuring the safe and reliable service of GFRP components. Reliability analysis studies [66, 67] have been carried out to determine and predict the longitudinal strength of an FRC hull under hogging, sagging and slamming conditions. Finite Element Analysis (FEA) has been carried out to simulate the behaviour of FRP structures under slamming impact conditions, with damage being present in the material [68].

Impact loads induce high local strain rates in a material. The mechanical properties of an FRC laminate under impact loading can significantly differ from the static and slow loading rate conditions [19]. The strain rate $\dot{\varepsilon}$ is defined as: $\dot{\varepsilon} = d\varepsilon/dt$. A static or slow strain rates introduced by waves and normal cruising conditions, lie in the range between 10^{-4} and $10^{-3}s^{-1}$. Under vibration loading conditions in the range of 10 to 50 Hz caused by the engine and propellers, strain rates of $10s^{-1}$ are induced in the FRC laminate. Under impact loading conditions caused by wave slamming, collisions, explosions and ballistic impacts, high strain rates up to $10^{3}s^{-1}$ may occur. Impact damage can cause multiple types of damage such as delamination, fibre breakage, matrix cracking and surface damage. As shown in Figure 3.1, an increase in the strain rates leads to a subsequent increase in strength and Young's modulus in FRC laminates[19, 69]. The effect of the strain rate on mechanical properties is greater in laminates with woven reinforcement fabrics than unidirectional laminates [19].

Khan et al. [69] presented the mechanical properties at increasing strains of an isophthalic polyester matrix composite reinforced with a 0/90 bidirectional woven fabric with an outer chopped strand mat. The laminates were subjected to compressive loading in the normal and in-plane orientations (Figure 3.2). When the FRC laminate is loaded to the normal direction, the maximum strength levels were five times higher compared with those obtained in the in-plane direction. However, the modulus levels obtained in the normal direction were lower than in the in-plane direction. Furthermore, in the normal direction of loading, high strain rates up to $10s^{-1}$ increases the maximum strength and modulus by 16% and 18% respectively. The strain rate had negligible effect on the maximum strength and modulus in the in-plane direction, due to the uniform shear stress concentration between the plies. The strain rate had no effect on the maximum strain in both loading directions [69].

Impact loads are commonly induced in maritime structures caused by transient hydrodynamic pressures (wave slamming) and impact forces arising from collisions or dropped weights caused from mishandling during maintenance or cargo loading. High impact loads can also be experienced due to air-blasts and explosions [19]. GFRPs provide significantly improved impact resistance compared to a conventional steel grades [17]. Improved resistance to impact load can be achieved by using rubber additives in the resin mixture, reducing however the Young's modulus of the resin system. Transverse impact strength can be enhanced by using fibre fabric preforms, which provide a degree of Z-direction reinforcement, at the expense of in-plane stiffness and strength [19].

FRCs provide satisfactory resistance against blast and ballistic impact loading, especially under collision with small ballistic arms [14, 19]. Chalmers et al. [14] reported that resistance to ballistic impact can be achieved with double skin structures, where the first skin absorbs part of the projectile's ballistic impact and the second skin stops the projectile. A similar structure can be used to provide blast protection and minimise local damage. A door or a hatch made of FRCs can provide both protection against ballistic impact and weight savings. Thus, FRCs exhibit sufficient resistance against high strain rates and impact loading. The resistance of FRPs in ballistic collisions and explosive blasts depends primarily on the type of fibre reinforcement. The resistance to explosive blasts is higher for GFRPs compared to the CFRPs. This property results from the higher flexural and tensile failure strain of GFRPs compared to CFRPs [70].

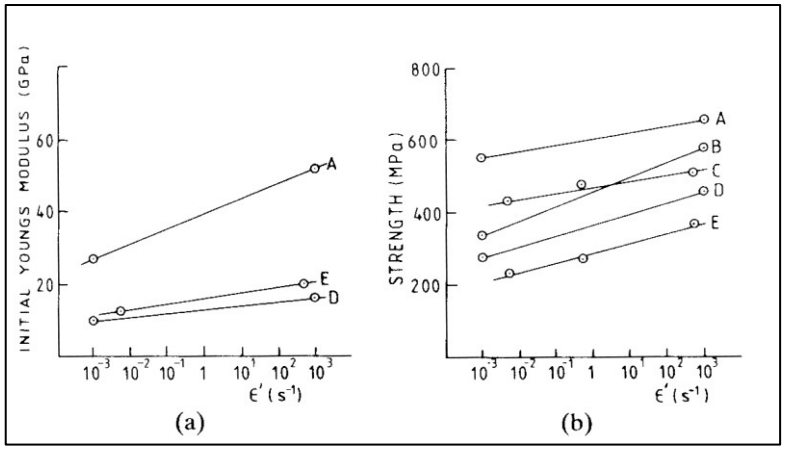

Figure 3.1: Effect of strain rate a) on the modulus and b) on the strength of FRC laminates [19].

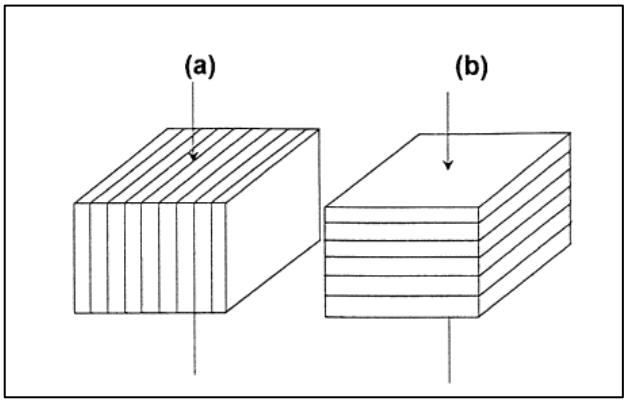

Figure 3.2: Direction of loading with respect to the ply planes on an FRC laminate a) in plane loading and b) normal loading [69].

3.2.3 Resistance of FRC materials to the environment

Conventional steel naval structures are prone to corrosion degradation due to exposure to the sea environment. The effect of corrosion on metallic structures has an adverse effect on

performance and safe operation of the vessel. FRCs exhibit superior corrosion resistance compared with steel structures.

Elevated temperatures can be experienced on a ship's decks, sides, and superstructure, and at local spots in the engine compartment. The mechanical properties of FRCs can be significantly affected at high temperatures. Carbon fibres retain their strength at temperatures exceeding 1000°C. However, the strength of E-glass is reduced by 25% at 350°C and by 50% at 500°C. The strength of aramid fibres is reduced by 25% at 200°C and by 50% at 300°C. Severe matrix degradation occurs at temperatures just above 150°C [19]. Further matrix degradation and possible matrix burn-off can occur at temperatures of about 500°C.

A very important feature of GFRP is the increase of stiffness and strength at very low temperatures [19]. This characteristic is valuable for the maritime industry for applications were temperature can drop to -50°C, particularly since the mechanical properties of certain steel grade can deteriorate at lower temperatures due to low temperature embrittlement.

Water absorption on FRCs can occur by diffusion through the resin and capillary flow through the cracks, voids and along the weak fibre/resin interfaces. Degradation of the mechanical properties occurs due to the plasticisation of the matrix. Extended water ingress can lead to a reduction in Young's modulus, tensile, flexural and compressive strengths of 20% 20% 30% and 35% respectively [19]. FRC structures are usually painted with appropriate gel coats to protect them against sunlight exposure. The effects of prolonged exposure to sunlight are only limited to cosmetic degradation like loss of gloss superficial crazing and blistering [71, 72] and do not lead to significant mechanical degradation.

3.2.4 Fire resistance of FRCs

When a fire starts, a significant increase in the temperature is required to cause reduction in the stiffness of a steel structure. However, the high thermal conductivity of the metal has adverse effect on limiting the temperature rise in adjoining compartments, possibly leading to thermal effects which can cause further damage [19]. However, steel structures cannot burn. The use of GFRPs despite low thermal conductivity can catch fire and produce toxic fumes such as carbon monoxide, dioxins, organo-chlorine-based substances like Polyvinyl chlorine (PVC) and styrene emissions. Special care needs to be given in addressing the fire retardation of FRC components in all transport applications including maritime. Fire is a source of serious concern for the application of FRCs in large-scale vessels.

3.2.5 Electromagnetic characteristics

Modern military naval operations require the development of vessels with low radar signature, paramagnetic characteristics and sufficient electromagnetic shielding. FRCs are inherently paramagnetic and exhibit, acoustic damping properties. They are effective absorbers of radar waves [18]. Furthermore, an angular and sharp-edged design can scatter the reflected radar waves and enhance the stealth performance of the ship. An example of a sharp-edged design is the Visby-class corvette (Figure 3.3). The permeability of GFRPs composites to electromagnetic emissions from various sources inside and outside the ship can lead to interference in sensitive electronic and control equipment [19]. Electromagnetic shielding can be achieved by incorporating conductive materials within the structure. CFRPs can be used in manufacturing of components where electromagnetic shielding is required, as

the carbon fibres exhibit higher electrical conductivity. However, due to the high manufacturing costs of CFRP laminates, metallic materials can be used as part of the GFRP structure [18, 19]. For example a fine copper mesh can be introduced on the surface of the GFRP structure during the manufacturing process [18]. Therefore, sufficient electromagnetic shielding can be established at a relative low cost.

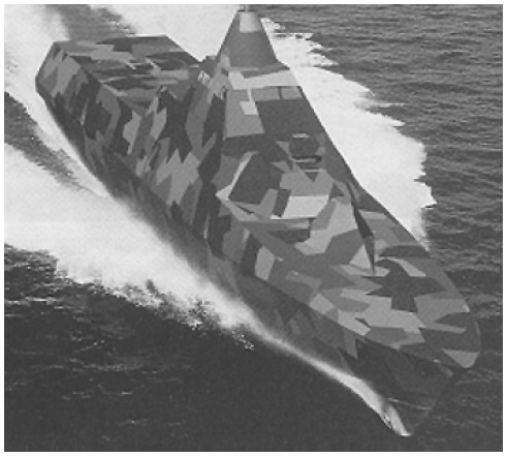

Figure 3.3: Visby class corvette [2].

3.3 Applications of FRC materials in the marine industry

GFRPs are increasingly used in manufacturing of leisure boats, small vessels, hulls, superstructures, submersibles and naval structures. Small vessels and fishing boats up to 25m in length are predominantly made of GFRPs. The use of GFRPs is extended in manufacturing of a wide range of leisure applications like canoes, speedboats and leisure yachts [19].

3.3.1 Ship reinforcements

Conventional ship structures suffering from fatigue cracking require significant repairs including re-welding, installation of metal inserts or, replacement of cracked components. An effective solution to that problem is the utilisation of CFRP laminates on the deck of the vessel. CFRP reinforcements are adhesively bonded on the metallic top deck and provide a significant strengthening effect. A layer of GFRP laminate can be introduced on top of the reinforcement to protect the underlying CFRP laminate. CFRP reinforcements increase the stiffness and strength of the hull leading to increased fatigue life. CFRP reinforcements can be also installed on structures where fatigue cracks have already occurred to reinforce the weak structure and delay crack propagation [15]. After prolonged service in aquatic environments, the FRC deck reinforcements will exhibit environmental and in-service degradation. As a consequence, attention must be taken to monitor and repair CFRP reinforcements.

3.3.2 Composite vessels

The performance and mechanical properties of the FRCs, along with recent improvements in design and fabrication methods, have led the maritime industry to make extensive use of such materials in the construction of certain naval warship types up to 160m long.

Patrol boats are a type of naval vessel commonly constructed of GFRPs. The Norwegian Skjold class vessel is manufactured entirely of a sandwich FRC consisting of glass and

carbon fibre skins with a PVC foam core [71-73]. The Skjøld patrol boat is shown in Figure 3.4.

Figure 3.4: Skjøld class patrol boat [2].

Mine-counter-measure vessels (MCMV) are predominantly made of GFRPs due to the electromagnetic, structural and maintenance requirements [22]. The use of FRCs in MCMV has led to innovative hull designs that are able to resist local buckling and provide the appropriate hull girder stiffness and underwater shock resistance [18]. A common hull structure for mine hunters is the single-skin design. The design consists of transverse frames and longitudinal girders that are bonded in transverse and longitudinal directions to a pre-laminated GFRP hull [19].

Monocoque construction is an alternative to single skin design. To obtain the required hull stiffness and underwater shock resistance, a monocoque structure consists of thick GFRP skins with thickness up to 200mm [74-76]. Minehunters can also be made of sandwich FRCs consisting of GFRP skins with a thick PVC core. The GFRP skins provide the required stiffness and strength, while a thick foam core provides sufficient shear strength and low

weight. Typical MCMV vessels with single skin, monocoque and sandwich construction are shown in Figure 3.5.

Figure 3.5: (a) Sandown class minehunter with single-skin structure,

(b) Huon class minehunter with a monocoque hull,

and (c) Bay class minehunter with a sandwich FRC hull [2].

Corvettes are the longest warship vessels that are entirely made of FRCs. The Visby class corvette is designed for a wide range of operations with capabilities for surveillance, combat, mine-laying, mine-hunting and anti-submarine warfare operations. The successful operation in these roles requires a light-weight, stiff and blast resistant vessel with stealth and non-magnetic properties. These demanding properties of the Visby class corvette are achieved with composite sandwich panels. The face skin of the panels consists of hybrid carbon and glass FRC laminates covering a PVC foam core. The use of carbon fibres reduces the hull's weight by 30%, without increasing significantly the fabrication cost [18].

Hydrofoils and hovercrafts are made of sandwich FRCs for weight reduction purposes. However the use of FRC instead of an Al-alloy can increase the fabrication cost by 15% [18].

3.3.3 Composite superstructures

FRC superstructures can overcome the corrosion problems and high weight of traditional steel structures. Weight savings up to 65% can be achieved by replacing the steel with FRCs [11].

An alternative solution to steel for weight saving was the use of Al-alloys. However, Al-alloys exhibit poor fire resistance because of their inherent high thermal conductivity and low softening and melting points. Aluminium superstructures can also suffer from severe fatigue cracking. Fatigue cracks initiate and propagate in the regions that are welded to the steel hull, where the hull induced girder bending strains are greatest [18]. The use of GFRPs can overcome the fatigue cracking and corrosion problems and lead to significant weight reductions. The yield strain of GFRP is about 8-10 times higher than that of steel, hence, the susceptibility to fatigue cracking of a composite superstructure bonded to a steel hull will be considerably decreased. The French La Fayette class frigate is a large warship operating with a GFRP superstructure. Section of the La Fayette's superstructure and helicopter hangar are made of a sandwich GFRP (Figure 3.6). The funnels of the ship are also made of FRCs [18].

Figure 3.6: La Fayette frigate with a composite superstructure section [2].

3.3.4 Composite masts

Conventional metallic masts with their open design and structure are a source of interference to the ship's radar and communication systems. Furthermore, metallic masts are prone to corrosion and increase the radar signature of the ship. The use of FRCs can easily overcome these problems. A mast made of FRCs is stiffer, lighter and has better fatigue resistance than a conventional metallic mast. Figure 3.7 shows the Advanced Enclosed Mast/Sensor (AEM/S), a composite mast developed by US Navy. Composite masts eliminate corrosion and improve the performance of the radar, communication and electronic systems, while the radar signature of the ship is reduced. A closed FRC mast structure can enclose all antennas and sensitive electronic equipment, protecting them from environmental conditions. Therefore, maintenance and replacement costs are significantly reduced [18].

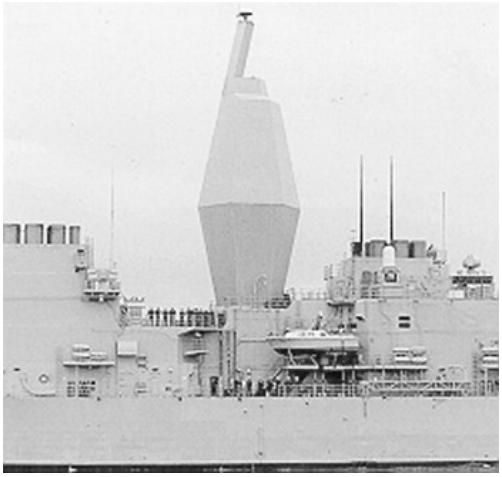

Figure 3.7: Composite mast system [2].

3.3.5 Propulsion systems

Propellers for ships and submarines can be made of FRCs, replacing expensive nickel-aluminium-bronze alloy-based ones. Conventional propellers are prone to fatigue cracking, inducing noise and vibrations to the hull [18]. FRC propellers are designed with fibre reinforcements aligned to the thrust direction for optimum performance, and withstand hydrodynamic and centrifugal loads more effectively (Figure 3.8) [18, 77]. Propellers made of FRCs reduce vibration and noise signature. FRC-made propellers are lightweight and exhibit improved fatigue resistance in comparison with conventional nickel-bronze-aluminium alloy propellers [18]. FRCs can be used to replace the heavy steel propulsion shafts on large vessels, reducing the overall weight of the ship by 2%. FRC shafts made of CFRP and GFRP have the potential to be 25-80% lighter than a steel shaft of similar size [78-80].

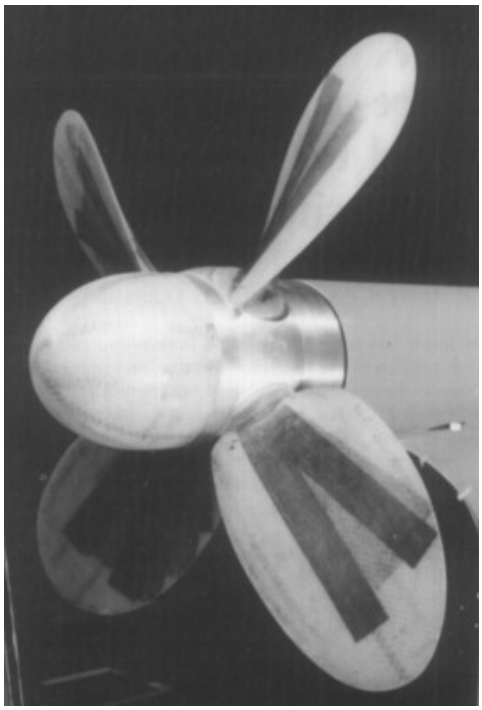

Figure 3.8: Composite propeller [77].

3.3.6 Secondary structures, machinery and fittings for naval ships

Secondary ship structures such as funnels, bulkheads, decks, rudders, hatch doors, pipes, ventilation systems, engine foundations, machinery and engine equipment can be made of FRCs.

3.3.7 Composite submarine structures

Submersible FRC hulls are predominantly fabricated with filament winding and provide low weight, improved hydrostatic strength and superior corrosion resistance [18, 19, 81]. A submarine hull made of FRCs has reduced magnetic, electrical and radar signatures,

enhancing the stealth capabilities during operations. In addition, pressure tests performed on hulls fabricated with FRCs showed the potential for operating depths that are 3 to 4 times greater than those achieved with a steel hull [82]. Sensors and sensitive surveillance equipment can be embedded in FRCs, improving the operational performance of the submersible vessel. Other structural components of the submarine like rudders, bow planes, fins, masts, decks and hatch doors can be manufactured of FRCs and provide valuable benefits over steel [18].

3.4 Hybrid Composite to Steel Joints

Hybrid composite to metal joints are gaining momentum for the construction of maritime components for the development of stiffer and lightweight structures [21, 22] leading to increased operation speeds and payload capabilities. The fabrication of hybrid composite–to-metal marine structures like decks and superstructure components employs the joining of large FRC parts to the metallic structure of the ship. FRC substructures can be effectively used with a metallic ship structure in areas where high stiffness is not critical and where high corrosion resistance and reduced weight is a key requirement. The purpose of the hybrid joint is to transfer load between the two FRCs and metallic structure.

Hybrid composite-to-metal connections in the marine industry are made by bolted, adhesive and laminated joints. Kabche et al. [23] investigated the performance of composite-to-metal bolted joints for the fabrication of an underwater lifting body. The bolted joints exhibited satisfactory structural performance, however failure and damage of the composite material occurred at the bolted region [23]. Riveted joints require the drilling of holes, leading to

decreased stiffness. Therefore, the thickness of the FRCs and metal plates must be increased to withstand the higher stresses at the vicinity of the hole. Increased thickness leads to heavier structures and higher manufacturing costs. The drilled region of the metal-to-composite connection is prone to corrosion attack leading to structural degradation of the joint [83]. To predict and monitor the corrosion degradation regular inspection and maintenance is required, thus significantly increasing running and maintenance cost.

Adhesively bonded hybrid connections can overcome the problems encountered with bolted connections as they eliminate the need of drilling holes, while load can be effectively borne by the bonded area. Furthermore, the load is uniformly distributed on the adhesively bonded region, leading to improved fatigue and stiffness performance. Therefore, the thickness of the jointed FRCs and metallic components can be kept low resulting in lower weight. In addition, the presence of adhesive and primer protects the metal adhered in the connected region from corrosion attack and associated degradation [83].

The mechanical performance and stress distribution within the bonded connection are drastically affected by the joint's geometry. The bond strength and geometry of the basic types of joints are shown in Figure 3.9. The joint's performance is further affected by the adhered materials, adhesive, adherent and adhesive thickness, and length of overlap [84]. Generally, increased lap length results in stronger connections. A 200% increase in the lap length leads to 100% increase in the joint's strength [85]. Additionally, in scarf joints, short scarf lengths lead to joint failure breakage at the initial failure. However, joints with increased scarf length are able to carry the increasing loads after initial failure occurs in the joint. Furthermore, increased scarf lengths lead to a flat stress distribution in the joint area [86].

The type of the adhesive can significantly affect the performance of the joint. A strong and brittle adhesive can lead to increased joint strength, but its brittle nature can have a negative impact on the fatigue performance of the joint. For this reason, a less stiff and ductile adhesive will be more preferable since it leads to joints with improved fatigue resistance [84].

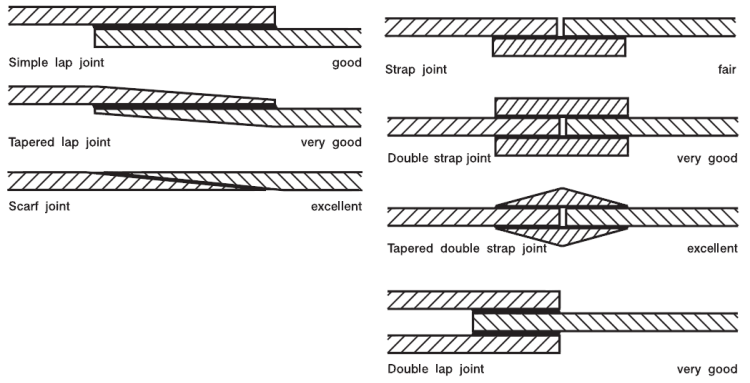

Figure 3.9: Basic types of joints[87].

An alternative to bolted joints are the laminated hybrid connections, where the steel insert is moulded within the composite structure during the lamination process [21, 88]. A type of laminated hybrid joint was presented by Boyd [24, 25]. The joint consisted of a steel insert within a GFRP sandwich material with a balsawood core, and was developed for the attachment of the helicopter hangar on the La Fayette class frigate. The laminated joints exhibited improved strength compared to a bolted joint [21].

A common problem that is encountered during the fabrication of hybrid connections is the elastic mismatch between the different adherent materials. The elastic mismatch between the FRC laminates and steel leads to high stiffness discrepancies between steel and FRC,

reducing thus the overall stiffness of the joint. Melograna and Grenestedt [88] used perforated steel for fabricating hybrid joints. The perforations decreased the stiffness of the steel leading to stronger joints due to reduced elastic mismatch between the GFRP and steel adherents.

Although effective joint design and high-quality adhesive can lead to the fabrication of strong joints, poor surface preparation has an adverse effect on the bond adhesion, resulting in poor joint quality. Therefore, appropriate surface preparation of the steel adherent is a critical step in fabricating strong hybrid connections [89]. The surface of the steel can be initially cleaned with sandblasting, which is followed by a subsequent surface solvent cleansing [90-93]. Sandblasting removes paint, rust and any unwanted material from the surface, leaving a clean and exposed metal surface. After sandblasting, the surface is further cleaned with an appropriate solvent such as acetone helping render the metal surface oil free.

Sandblasting followed by subsequent surface cleaning is an effective way of producing high strength joints. The bond quality can be further improved by priming the metal's surface. Priming improves the adhesion of FRCs and adhesives to steel, resulting in stronger interfaces and significantly improved joint connections [90, 93, 94]. Improved bond strength between steel and FRCs can be also achieved with plasma treatment on the steel's surface [95].

FRCs based on thermosetting resins are generally easy to bond and require a simple surface preparation that consists of soft sanding followed by surface degreasing with acetone [92].

It can be very difficult to perform strong hybrid composite-to-metal connections in a shipyard environment, where the conditions in terms of cleanliness, humidity and temperature form a

severe obstacle for achieving high quality adhesively bonded joints. A way to overcome these problems is to prefabricate the FRC substructure with the hybrid joint elements in a suitable and environment, and transfer the components to the shipyard where the steel element of the FRC-to-steel joint can be welded on the ship's structure [21].

CHAPTER 4

DEFECTS AND DAMAGE IN COMPOSITEMATERIALS

4.1 Introduction

Defects and structural faults have an adverse effect on the mechanical properties of FRCs. Structural defects can develop during manufacturing due to various reasons including inappropriate fabrication parameters, lack of attention or skills. Damage in FRCs can also occur due to poor handling or inappropriate installation. While in-service damage initiation and subsequently propagation may arise in FRC components due to cyclic dynamic loading and/or exposure to environmental conditions.

Defects result in decreased mechanical properties, limiting fatigue resistance and hence in-service lifetime of FRC components. Defects can act as damage initiation points during cyclic loading. If damage remains undetected, it can propagate to critical level eventually leading to sudden catastrophic failure. Catastrophic failure of a critical structural component can cause further collateral damage to a larger structural system. It is important that all defects are detected and evaluated with a suitable inspection technique at an early stage to avoid catastrophic failure and ensure consistent performance throughout the intended design lifetime.

To predict the performance of FRCs, the type of defect, its location, orientation and size need to be determined since they will influence the rate of damage propagation with time. Knowledge and understanding of these parameters can help optimise the maintenance decision-making process.

4.2 Manufacturing defects

During fabrication of FRC components, several types of defects may arise regardless of the manufacturing route used. Despite advances and improvements in production processes resulting in fabrication of high quality parts, it is still possible that manufacturing defects may occur. The probability of occurrence of manufacturing defects can increase due to lack of experience of the manufacturer and inadequate preparation followed by improper handling of raw materials prior to fabrication.

The often large size of FRC components increases the possibility of manufacturing defects occurring during fabrication. There is a tendency for mechanical properties to deteriorate with increasing volume. Damage propagation and failure characteristics depend on the type and severity of the most critical defect [96]. It is essential that consistent manufacturing quality is ensured to limit the influence of size effect on the structural performance of the finished component.

The most common types of manufacturing defects are:

- Fibre misalignment
- Stacking sequence errors
- Fibre distribution
- Inclusions
- Fibre waviness
- Voids
- Gaps, fibre overlaps, half gap/overlap and missing fibre tows

4.2.1 Fibre Misalignment

Unidirectional FRCs exhibit high strength and stiffness along the fibre orientation and low strength in the transverse direction. Therefore, fibre orientation is a key factor in FRCs. The load bearing capability of FRCs strongly depends on the level of alignment of the fibres to the load direction. Misalignment of up to 10° causes limited decrease in the strength. In the range of 10-20°, fibre loading changes from tension/compression mode to shear loading of the weak interface, leading to a considerable drop in strength. A misalignment angle beyond 20° results in the fibre/matrix interface being loaded by direct tension or compression, and strength is further reduced as the fibres are no longer able to effectively carry the applied load [29].

4.2.2 Stacking Sequence errors

To achieve the required strength and stiffness, a series of fibre layers are arranged into appropriate orientations during fabrication. The selection of orientation of the fibre layers is determined by the loading conditions expected in-service. If a component is expected to be exposed to bi-axial tension fibre layers need to be orientated to the direction of the two orthogonal axes at 0° and 90° respectively. However, if stress is also introduced at an angle of 45° between the two orthogonal axes, then neither of the two layers will carry the load effectively. As a result, during fabrication it is necessary to introduce a fibre layer at 45° in order to further reinforce the structure in this direction [29]. Errors in the stacking sequence during manufacturing can result in less stiffer structures that are not able to effectively carry the designed loads.

For tensile or compressive loads, the positioning of the fibre plies is not crucial, provided the layup is balanced and symmetrical. However, under flexural bending conditions the stacking sequence of the fibres can affect the mechanical behaviour of FRCs, and fibres on the surface layers must be aligned to the bending direction [29].

4.2.3 Fibre distribution

Fibre distribution within the material impacts on the mechanical properties of FRCs. A rich resin area will generate a high transverse tensile stress concentration along the sides of the fibres that surround the unreinforced area, resulting in interfacial debonding. In addition, fibre buckling can occur at the boundaries of the resin-rich areas under compressive loading acting as damage initiation areas [97]. Generally the existence of a several resin-rich areas can promote transverse stress concentration, leading to premature failure even if the fibres are distributed randomly within the structure of the FRC [29].

4.2.4 Inclusions

During FRC fabrication inclusions can be introduced accidentally. Inclusions can act as stress concentration points where crack initiation can occur, potentially leading to premature fatigue failure. Inclusions can be in the form of debris and dust particles from the workplace environment [29].

4.2.5 Fibre waviness

Fibre waviness is a region of distorted fibres that diverge from their initial straight state. Fibre waviness induces a region of stress concentration causing deterioration of the mechanical properties of FRCs [29]. Increased misalignment of wavy fibres leads to significant reduction in the Young's modulus and strength [98, 99]. The parameters used to define the severity of fibre waviness are the ratio of wave amplitude, δ, to the wavelength, λ, and maximum angle of fibre rotation, θ_{max} [100]. The relationship between these parameters is mathematically described by the following equation:

$$\theta_{max} = \tan^{-1}(\pi\delta/\lambda)$$

For moderate fibre wave geometries ($\delta/\lambda < 6\%$), failure occurs at 88% of the design strength in comparison with baseline specimens. The fractured area exhibits a brooming failure effect thorough thickness splaying off the layers and causing further delamination. For severe waviness ($\delta/\lambda > 6\%$), failure occurs at 63% of the defect free material design strength, resulting in the specimen's catastrophic failure at the location of the wavy region [100]. Wisnom and Atkinson [101] showed that out-of-plane fibre waviness misalignment up to 1° leads to a reduction in compressive and tensile surface strain of 17% and 26% respectively in comparison with baseline material.

Wisnom et al. [102] showed that the maximum compressive stress depends on the fibre misalignment angle. A misalignment angle in the range of 0.75-3°, reduces significantly the maximum compressive stress from 1949MPa to 940 MPa. As the stress approaches the point of shear instability, the misalignment angle of the fibres increases further and deformation

becomes concentrated in a narrow band at the region of maximum fibre misalignment. A similar failure mechanism applies under pure bending conditions. As compressive load increases, shear stress resulting from misalignment causes the fibres to rotate further increasing the misalignment angle. The reduction in shear tangent modulus while increasing shear strain leads to instability with further fibre rotation occurring without any increase in the applied load. This mechanism is believed to be responsible for the kink-bands formation which is typically observed under compressive failure of FRCs [103].

Lemanski and Sutclife [104] investigating the impact of fibre waviness showed that the reduction in the compressive strength is greatest when all layers contain a region of fibre waviness. For small fibre misalignment angles up to 10°, the strength of the laminate with a region of fibre waviness at the central ply is similar to that of a laminate with a waviness region at a surface ply. For larger misalignment angles, the laminate with a fibre waviness region at the central ply exhibits slightly higher strength in comparison with a laminate with a wavy region at a surface ply. This is due to the fact that a central ply is supported by the adjacent plies. The influence of fibre waviness increases for FRC structures made of bidirectional fabrics, since they generally suffer from inherent fibre waviness due to the presence of crimps in their weave, as shown in Figure 4.1 [29].

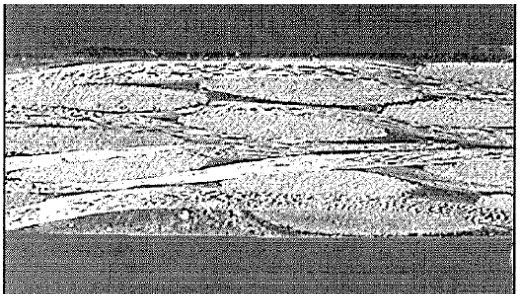

Figure 4.1: Inherent fibre waviness in a bidirectional fabric [29].

4.2.6 Voids

Voids are the most frequently occurring defect type during manufacturing. Void formation can arise due to a wide variety of reasons including trapped air, volatile compounds in the composite structure, trapped air in the liquid resin or high moisture levels during manufacturing process. The void content can also be affected by the applied autoclave pressure during the curing process.

Voids are highly undesirable since they weaken the structure and act as stress concentration points [105]. Cracking can initiate and propagate from voids under loading, resulting in serious mechanical degradation of the component and premature failure. The presence of voids, even at low volume fraction has a detrimental effect on the performance of FRCs [36, 106-108]. Ghiorse et al. [35] showed that the in range of 0-5%, each 1% increase in void content, causes a decrease of 9.7% in the interlaminar shear strength (ILSS), and a decrease of 10.3% in the flexural strength. The flexural modulus decreases by 5%. A further increase of 2% in void content will cause an additional 20% decrease in the ILSS and flexural strength, while the flexural modulus decreases by 10%. Similar results were reported by Liu et al. [34].

The tensile strength decreases by 14% when the void content increases from 0.6 to 3.2%. The drop rate is 4% in the porosity range of 0 to 3.5%. The effect of voids on the Young's modulus is negligible [34]. This decrease in the tensile strength is due to voids that push aside the surrounding fibres as they expand, resulting in localised fibre deformation [34, 109]. Figure 4.2 shows the ILSS, flexural and tensile strengths as function of the void content.

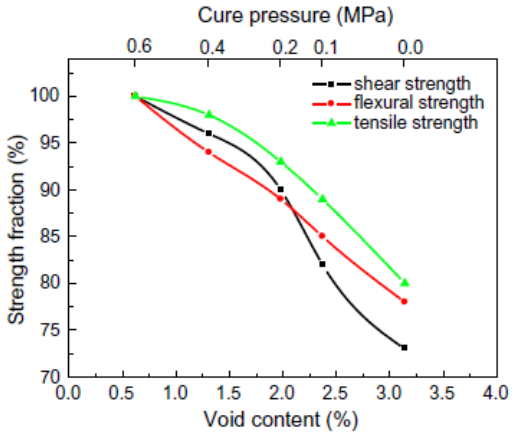

Figure 4.2: Shear, flexural and tensile strength vs void content [34].

Reprinted from Composite Structures, Vol.73/3, Ling Liu,Bo-Ming Zhang,Dian-Fu Wang,Zhan-Jun Wu, Effects of cure cycles on void content and mechanical properties of composite laminates, 303-309, Copyright 2006, with permission from Elsevier

A key reason for the occurrence of voids within FRCs is trapped air in the resin during vacuum impregnation of the fibre array. A high amount of dissolved air and gas bubbles in the resin will result in the production of poor quality FRCs with high void content. A way of overcoming this problem is to degas the resin prior to impregnation [32, 110]. A simple and common degassing procedure is to expose the liquid resin mixture to vacuum in order to drive the bubbles out of the resin. As the pressure is reduced, the air bubbles will increase in size rising out of the liquid [110]. To accelerate and improve degassing of the resin bubble nucleation material can be used [32, 110]. During resin impregnation voids are formed because of the entrapment of air pockets as resin flows. Under vacuum resin infusion the dry fibre reinforcement must be wetted by the resin during impregnation. The flow pattern of the resin and void formation can be affected by the geometry of the fibre reinforcement employed.

Jinlian et al. [111] presented a theoretical analysis on void formation during impregnation of multi-woven fabrics, where differences between the fabric's axial permeability (K^a_b) and transverse (K^t_b) permeability can affect the size of the resulting void. High K^a_b / K^t_b ratios lead to increased void content [111]. Patel et al. [112, 113] studied the influence of the flow front though a unidirectional fibre mat [113], bidirectional stitched and woven fabrics [112] on void formation. Two main flow fronts were observed during impregnation. A flow front through the gaps of the fibre tows and a second flow front, which is drawn through the fibre tows due to capillary forces. At low flow rates the flow which impregnates the fibre tows is the leading flow. When the flow within the tows reaches an obstruction, such as stiches of a transverse tow, cross flow occurs. If this transverse flow is completed before the front between the fibre tows reaches the stitches, then macro-voids form. At high flow rates the leading flow between the gaps of the fibre tows was followed by the flow through the fibre tows. The leading flow between the tows is wicked into the tows and meets the lagging front which flows within the fibre tows (round-up mechanism). As these flow fronts meet they result in the entrapment of micro voids in the fibre tows, and no macro voids are formed [112, 113].

When the flow is perpendicular to the fibre tows, similar results are observed. Macro-void formation is caused by flow fingering at the stiches or at transverse tows, followed by transverse flow along the tows. In addition, when the flow reaches the fibre tow, it initially flows around it and then impregnates it. As the impregnation flows are met, micro-voids are trapped in the centre of the tow [112, 113].

The macro-voids can be eliminated by injecting resin at high flow rates after the initial low flow rate is completed. The macro-void removal involves the elongation and breakage of

larger voids into smaller voids which are then purged out of the fibre mat. Micro-voids may coagulate to form meso-voids that can be purged out if the resin injection is continued for sufficient time [112].

When autoclave processing is used to build FRC components, void formation and content are influenced by the applied autoclave pressure and cure circle. Several studies [33, 34, 108, 114-116] have shown that increasing the applied autoclave pressure leads to a reduction of void content within the laminate. The influence of the applied pressure on the void content is shown in Figure 4.3. Resin viscosity also affects the void content. Therefore, the dwell time at which the autoclave pressure is applied influences void formation [34].

If an FRC component is not cured in an autoclave where the high pressure depresses the void formation, a high moisture intake in the resin will lead to increased void content. The void fraction is sensitive to the humidity levels and a sharp increase in the void content occurs if high moisture ingress takes place [33].

Low void content, <1%, is essential in the aerospace industry, due to the strict safety and performance requirements. FRC components with void content >1% are rejected [34]. However, in less critical applications such as maritime structures, higher void levels, >5% are acceptable [19]. This is due to the lack of specific requirements for void content in existing maritime manufacturing standards, allowing fabrication of FRC components with void content ≤11% [37].

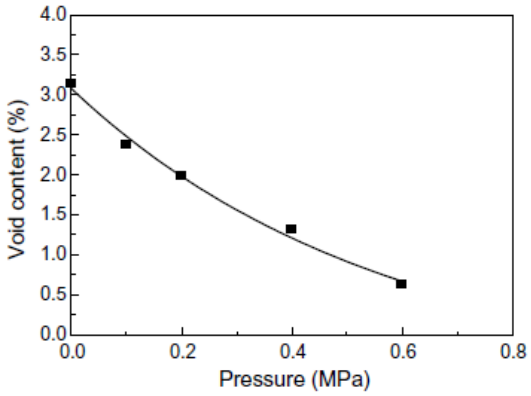

Figure 4.3: Void content as a function of the applied autoclave pressure [34].

Reprinted from Composite Structures, Vol.73/3, Ling Liu,Bo-Ming Zhang,Dian-Fu Wang, Zhan-Jun Wu, Effects of cure cycles on void content and mechanical properties of composite laminates, 303-309, Copyright 2006, with permission from Elsevier

4.2.7 Gaps and fibre overlaps

In Automated Fibre Placement (AFP), resin impregnated fibre tows are automatically arranged on a work surface to form the component. During fabrication, discontinuities in fibre placement such as gaps, fibre overlaps and placement of twisted tows may occur. These defects cause thickness variations in the component and induce fibre waviness at the region of the discontinuity. Structural discontinuities of this type cause degradation of the mechanical properties of the laminate [30].

4.3 In-service and handling defects

In-service FRC components can develop various types of defects. Additional defects can be introduced as a result of poor handling and inappropriate installation. Common in-service and handling defects that cause reduction in the strength of FRCs include fatigue cracking, impact damage, hole drilling damage, moisture ingress and cut fibres.

4.3.1 Hole drilling

During installation of FRC components drilling of holes is often required. However, holes are stress concentration points leading to reduced strength [117]. Failure is likely to initiate from the vicinity of a hole under dynamic loading conditions. The drilling process itself can cause collateral damage in its surroundings in the form of splintering, delamination and overheating due to friction[118]. Figure 4.4 shows splintering caused after drilling of an FRC panel. The extent of drilling damage is dependent on the method applied and condition of the drill. A sharp drill will induce less damage to the material compared to a blunt one. Certain drilling methods and types of drills cause limited collateral damage around the hole and result in high quality drilling. An effective drilling method involves the machining of the composite part in both axial and radial directions by rotating the cutting tool around its axis and orbiting around a principal axis while the tool is being fed through the laminate [118]. The use of high quality carbide and diamond coated drills can further improve the drilling quality and reduce the collateral damage [2, 118].

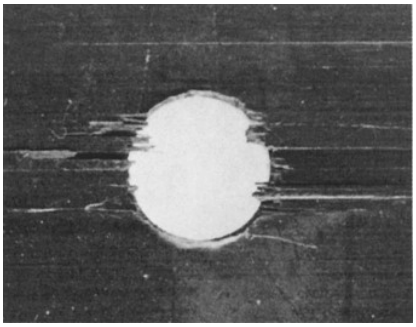

Figure 4.4: Splintering damage around the hole [2]

4.3.2 Moisture ingress

During operation water or moisture can be absorbed by the polymer matrix causing mechanical degradation and reduction of the interfacial strength. As water penetrates the polymer's molecular structure it reduces the interactions between the molecular chains and leads to volume changes in the matrix. Softening and plasticisation of the matrix occurs but cracking can also take place as a result of non-uniform volume changes. The effect is reversible since absorbed water can be removed by controlled heating. [29, 119]. Water absorption can also cause chemical hydrolysis, breaking the polymer chains and resulting in reduced mechanical strength. These diffusional and chemical processes are temperature influenced and are governed by Arrhenius's kinetics. Consequently, accelerated water ingress and hydrolytic ageing can occur at high temperatures [119].

4.3.3 Environmental degradation in composite materials

In-service FRC components and structures are subjected to various environmental degradation mechanisms due to constant exposure to the operational environment. Ultra-

violet (UV) radiation and moisture are the leading factors that promote environmentally-induced structural degradation in FRCs. UV radiation causes polymeric chain scission or cross-linking to the polymer molecules of the matrix. Polymer scission breaks the polymer chain into smaller components causing significant strength reduction. In contrast, chain cross-linking increases the density of the cross-links in the polymer chain leading to excessive brittleness and micro-cracking. These reactions cause discolouration of the matrix. Hence, photo-oxidation can be visually detected as changes in the colour and overall appearance of the FRC component. The effect of UV radiation can be moderated by adding suitable photo-stabilising agents to the matrix during manufacturing [120].

Water ingress has a deteriorating effect on the polymer matrix. However, further to matrix plasticisation and hydrolysis of chemical bonds, water can wick along the fibre/matrix interface causing interfacial degradation. UV radiation and water ingress can simultaneously act upon a FRC structure and accelerate the environmentally-induced structural degradation process. Micro-cracks which have been previously developed on a UV affected area can promote moisture ingress. Condensed water on the cracked composite can remove soluble by-products from photo-oxidation reactions and expose fresh material to further UV degradation [120].

UV radiation and water ingress act mainly upon the polymer matrix which transfers load to the fibres. Excessive environmental degradation to the matrix can significantly limit this ability and leading to deterioration of the overall mechanical properties [120]. Prolonged exposure to UV radiation and to moisture can cause environmentally-induced degradation to the reinforcing fibres of the FRC structure. Degradation of the molecular structure of the fibres results in reduced strength and can potentially cause catastrophic failure [120, 121].

Cyclic exposure to UV radiation and moisture for 1000h caused a reduction of 29% on the transverse tensile strength of unidirectional carbon fibre composites [120]. Accelerated exposure to UV radiation for 100h (a year of normal exposure to direct sunlight) reduced the tensile strength and the Young's modulus of a GFRC material by 34% and 18.9% respectively. The shear strength and shear modulus were reduced by 18.8% and 25.4% respectively [122]. However, the use of photo-stabilising agents and application of suitable surface coatings can limit the effects of environmental degradation, and increase the life-span of the FRC structure.

Impact from tiny salt particles and possible dust particles can result in abrasive erosion of the FRC structure. Solid particle erosion can cause surface abrasive damage and further deterioration on the FRC material. Particle erosion introduces gradual wear of the surface causing matrix micro-cracking and spalling. Abrasive erosion removes the surface matrix layer and exposes the fibres. Prolonged exposure to solid particle erosion conditions causes fibre fracture to the surface of the component and subsequent fibre removal. The fibre fragments can lose their orientation and be randomly distributed on the surface [123]. Therefore, eroded areas on the component's surface can act as stress concentration areas and cause early damage initiation under in-service conditions.

4.3.4 Impact damage

In-service FRC components can be damaged due to impact loading. Impact damage is difficult to predict since it can happen unexpectedly during manufacturing, handling or in-service. Figure 4.5 shows a damaged aircraft radar dome as a result of impact with a bird.

Impact damage leads to reduced strength and fatigue lifetime. Damage can propagate from the affected region under dynamic loading. In-service impact can lead to surface buckling, matrix cracking, and delamination (Figure 4.6) [124, 125]. The severity of impact damage affects the residual strength and load bearing capability of FRCs [126-128].

Figure 4.5: Damaged radome after bird-strike impact

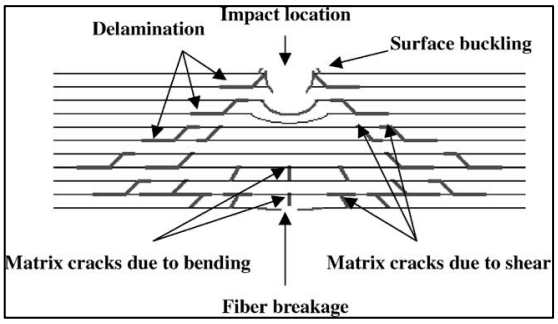

Figure 4.6: Impact damage around the impact location [124].

Reprinted from Composite Structures, Vol.62/2, Tien-Wei Shyr,Yu-Hao Pan, Impact resistance and damage characteristics of composite laminates, 193-203, Copyright 2003, with permission from Elsevier

4.4 Damage mechanisms in composite materials

The main damage mechanisms in FRCs include matrix cracking, fibre-matrix debonding, fibre pull-out, fibre fracture and delamination (Figure 4.7). The occurrence of each failure mode depends on the composite's structure and loading configuration. Under tension, failure starts with matrix cracking, which subsequently leads to fibre-matrix interfacial failure. This is followed subsequently by fibre fracture, fibre pull-out and eventually rupture.

Matrix cracking appears as cracks perpendicular to the loading direction. A severe type of matrix cracking is the matrix splitting appearing as a long crack parallel to the fibres. Matrix cracking causes stress concentration at the edge of the crack tip forming delaminations, causing a decrease in mechanical strength [129].

Fibre-matrix debonding occurs when the fibre-matrix interfacial stress exceeds the bonding strength leading to interfacial failure and thus, separation of the matrix from the fibre. Fibre-matrix interfacial failure depends on the interfacial bonding strength between fibre and matrix. Appropriate fibre surface treatment results in a strong bond forming at the interface, reducing debonding [129]. After debonding, the fibres slide through the matrix with further loading. The fibre matrix sliding after debonding is an energy absorption mechanism and contributes to high toughness exhibited by FRCs [130].

At the tip of a propagating crack, fibre fracture can take place. Fibres are pulled out of the surrounding matrix as the crack advances further. Fibre pull-out depends on the fibre length that is still embedded in the matrix. If the fibre length exceeds a critical length, then fibre pull-out is possible and fracture occurs. Like in fibre-matrix debonding, fibre pull-out is

sensitive to the surface treatment of the fibres. Adequate surface treatment promotes strong bonding and decreases the critical fibre length [130].

The reinforcing fibres are responsible for carrying the applied loads. Consequently, fibre fracture even at small amounts results in major reduction of strength and stiffness, which can result in rupture [131]. During fibre fracture, load is redistributed to the remaining fibres and surrounding matrix. As a result, the same load must be carried by a reduced amount of fibres that will in turn fail under loading, reducing further the material's strength and causing further damage. After a critical point, the remaining fibres are unable to sustain the load, failing catastrophically.

Delamination is a common damage mechanism propagating at the ply interface under sufficient load. Impact loads can also result in delamination. Delamination can compromise the structural integrity. Even a small area of delamination can decrease the compression strength by over 50% [131]. Therefore, delamination can significantly reduce the load-bearing capability and the service life leading to premature failure.

The effect of delamination has been investigated in several studies [132-134], where small pieces of thin Teflon film were implanted in the lay-up of the composite material to simulate the effect of delamination under load. A considerable decrease in the strength of FRCs has been reported by increasing the size of the delaminated region. Gillepsie et al. [132] reported a 41.5% reduction in the failure strength even at small through-width delamination lengths of 12.7mm. The failure strength can be further reduced by 87% at increased delamination lengths of 38.1mm. The impact of the delamination can be determined by the position of the delaminated region within the material's lay-up. The impact of the delamination on the

strength increases as the delamination is located into the centre of the lay-up. However, this impact is less severe when the delamination is located closer to the outer surface of the laminates [134]. Liu et al. [135] showed that at the ply interfaces, where the angle difference in the fibre orientation of the upper and low plies is high, delamination can be more severe, leading in major reduction in mechanical strength.

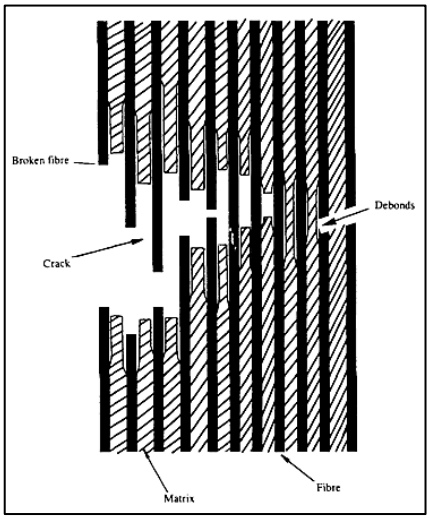

Figure 4.7: Schematic representation of damage modes in FRC materials [129].

CHAPTER 5

NON-DESTRUCTIVE TESTING IN COMPOSITE MATERIALS

5.1 Introduction

The presence of defects and damage can compromise the structural integrity of FRCs. If damage remains undetected catastrophic failure may occur eventually. To diagnose the type and extent of damage before it propagates beyond a critical size and cause catastrophic failure, inspection using one or more appropriate NDT technique needs to be carried out. Apart from detecting defects, their characteristics, location, orientation and severity need to be ascertained. Once these parameters are assessed, and damage severity has been quantified, maintenance or replacement of the affected component can be carried out, avoiding thus a catastrophic failure and further damage to the rest of the structure.

It is important that FRC components are inspected at regular intervals during their in-service lifetime. Initial quality control should also be carried out prior to commissioning critical FRC components. The regularity of inspection and maintenance scheduling heavily depend on the criticality of the structure, the anticipated loading and environmental conditions, and maintenance costs.

Unscheduled inspections can be carried out, if abnormal and unexpected events have occurred that may have caused damage or activated certain damage mechanisms that can contribute to the reduction of the mechanical performance of the component. Such a case is the accidental impact of an FRC structure with a foreign object.

In order to inspect FRC components, among the possible NDT techniques that can be employed are visual inspection, ultrasonic testing (UT) and its variants like C-scan and long-range ultrasonics (LRU), infrared (IR) thermography, eddy current testing (ECT),

shearography and radiography. The utilisation of ECT is only applicable for CFRP composites due to the electrical conductivity of carbon fibres, allowing the generation of weak eddy currents within the material. To identify the defect type and the extent of the damaged area, extensive calibration and several samples with certain pre-introduced damage and flaws may be required.

5.2 Visual inspection

Visual inspection is a simple, rapid and inexpensive inspection technique. It does not require the use of sophisticated and complex equipment unless there is a requirement to automate the process. Visual inspection is performed using naked eye observations and possibly simple optical equipment such as magnifying glasses and travelling microscopes. Borescopes, flexiscopes, high definition and high speed digital cameras and portable digital optical microscopes may be employed in combination with automatic pattern recognition capability to remove operator subjectivity. Image enhancement techniques are often used to improve the visualisation of defects and damage within the material by highlighting the differences in the light intensity of the recorded image.

Visual inspection can only be used for surface inspection of an FRC component for visible defects. It is unable to detect defects that lie beneath the surface. It is carried out to evaluate the location and visible length of surface-breaking flaws including areas that have sustained impact or delamination damage. Unfortunately, it cannot provide any information regarding the depth of the defect. In translucent or relatively thin materials it is often possible to detect porosity and assess the type of the detected defect using appropriate illumination.

Due to its limitations, visual inspection cannot be used on its own as an inspection technique and must be combined with other NDT techniques that are capable of detecting and quantifying damage located deeper within the component [38].

5.3 Dye Penetrant Inspection

Dye Penetrant Inspection (DPI) or Liquid Penetrant Inspection (LPI) is another surface inspection technique that makes use of special high contrast coloured or fluorescent dyes in order to reveal the presence of surface damage not reliably confirmed with ordinary visual inspection. DPI is performed by applying dye on the surface of the component. After allowing the dye to penetrate in the surface cracks, excess dye is wiped and a developer is applied. The dye that has penetrated in the cracks will be drawn back to the surface providing a clearly visible indication of the flaw. If fluorescent dies are employed UV lighting conditions are necessary. DPI does not provide any information regarding the depth of the defect but only the surface length. Furthermore, DPI is unable to reveal defects located beneath the surface of the test piece being assessed. Therefore, delamination and internal cracking caused as a result of impact may not be observed with this technique. DPI is not applicable on porous materials, and requires thorough cleaning of the test surface. The quality of DPI results can be adversely affected by surface roughness and poor cleanliness.

5.4 Ultrasonic Testing

Ultrasonic testing (UT) is one of the most commonly employed NDT methods for inspecting FRCs for the presence of defects and quantifying their severity. This technique uses piezoelectric transducers normally made of Lead Zirconate Titanate (PZT) crystals excited by rapid electric pulses each second. The electric pulses give rise to strain changes at ultrasonic frequencies causing ultrasonic waves to be generated. Typical UT frequencies range between 20kHz-5MHz depending on material characteristics, type of component, geometry and resolution required. Ultrasonic waves travel through the material until reflected by defects present. Ultrasonic wave energy can be attenuated due to scattering or absorption from microstructural constituents of the material being tested. More complex testing procedures may be necessary. The material characteristics and component geometry together with the resolution required are the main factors influencing the testing frequency employed. UT techniques are capable of detecting surface and sub-surface defects, and assess their exact location, size, orientation and type. However, due to the highly attenuating characteristics and anisotropy exhibited by FRCs detection of smaller defects located deep in the material may be challenging. Different types of UT techniques such as pulse-echo, through transmission UT, C-scan, backscatter UT, and Ultrasonic Phased Arrays can be used to inspect FRC components [38].

Pulse-echo UT is a widely used NDT technique, where an ultrasonic wave beam is transmitted into the specimen normal to its surface. The pulse is reflected from the damaged and defective areas. The reflected waves travel back to the transducer. The location, orientation and size of a flaw are determined from the travel time and signal amplitude respectively. This technique is also known as A-scan. The principles of the pulse-echo

technique are shown schematically in Figure 5.1. The pulse-echo technique can be used to detect delamination, cracking and inclusions. Based on the attenuation of the ultrasonic waves, fibre fraction and void content can be assessed. The technique is applicable in cases where access to the component is possible only from one side [38].

Through-transmission is a common UT technique which makes use of two transducers, one emitter and one receiver. The receiver is placed at the opposite side of the component facing the transmitter. Through-transmission can be used to detect cracking and other defects, including delamination, inclusions, and voids through the thickness of an FRC component. Through-transmission UT cannot provide information regarding the depth of a flaw but helps address attenuation issues that may affect the results of conventional pulse-echo UT. It can be used only when access to both sides of the component is possible [38].

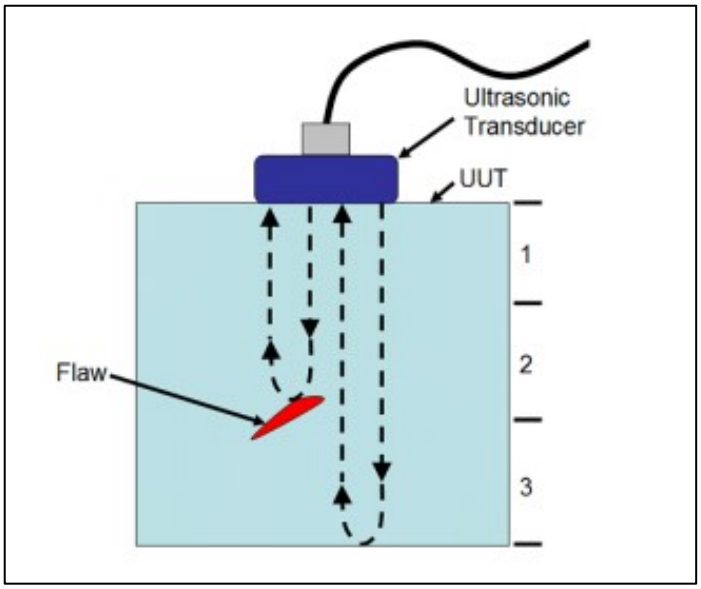

Figure 5.1: Pulse-echo ultrasonic technique [136]

Immersion UT is a method in which the component is immersed into a water tank and a transducer sweeps across the surface of the component, emitting and receiving the reflected signals. The collected signals are analysed by appropriate software to generate a mapping image known as the C-scan. The immersion UT technique can provide information regarding the size, orientation and position of the defect. It can be applied to detect impact damage, delamination, voids as well as large inclusions. Based on the attenuation of the ultrasonic waves, the overall void fraction of an FRC component can be determined. Any detected defects are indicated in the C-scan image using different colours, as it is shown in (Figure 5.2).

The immersion UT technique can generate only a 2-D image of the scanned area and cannot provide sufficient information regarding the depth of the damage [137]. Defects with sharp corners are not easily detected with this technique [138]. The size of a component may be such that the immersion tank is not big enough for this type of test to be carried out. More advanced signal processing techniques and testing configurations can permit the generation of 3D images but this is not currently common.

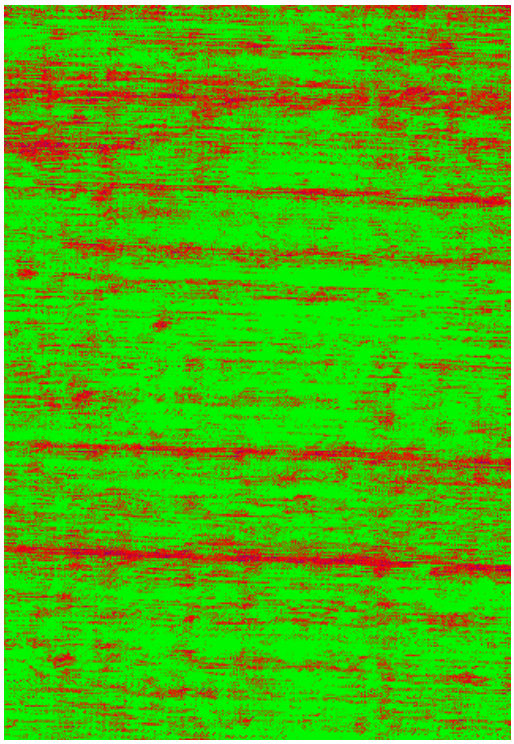

Figure 5.2 C-scan result of a scanned GFRP plate with high void content [37]. The red-coloured areas are heavily voided.

Backscatter UT is a variation of pulse-echo UT where the ultrasonic transducer is placed at an angle to the surface of the tested component. The reflected ultrasonic wave beams are received by the ultrasonic transfer and backscattered signals are generated. This technique can reveal the stacking sequence of the laminate, and detect voids, fibre waviness, translaminar and matrix cracking. However, this method is sensitive to the surface orientation. It is important that the angle and alignment of the transducer are maintained precisely throughout the inspection process [38].

Ultrasonic phased arrays make use of a multi-element piezoelectric transducer instead of a single crystal. As a result, the quality of the inspection can be considerably improved. Each individual element of the phased array probe can transmit and receive signals independently.

The ultrasonic beam can be stirred and focused by applying appropriate time delays to the individual elements to cause the desired constructive and destructive interference patterns in the interrogating wave front [139]. A phased array probe and the resulting image during inspection of a component are shown in Figure 5.3. The stirring and focusing of ultrasonic energy into required positions offers increased flexibility, helping improve the quality of inspection. This can also contribute in improving the probability of detection and quantification of smaller defects.

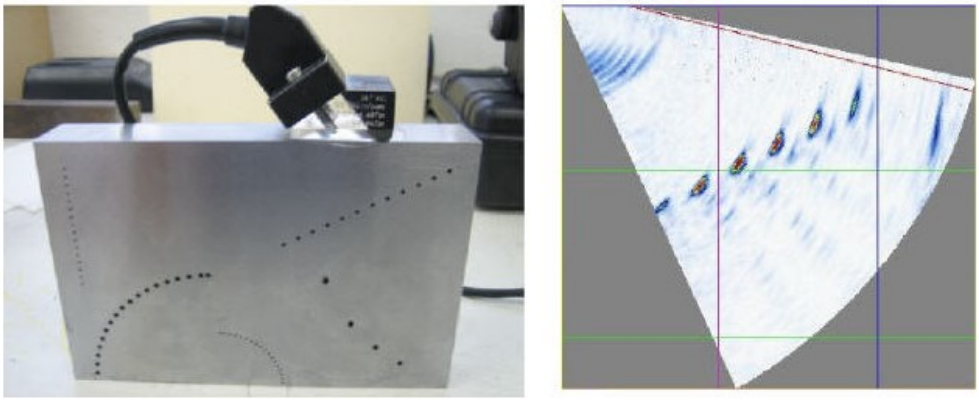

Figure 5.3: Ultrasonic Phased Array probe and resulting inspection imaging [140].

5.5 Infrared thermography

Infrared (IR) thermography is a non-contact inspection method. The presence of damage and defects is determined by monitoring the temperature distribution in the material based on the infrared radiation emitted. The temperature distribution is monitored using IR thermal cameras that generate a 2D thermal image of the inspected component. The presence of defects disturbs the heat flow in the material and generates temperature gradients around the

damaged area. The temperature variations are detected by the IR camera and are visualised in the form of thermograms. A thermogram of a delamination is shown in Figure 5.4.

Thermographic inspection can be either passive or active. In passive IR thermography the inspection is carried out according to the heat that is generated inside the specimen during loading. In active thermography powerful flashing light lamps are normally used to thermally excite the component. The photons emitted from the flashing lamps generate heat as they are absorbed by the component causing very small rising of its temperature. The setup for active IR thermography is schematically shown in Figure 5.5.

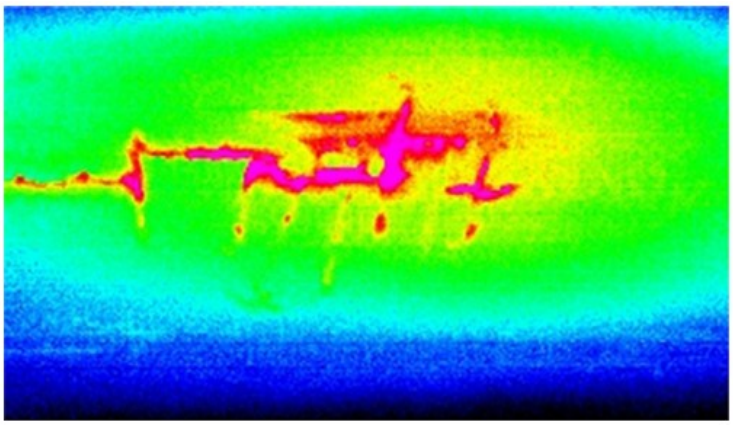

Figure 5.4: Thermographic image of a region with delamination damage [141].

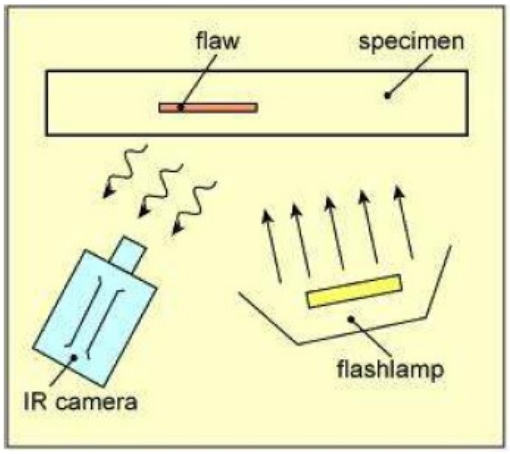

Figure 5.5: Active IR thermography set-up [38].

There are two types of active IR thermography; pulsed thermography and lock-in thermography. In pulsed thermography, a thermal pulse is applied to the inspected component and temperature variations in the component are monitored using an IR camera. Thermal transfer occurs under the surface via diffusion and convection. Once a heat wave reaches a defect the diffusion rate is disrupted. This appears as a region of different colour in the captured thermogram. As a result of convection losses, defects that are located deeper in the material will be detected later and at reduced detail in compared with those located closer to the surface [142].

In lock-in thermography a continuous harmonic modulated heat wave is generated to thermally excite the tested component. The generated heat pulses propagate in the material and are reflected once they meet a defect. The interference of the incoming and reflected heat waves generates a harmonic oscillation heat pattern on the component's surface detected by the IR camera. The presence of defects is identified as phase differences in the heat oscillation pattern between the defects and the healthy region [142].

The modulation frequency of the generated heat waves affects their penetration depth in the material. Low frequencies increase the penetration depth and can allow the detection of flaws and damage that are located deeper in the material. However, low modulation frequencies result in increased lateral heat loses decreasing resolution and hence sensitivity for smaller defects is reduced. This effect is illustrated by the decrease of the contrast in the thermographic image at greater depths. As a result, the assessment of flaws located deeper in the material can be affected by greater measurement errors. Higher modulation frequencies increase the sensitivity and accuracy of lock-in thermography but the generated heat waves penetrate less deep in the material. Delaminations of 10mm can be detected to a depth of 6mm at low excitation frequencies of 0.0032Hz, while heat waves with higher frequencies of 0.038Hz can penetrate up to 1.5mm [143].

In lock in thermography, there are certain modulation frequencies where the incident and reflected waves are in phase and cannot produce contrast differences in the thermographic image [142-144]. These frequencies are called “blind” and should be avoided, as they can mask the presence of flaws in the tested component. The blind frequency depends on the material and thickness of the component tested. It can be determined and avoided by experimental evaluation and testing at several frequencies before any thermographic inspection is carried out.

IR thermographic inspection can be used for the rapid inspection of large FRC components like aircraft wings, fuselage, hull, etc. It can detect inclusions, voids, cracks, impact and delamination damage [38]. Low velocity impact damage can be detected and assessed using IR thermography [145]. However, the applicability of the thermographic inspection is limited

by the thickness of the tested component, since higher lateral heat losses make the accurate detection of flaws located deeper in the material increasingly challenging.

5.6 Eddy Current Testing

ECT can be performed on materials that exhibit electrical conductivity. As a result, the applicability of this method on FRCs is limited to CFRPs due to the electrical conductivity of carbon fibres. ECT is based on the induction of eddy currents using a coil excited at a particular AC frequency placed above the surface of the CFRP test piece. Damage zones and defects disrupt the eddy currents induced in the material giving rise to changes in the magnetic field generated above them. The changes in the magnetic field cause measurable variations in the impedance of the coil. The severity of a defect can be assessed by the level of changes in the phase angle and amplitude of the impedance [137].

ECT can detect surface and subsurface flaws in CFRP components. However, the maximum effective depth of detection will be dependent on the electrical conductivity of the material and the operational frequency of the test coil. The lower the operational frequency, the higher the penetration depth achieved but at the expense of resolution. Hence, smaller defects buried deep in a thick FRC component may remain undetected. ECT can be used to detect delamination, impact damage broken fibres, undulations, missing fibre bundles, fibre fringes, missing sewing threads and angle errors [146].

5.7 Shearography

Shearography is an inspection technique which is commonly used for the inspection of FRCs for detection of defects, including inclusions and delaminations. The technique uses a divergent laser beam to illuminate the tested sample. The scattered light is projected onto an image plane using appropriate shearing lens. The lens shears the image and generates interference between the shear and the direct image of the tested piece. The interference between the sheared and direct images creates a shearographic pattern which maps the distribution of local surface strain [38].

During inspection a reference pattern image is initially taken from a structurally sound area of the tested piece. A stress distribution using vibration, pressure or thermal loading is then applied to the inspected specimen and a second interference pattern is recorded. The two interference patterns are superimposed and a fringe pattern occurs. Changes and disturbance in the fringe pattern during inspection are identified as defects and damaged regions [38].

5.8 Radiography

Radiographic inspection is carried out either using gamma or X-ray ionising radiation. Due to the low density of FRC materials and relatively small thicknesses, and inherent high energy of gamma ray sources, only adjustable X-ray sources and relatively low energy X-rays are normally used. In X-ray radiography, a beam of X-rays passes through the FRC component. The through-transmitted radiation excites a film or a fluorescent detector producing a radiographic image. The level of the absorbed or unabsorbed radiation that has passed

through the FRC component appears as variations in the contrast in the resulting radiograph. The evaluation of the radiograph is carried out by comparing the differences in the contrast and intensity between the damaged and the neighbouring area. To further improve the visualisation of damage and defects, appropriate penetrant fluids are used, which increase the radiograph contrast. Prior to radiography, penetrant fluid is applied on the surface of the specimen and allowed to penetrate into the damaged region for a sufficient time. The excess fluid is wiped out of the surface. The radiation that passes through the defected or damaged region is now strongly absorbed causing flaws to become more visible [38]. The NDT methods that are used to monitor defects in FRPs are summarised in Table 5.1.

Table 5.1 Summary of NDT methods

NDT method	**Method summary**	**Limitations**
Visual Inspection (VI)	Simple, rapid and versatile technique. VI is used for the surface inspection It does not require the use of sophisticated equipment.	VI is used only for surface inspection for visible defects. Unable to detect defects and damage that lie beneath the surface. VI must be combined with other NDT methods capable of detecting defects located deeper in the material.
Dye Penetrant Inspection (DPI)	Surface inspection technique that makes used of special coloured or fluorescent dyes. DPI is used to reveal the presence of smaller defects not detectable with VI.	DPI does not provide further information in regards with the depth of the defect. Unable to detect defects and damage that lie beneath the surface. Not applicable on porous materials. Surface roughness and poor cleanliness can adversely affect the quality of the results.

Ultrasonic Testing (UT)	Widely used NDT method. Is based on the use of ultrasonic PZT transducers capable of both transmitting and receiving ultrasonic waves. Defects and damage is detectable based on the scattering, reflection and attenuation of the ultrasonic waves. Through Thickness inspection is possible.	Contact method, access to the tested component cannot be always possible. Due to the attenuating characteristics of FRPs, the detection of smaller defects that lie deeper in the material can be challenging.
C-Scanning	UT-based method where the test piece is immersed in a water tank and the transducer sweeps across the surface of the component. A 2-D mapping image of the test piece is generated. The defects and damage zones are indicated in the C-Scan image as areas with different colours.	The size of the components may be such that the immersion tank is not big enough for this type of test to be carried out. The C-Scan image cannot provide information regarding the depth of the defects. Defects and damage zones with sharp corners are not easily seen with this technique.
Phased arrays	UT method based on the use of multi-element transducers. Multi-element transducers offer the capability of focusing and stirring the ultrasonic wave into required positions. Improved quality inspection. Improved probabilities of detecting smaller defects	Contact method, access to the tested component cannot be always possible. Due to the attenuating characteristics of FRPs, the detection of smaller defects that lie deeper in the material can be challenging.
Infra-Red (IR) thermography	Non-contact optical method NDT technique based on the monitoring of the temperature distribution in	The applicability of the technique is limited by the thickness of the components and by the depth of the defect

	the material. The presence of defects disturbs the temperature distribution generating temperature gradients around the damaged area. Temperature variations are detected by an IR camera and they are visualised into thermogram images. Non-contact method, it can be used to inspect large sections and components.	Large defects can be detected at low modulation frequencies up to 6mm, but the sensitivity is limited due to the increased lateral heat loses. Higher modulation frequencies increase the sensitivity but the generated heat waves can penetrate up to 1.5mm – 2mm. Lateral heat loses make the accurate detection of defects or damaged zones located deeper in the material challenging.
Eddy Current Testing (ECT)	ECT is based on the induction of electrical currents using an excitation AC coil. Damage zones and defects disrupt the electric currents in the material generating magnetic field causing changes in the impedance of the coil, which are detected and measured. ECT is capable of detected surface and subsurface flaws.	ECT is limited only on conductive materials. The maximum detection depth depends on the material's electrical conductivity and on the operational frequency of the coil. Lower frequencies can penetrate deeper in the material, but it will reduce the sensitivity of the method. Smaller defects that are located deep in the material will remain undetected.
Shearography	Non-contact optical method. The method is based on the use of a divergent laser beam to illuminate the test piece. A shearing lens shears the image and projects it onto a focusing plane. The interference between the sheared and direct image	Inspection of large sized components can be difficult. The test piece can become damaged when excitation stress or heat is applied on it. Poor lighting conditions can adversely affect the quality of the measurement.

	creates a shearographic pattern which maps the distribution of local surface strain.	
Radiography	Method is based on the use of gamma-ray of X-ray ionising radiation. The X-rays pass through the test piece and excites a photographic film or a fluorescent sensor producing the radiographic image The evaluation of the radiograph is carried out by comparing the differences in the contrast and the intensity between the damaged and unaffected areas. Improved visualisation is achieved by using appropriate penetrant fluid which increase the contrast in the radiographic image	Due to low density of FRP materials and to the high energy of the ionising radiation, only low energy X-rays can be used. Access for placing the film or the detector may not be always possible. High energy ionising radiation health hazards

CHAPTER 6

STRUCTURAL HEALTH MONITORING OF COMPOSITE MATERIALS USING ACOUSTIC EMISSION TESTING

6.1 Introduction

NDT of FRC components can be very challenging due to the anisotropic microstructural characteristics. Inspection of larger structures based on traditional NDT methodologies can be time consuming and smaller defects may have low probability of detection Normally inspection requires temporary interruption of operation in order to be performed. This can result in higher maintenance costs and reduced availability of an asset.

The limitations of conventional NDT methods have led to extensive research on development and implementation of SHM techniques. SHM permits continuous evaluation of the structural integrity of in-service components. Instead of manually inspecting a structure damage-related data are recorded through an SHM system. This limits the requirement to stop operations to perform manual inspections. In addition, when damage has been detected, inspection and maintenance crews can focus their attention readily in the area of interest minimising disruption and enhancing availability without compromising reliability and safety. In-service evaluation of the structural integrity of FRC components can be performed using strain gauges, vibration analysis, Fibre-Bragg Gratings (FBGs) and acoustic emission techniques.

Strain gauges are surface mounted sensors used to measure strain. A strain gauge is made of an insulating flexible plastic film which supports a metallic foil pattern. The strain gauge is adhesively attached on the surface of the component or test piece. Under loading the deformation of the strain gauge follows the deformation of the tested component. As the foil pattern of the strain gauge deforms its electrical resistance changes. The changes in electrical resistance are measured using a Wheatstone bridge and voltage output is then converted to

strain values. Normally, strain measurements need to be compensated for temperature variations that may occur.

Vibration analysis can be applied for continuous monitoring of damage evolution and loads sustained by a composite structure [147-149]. Vibrations are measured using piezoelectric accelerometers that are able to detect variations in acceleration during dynamic loading. Damage evolution is determined through spectral analysis of the recorded signals providing indications of the structural condition of the structure. Generally, vibration analysis can provide useful information regarding the extent at which a structure is stressed and damaged when in service.

Fibre Bragg Gratings (FBGs) are optical fibre-based sensors commonly mounted but sometimes also embedded in an FRC structure. FBG sensors are optical fibres with Bragg gratings reflectors printed at predetermined locations along their length. The exact location where strain changes occur on a monitored structure using FBGs is determined by the wavelength of the grating. Each grating has its own characteristic wavelength [43]. FBGs are increasingly used in SHM of various structures and components including aircraft sections and wind turbine blades [150, 151].

Acoustic Emission (AE) is another SHM technique which can be used to monitor in-service structural components. AE is based on the detection of stress waves from localised damage sources under load. Stress waves can only be detected from a damage source only if it is active and hence it is propagating further under certain load which can be either static or dynamic. AE can be used for the monitoring large structures [44], manufactured from a wide variety of engineering material including metals, ceramics or FRCs.

6.2 Acoustic Emission Testing

6.2.1 Fundamentals of AE Testing

AE testing is based on the detection of elastic transient waves produced from localised sources when deformation or damage occurs in a material. PZT piezoelectric sensors attached on the tested component detect the surface displacements arising from a damage source. These surface displacements propagate in form of waves, are detected by the piezoelectric element and converted to a weak electric signal. These signals are amplified using an amplifier with appropriate gain selected and digitised at the selected sampling rate using a data acquisition card (DAQ). The data are subsequently logged, visualised and analysed through appropriate software [44-46, 152, 153]. The fundamentals of AE testing are illustrated in Figure 6.1. The recorded AE activity can be used to evaluate the structural integrity of engineering components and monitor in-service damage growth.

Conventional NDT methods such as UT are active and hence need to generate the interrogating signal. AE instead is a passive method based on the detection of signals generated from active damage sources in the material.

AE is applicable for monitoring inhomogeneous and anisotropic materials, including FRCs. However, SHM of FRCs based on AE can be quite challenging due to the anisotropy exhibited and the variety of damage mechanisms affecting them during damage initiation and subsequent evolution under static or dynamic loading conditions. Different damage modes in FRCs can give rise to different AE signal features that need to be analysed in order to assess damage evolution and evaluate the structural integrity of in-service structures effectively.

Unwanted AE activity, such as background noise signals, not related to actual damage sources, can contaminate the results. The presence of noise signals that have not been successfully filtered out can influence adversely the quality of SHM results obtained with AE.

Efficient data acquisition parameterisation together with extensive data processing and statistical analysis are required in order to ascertain correctly damage evolution and severity in FRC components and structures. The damage evolution history must be further assessed by examining the AE evolution throughout the monitoring history of the component.

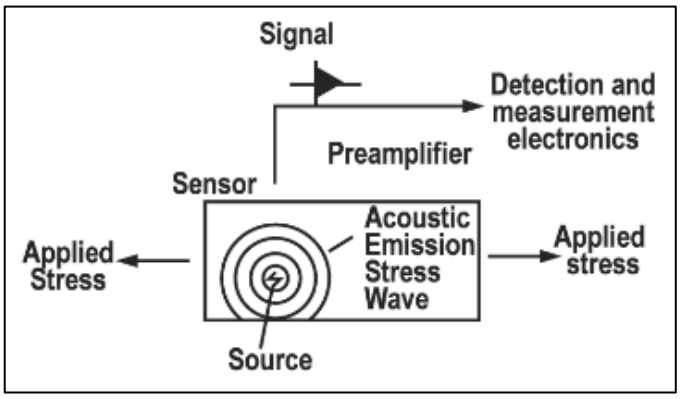

Figure 6.1: Schematic description of the AE testing [44]

AE activity is generated while the component is under sufficient loading for damage to evolve. If the load is removed, further AE signals will not be generated unless the previously attained maximum load is exceeded. This is known as the Kaiser effect. Significant AE activity resuming at a load below the previous maximum load level can occur when damage has evolved closer to critical levels. This phenomenon is known as the Felicity effect [44].

Understanding of both Kaiser and Felicity effects is very important in AE testing because they can provide significant insight regarding the actual condition of the component monitored.

6.2.2 Acoustic Emission waves and propagation

Stress waves emitted from a source will typically propagate towards all directions in the component although some directionality is also possible. Accurate analysis of wave propagation can be a complex task. The propagation of stress waves can be disturbed by the presence of discontinuities causing scattering and reflections. As the waves propagate through the material, several phenomena associated with wave interactions with the microstructure of the material including attenuation, dispersion, diffraction, and scattering will take place [154]. The edges of the specimen can reflect stress waves back into the test piece causing constructive and destructive interference with originally emitted waves from the source [155]. Numerous elastic stress waves can be simultaneously generated by multiple sources also resulting in destructive and constructive interference of the propagating waves. As a result, the stress waves eventually detected by the AE sensors can be essentially superpositions of reflections, complex wave interactions and wave interference phenomena that may have occurred during the propagation of numerous stress waves in the material [44].

A common and important wave type occurring in plates are the Lamb or plate waves. Lamb waves cause particle motion along the direction of their travel, propagating parallel to the plane of the plate component. The family of Lamb waves includes two different wave modes, the symmetrical, s_0, or extensional mode, and the asymmetrical, a_0, or flexural mode. In s_0

mode, the plate is alternately stretching and compressing in the direction of the wave's propagation, while the top and bottom surfaces of the plate are stretching and compressing symmetrically. In a_0 mode the plate bends alternately with the top and bottom surfaces of the plate to follow the same bending direction. The s_0 is caused by in plane strain energy release, while the a_0 is caused by out-of plane energy release perpendicular to the plate. In general both modes propagate independently without interfering with each other. However, the a_0 waves generate signals with higher amplitudes and propagate faster in the material compared with the s_0 waves. Other types of waves such as the a_1 and s_1 exhibit higher propagation velocity compared with both a_0 and s_0 waves, but they cannot be utilised for SHM purposes since they generate AE signals with low amplitudes [156].

6.2.3 The Acoustic Emission Signal

AE signals can be classified into two fundamental types, transient or burst-type and continuous. The transient signals appear as decaying sinusoidal waveforms. They normally arise from damage sources. Continuous signals are normally related to unwanted noise signals generated during testing [157-159]. They can be related to electrical noise, mechanical noise, friction and echoes of primary AE signals. Examples of transient and continuous signals are shown in Figure 6.2.

AE signals detected by the PZT sensors are normally generated in the frequency range between 20-1200kHz. A typical AE signal is represented as a voltage excitation waveform over time. An AE signal or hit exceeding the pre-set threshold limit is recorded by the data acquisition board, logged and visualised [160]. Each recorded AE signal contains several

features such as amplitude, duration, counts, rise time, peak frequency and energy. Figure 6.3 shows another example of a signal waveform and some basic signal features.

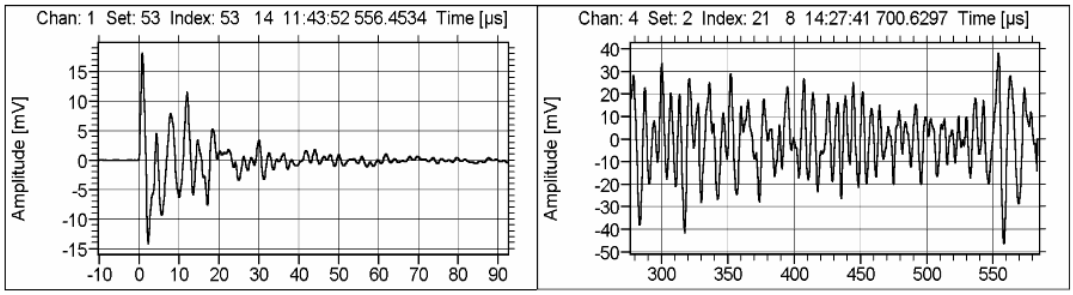

Figure 6.2: Transient (left) and continuous (right) AE signal [159]

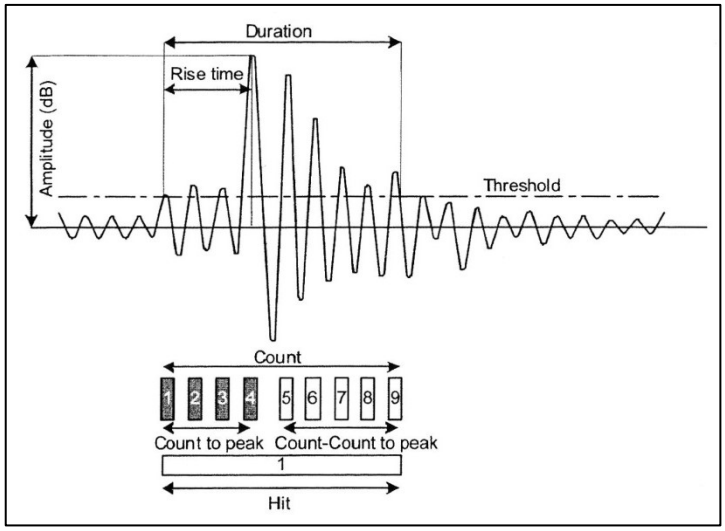

Figure 6.3: Example AE waveform and signal features [160].

Based on the differences between the signal features of the recorded AE signals, it is possible to identify and separate the unwanted noise signals from the damage related AE signals. Although the DAQ system has the capability of employing a wide variety of AE signal

parameters, not all of them can be used for the identification of the damage and noise-related signals. The signal features that can be used to discriminate the damage-related AE signals from the noise signals are the amplitude, duration, rise time, counts, counts to peak, and energy. As it can be seen in Figure 6.4 a classification methodology for identifying the noise from the damage-related AE signals is carried out in four steps. Initially the AE signals are recorded during the testing. In the next step data clustering is carried out based on the analysis of the AE signal features. The data clustering process groups into clusters the different types of AE signals, using automated data clustering algorithms. After data clustering the characteristics for the different types of AE signals are analysed and compared with each other. In the last step the different groups of AE signals are differentiated and classified based on the differences between their basic signal features.

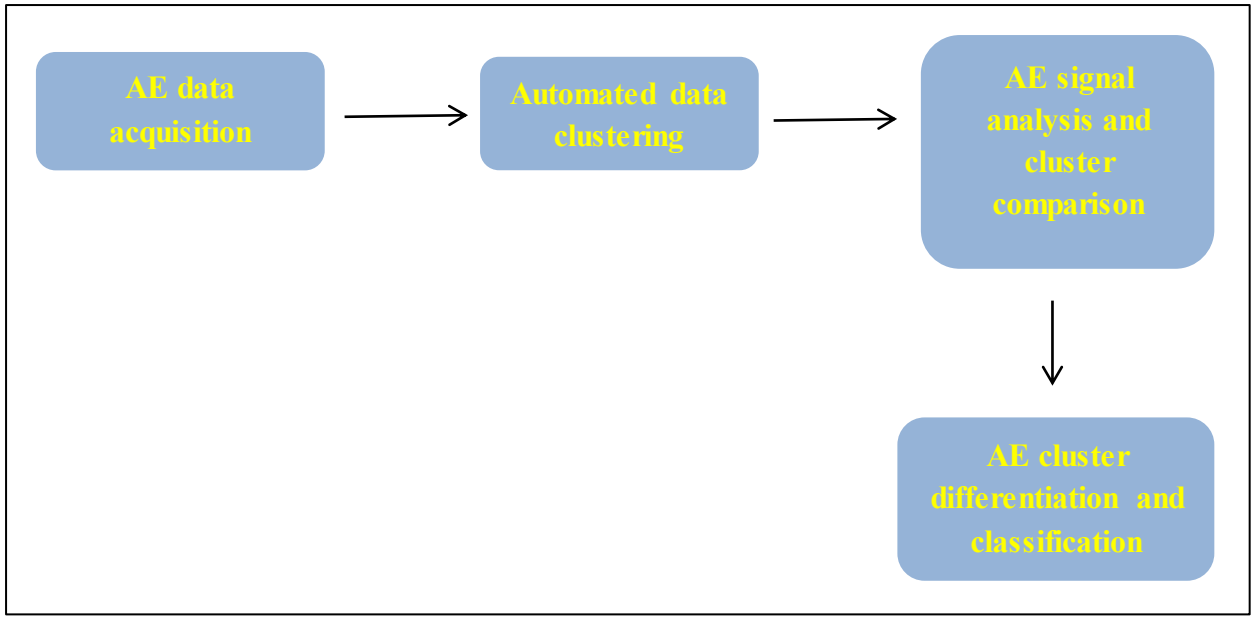

Figure 6.4: Methodology for the classification of the different types of AE signals

Specialised AE signal processing software, such as the "AE-Win" developed by Mistras Group Inc. (previously Physical Acoustics Corporation- PAC) extracts and calculates the following signal features from each recorded AE signal during acquisition. The resolution, range and units of the signal features are shown in Table 6.1.

- **Time of Hit**

This is the time at which the AE signal has been logged by the AE system [161].

- **Amplitude**

Amplitude is the maximum (positive or negative) AE signal excursion during an AE hit. The amplitude is expressed in decibels (dB) as follows [161]:

$$dB = 20 \log (V_{max}/1\mu\text{-volt}) - (\text{Preamplifier Gain in dB})$$

For example, if the preamplifier gain is 40 dB, and the maximum voltage detected is 1 volt, the amplitude is 80 dB.

- **Energy:**

AE signal energy also called PAC-energy is a parameter defined by the manufacturer of the AE system. It is defined as the integral of the rectified voltage signal over the duration

of the AE hit. The energy is expressed by the PAC acquisition system in 10μVolt-sec/count [161]. The actual energy of the signal is called absolute energy.

- **Counts**

This AE hit feature counts the total AE signal's excursions over the threshold [161].

- **Duration**

Duration is defined as the time from the first threshold crossing until the last threshold crossing of the AE signal [161].

- **RMS**

Root Mean Square is a measure of the continuously varying signal voltage. RMS is defined as the rectified, time averaged AE signal, measured on a linear scale and reported in volts. In terms of an AE hit feature, the instantaneous value of RMS voltage is collected and processed along with the other AE features when an AE hit is detected [161].

- **ASL**

Average Signal Level is a measure of the average amplitude variations of the AE signal. The measurement of ASL is similar to RMS. However, RMS is measured in volts, while the ASL is measured in dB [161].

- **Rise Time**

Rise Time is the time between the first Threshold crossing and the peak amplitude of the AE Hit [161].

- **Counts to Peak**

Counts to Peak is a measure of the number of AE Counts between the first Threshold crossing and the Peak Amplitude of the AE Hit [161].

- **Average Frequency**

The average frequency over the entire AE hit is derived from the collected AE Counts and Duration of the recorded signal according to [161]:

(AE Counts) / (Duration)

- **Reverberation frequency**

Reverberation frequency is also known as “ring down” frequency and it is the average frequency after the signal after its peak amplitude. Reverberation frequency is calculated from the collected Counts, Counts to Peak, Duration and Risetime parameters according to [161]:

(AE counts - counts to peak) / (duration - risetime)

- **Initiation frequency**

Initiation Frequency is the “Rise Time” frequency. This feature calculates the average frequency during the portion of the waveform from initial threshold crossing to the peak of the AE waveform. Initiation frequency is calculated from the collected Counts to Peak and Risetime according to [161]:

(AE counts to peak) / (rise time)

- **Signal Strength**

Signal Strength is defined as the integral of the rectified voltage signal over the duration of the AE waveform packet. This parameter is similar to the “PAC Energy” feature, except that it is calculated over the entire AE signal dynamic range and is independent of the gain setting [161].

- **Absolute Energy**

Absolute Energy is a feature whose units are measured in atto-Joules (aJ). This feature is the true energy measure of the AE signal. Absolute energy is calculated from the Integral of the squared voltage signal divided by the system's reference resistance (10k-ohm) over the duration of the AE waveform packet [161].

- **Frequency Centroid**

Frequency Centroid is a real time Frequency feature which is determined by performing a real-time Fast Fourier Transform (FFT) on the original AE signal and carrying out the following calculation on each FFT element [161]:

$$\text{SUM}(\text{magnitude} * \text{frequency}) \ / \ \text{SUM}(\text{magnitude})$$

- **Peak frequency**

The Peak frequency is determined by performing an FFT on the recorded AE signal. The Peak frequency value is defined as the frequency in the FFT Power Spectrum where the peak magnitude is observed. The accuracy of the Peak frequency measurement is sensitive to the waveform's length which indicates the number of points that compose the waveform. Increased waveform length increases the sensitivity of the Peak frequency calculation and leads to more accurate results [161].

- **Partial Power**

Partial Power is a set of waveform and frequency features derived from the signals power spectrum collected waveform. Partial Power features are derived from the power spectrum of the waveform associated with a hit. Partial Power is a percentage which is calculated by summing the signal's power spectrum in a user specified frequency range, divided by the signal's total power across the full range of frequencies, and multiplying the result by 100 [161].

Table 6.1: Resolution, range and units for each signal feature [161].

Signal Characteristics	Resolution	Units	Range
Time of Hit/Time of Test	0.250	µsec	0 – 407 days
(PAC) Energy	1 count	10µvolt-sec/count	0–65535 µvolt-sec/count
Signal Strength	1 count	3.5 picovolt-sec	0 – 1.31×10^{8} picovolt-sec
Absolute Energy	1 count	9.31×10^{-22} Joules	2.61×10^{-8} Joules
Amplitude	1 dB	1 dB	10 – 100 dB
Rise Time	1 µsec	µsec	0 – 65.535 msec
Duration	1 µsec	µsec	0 – 1000 msec
Counts	1 count	Count (Threshold crossing)	0 – 65535 counts
Counts to Peak	1 count	Counts	0 – 32768 counts
Partial Power	0.01 %	Percent of Total Power	0 – 100%
Frequency Centroid	1 kHz	kHz	1 kHz – 2100 kHz
Peak Frequency	1 kHz	kHz	1 kHz – 2100 kHz
Initiation Frequency	1 kHz	kHz	0 – 65535 kHz
Reverberation Frequency	1 kHz	kHz	0 – 65535 kHz
Average Frequency	1 kHz	kHz	0 – 65535 kHz
RMS	0.2 millivolts	millivolts	0 – 6 Volts
ASL	1 dB	dB	0 – 100 dB
Threshold	1dB	dB	14 – 99 dB

Additional signal parameters can be extracted by using the main signal features that are initially produced by the DAQ system. The new signal parameters can provide further information about the AE signal characteristics and they can improve the effectiveness of AE

testing in monitoring structural degradation, as well as discriminating between the different types of damage in the material.

A large variety of additional signal features can be created after the testing and during the AE data processing stage. Different main signal features can be combined to create new useful parameters.

Further to the main signal features, the following parameters were examined in past studies.

- Decay Time (DT=Duration-Rise Time), which is the measure of the time after the signal's peak amplitude until the last threshold crossing [162, 163] .
- Decay counts (CND=Counts – Counts to peak), which is a measure of the number of AE Counts between the peak and the last threshold crossing [162].
- Decay Angle, (DAN=Amplitude/Duration) [162-164].
- Rise Time to total area (RTA=Rise Time/Duration) [162-164].
- Ratio of Decay counts to Counts to Peak (CDP=Decay counts/Counts to peak) [162-164].
- Normalised Counts to peak (CPC=Counts to peak/ Counts) [164].
- RA ratio (RA= Rise Time / Amplitude) [165, 166].
- Counts / Counts to peak [167-170].
- Energy / Amplitude [167-170].
- Rise Time / Decay Time (or Fall Time) [167, 169].
- Counts / Decay Counts (or Fall Counts) [169]
- Counts to peak / Rise Time [169]
- Decay Counts / Decay Time (or Fall counts / Fall Time) [169]

- Counts to Peak / Counts to Decay [167].

Kappatos et al. in previous studies [167, 168] extracted several frequency and time domain AE signal features. Among an initial and large set of AE signal features, a smaller and more robust set of signal features was defined. This can improve the performance of an AE system in monitoring crack growth, especially in noisy environments.

6.2.4 Acoustic Emission sensors and Pre-amplifiers

The type of crystal mostly used for AE applications is PZT. The active element of the sensor is a thin piezoelectric crystal which is metallised on both surfaces for improved electrical conductivity. The crystal is mounted on a metal housing providing protection and electromagnetic shielding [161]. Part of the casing is a ceramic wear plate at the bottom of the sensor, acting as the contact surface, and protecting the crystal against wear and corrosion. When stress waves reach the sensor they cause the crystal to deform.

Based on their frequency response AE sensors are classified in resonant and wide-band sensors. Resonant sensors are highly sensitive to a narrow frequency band around the natural resonant oscillation frequency of the crystal. These sensors can have secondary resonance frequencies but the sensor's sensitivity will be reduced at these frequency bands. Generally, the resonant frequency of the sensor is affected by the size of the piezoelectric crystal [44, 171]. Small crystals exhibit higher resonance frequencies, while low frequencies are obtained by larger elements [171].

In wide-band sensors a damper is bonded to the crystal to suppress the resonance and allow the sensor to operate in a wide frequency range. This results in the sensor to have a flat frequency response over a wide bandwidth. Wide-band sensors are used in applications where damage monitoring frequency is still unknown and for the detection and analysis of various AE wave modes with different frequency response. The main characteristics of resonant and wide-band AE sensors are shown in Figure 6.5.

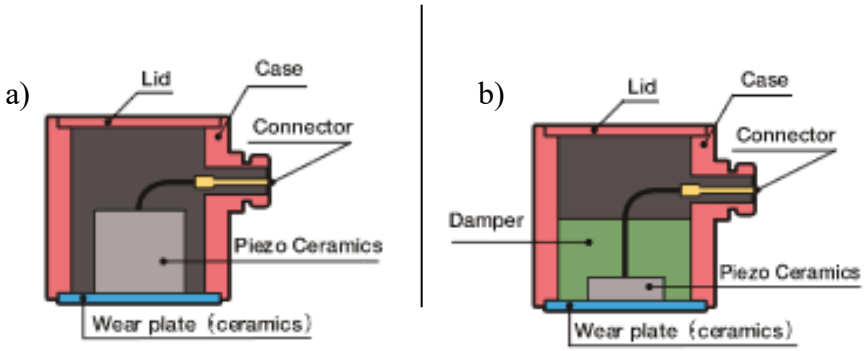

Figure 6.5: Structure of a) resonant and b) wideband AE sensors [172]

Due to operational and enviromental degradation of AE sensors, a verification of the sensor's frequency response is often required. Before AE testing the sensor is attached on the test piece and pencil lead breaks (PLB) or Hsu-Nielsen tests are performed to verify its response. In PLB testing, a wide frequency AE signal similar to natural transient signals is generated. After PLB testing the frequency response of the sensor is assessed by analysing the recorded AE signals. As shown in Figure 6.6, a PLB test is perfomed using a mechanical pencil to break a 0.5mm 2H graphite lead of approximatelly 3mm in length. A guiding plastic shoe or guide-ring is used to maintain constant break angle of the tip in each test.

A factor that affects the acquisition capability of the AE sensors is the coupling quality of the sensor with the component's surface. A suitable couplant is used to ultrasonically couple the

AE sensors on the tested component. The AE sensor is held in place by applying sufficient pressure on it throught the test. The couplant increases the transmittance of the stress waves to the sensor and eliminates any signal loss caused by wave scattering between the sensor and the specimen.

In addition to the AE sensors, the use of preamplifiers is also vitally important for the acquisition of AE signals. The preamplifiers are connected to the sensors and are used to amplify the electrical output signals. The amplification level or gain is selected according to the requirements of the application. Commonly the gain level is set to 40dB. However, lower and higher gain levels are available. The preamplifiers include a band pass filter to eliminate the detection of noise signals and optimise the sensor's sensitivity. A wideband-pass preamplifier is used in applications where the frequency bandwidth is unknown [161].

The advancements in the field of AE are represented by the development of integral preamplifier sensors which enclose a preamplifier inside a standard AE sensor. Integral preamplifier sensors eliminate the need for external preamplifiers by incorporating two functional components in one [161].

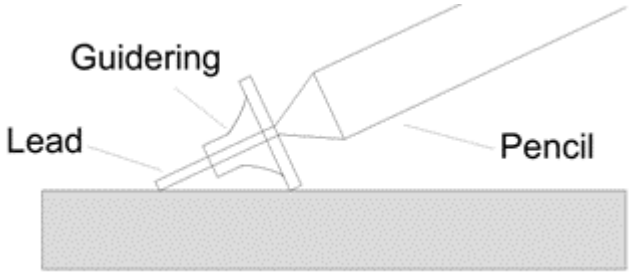

Figure 6.6: Pencil Lead Break testing [173].

6.3 Damage evolution monitoring in composite materials using AE testing

Damage progression in FRC can be monitored using AE methods. Damage-related events occurring during loading generate AE activity, which can be used to monitor and assess its progression in an FRC component. In FRC materials, damage modes such as matrix cracking, delamination, debonding and fibre pull-out are the main sources of AE activity. In-depth data processing of the recorded AE activity can provide important information regarding the type and severity of the damage evolution. However, noise AE signals may also be recorded as a result of friction, sensor slippage, environmental and electrical noise. Unwanted noise signals can be generated in significant numbers during loading masking out the damage-related AE signals. Thus, it is important to obtain the key noise signal features in order to identify and separate them from damage-related signals. The electrical noise can be minimised by adjusting the threshold level to a value that is above the amplitude of the electrical noise signals.

The damage evolution during loading is commonly assessed by examining the loading history and AE response arising during testing. Plotting the load or stress displacement with the AE cumulative hits evolution gives an indication of the damage evolution during testing (Figure 6.7). As the load increases, damage occurs in the material generating AE activity. It can be thereby seen that as a result of damage progression, sudden increases in the AE cumulative counts are observed until final failure, identified as a steep increase in the AE history plot, occurs. At the early stages of loading, no or little AE activity is observed, since no or little damage can initiate at low loads. Damage initiation can be identified as the point at which the AE activity starts. Further increase in the load results in damage propagation indicated by sudden and steep increase in the cumulative AE parameters. At high loads and prior to

failure, high damage propagation rates are identified as a steep and sharp increase in the generated AE activity until final catastrophic failure of the material takes place [166, 174, 175]. Steep increase in AE activity is also observed as a result of damage evolution during fatigue tests [176, 177]. The generation of AE activity can be strongly affected by water absorption in FRC components. Moisture ingress causes plasticisation of the polymer matrix resulting in the generation of limited AE signals associated to matrix cracking [119]. Moisture ingress is an important factor that should be considered, when AE is used for field structural health monitoring of maritime structures, since reduced AE activity may be generated from in-service components with high moisture pick-up.

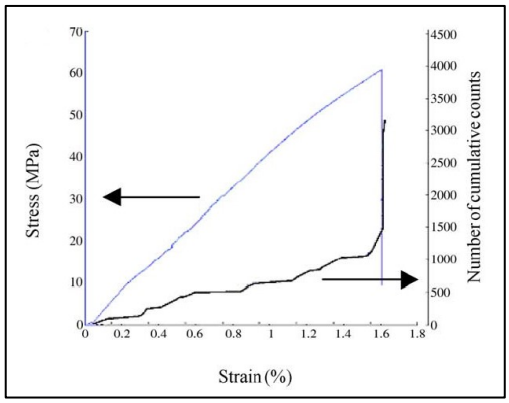

Figure 6.7: Stress displacement and AE cumulative counts [178].

Conventional AE analysis is based on the investigation of the cumulative hits evolution over time, and commonly on the analysis of the amplitude distribution of the recorded signals. However, an alternative and more effective analysis involves the analysis of the identification of AE signals that are generated by the different failure modes in FRCs.

The different failure modes of FRCs give rise to a variety of AE signals, each with distinctive characteristics. By analysing the characteristics of the recorded signals it is possible to identify and discriminate between the main damage modes of FRCs. Godin et al. [178, 179], reported the presence of three main types of signals which are associated to the main damage modes in composite materials. These types of signals are denoted as Type-A, Type-B, Type-C and are associated to matrix cracking, interfacial debonding, and fibre fracture respectively. Type-A signals are generated in an amplitude range of 55-70dB with long rise time and long decaying time. Type-B signals are generated in an amplitude range between 70-90dB and have short rise time, short decaying time and higher signal energy compared to the Type-A [180]. Type-C signals are similar to Type-B. It is difficult to identify and differentiate them [179]. A fourth type of signal with high amplitude, long risetime and high duration is denoted as Type-D and is associated to delamination events [178].

The identification of the different damage modes in FRCs can be effectively carried out by discriminating between the respective types of AE signals that are generated during testing. Signal identification is based on the analysis of different AE signal parameters. However, signal identification is not successful when it is based on one signal feature only. Therefore, multi-parametric signal analysis is required for effective signal discrimination.

Multi-parametric analysis is based on the analysis of the signal features such as the amplitude, duration, risetime, counts, and energy, or on the frequency content of the signal. A large number of authors [119, 152, 178-186] perform multi-parametric analysis on the recorded AE signals to identify the different damage mechanisms in composite materials, whereas in other studies [183, 187, 188] the signal parameter analysis is based on the frequency characteristics of the AE signals. By evaluating AE signals based on their

characteristics it is possible to group them into clusters. The clustering process is time-consuming and non-realistic process if attempted manually. Instead, data clustering can be achieved by using automated algorithms. Data clustering can be achieved by using supervised and unsupervised clustering algorithms. Unsupervised clustering algorithms like K-means, Forgy, and ISODATA group the AE signals into clusters according to key differences between their characteristics.

The use of unsupervised algorithms does not require any knowledge on the structure of the collected data, but the expected number of clusters must be estimated in advance. Supervised clustering methods like the k-Nearest Neighbour (k-NN) involve a learning process where a known and pre-defined set of data is used to train the algorithm. Any new set of data is processed and classified according to the patterns and structure that derive from the learning step.

A common data clustering methodology is the combined use of the unsupervised k-means algorithm with the Kohonen's Self-Organising Map (SOM) [119, 152, 178-185, 187]. Anastassopoulos and Philippidis [162] presented a data clustering methodology for the evaluation of AE from FRCs based on a two-step clustering method. In the first step the maximum distance algorithm creates an initial partition, which is further optimised in the second step by the Forgy algorithm. The environmental and mechanical noise signals that are recorded must be taken into consideration and included into the data clustering analysis. The AE noise signals can be identified and grouped into a separate cluster. In this way the AE noise signals can be effectively separated from the damage-related signals, improving the effectiveness of AE testing in monitoring damage growth in FRCs.

After the noise and individual failure types are grouped into classes, damage growth can be assessed by examining the AE evolution of the individual failure modes. Figure 6.8 shows a typical example of the AE evolution of individual damage modes for epoxy and polyurethane GFRP composites loaded parallel to the direction of the fibres. In both cases damage initiates by fibre/matrix interfacial failure followed by fibre fracture and matrix cracking. In the epoxy composite matrix cracking initiates earlier and grows faster compared to the polyurethane composite. This behaviour is attributed to the brittle nature of the epoxy system, which further results in increased generation of matrix cracking-associated signals. In both samples the evolution of fibre fracture signals follows the interfacial failure until rupture which is identified by sharp increase in the AE signals associated with interfacial failure and fibre fracture [187].

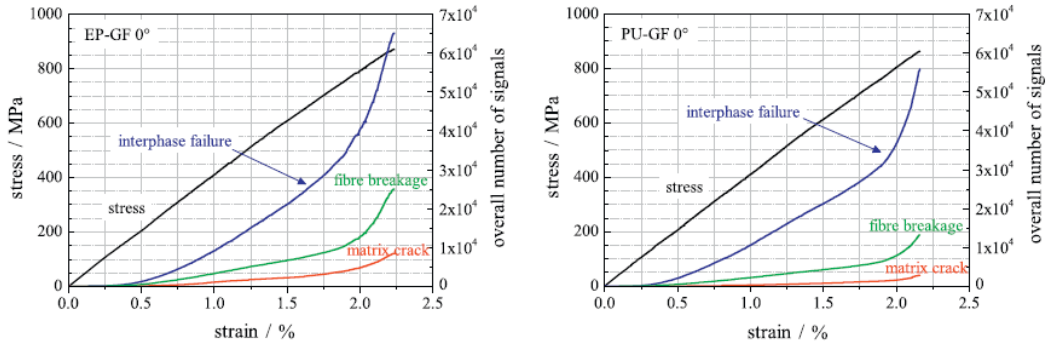

Figure 6.8: Stress-strain diagrams and damage modes evolution monitoring for glass fibre reinforced epoxy (EP) and polyurethane (PU) composites [187].

Reprinted from Composites Part B: Engineering, Vol.56 , M. Kempf, O. Skrabala, V. Altstädt, Acoustic emission analysis for characterisation of damage mechanisms in fibre reinforced thermosetting polyurethane and epoxy, 477-483, Copyright 2014, with permission from Elsevier

The resulting clusters may have similar signal features. Clear differentiation between them can often be difficult and complicated. Different clusters may exhibit similar and parallel

growth. This behaviour can indicate the simultaneous evolution of different damage mechanisms, or it can represent the evolution of the same damage mechanism [163]. In the second case, different clusters can be merged into a single cluster so multiple damage mechanisms are represented by one cluster only. Conventional monitoring of damage growth for the main types of failure in an FRC material is commonly achieved by using the cumulative number of AE hits for each cluster. However, an alternative and more effective way in monitoring damage growth is the examination of the cumulative energy. Delamination, fibre fracture and matrix cracking cause the generation of AE signals with high energy content. Consequently, the damage growth for each failure mode can be monitored and identified as sharp and abrupt increases in the cumulative energy plot for different signal clusters.

6.4 Automated data clustering

In this study clustering of AE signals is carried out using common clustering algorithms such as k-means, Forgy, ISODATA and Learning Vector Quantiser (L.V.Q.). The performance of each clustering algorithm considered in this study is discussed in the following chapters. A detailed description of the clustering algorithms is presented in the Appendix.

6.5 Fast Fourier Transform

One of the most common signal processing techniques for spectral analysis of AE waveforms is the Fast Fourier Transform (FFT) algorithm. A detailed description of the FFT algorithm is presented in the Appendix.

CHAPTER 7

EXPERIMENTAL METHODOLOGY

7.1 Introduction

Chapter 7 describes the experimental methodology employed in this study. The materials, specimen types, fabrication methods, and tests carried out are described in detail. The main aim of the tests was to evaluate the effectiveness of AE for monitoring damage initiation and subsequent damage evolution in FRC materials and components.

7.2 E-glass fibre bundle samples

Small E-glass fibre bundles containing a few filaments only were prepared for tensile testing. The small fibre bundles were manually separated from an as-received PPG Hybon® 2026-Tex 2400 E-glass fibre roving. The separation of the smaller bundles from the original one was done carefully to protect the separated filaments from damage during handling. Since the separation of the filaments was done manually, the resulting number of filaments could not be controlled. The number of filaments in the smaller sample bundles obtained ranged between 7 and 42. After testing of the small bundles, the end tabs of the samples were cut in half and polished to count the exact number of filaments present in each bundle with the help of an optical microscope.

Tensile tests were carried out on dry and lubricated PPG Hybon® 2001-Tex 300 E-glass roving consisting of 700 filaments. As-received (dry) lubricated fibre bundles were prepared for tensile testing. The lubrication was performed by submerging the fibre bundles in vegetable oil for 30 minutes. Prior to testing the samples were removed from the vegetable oil allowing any excess oil to drip from the samples. The gauge length for all bundle samples

was 100mm. The fibre bundles were end-tabbed in a wooden end-tab jig. The two free ends of the fibre bundles were laid in the middle of 60x25x1.5mm aluminium end-tabs and tightly bonded together using 3M Scotchweld-9323 adhesive. The end tabs were used to mount the fibre bundles on the tensile machine and accommodate the AE sensor mounting on the samples during tensile testing.

Attention was paid to ensure even tension distribution across the fibre bundle, by pulling gently the two ends of the bundles prior to end-tabbing. However, perfect tension distribution between all the filaments in the fibre bundles could not be achieved due to their large number. During mechanical testing fibre failure was monitored using AE. This was done in order to evaluate the capability of AE testing in detecting and monitoring individual fibre fracture events, and to assess the factors that can influence the AE activity recorded.

7.3 Glass fibre reinforced composite samples

Several types of GFRP samples were subjected to mechanical testing. During mechanical testing failure in GFRP samples was monitored using AE testing. This was done in order to evaluate the capability of AE in continuously monitoring damage evolution in FRPs. Test specimens were cut using water jet cutting and prepared from GFRP plates provided from industrial partners and manufactured in-house. Water jet cutting was used to ensure smooth edges and minimise the edge effect on the test pieces.

7.3.1 Vacuum bagging glass/vinyl-ester samples

Glass/vinyl-ester plates were fabricated by a shipyard using vacuum bagging. The plates were made using a biaxial stitched E-glass fabric with density of 813gm^2 provided by METYX composites. The polymer matrix of the samples consisted of the CRYSTIC VE679PA vinyl-ester resin system, provided by SCOTT BADER.

The Vacuum bagged glass/vinylester samples were prepared using the following fabrication route [189]:

- A layer of demoulding agent was coated on a flat work surface.
- Layers of glass reinforcement fabric were impregnated with resin and placed on the work surface until the desired number of layers and stacking sequence was achieved.
- A piece of peel-ply was applied on the resin/glass fabric lay-up.
- A piece of release film was applied on the peel-ply.
- A piece of breather fabric was applied on release film to improve the evacuation process.
- Spiral vacuum hoses were placed on the breather fabric.
- The lay-up was covered with plastic sheet and sealed with appropriate sealant tape.
- The vacuum hoses were connected to the vacuum pump.
- After the desired vacuum level was reached, the plate was cured under vacuum for 12 hours.
- After curing, the cured plate was removed.

Different batches of vacuum bagged fibre/vinyl-ester plates were provided by the shipyard for characterisation including evaluation of fibre fraction, void content and mechanical properties.

7.3.2 Resin infusion glass/vinyl-ester samples

Glass/vinyl-ester plates were fabricated in-house using resin infusion (RI). The plates were made using a biaxial stitched E-glass fabric with density of 813gm^2 provided by METYX composites. The resin system used for the fabrication of the composite plates consisted of the polymer matrix, CRYSTIC VE679PA-03PA vinyl-ester resin and Butanox M50 hardener, provided by SCOTT BADER.

The resin infusion equipment used for the fabrication of the glass fibre vinyl-ester plates included a vacuum pump, a liquid resin trap, an aluminium base plate, plastic sheets, peel plies, flow media mesh, plastic hoses, omega flow tubes, and sealant tape.

The process started with the preparation of the vacuum bagging system. The resin infusion vacuum bagging lay-up is shown in Figure 7.1.

- Initially, a plastic film was placed onto the metal plate in order to easily remove the cured part.
- A first piece of peel ply fabric was then placed on the plastic film. It was necessary that the size of the peel ply layer be larger than the size of the composite plate.

- Next, four layers of the reinforcement glass fibre fabric were stacked on the peel ply, and a second piece of peel ply was placed on the top of the reinforcement layers.
- A layer of resin flow media mesh was then placed on the second peel ply in order to improve the resin flow and vertical resin impregnation to the lay-up.
- A piece of omega tube inlet was placed on the resin flow media, while another piece of omega tube as the outlet was placed on the first peel ply. Additional pieces of omega tubes can be laced on the first peel ply in order to improve the evacuation of the lay-up.
- Sealant tape was the used to stick to the periphery of the lay-up on the metal plate.
- Plastic tubes were inserted in the omega tube resin inlet and tightly clamped. Plastic hoses were connected to the omega tubes.
- The entire aforementioned lay-up was covered with plastic sheet and sealed.
- The plastic hoses are connected to the resin vacuum trap, which was then connected to the vacuum pump.

In the next steps the bagging system was evacuated and resin impregnation took place.

- During the evacuation process, when the vacuum pressure reached 0.9 bar, the resin impregnation took place.
- The end of the resin inlet hose was immersed in the resin tank, and liquid resin impregnated the lay-up.
- The impregnation can be stopped when the resin impregnated the glass fibre reinforcement fabric and some resin can enter the outlet.
- After impregnation, the lay-up was cured under vacuum.
- After the curing process was complete, the cured plate was removed

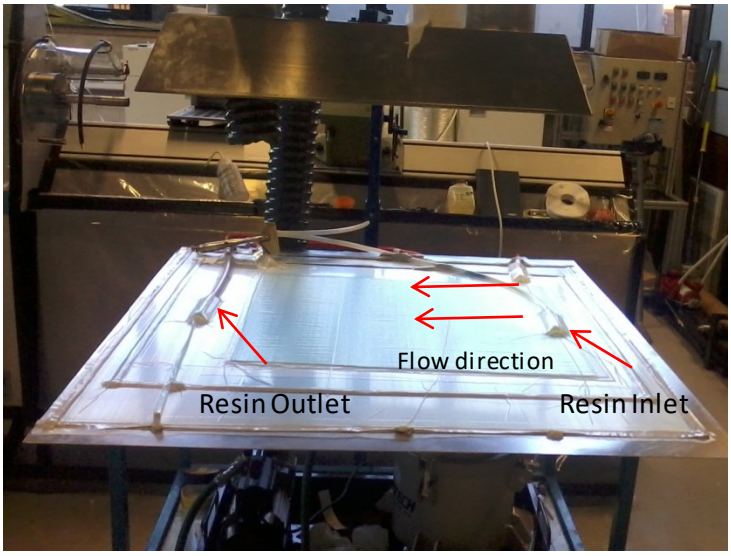

Figure 7.1: The resin infusion set-up employed

The different glass/vinyl-ester plates provided by the shipyard were consistently found to have high void content (>5%). In comparison, the plates fabricated in-house using resin infusion, were found to have low void content (<1%). To study the influence of voids on the mechanical performance of glass reinforced vinyl-ester composite plates and on AE activity recorded, test samples were cut from the plates using a water jet and prepared for mechanical testing.

Tensile tests were carried out on composite coupons according to the ASTM D 3039 standard test method [190]. The coupons were tested in tension in both warp and fill directions. The ends of the tensile samples were end-tabbed with 50mm x 25mm aluminium tabs using 9323 Scotch weld adhesive to protect the sample from potential damage due to the high clamping force during tensile testing. The dimensions and configuration of the tested specimens for the tensile tests are summarised in Table 7.1. Three-point bending tests were carried out

according to the ASTM D 790 test method [191]. In addition 25mm×25mm aluminium tabs were bonded on the surface of the bending samples to enable the mounting of the AE sensors. The dimensions and configuration of the tested specimens for the bending tests are summarised in Table 7.2.

Table 7.1: Configuration and dimensions for the tensile tests

Type of specimens	Specimen identification name	Number of reinforcement layers	Orientation	Gauge length	Average width	Average thickness
Shipyard_A sample	SY_A	4	both warp and fill	150 mm	25 mm	2.55 mm
Shipyard_B sample	SY_B	4		150 mm	25 mm	2.7 mm
Resin Infusion sample	RI	4		150 mm	25 mm	2.6 mm

Table 7.2: Configuration and dimensions for the 3-point bending tests

Type of specimens	Specimen identification name	Number of reinforcement layers	Span to depth ratio	Length	Average width	Average thickness
Shipyard sample_A	SY_A	4	16:1	120 mm	12 mm	2.55 mm
Shipyard sample_B	SY_B	4	16:1	120 mm	12 mm	2.7 mm
Resin Infusion sample	RI	4	16:1	120 mm	12 mm	2.6 mm

7.3.3 Glass/epoxy pre-preg samples

Glass fibre/epoxy composite plates were fabricated using VTM-264 unidirectional glass fibre epoxy pre-pregs with density of 400g/m^2. Initially several plies of 300mm×300mm were cut from the prepreg creel. The individual prepreg plies were manually laid up on a flat surface to form an 8-ply 0^o/90^o symmetrical lay-up. Caution was taken during the lay-up process to

ensure proper alignment of the plies and correct lay-up sequence. During the lay-up process trapped air between the plies was removed using a hand roller.

The process then continued with the preparation of the autoclave bagging system prior to curing. The autoclave bagging set up is shown on Figure 7.2.

- The prepreg laminates were placed between two layers of release film, on a flat tool surface.
- A piece of breather fabric was initially placed on the release film on the laminate. Further pieces of breather were placed on the periphery of the laminates. The use of breather improved the evacuation process.
- The vacuum valve attachments were placed on the breather in an area away from the laminates.
- The lay-up was then covered with plastic film.
- The vacuum hoses were attached and the evacuation of the bagging system started.
- In addition to the applied vacuum, a hand roller was used to further assist the removal of any trapped air pockets in the bagging system.
- The tool surface with the bagging lay-up was then placed in the autoclave for curing.
- The curing cycle of the laminates is shown on Table 7.3.
- After the curing process was completed, the cured part was removed.

Table 7.3: Autoclave curing cycle

Cure cycle	
Vacuum bag pressure	980mbar
Applied autoclave pressure	70psi
Ramp rate	2°C / min
Temperature cure cycle	5 hours at 80°C
Cool down	3°C / min to room temperature
Post Cure	
Ramp rate	0.3°C / min
Temperature cure cycle	1 hour at 120°C
Cool down	3°C / min to room temperature

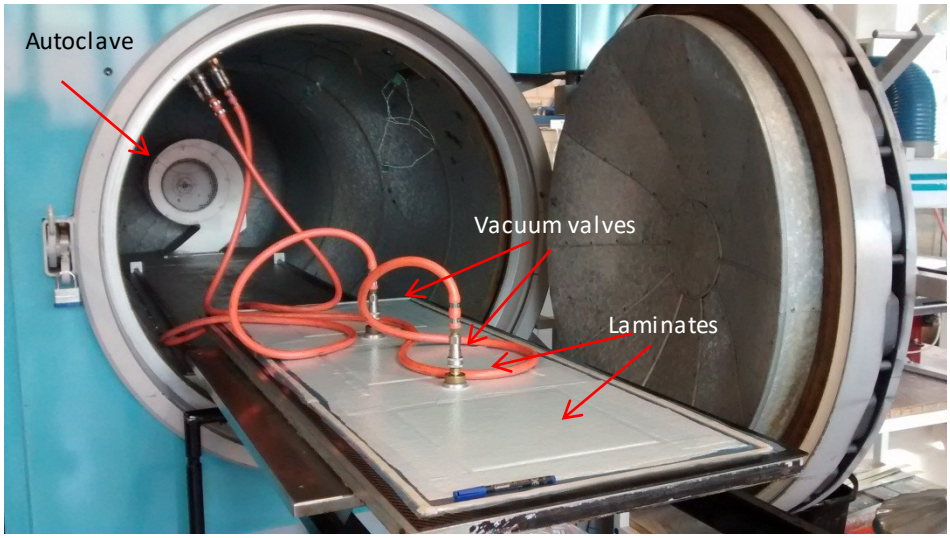

Figure 7.2: Autoclave bagging set-up

To study the influence of defects on the AE signals and on the monitoring of damage initiation and evolution, artificial defects were introduced on the bending samples. After curing and cutting, 1.5mm holes were initially drilled in the middle of bending samples. As shown on Figure 7.3, 1.5mm bolts and nuts were placed in the holes after drilling. The dimensions and configuration of the tested specimens for the tests are summarised in Table 7.4.

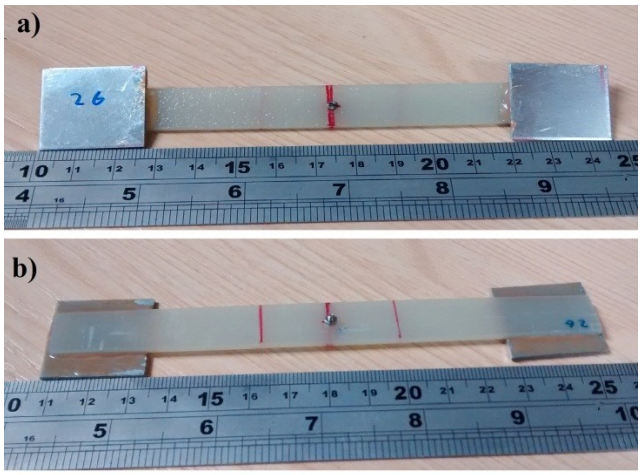

Figure 7.3: Bending specimen with drilled hole and bolt on a) top surface and b) bottom surface.

Table 7.4: Configuration and dimensions for the 3-point bending tests of the epoxy pre-preg samples

Specimen identification name	Number of ply layers	Lay-up	Gauge length	Average width	Average thickness
no_hole prepreg	8	0/90 symetrical	120 mm	12 mm	2.22 mm
hole prepreg	8	0/90 symetrical	120 mm	12 mm	2.22 mm

7.4 Steel/composite hybrid joints

Composite-to-steel hybrid joints were fabricated in-house. The joints consisted of a steel insert, which was co-laminated with a four-layer fibre fabric reinforced vinyl-ester skin with a balsa wood core through resin infusion. The reinforcement was a 0°/90° biaxial stitched E-

glass fabric with density of 813g/m^2 provided by METYX composites. The resin system used for the fabrication of joints was a CRYSTIC VE679PA-03PA provided by SCOTT BADER.

A 100mm×10mm piece of steel was bent at an angle of 15° and the bended edge was chamfered. Sections of 30mm balsa wood were also prepared. The one edge of the balsa wood core was wedge shaped to accommodate the chamfered steel plate. The prepared steel and balsa wood section are shown in Figure 7.4. Surface cleanliness was a very important factor in achieving strong interfacial bonding. Therefore, steel plates were sandblasted to a SA 2 ½ level. After sandblasting the steel plate was further cleaned with acetone to remove any organic residue.

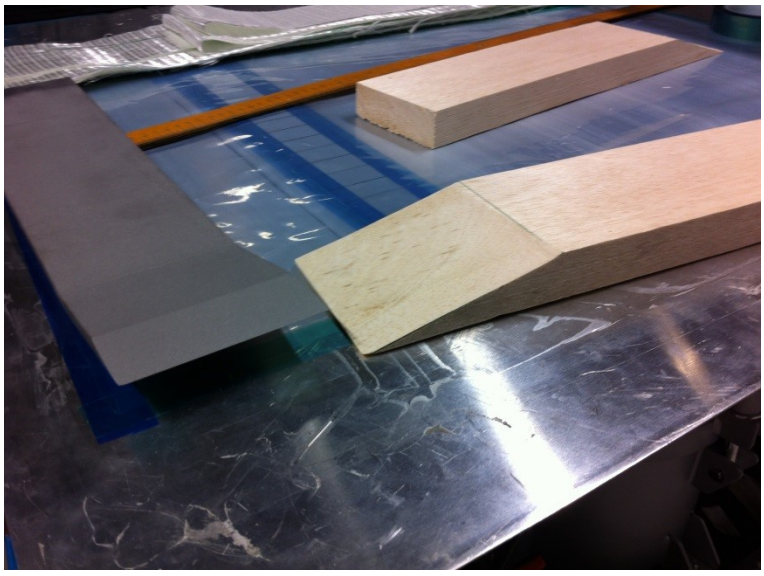

Figure 7.4: Cut balsa wood and steel sections [192]

The resin infusion was made on a flat aluminium tool plate. The resin infusion process was similar to that described in section 7.3.2. Two main types of joints were made according to a design agreed with industrial partners participating in the FP7 MOSAIC project. These joints were coded as Joint-A and Joint-B. After curing a 10mm hole was drilled in the middle of the

steel section of Joint-B, to simulate the effect of bolted connections on the load bearing capabilities of the joint. Prior to testing a 10mm bolt was placed in the hole. Each type of joint was subdivided into three different types, as shown in Table 7.5. For each joint type, two test specimens were manufactured. The resin infusion process for each type of joint was carried out according to the MOSAIC's consortium guidelines as follows:

- Type 1:

Four layers of the glass fabric preform were placed on the flat tool surface. The steel and balsa wood pieces were then placed on the dry reinforcements. Another four layers of glass fabric were placed on top of the steel and balsa wood. The lay-up was then covered with peel-ply and flow media mesh. The resin inlet, outlet and hose connections were made. The lay-up and vacuum hoses were covered with a plastic sheet sealed against the tool plate with sealant tape. The plastic hoses were connected to the resin vacuum trap, which was then connected to the vacuum pump. Under vacuum, resin impregnation took place. The resin impregnated joint was cured under vacuum. Figure 7.5 shows the resin infusion set-up used to fabricate the hybrid composite to steel joints.

- Type 2:

The structure of this joint type was similar to the one described above. However, 4 additional layers of glass fabric were incorporated at the top and bottom of the joint's weak point. The manufacturing route for the joint was the same to the one described earlier.

- Type 3:

In this type of joint Scotch-Weld 9323 adhesive was applied on the steel and balsa wood prior to resin infusion. A layer of dry reinforcement was placed on both top and bottom of the balsa wood and steel inserts which were covered in adhesive. The adhesive was left to cure for a day. Then, three additional layers of glass fibre fabric were added on both sides of the joint. The manufacturing route for the joint was the same to the one described earlier.

Table 7.5: Types of Joints

Joint main type	**Main MOSAIC's Consortium design**	**Reinforcement at the weak point**	**Main MOSAIC's Consortium design with adhesive**
A	A11 and A12	A21 and A22	A31 and A32
B	B11 and B12	B21 and B22	B31 and B32

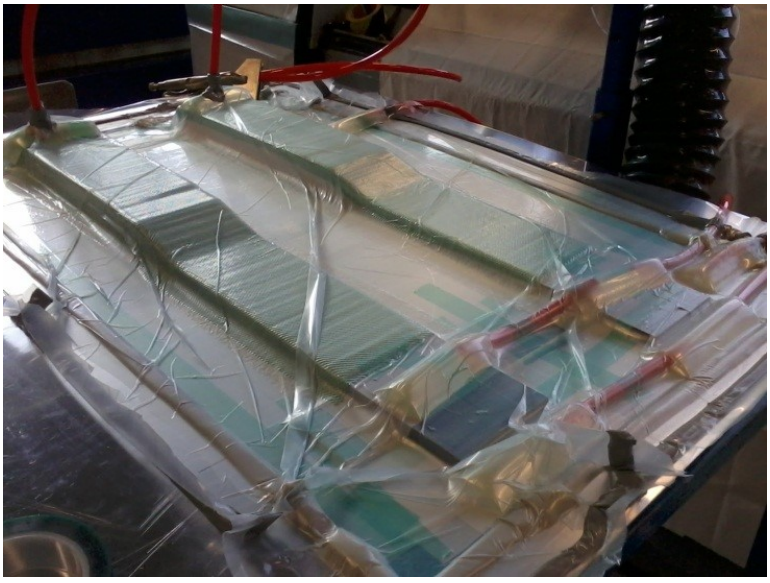

Figure 7.5: Joint manufacturing set-up

The joints were subjected to 3-point bending tests. In addition, strain gauges were attached on several points of the joint to monitor the strain during loading. The main joint design and load configuration are shown in Figure 7.6. The overall width of the joint is 100mm. The thicknesses for the steel insert, balsa wood core and GFRP skin are 10mm, 30mm, and 2.5mm respectively.

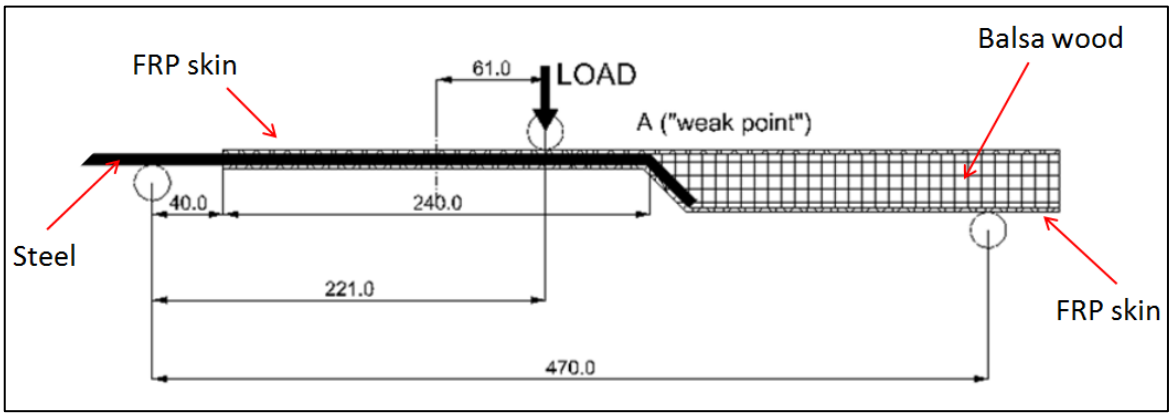

Figure 7.6: Joint design and loading configuration

7.5 Balsa wood samples

Balsa wood cores were used in the fabrication of the composite-steel joint samples. To further evaluate the AE response generated during damage evolution in joints, bending tests were carried out on balsa wood samples. This was done so as to obtain the key AE signal features arising from balsa wood fracture. The length, width and thickness of the balsa wood samples tested were 300mm, 25mm and 16mm respectively. In addition, 25mm×25mm aluminium end-tabs were bonded on the test samples to accommodate the AE sensors during testing.

7.6 Mechanical tests

7.6.1 Tensile tests

Tensile tests on fibre bundles were carried out using a 10kN universal Instron-5566 testing machine with a 10kN load cell. During tests, the displacement rate for the fibre bundles consisting of few filaments was set to 0.01mm/min, while the dry and lubricated fibre bundles with 700 filaments were tested under a displacement rate of 0.1mm/min. The low displacement rate of 0.01mm/min was selected so as the failure rate of the fibres is as slow as possible to allow the AE system to detect individual fibre fracture AE signals generated every time an individual filament fractured. A fibre bundle mounted on the grips of the testing machine is shown in Figure 7.7.

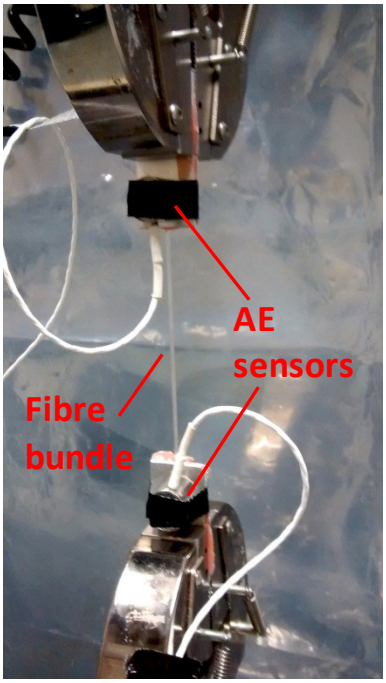

Figure 7.7: Fibre bundle mounted on the testing machine

Tensile tests on glass fibre reinforced vinyl-ester coupons were carried out on a 200kN Zwick-Roell 1484 tensile machine with a displacement rate of 1mm/min according to the ASTM D 3039 test method. A composite specimen mounted on the grips of the testing machine is shown in Figure 7.8.

The failure of the composite specimens was recorded with a video camera in order to correlate the visually observed damage propagation in the video with the recorded AE signals. As shown on Figure 7.9, during tensile testing the composite coupons were backlighted with a portable light source placed behind the specimen. The glass fibre composite samples with thickness of ~2.5mm, allowed some light to be transmitted through. The light transmitted through the tested sample illuminated the GFRP specimens. Thus, the damaged area could be visually observed in the recorded videos.

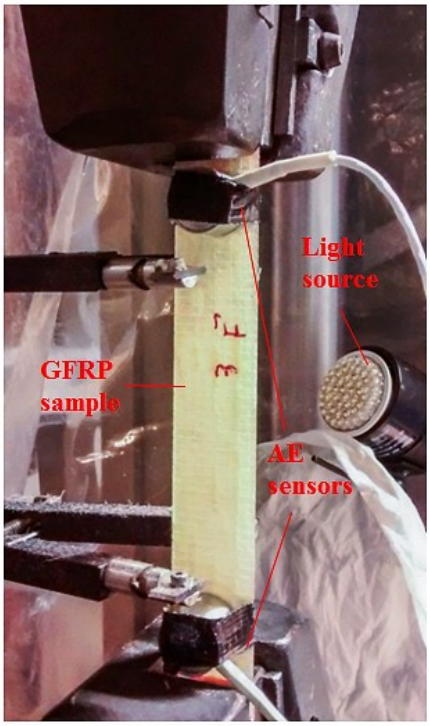

Figure 7.8: Composite sample loaded on tensile machine.

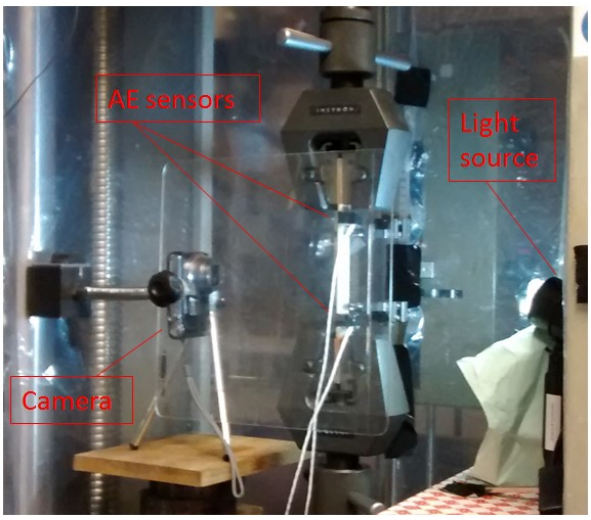

Figure 7.9: Experimental set up for the tensile tests.

7.6.2 Three-point bending tests

Three-point branding tests were carried out on GFRP composite samples using an Instron-5566 testing machine according to the ASTM D 790 test method, with a displacement rate of 1mm/min according and a span to depth ratio of 16:1. The tests were carried out on an appropriate bending fixture, while the bending displacement of the tested specimen was measured with a Linear Variable Differential Transformer (LVDT). A composite sample subjected to bending test is shown in Figure 7.10. During the bending tests the sample was rubbing against the rollers of the support fixture under load. As a result, AE noise signals associated with friction are generated. These AE signals have low amplitude and frequency values. Such signals are not recorded because of the Threshold and the band-pass acquisition filters that are used during the AE testing.

Three-point bending tests were also carried out on balsa wood samples. The span length of the balsa wood bending tests was set to 210mm. As shown in Figure 7.11, an aluminium plate

was placed under the loading roller to prevent any indentation on the soft balsa wood during the tests.

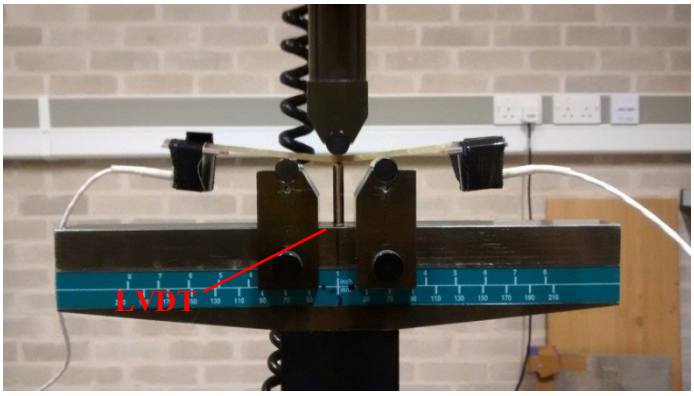

Figure 7.10: Bending test of a composite sample.

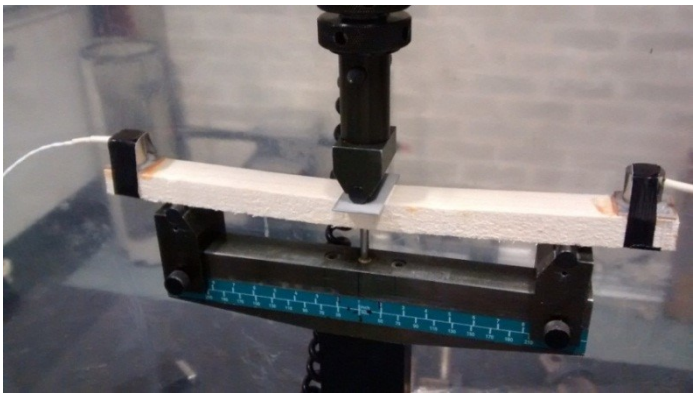

Figure 7.11: Bending test of balsa wood sample.

7.6.3 Bending tests on composite to steel joints

Three-point bending tests were performed on the steel /composite hybrid joints using a Mand testing machine. To measure the strain along the joint five strain gauges with a gauge length of 5mm were attached on the weak point and four other locations.

The strain gauge measurements indicate the areas that sustain the highest strains during loading, since failure will occur in these areas. AE testing was carried out during the bending tests using 4 AE wideband sensors positioned on the weak point and on various pre-selected locations along the joints. In addition, a video camera was used to record the failure of the joints during the tests. The strain gauge and the AE sensor positions are shown in Figure 7.12. Figure 7.13 shows the set-up for the bending tests of the joints.

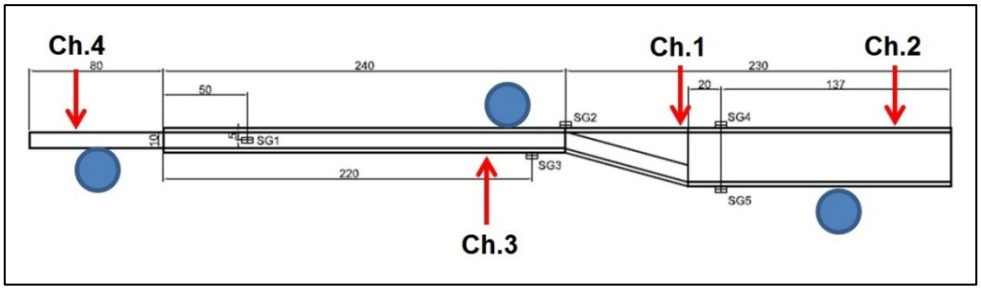

Figure 7.12: Strain gauge and AE sensor positions on the joint

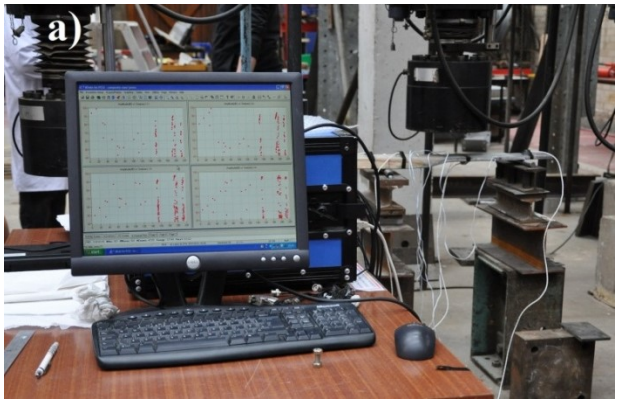

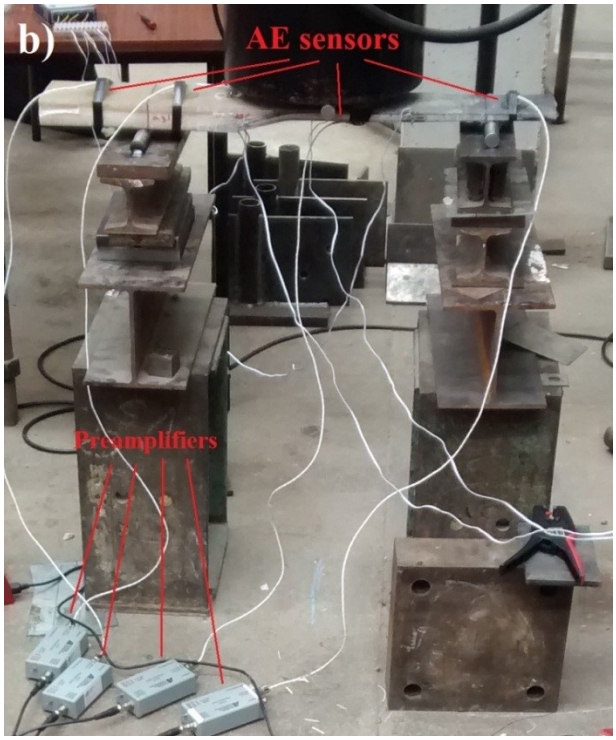

Figure 7.13: AE testing setup for the bending tests on the joints

a) AE acquisition system and b) position of AE sensors and preamplifiers

7.7 Acoustic emission testing

AE measurements were carried out during the mechanical tests of all the specimen types to monitor and evaluate damage evolution during loading. The AE signals were detected and recorded using a 4-channel DAQ AE system procured from Physical Acoustics Corporation (PAC, now Mistras). The data acquisition was performed using "AE-Win" software. The AE signals were detected using wideband PAC-WD piezoelectric acoustic emission transducers operating at frequency range of 20-1000kHz. Due to the lack of former knowledge on the frequency characteristics of AE signals generated during these tests wideband sensors were

used. The frequency response of these sensors allows the detection of AE signals over a wide frequency range. In this way the AE signal characteristics associated with the different failure modes in GFRPs were assessed. In addition each sensor was connected to PAC 2/4/6 preamplifier operating in the frequency bandwidth of 20-1200kHz. The amplification level of the pre-amplifiers was set to 40dB prior to testing. A higher amplification level of 60dB would increase the noise content as well as the amplitude of the unwanted AE signals. In contrast, a lower amplification level of 20dB would result in lower noise levels, but the damage related signals would not be sufficiently amplified. Adequate amplification while maintaining the AE noise at relatively low levels was achieved by setting the pre-amplifier at 40dB. The AE sensors were coupled on the samples using Vaseline petroleum jelly and held in place with duct tape. The use of coupling agent removes the air between the sensor and the surface of the sample, ensuring effective transmission of the AE signals with limited signal loss. In contrast, poor coupling quality has an adverse effect on the transmission of the AE signals and leads to increased signal loss during the tests. Furthermore, pencil lead break tests were performed before each single test to ensure consistency in the coupling quality between the samples and AE sensors.

During fibre bundle, balsa wood testing, and tensile and bending tests of glass fibre composites two AE sensors were used, attached on the two edges of the test specimens. However, during the bending tests of composite to steel joints, four AE sensors were used instead due to the size and geometry of the sample. The AE acquisition parameters and the AE timing parameters for each type of tests are presented in Tables 7.6 and 7.7 respectively. The acquisition and timing parameters were determined after preliminary testing, to minimise the noise pick-up and optimise the performance of the DAQ system. Lower threshold values were also considered, but larger noise levels were recorded.

The acquisition timing parameters are the Peak definition time (PDT), Hit definition time (HDT) and the Hit lockout time (HLT). A proper setting of these parameters allows the correct identification of the AE waveforms. The function of the PDT is to determine the time between the first threshold crossing and the maximum peak of the collected AE waveform. The function of the HDT is to determine the time between the first and the last threshold crossing of the recorded signal, to stop the acquisition process and store the measured features of the recorded AE signal. The HDT allows the determination of the hit duration. The HDT must be long enough so as the AE waveform is recorded effectively. However, the HDT must be as short as possible to avoid separate signals recorded as one. Furthermore, an appropriate setting of the HDT increases the acquisition rate. HLT is the time after the HDT in which the acquisition stops in order to inhibit the detection of reflections and late arriving parts of the AE signals.

Table 7.6: AE acquisition parameters setup

Type of tests	**Parameters**	**Value**
Tensile tests on fibre bundles Tensile tests on glass fibre composites Bending tests on glass fibre composites Bending tests on balsa wood	Threshold	40dB
	Pre-Amplification level	40dB
	Analogue filter	100kHz-1MHz
	Sampling rate	10MSPS
	Pre-Trigger	256.00 µs
	Length	10k
Composite/steel hybrid joints bending	Threshold	40dB
	Pre-Amplification level	40dB
	Analogue filter	100kHz-1MHz
	Sampling rate	1MSPS
	Pre-Trigger	256.00 µs
	Length	1k

Table 7.7: Acquisition timing parameters

PDT (Peak Definition Time)	50 µs
HDT (Hit Definition Time)	100 µs
HLT (Hit Lockout Time)	100 µs
Duration	25 ms

After the tests, data analysis and automated data clustering have been performed on the original AE dataset using Noesis software developed by Envirocoustics (now Mistras Hellas). Automated data clustering was performed using the k-means, Forgy and ISODATA clustering algorithms. Data clustering was performed to group into separate clusters the noise signals and AE signals that are generated from the different failure mechanisms that are active in a composite material under sufficient load.

To further investigate the frequency characteristics of AE signals, testing was carried out on dry and lubricated fibre bundles to record noise and fibre fracture signals that are generated during tensile testing of the fibre bundles. The aim of these tests were to compare the actual fibre fracture AE signals with the noise signals, by applying FFT analysis on the recorded waveforms and extract the frequency content of the recorded signals. The FFT analysis has been performed using the "Origin" software package.

The data acquisition system used was a custom-built AE and vibration acquisition system capable of continuously recording the complete waveform for periods of few seconds. The custom-built acquisition system consisted of the following components.

- A computer with a customised data logging software.
- An Agilent U2531A 4 channel data acquisition card.
- A 4 channel decoupling hub.
- A MISTRAS Wide bandwidth AE amplifier provided by PAC.
- A PAC model 2/4/6 preamplifier operating in the frequency range of 20-1200 kHz.
- A wideband PAC-WD piezoelectric AE sensor operating in the frequency range of 20-1000 kHz.

The customised AE system continuously recorded the generated AE activity in time windows of 5 seconds, throughout the test of each sample. The sampling rate of the acquisition system was set to 1MSPS. A different sampling rate could affect the Nyquist frequency and the peaks that are present in the FFT spectrum. More peaks could appear at higher sampling rates, whereas some peaks will be removed at lower sampling rates. However a different sampling rate will have no effect on the FFT results, since major peaks are expected to appear at considerably lower frequencies than the sampling frequency.

7.8 Void content characterisation with visual methods

In addition to density measurements, the void content and void distribution on the glass fibre composite plates has been determined with visual methods and digital image analysis. Due to the semi-transparency of glass fibre reinforced plates, the voids in the samples could be visually seen under magnification. Close-up pictures were taken from the glass-fibre composite plates using a photographic camera. To capture close-up images from the composite plates a Nikon D90 camera with a Nikon 28mm–80mm f/3.3-5.6 lens was used. The focal distance of the lens was set to 80mm, while a close-up ring was attached on the lens to produce a high resolution macro image of a small region of the plate with dimensions of 40mm x 25mm. In order to determine the void content and void distribution through the composite samples, the whole plate and test specimens were scanned.

Initially a 40mm×25 mm mapping grid was printed on a transparency film which was placed on the plate as shown in Figure 7.14. Each frame of the grid was identified by its own mapping coordinates x_i,y_i. The plate was then placed upright and held steady on the work

bench using clamp stands. The camera was mounted to a tripod and positioned at a close range from the plate, so as a single 40mm×25mm frame on the grid to cover the whole view-finder of the camera. The head of the tripod had a translation stage fixture that allowed the camera to move sideways and move to the next frame on the grid. The upper frames on the grid were photographed by lifting the centre column of the tripod. A close up image was taken for each frame on the grid. During shooting, the plates were backlighted using a Nikon SB900 flashgun. A light diffuser dome was placed on the flashgun to ensure even lighting distribution. The flashgun was firing remotely as it was wirelessly connected with the camera. A polarising filter was attached on the lens to cut-off any unwanted flare and light reflections from the images. The set-up for close-up photographic scanning of the composite samples is shown in Figure 7.15.

After shooting, the images were digitally processed to highlight the voided regions. The total area of the voids on the image was determined using the Fiji image analyser. In this way, the void content on the image was determined and was further compared with the density measurements. The Fiji image analyser was also used to determine the void content from high magnification images taken with an optical microscope.

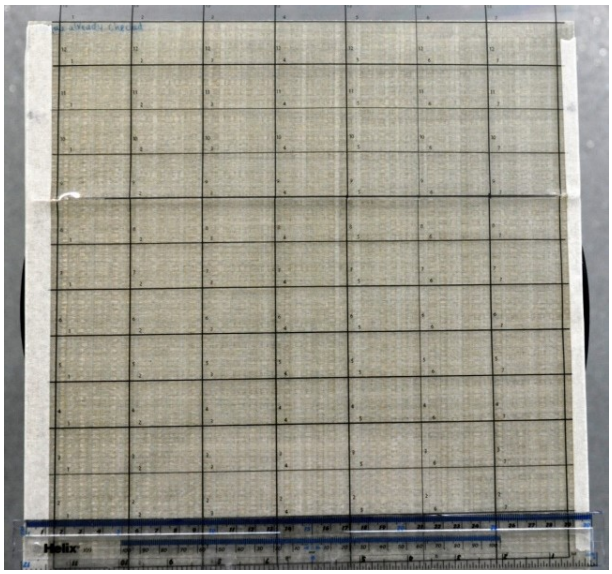

Figure 7.14: GFRP plate with mapping grid.

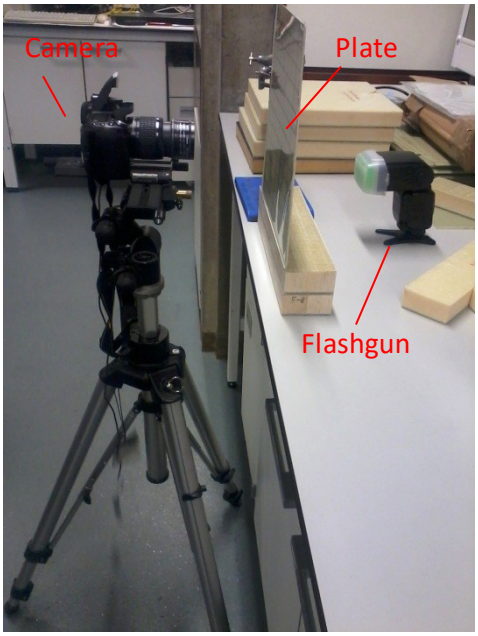

Figure 7.15: Experimental set-up for the close-up scanning.

CHAPTER 8

CHARACTERISATION OF GFRP PLATES

8.1 Introduction

Manufacturing quality and presence of defects affect significantly the performance of FRC components. The quality of GFRP plates used in this study was assessed. The quality of glass fibre fabric, stacking sequence, void content and distribution in the plates was evaluated.

8.2 Fabric characterisation

The type and quality of the reinforcing fibre preform have a significant impact on the properties of the resulting composite component. Therefore, the quality of the bidirectional glass fibre fabric used in fabrication of the test plates has been assessed. The glass fibre fabric was visually inspected for manufacturing flaws in both fill and warp sides of the roll.

The fill direction consisted of glass fibre tows with an average width of 2.5-4mm stitched with the fibres in the warp direction. Manufacturing flaws were identified as gaps between the fibre tows at the fibres direction. As it is seen in Figure 8.1, the gaps are randomly distributed in the fill direction. These gaps have resulted from the manufacturing process. The spacing of the gaps is irregular and their width varies from 1.5–5mm. The gap allows the fibres of a tow to move as they are not restrained by a neighbouring bundle. Since the gap's width along the fill direction is irregular, the resulting fibre misalignment will also be irregular. As it can be seen in Figure 8.2, limited fibre misalignment is observed at the areas with small gaps.

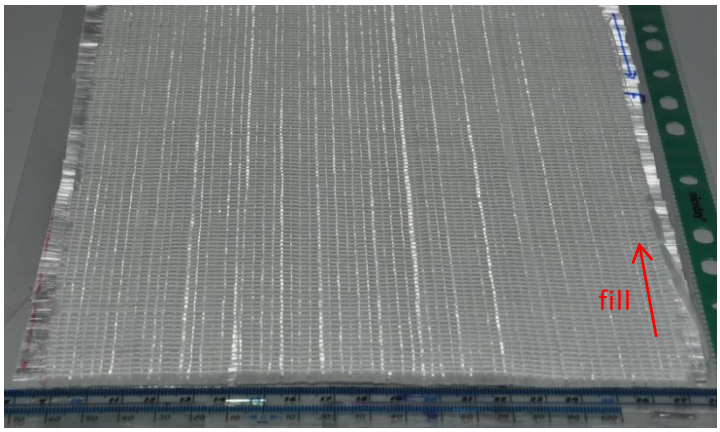

Figure 8.1: Gaps between the fibre tows along the fill direction

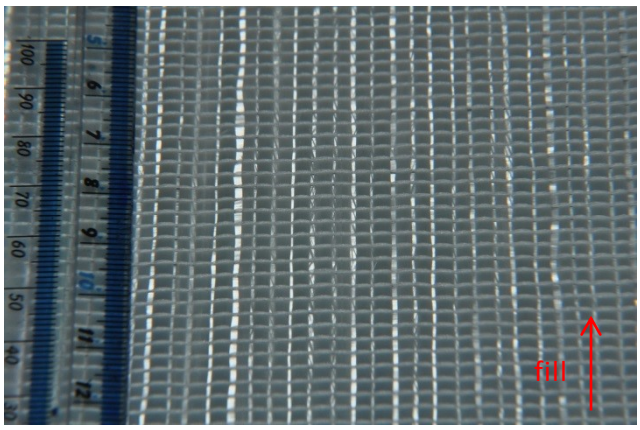

Figure8.2: Fibre misalignment between the gaps in the fill direction

The wrap direction consisted of glass fibre tows with an average width of 3-4mm stitched with the fibres in the fill side of the roll. The warp direction exhibited better characteristics with fewer flaws present than then fill side of the preform. Small gaps with a width smaller than 0.5mm appeared regularly between the tows in the direction of the fabric. In-plane fibre waviness was observed between the stiches of the warp. The waviness was regular and observed throughout the whole length of the fibres. Therefore, limited in-plane fibre waviness with a misalignment of 1mm was a characteristic of the warp side of the preform. Small gaps and fibre misalignment along warp direction of the fabric were observed in Figure 8.3.

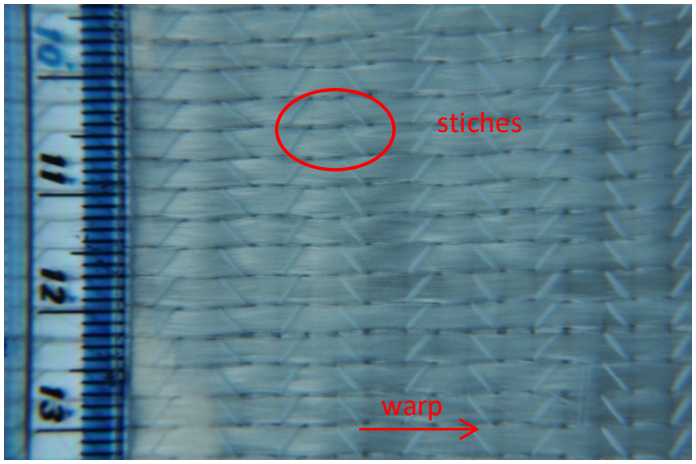

Figure 8.3: Features of the warp direction

Cutting the fabric with scissors induced local fibre distortion and misalignments in the cut edges of both fill and warp side of the fibre preform. As it can be seen in Figures 8.4 and 8.5 the cutting caused a fibre tow misalignment of 2-4mm, which was limited within a region of 2cm from the cut edges. Beyond the cut affected region the fabric regained its normal geometrical features and cut-induced fibre turning was no longer observed. Such misalignments have a detrimental effect on the mechanical properties at the edges of a composite plate. Test samples from the cut-affected regions are not representative of the material. Therefore after curing, 2cm are trimmed off from the edges of the composite plates. In addition as it can be seen in Figure 8.6 cutting can cause further increase in the width of the gaps between the fibre tows and lead to increased fibre distortion.

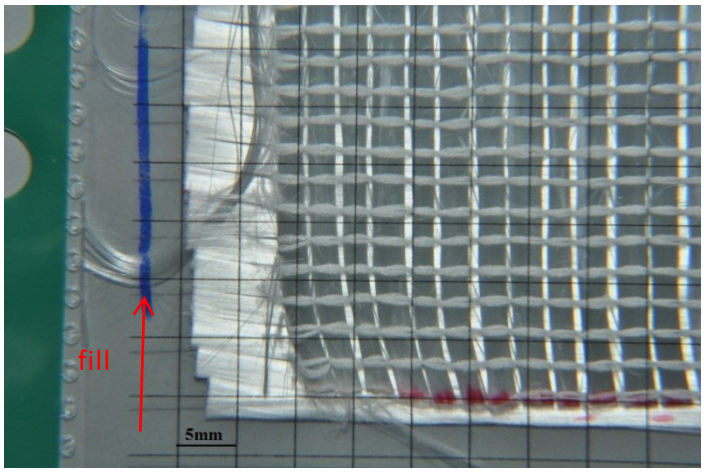

Figure 8.4: Fibre misalignment at the cut edges of the fabric in the fill direction

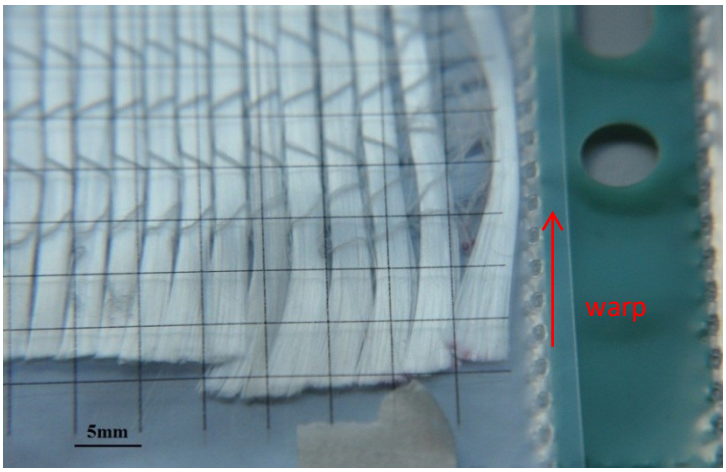

Figure 8.5: Fibre misalignment at the cut edges of the fabric in the warp direction

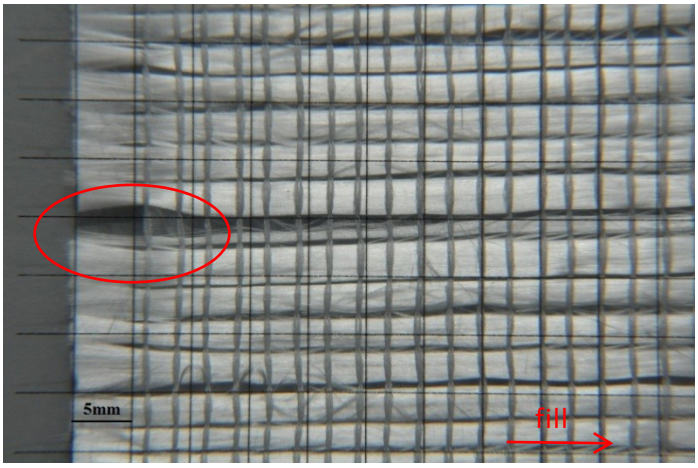

Figure 8.6: Opening of the gap at the cut edge

8.3 Void content characterisation

Before any mechanical testing was carried out, the void content and distribution of the composite plates were assessed. The void content can greatly affect the flexural properties of the composite samples as mechanical damage and cracking can initiate from the vicinity of the voids. The composite plates tested in this study were subjected to void content measurements. The void content and morphology of the voids were determined using digital image analysis. The determined void content values were compared to density measurements. During image analysis several representative frames that cover the whole plate were measured. Further image analysis was performed on polished cross-section images taken using an optical microscope.

The void distribution in the glass fibre reinforced vinyl-ester composite plates can be determined by examining macro-images of the composite plates. A close-up macro-image is shown in Figure 8.7. It can be seen that large and elongated macro-voids are visible in the gaps between the fibre tows of the fabric. The elongated voids are arranged in line on both warp and fill directions. Similar results have also been reported by Patel et al. [112]. Smaller voids had formed in front of the larger voids. During curing and resin flow after impregnation, small voids can merge with large voids or with each other resulting in the formation of larger elongated voids. Voids form as a result of poor impregnation, improper manufacturing techniques, and resin shrinkage during curing.

The voids observed in the macro-images were initially highlighted using digital image processing software in order to determine content. The image with the highlighted voids was then imported in the image analyser to automatically determine the total area percentage of

the voids in the image. An example of the highlighted voids for a macro-image is shown in Figure 8.8. According to the digital image analysis, the void content of Figure 8.8 is 11.95%. Macro-images were also taken from composite plates with low void content manufactured in-house using resin infusion. An example of a macro-image taken from a plate with low void content is shown in Figure 8.9. It can be seen that the composite plate is void free and no voids between the fibre tows are observed.

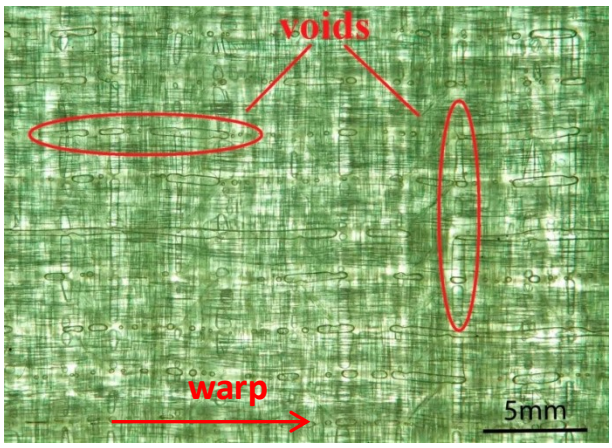

Figure 8.7: Typical macro image with voids taken from a composite plate

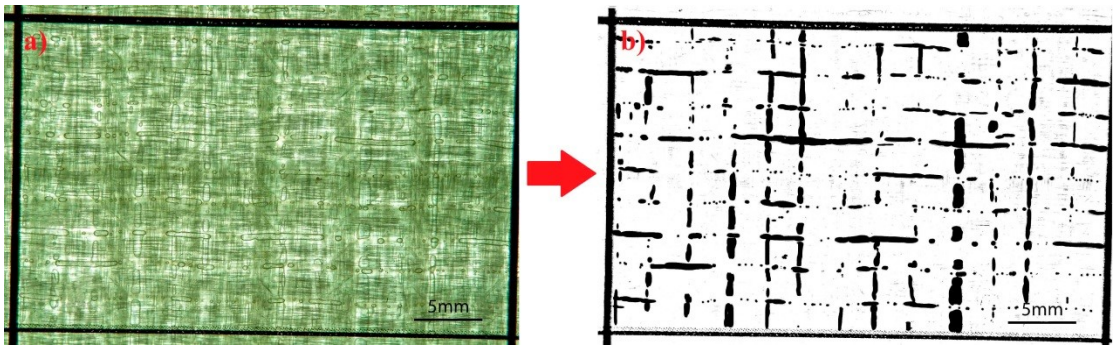

Figure 8.8: a) Macro image with voids and b) highlighted voids

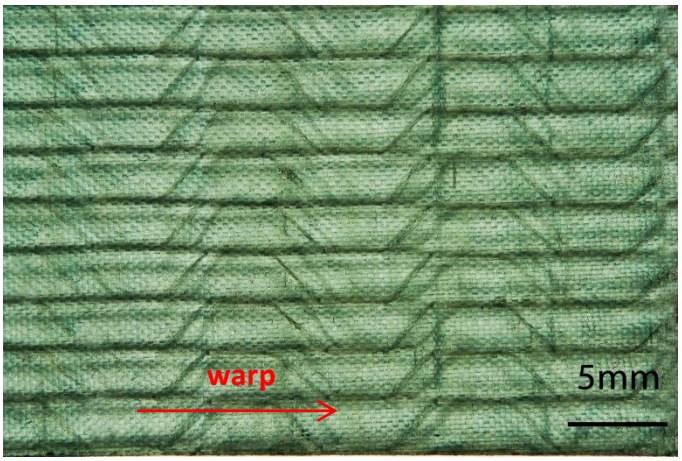

Figure 8.9: Macro image taken from a void free composite plate

Close–up images revealed mainly macro-voids and large elongated voids between the fibre tows. Voids trapped between the fibres were observed in high magnification cross-section images acquired using optical microscopy. Micrographs obtained from a composite plate containing voids are shown in Figures 8.10 and 8.11. Large voids were observed in the centre of the sample between the reinforcement layers. Smaller voids were observed between the fibres in tows. Smaller macro-voids were visible in front of the large elongated voids (Figure 8.10). Similarly to the macro-images, the void content on the images taken with an optical microscope was automatically determined using image analysis software. According to the image analysis results obtained, the void content of Figure 8.10 is 11.31% and is similar to the value that was determined from the close-up images. A microscope image from a void-free composite sample is shown in Figure 8.12. No macro-voids were observed and limited void formation was visible between the fibres. The void content of the void-free samples was determined to be <1%. The void content in the voided plates was determined to be ~7%.

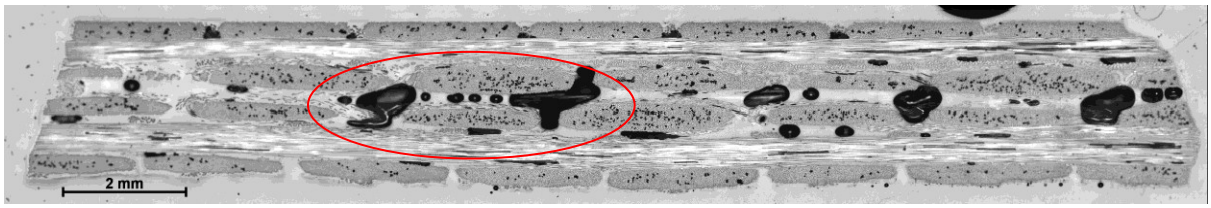

Figure 8.10: Microscope image from a voided plate

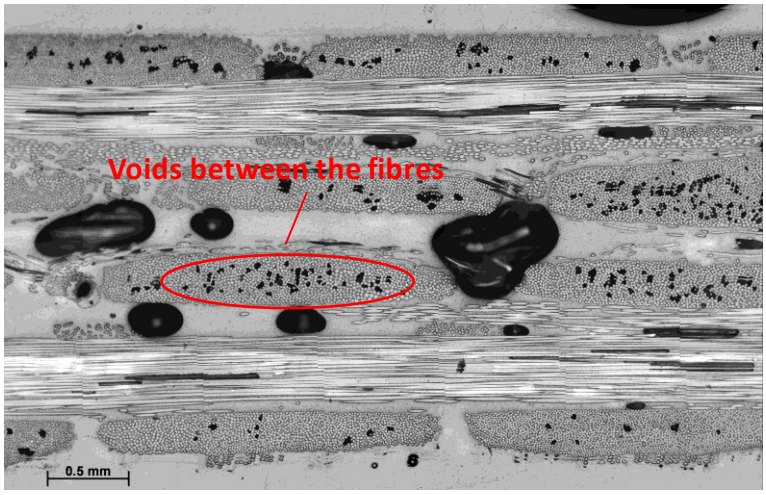

Figure 8.11: Microscope image from a voided plate

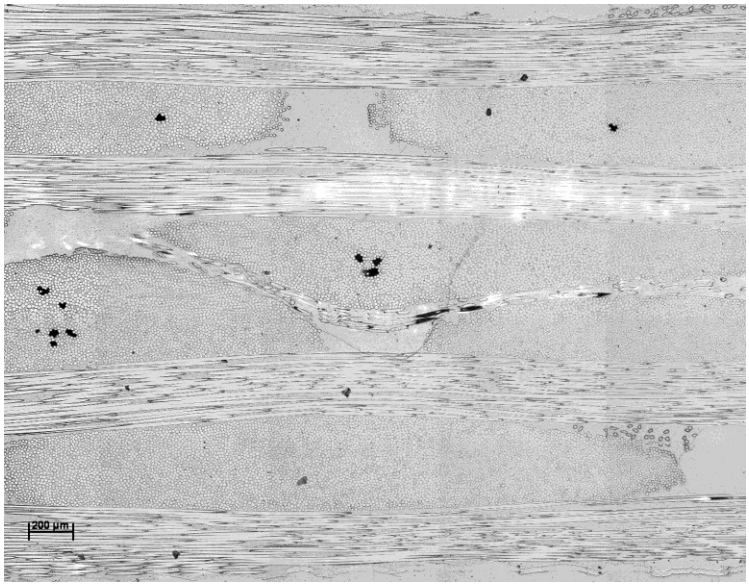

Figure 8.12: Microscope image from a void-free plate

The average void content determined from the digital image analysis method and void content values determined from the density measurements together with fibre fraction for the different types of composite plates are presented in Table 8.1.

The void content value from the digital image analysis method closely matches the values obtained from density measurements. As it can be seen in Table 8.1 for the first batch of shipyard samples, the void content determined from the macro-images is slightly larger than the density measurements. This discrepancy is due to the surface voids and crevices on the composite plate, which were clearly observed on the images and affect the void levels calculation. The density measurements are only sensitive to voids that are located inside the structure, and not to superficial voids and gaps. Highly voided areas were also detected during C-scan inspection in the immersion tank (Figure 8.13). The green areas on the C-Scan image represent void-free areas, while red areas indicate the presence of voids.

Void formation was influenced by the quality of the fabric. Missing tows in the fill direction resulted in increased spacing between the fibre tows. Therefore, large voids formed in these areas. Local resin-rich areas at the missing tows can influence the mechanical performance of the composite plates. Void formation is sensitive to the resin's pot life. If the pot life of the resin is exceeded prior to impregnation, the resin viscosity will increase dramatically leading to poor impregnation and void removal. The high viscosity of the liquid limits the movement of voids and their subsequent removal. The high void content of the shipyard plates resulted from the combined effect of the fabric's poor quality and a possible use of a resin system beyond its pot life.

Table 8.1: Void content for the different types of composite samples

Type of glass fibre reinforced composite samples	Average void content determined from the macro images	Average void content determined from the microscope images	Average void content determined from the density measurements	Fibre volume fraction
Shipyard plate_A	13.04 %	11.3 %	9.69 % [37]	50.40 % [37]
Shipyard plate_B	6.25 %	6.9 %	6.65 % [193]	46.9 % [193]
Resin Infusion plate	N/A – no voids observed	0.5 %	0.5 % [37]	48.57 % [37]

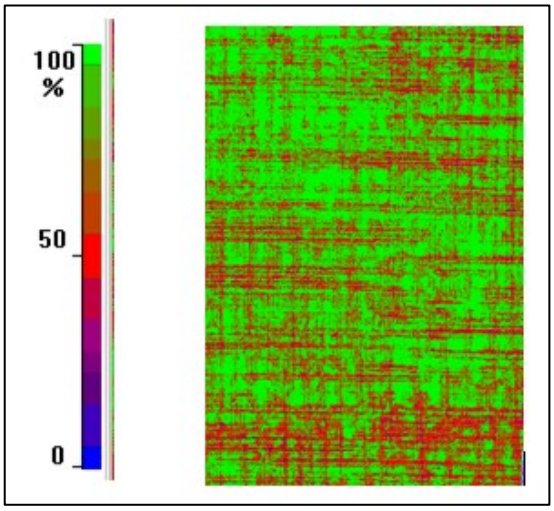

Figure 8.13: C-Scan image from a heavily voided plate [37].

8.4 Stacking sequence of glass fibre vinyl-ester composite plates

Apart from the void content, the stacking sequence of the composite plates was assessed. Stacking sequence can greatly affect the mechanical properties and performance of FRCs. The stacking sequence of the fibre fabric and representative cross-section microscope images for each type of composite plate is shown on Table 8.2. The lay-up of the shipyard samples is not symmetrical. The non-symmetrical stacking sequence has an adverse effect on the mechanical performance, particularly on the flexural properties of the material making it more complicated to assess the void effect. However, the samples manufactured in-house using resin infusion had symmetrical lay-up, resulting in consistent mechanical properties.

Table 8.2: Composite plates cross section images and stacking sequence

Cross section image	Stacking sequence
Shipyard plate_A 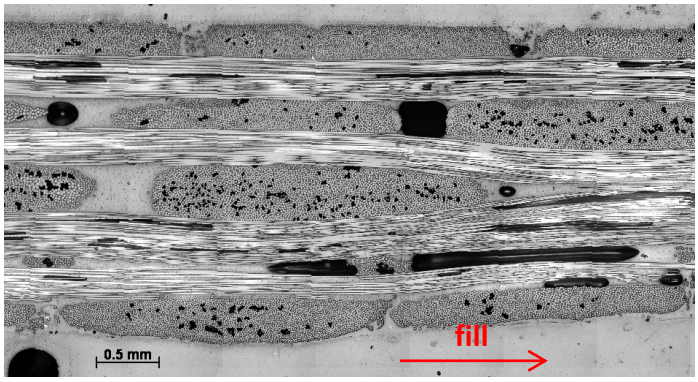	Lay-up from top bottom: **(90°/0°, 90°/0°, 90°/0°,0°/90°)** Or: **(0°/90°, 0°/90°, 0°/90°,/90°/0°)** From the side parallel to the weft Asymmetrical lay-up

Shipyard plate_B 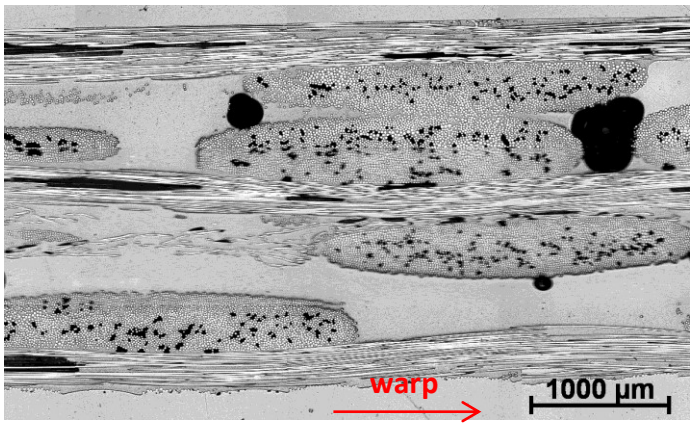 	Lay-up from top bottom: **(0°/90°, 90°/0°, 90°/0°, 90°/0°)** Or: **(90°/0°, 0°/90°, 0°/90°,/0°/90°)** From the side parallel to the fill Asymmetrical lay-up
Resin Infusion plate 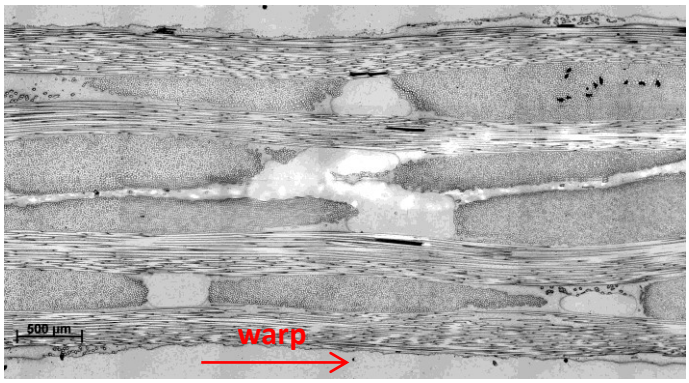 	Lay-up from top bottom: **(0°/90°, 0°/90°, 90°/0°, 90°/0°)** Or: **(90°/0°, 90°/0°, 0°/90°,/0°/90°)** From the side parallel to the fill Symmetrical lay-up

8.5 Characterisation of pre-preg glass fibre epoxy plates

Digital image analysis was performed on pre-preg glass fibre reinforced epoxy plates to determine the distribution and void content. Representative close-up images from the pre-preg plates are shown in Table 8.3. At local points larger air pockets are observed, resulting in increased void content in some areas of the plate. Nonetheless, the pre-preg plate has limited void formation (~1.6% on average).

To simulate the effect of a bolted connection on the GFRP material, 1mm holes were initially drilled in the middle of bending pre-preg samples, and 1mm bolts were placed in the holes. The holes act as stress concentrators and hence, damage can initiate form these regions during dynamic loading.

Table 8.3: Typical Close-up images from pre-preg plate and trapped air pockets

Cross section image	Comments
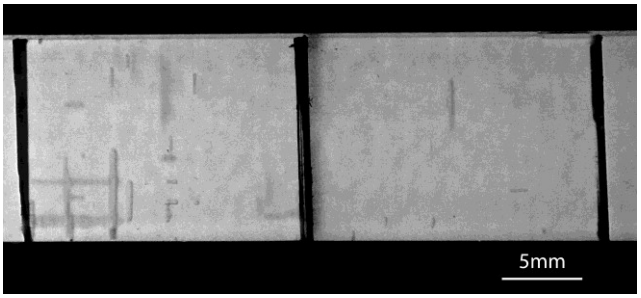	Local trapped air pockets Local void content of 3.24%
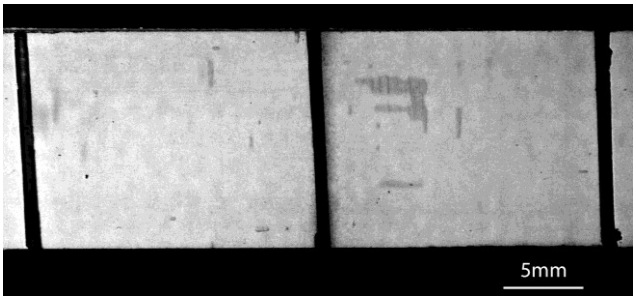	Local trapped air pockets Local void content of 1.92%

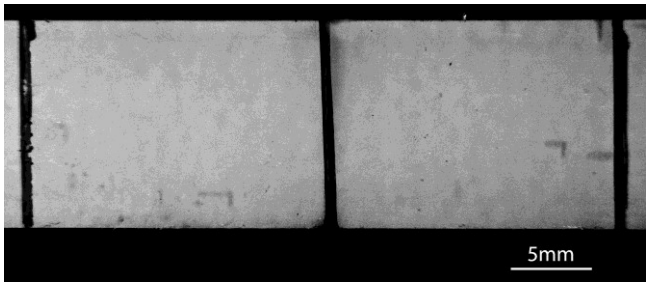	Local trapped air pockets Local void content of 0.58 %
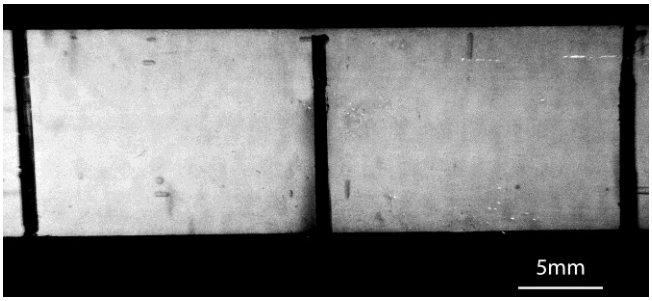	Local trapped air pockets Local void content of 0.67%

CHAPTER 9

RESULTS AND DISCUSSION

9.1 Introduction

This chapter presents in detail the experimental results obtained together with the associated analysis. Firstly, tests on small fibre bundles consisting of few filaments were carried out. These were followed by tests on as-received and lubricated fibre bundles containing 700 filaments. These tests were carried out to assess the capability of AE testing in detecting individual fibre fracture signals, and assess the factors that affect the performance of AE testing in detecting damage in the simplified case where only fibres are present. The collected AE signals arising from fibre fractures enabled the evaluation of the main features including amplitude, duration, rise-time, counts and energy. The data analysis from the glass fibre bundle tests was used to establish a methodology for the effective analysis of AE data collected from the tests on composite plate and composite-steel joint samples involving multiple damage mechanisms.

Tensile and flexural tests were carried out on composite samples to evaluate the applicability of AE testing for continuously monitoring the structural integrity and damage growth in such materials. The effect of voids on failure mechanics of GFRP has been assessed based on the analysis of AE signals recorded during tests. Multiple failure mechanisms such as matrix cracking, fibre fracture, debonding and delamination can become active resulting in the generation of AE signals with distinct waveform characteristics. The AE signals were grouped into clusters based on waveform characteristics using appropriate automated data clustering algorithms. Data clustering was carried out to establish an automatic AE signal processing methodology for monitoring damage in actual composite structures in the field. Automated data clustering is based on multi-parametric analysis of the AE data collected during tensile and bending tests on GFRP samples. The performance of each clustering

algorithm was assessed, while clustering results were compared with manual filtering techniques.

Further to the tests on composite coupons, bending tests were carried out on composite-to-steel joints. The structural integrity and damage propagation in the joints were evaluated using AE data analysis.

9.2 Fibre bundle tests

9.2.1 Testing and data clustering on E-glass fibre bundles with few filaments

Tensile tests were performed on small E-glass fibre bundles consisting of 7 to 27 filaments. AE measurements were used to monitor individual fibre failure during the tests. The AE acquisition system recorded acoustic activity generated by fibre failure. After testing k-means, Forgy, ISODATA and SOM-LVQ clustering algorithms were applied on raw AE datasets to group noise and fibre failure-related AE signals in separate clusters.

The total number of clusters is a user defined input parameter and must be known in advance. In this work the noise and fibre fracture AE signals are grouped in two different clusters. The data clustering for the glass fibre bundles was performed by selecting the following AE signal features; risetime, counts, counts to peak, duration, energy and amplitude. These signal features were also used for data clustering by Godin et al. [178, 179].

The raw dataset of the AE hits collected during the tensile testing of fibre bundles are consisted of noise and fibre fracture AE signals that needed to be distinguished to remove the effect of unrelated noise signals in the results. The AE signal amplitude scatter distribution versus strain obtained for a small fibre bundle consisting of 7 filaments is shown in Figure 9.1 a). The dataset comprises high and low amplitude noise signals. Figure 9.1 b) shows the amplitude scatter distribution after automated data clustering was applied on the AE data set. The noise and fibre fracture AE signals were classified. Noise was effectively separated from the high amplitude fibre fracture AE signals. The proposed signal identification and noise filtering procedure is also applied to the AE data sets acquired for as-received and lubricated fibre bundles consisting of 700 filaments.

Table 9.1 summarises the results for the small bundle tests, including number of filaments counted with an optical microscope, total number of AE signals recorded, number of fibre fracture AE signals identified with several unsupervised data clustering algorithms, and resulting error between the actual number of filaments and fibre fracture AE signals. All clustering algorithms produced the same results with the same number of identified fibre failure-related AE events. It can be thereby seen that the performance of k-means, Forgy, ISODATA and SOM-LVQ algorithms is the same. This happens primarily due to the simplicity and small size of the AE data set, since very few fibre fracture and noise signals were generated during testing. Therefore, all clustering algorithms have been able to sufficiently separate the noise from the fibre fracture-related AE signals and group them into two separate clusters.

For bundles #4, #5, #6 and #9, the number of the fibre fracture-related AE events coincides with the number of filaments present. For the rest of the samples 1 or 2 fibre fracture-related

AE events less than the actual number of filaments present were detected. This may have occurred due to some filaments breaking during sample preparation and handling, since small test bundles were very delicate and easy to damage. Simultaneous failure of two fibres may have been impossible to be detected if the AE system was in lock-out time and not recording. The error between the recorded AE fibre failures and actual number of filaments present varied from 4.7-15.38%. Similar error was observed for the as-received and lubricated fibre bundles tested.

The recorded AE data, apart from the actual fibre-related events contained a significant population of noise signals. The total population of recorded noise AE signals cannot be easily controlled as the sensors are sensitive to fibre friction and echoes. Despite a certain level of experimental error due to the technical limitations of the AE technique, the number of failed filaments can largely be evaluated during tensile testing provided multiple simultaneous fractures do not occur.

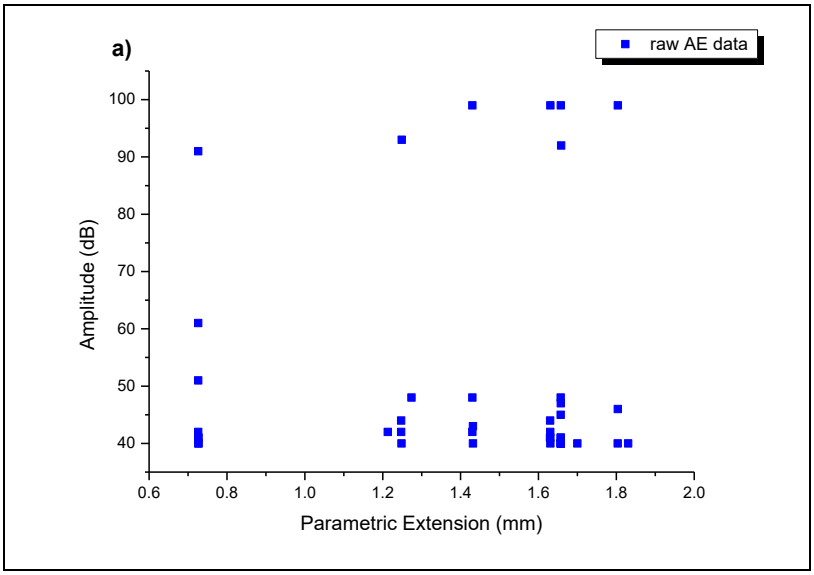

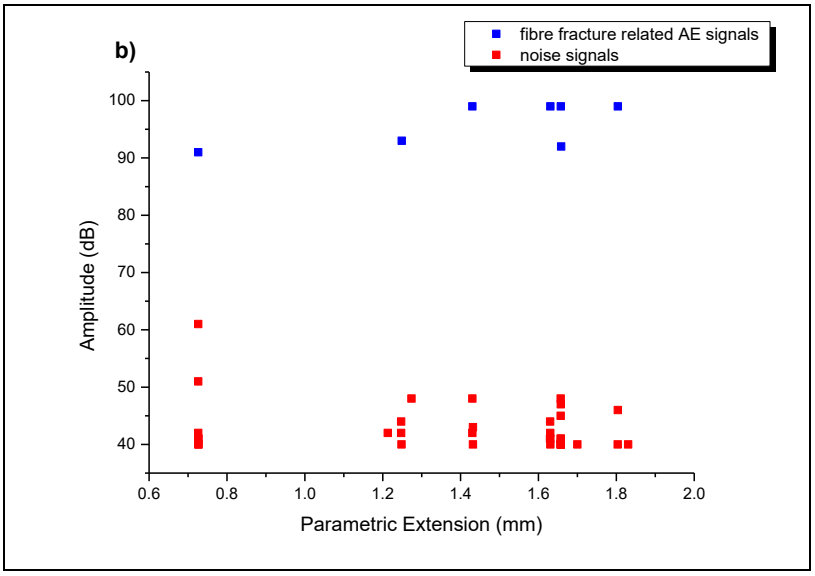

Figure 9.1: Amplitude scatter distribution a) of the raw AE data and b) after data clustering for a fibre bundle consisted of 7 filaments.

Table 9.1: Actual number of fibres, number of the recorded AE hits, number of fibre failure AE hits after data clustering and Error between the fibre fracture AE signals and the number of filaments

Fibre Bundle	Number of filaments in the fibre bundle	Number of the recorded AE hits	Fibre fracture AE events identified with k-means	Fibre fracture AE events identified with Forgy	Fibre fracture AE events identified with ISODATA	Fibre fracture AE events identified with SOM-LVQ	Error between the fibre fracture AE signals and the number of filaments (%)
1	25	104	22	22	22	22	-12
2	27	86	25	25	25	25	-7.4
3	21	70	20	20	20	20	-4.7
4	17	118	17	17	17	17	0
5	13	62	13	13	13	13	0
6	16	68	16	16	16	16	0
7	19	72	18	18	18	18	-5.2
8	19	107	17	17	17	17	-10.52
9	7	42	7	7	7	7	0
10	13	55	11	11	11	11	-15.38

Typical polished cross-sections of fibre bundles consisting of 7, 19, and 21filaments are shown in Figures 9.2 a), 9.3 a) and 9.4 a) respectively. The cumulative hits evolution and amplitude scatter distribution plots are shown in Figures 9.2 b), 9.3 b) and 9.4 b). The cumulative hits evolution and amplitude scatter distribution are plotted with respect to parametric extension after data clustering was applied. From Figure 9.2 it can be seen that 7 fibre fracture-related AE signals have been recorded corresponding to the actual amount of filaments present in the sample. Hence, all individual fibre fractures have been recorded successfully. From the AE plots presented in Figures 9.3 and 9.4 it can be seen that 17 and 20 fibre-fracture related AE signals have been detected, hence, 2 and 1 hits less than the actual number of filaments present respectively. The cumulative hits evolution plots increase rapidly when the scatter distribution of the recorded hits becomes denser, indicating rapid filament failure and damage propagation.

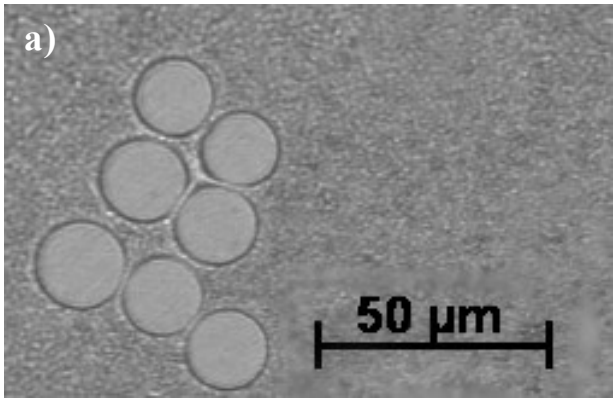

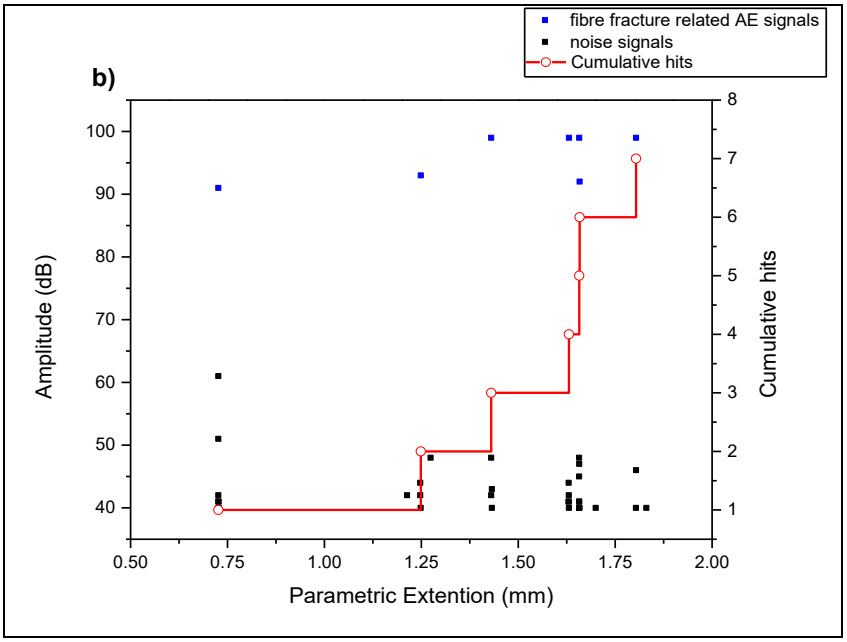

Figure 9.2: a) Cross section of a fibre bundle and b) Amplitude distribution and AE cumulative hits evolution for a fibre bundle consisting of 7 filaments tested in tension.

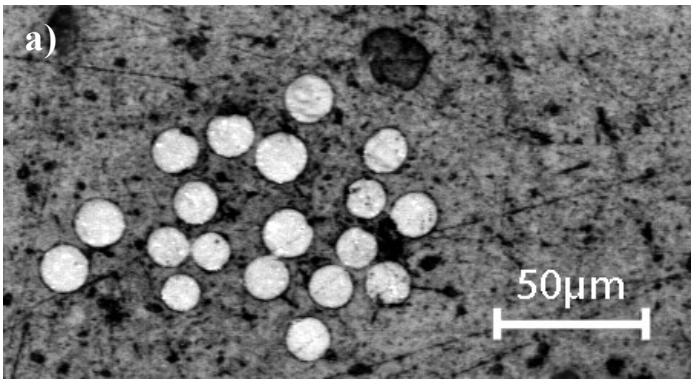

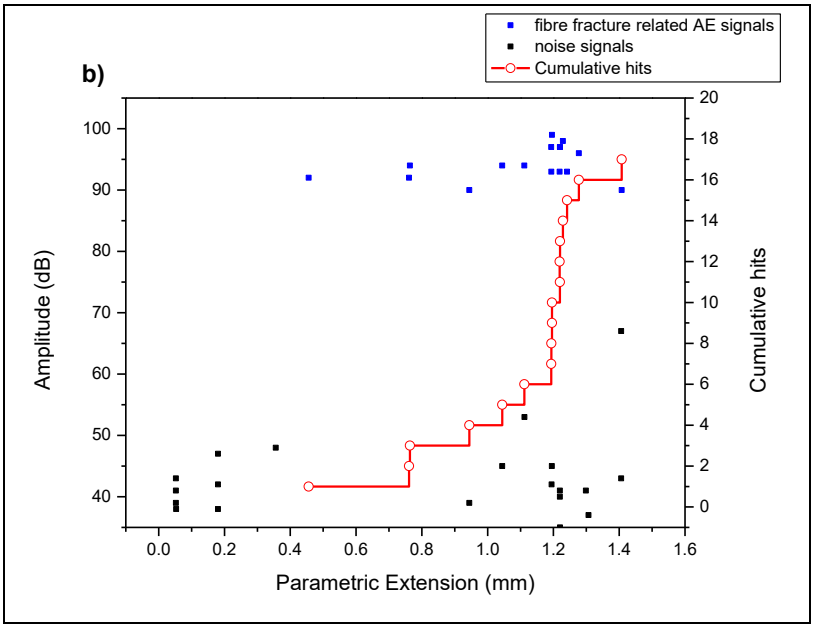

Figure 9.3: a) Cross section of a fibre bundle and b) Amplitude distribution and AE cumulative hits evolution for a fibre bundle consisting of 19 filaments tested in tension.

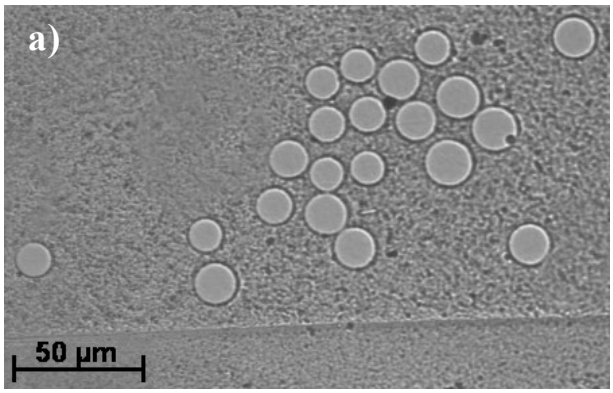

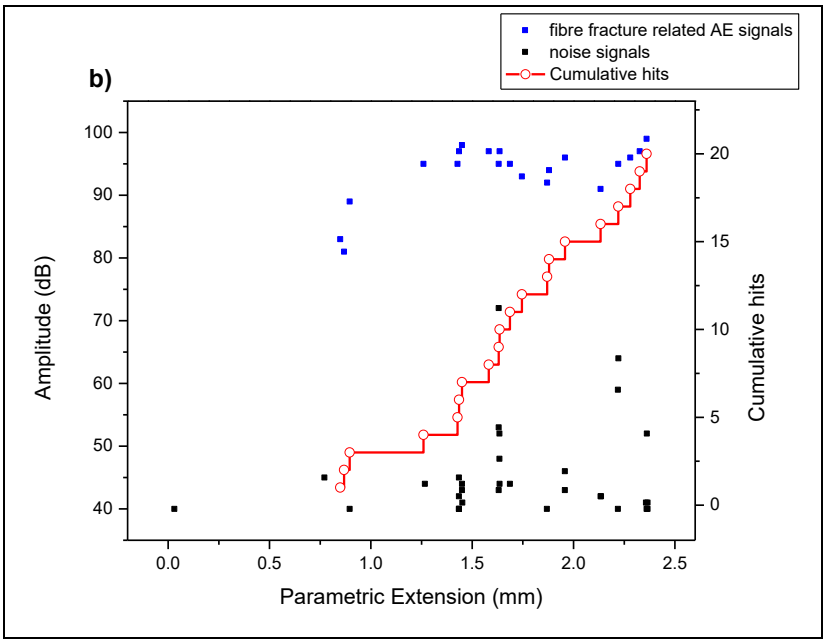

Figure 9.4: a) Cross section of a fibre bundle and b) Amplitude distribution and AE cumulative hits evolution for a fibre bundle consisting of 21 filaments tested in tension.

Typical fibre fracture and noise signal waveforms obtained during the tensile tests of the small fibre bundles are shown in Figure 9.5 a) and 9.5b) respectively. The fibre fracture AE signal has the appearance of a decaying sinusoidal, while the noise signal appears as a continuous waveform. Table 9.2 shows the key characteristics of the fibre fracture and noise

signals. Fibre fracture AE signals are characterised by short rise time, high counts and high duration amplitude and energy values, while noise signals are governed by high rise times, low counts and low duration amplitude and energy values.

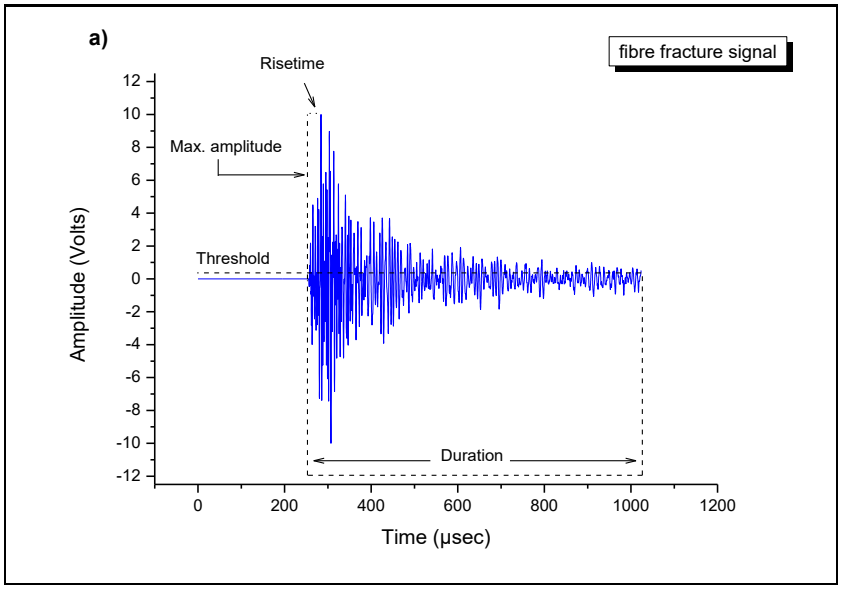

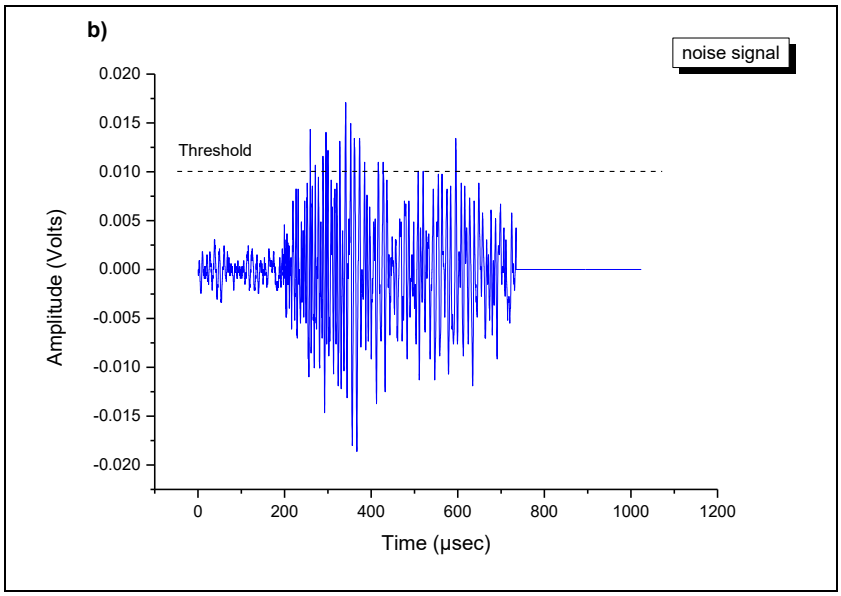

Figure 9.5: a) Fibre fracture signal and b) noise signal.

Table 9.2: Characteristics of fibre fracture and noise signals

	Fibre fracture signal	**Noise signal**
Risetime (μs)	27	110
Counts	845	16
Duration (μs)	9869	379
Amplitude (dB)	99	45
Energy (10μVolt-sec/count)	1618	2

Figure 9.6 shows the load-displacement plot and amplitude scatter distribution of the recorded AE fibre fracture events for the bundle consisting of 7 filaments. The load-displacement plot exhibits several load drops associated with the failure of individual fibres. The high amplitude fibre fracture AE signals are recorded whenever the load drops.

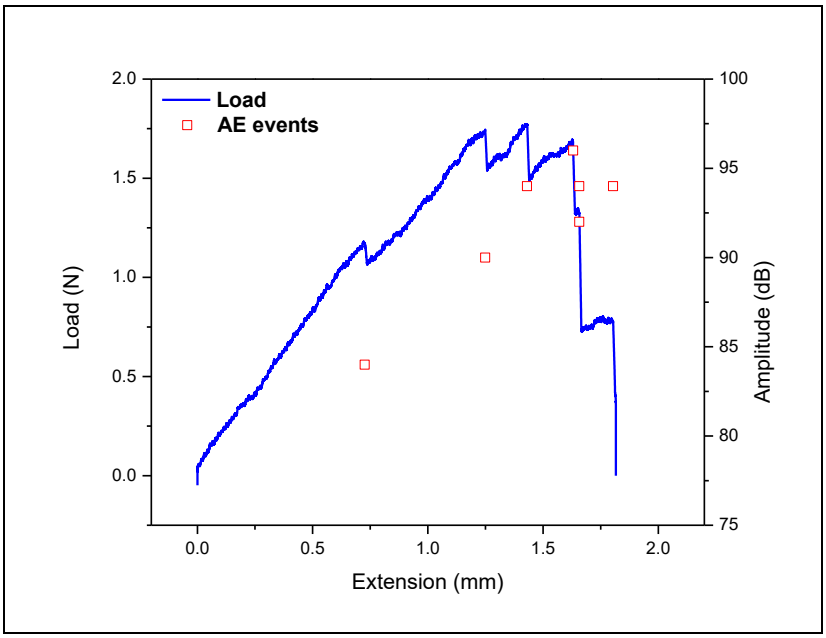

Figure 9.6: Load-displacement plot and AE amplitude scatter distribution for a bundle consisting of 7 filaments.

9.2.2 Testing and data clustering on E-glass fibre bundles with 700 filaments

Tensile tests were also carried out on as-received and lubricated E-glass fibre bundles consisting of 700 filaments. The structural health of the fibre bundles were monitored using AE testing. After testing unsupervised data clustering based on k-means, Forgy, ISODATA and SOM-LVQ algorithms was applied on the collected datasets.

When a fibre fails it retracts, recoils and induces a relative displacement to the neighbouring fibres causing inter-fibral friction. Inter-fibral interactions cause surface damage leading to weakening and premature failure of the affected filaments. Friction and inter-fibral interactions can be significantly reduced by lubricating the fibre bundles prior to testing [194-196]. Due to reduced friction and inter-fibral interactions, significantly less surface damage will occur on the fibres during failure. Consequently, the lubricated bundle exhibits higher strength and maximum strain to failure in comparison with the dry bundle. The difference between the average maximum strength and strain at failure for the as-received and lubricated fibre bundles is shown in Figures 9.7 and 9.8 respectively. Typical load-displacement plots for an as-received and a lubricated glass fibre bundle are shown in Figure 9.9.

The appearance of the as-received and lubricated fibre bundles after testing is shown in Figure 9.10. The failed as-received bundle had the appearance of cotton-wool, while in the failed lubricated bundle the fibres remain packed together without interacting and tangling with the neighbouring fibres in the bundle. The same failed bundle characteristics have also been observed in previous studies [194, 196].

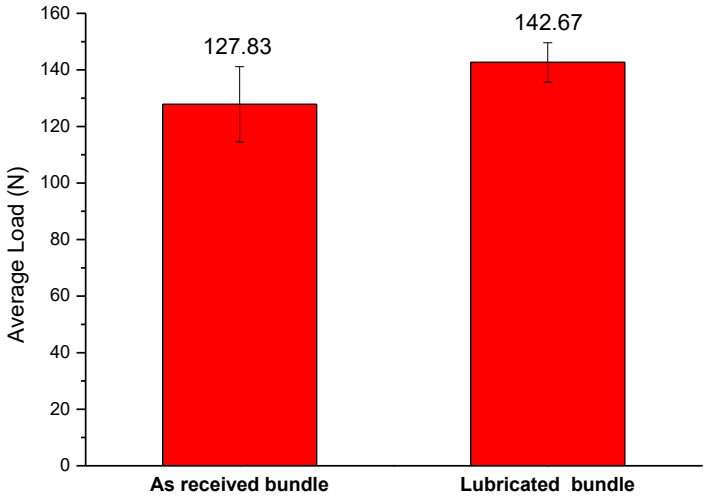

Figure 9.7: Average maximum load for the as received and for the lubricated fibre bundles.

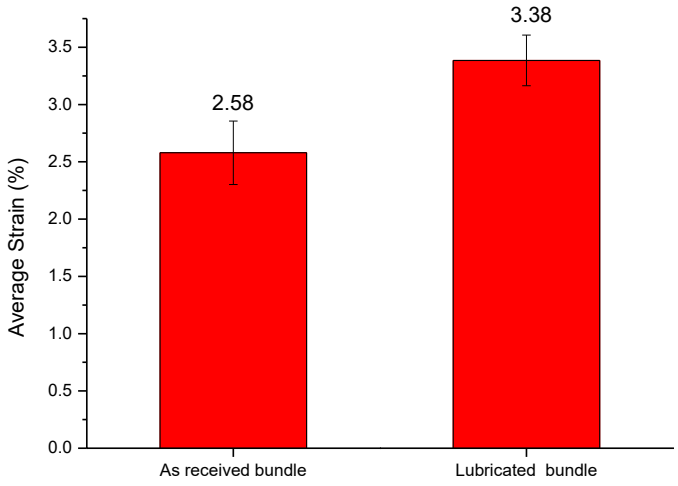

Figure 9.8: Average strain to failure for the as received and for the lubricated fibre bundles.

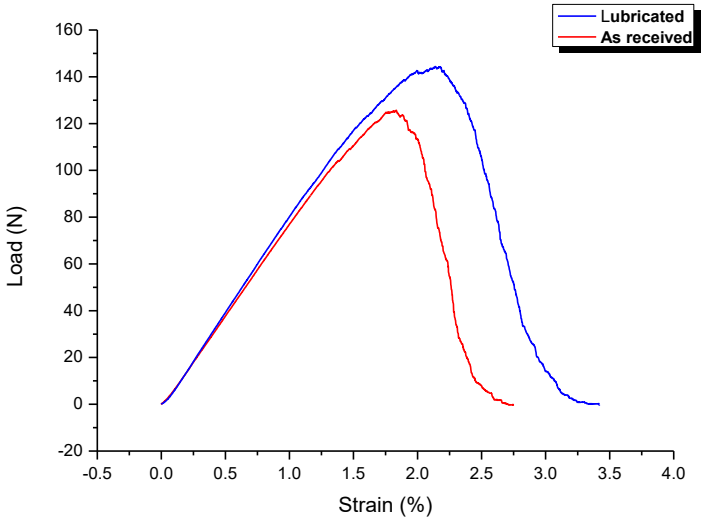

Figure 9.9: Typical load-displacement plots of an as- received and of a lubricated fibre bundle.

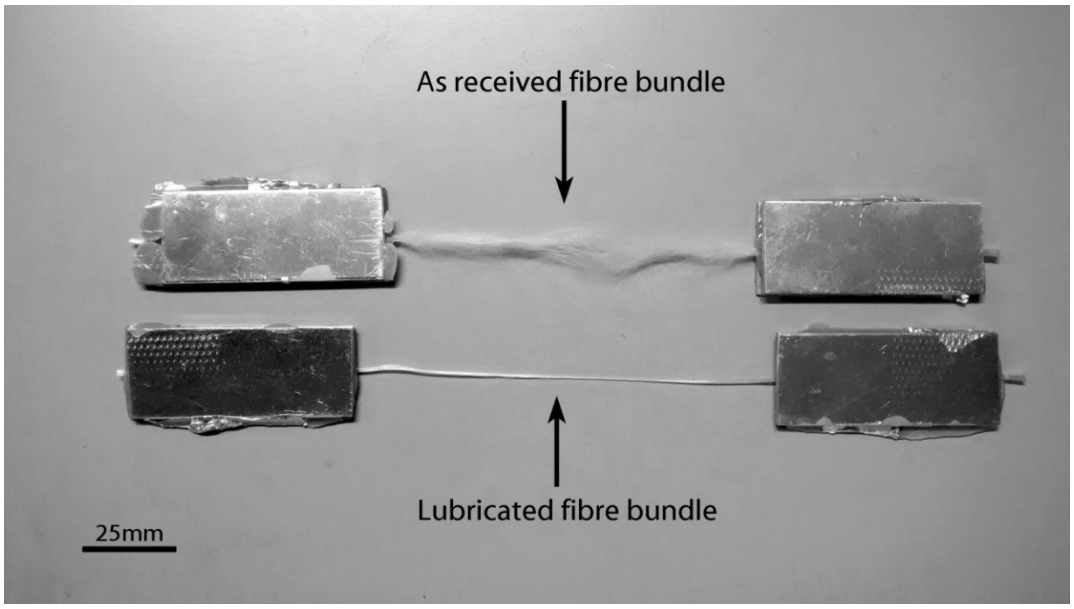

Figure 9.10: As-received and lubricated fibre bundles after failure

Representative load-displacement plots with the AE cumulative hits evolution for an as-received and a lubricated glass fibre bundle are shown in Figure 9.11. The evolution of the

fibre fracture AE hits provides important information about the failure behaviour of the fibre bundles. The cumulative hits evolution plots exhibit a sharp increase after maximum load is reached, indicating rapid fibre fracture prior to final failure of the bundle. The evolution of the fibre fracture-related cumulative hits was plotted after data clustering had been applied on the raw dataset.

The AE cumulative hits evolution of the dry bundle exhibits a sudden increase at approximately 1.7mm displacement. The AE cumulative hits evolution for the lubricated bundle exhibits a gradual and less sudden increase between 2.00-2.25mm. The load-displacement and AE hit evolution plots indicate that fibre failure initiates earlier and progresses faster in the dry bundles. The lubricated bundles exhibit higher strength and extension values compared with the dry bundle, as the failure initiates later and evolves slower.

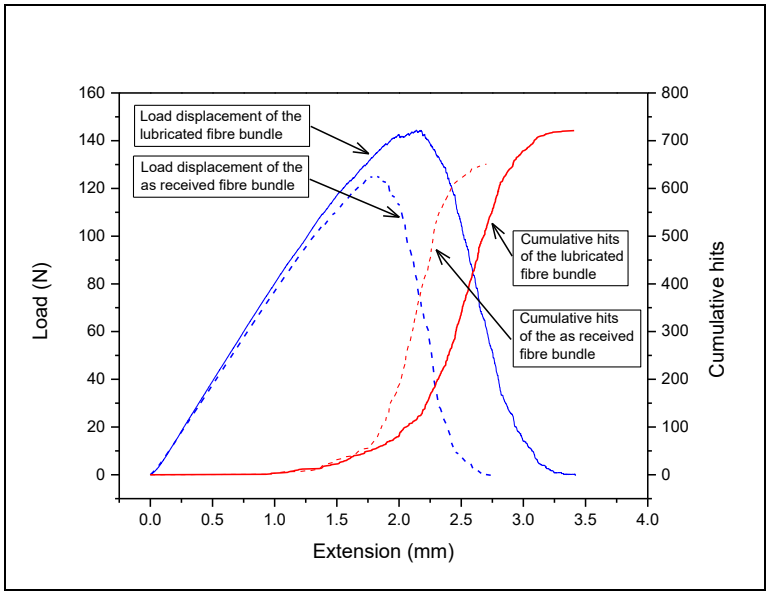

Figure 9.11: Load-Strain and AE cumulative hits for the as received and for the lubricated fibre bundle.

The evolution of the cumulative hits of the AE signals against time provides vital information regarding the failure behaviour of the fibre bundles. Amplitude scatter distribution and cumulative evolution plots of the fibre fracture AE signals are shown in Figures 9.12 and 9.13 for a dry and for a lubricated fibre bundle respectively. The AE scatter distribution and cumulative hits evolution are plotted with respect to amplitude and parametric extension. The scatter distribution for the dry bundles consists of a dense scatter region between 1.75-2.5 mm followed by a sharp increase in the cumulative hits evolution plot. This dense region follows also the sharp drop in load that is observed in Figure 9.11 and indicates rapid fibre failure after the maximum load is reached. Beyond 2.5mm the scatter distribution becomes less dense and the slope of the AE cumulative hits plot is slightly reduced until final failure of the bundle.

The number of the recorded fibre fracture signals for the dry bundle is 651 despite the fact that the bundle consists of approximately 700 filaments. Due to rapid failure, multiple filaments fail simultaneously. The AE system is unable to detect individual fibre fractures at this stage due to the limitations of the acquisition hardware. Despite the limitations in the DAQ system, the resulting error in the recorded fibre fracture signals is 7%. Fibre interactions and rapid failure give rise to noise signals and multiple fibre fractures can be recorded in a single waveform. An example of a multiple fracture waveform is shown in Figure 9.14. In contrast to the dry bundle, the number of the recorded fibre fracture signals for the lubricated bundle is 721. Due to slower failure rates the AE system in capable of detecting more individual AE fibre fracture events. In addition to the slower failure rates, more fibre fracture events could be identified due to the presence of echoes that can have similar features to the fibre fracture AE events. The resulting error in the identified fibre

fracture AE signals is 3%. However, a limited amount of multiple fracture and noise signals may also be recorded.

The effect of lubrication on the fibre bundle is reflected on the AE distribution plots. From Figure 9.13 it can be seen that the lubricated bundles exhibit an even amplitude scatter distribution without dense regions or sharp increases in the AE cumulative hits evolution plot. The AE plots indicate that the failure process in the lubricated bundles is slower and more stable compared to the as-received bundles. Prior to the final failure of the fibre bundles the scatter distribution becomes less dense and slope of the AE cumulative hits plot is reduced until the failure of the remaining filaments in the bundle.

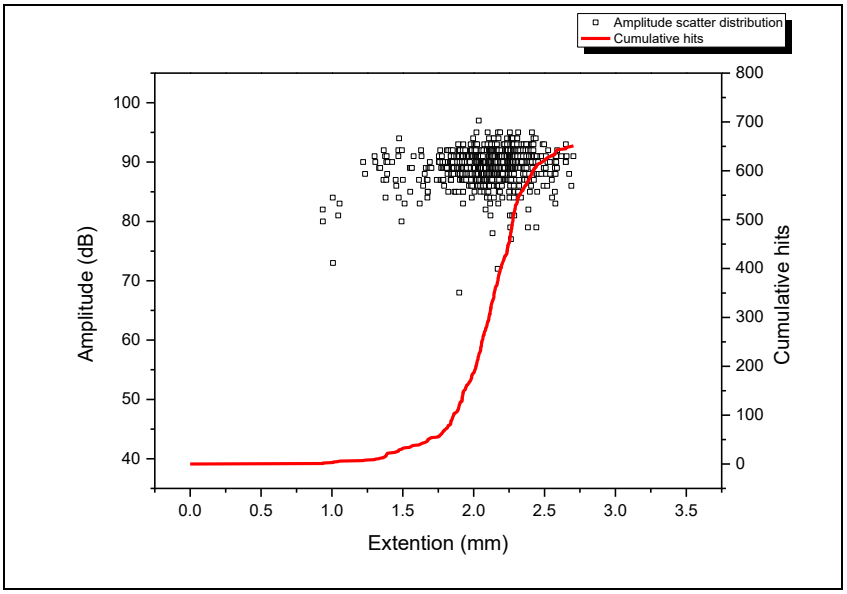

Figure 9.12: Amplitude distribution and AE cumulative hits evolution over time for a dry bundle.

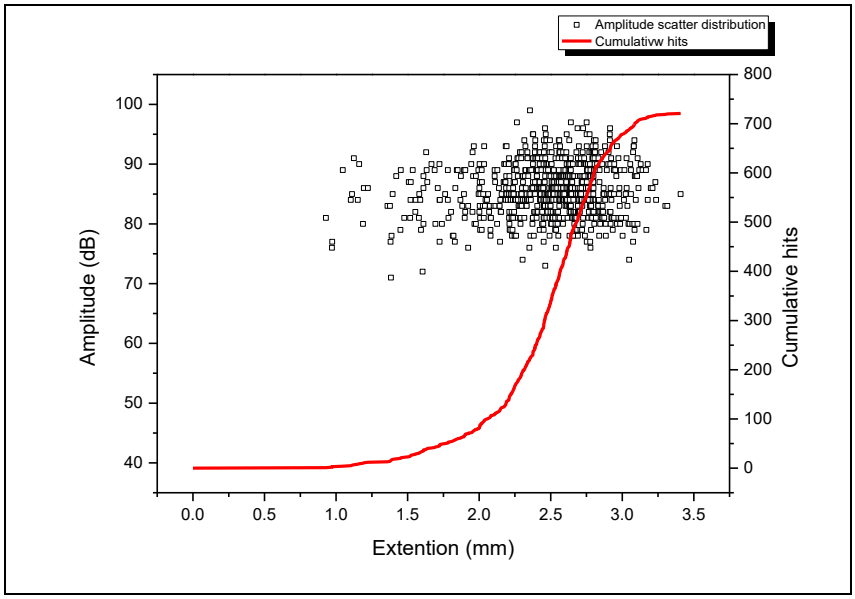

Figure 9.13: Amplitude distribution and AE cumulative hits evolution over time for a lubricated bundle.

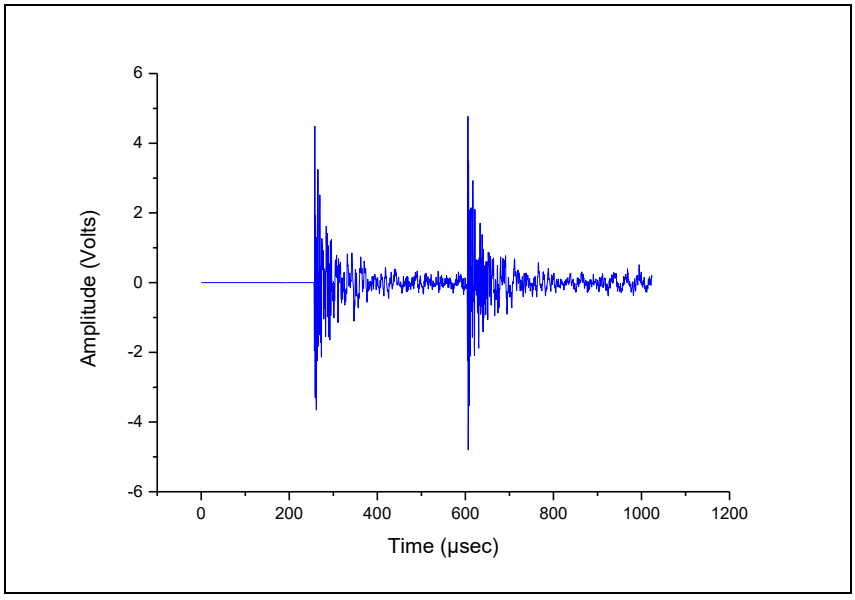

Figure 9.14: Multiple filament fracture waveform.

Table 9.3 presents the approximate number of filaments in the fibre bundle, number of the raw AE collected hits, and number of fibre fracture AE signals identified after several unsupervised data clustering algorithms were applied on the AE data. The as-received bundles generated higher levels of AE activity during testing. The raw AE data set of the dry fibre bundles consists of a considerably high amount of noise AE signals caused by friction and inter-fibre interactions. During testing of lubricated bundles though, significantly less AE activity was generated. The recorded noise AE signals cannot be easily filtered out entirely. By lubricating the fibre bundle, friction and inter-fibre interactions were substantially reduced, resulting in limited generation of noise signals. However, the lubrication cannot eliminate completely the friction.

In Table 9.3 it can be seen that for all the clustering algorithms the number of the identified fibre fracture signals for the dry fibre bundles is smaller than the approximate number of filaments in the bundles. The number of the recorded fibre fracture AE signals for the lubricated fibre bundles is slightly greater than the approximate number of filaments. Due to surface tension, the lubricant stays on and between the fibres during testing. Therefore, the fibres did not recoil, or recoiled less after failure. The lubrication also resulted in reduced friction and inter-fibre interactions slowing damage propagation and enabling the AE system to capture more individual fibre failures. Another reason that leads to the identification of more fibre fracture AE signals is the recording of echoes. Echoes from fibre failure have similar characteristics to the actual fibre fracture AE signals and cannot be classified as noise by the clustering algorithms. Fibre failure at the end of the test can still be fairly rapid rendering the AE system unable to record some filaments failing almost simultaneously.

Table 9.3: Actual number of fibres, number of raw AE hits, number of fibre failure AE hits after data clustering with k-means, Forgy, ISODATA and SOM-LVQ algorithms

Fibre Bundle	Number of filaments in the fibre bundle	Number of raw AE data	Fibre fracture AE events identified with k-means	Fibre fracture AE events identified with Forgy	Fibre fracture AE events identified with ISODATA	Fibre fracture AE events identified with SOM-LVQ
As received 1	700	**N/A, sample has accidentally broken before testing**				
As received 2	700	1981	650	664	650	651
As received 3	700	1144	662	669	662	662
As received 4	700	1434	561	583	561	561
As received 5	700	1436	615	625	615	615
As received 6	700	2118	594	616	594	595
As received 7	700	1659	605	612	572	572
As received 8	700	1519	610	613	610	610
As received 9	700	2002	631	726	698	699
As received 10	700	1466	651	668	651	651
Average	**700**	**1640 ±307**	**620 ±30**	**642 ±41**	**623 ±42**	**624 ±42**
Lubricated 1	700	1092	738	745	731	731
Lubricated 2	700	1095	680	771	761	760
Lubricated 3	700	892	712	712	712	712
Lubricated 4	700	1080	717	729	717	716
Lubricated 5	700	1210	734	764	767	767
Lubricated 6	700	983	721	719	718	717
Lubricated 7	700	1003	712	719	714	714
Lubricated 8	700	1033	699	724	719	719
Lubricated 9	700	933	707	707	707	707
Lubricated 10	700	1006	712	718	712	712
Average	**700**	**1033 ±86**	**713 ±16**	**730 ±21**	**726 ±20**	**725 ±20**

The error percentage between the number of filaments and number of identified fibre fracture AE signals for each clustering algorithm are shown on Table 9.4. For the dry bundles all clustering algorithms produced similar results. The k-means algorithm resulted in the largest error and produced similar results with ISODATA and LVQ. However, Forgy performed slightly better as it resulted to the smallest average error among the tested algorithms. The slightly improved performance of Forgy is also seen in Table 9.3.

For the lubricated bundles, all algorithms produce similar clustering results. In this case, k-means performed better, resulting to the smallest experimental error. ISODATA and LVQ algorithm had the same performance and led to similar error values. Forgy led to larger error as it identified more fibre fracture AE signals. Due to the acoustic coupling effect of the lubricant, more fracture waves and echoes of actual fibre fractures could be passing through the fibre bundle and reaching the AE sensors. The echoes could have similar characteristics to the actual fibre fracture AE signals and identified by the algorithms as fibre fracture signals. This is more actively observed in clustering using Forgy resulting to the largest experimental error among the rest of the clustering algorithms. In general, the slower failure rate of the lubricated bundles allowed the AE acquisition system to detect more individual fibre fracture signals leading to significantly lower error values compared with those obtained for dry bundles.

The performance of clustering algorithms depends on failure rate. More actual damage AE signals will be recorded and separated from the noise signals if failure rate is slow. Fast failure rates will result in the AE system recording less damage-related AE signals. However, the resulting experimental error values can be relatively low. Therefore the recorded AE

activity information is still valuable and can be used to assess and monitor the damage progression effectively.

Despite the limitations of the AE acquisition system and an average error of 10.57%, most of the filament fractures in the as-received samples have been identified. The average error for the automated clustering algorithms applied on the AE data obtained for the lubricated bundles is 3.47%. The resulting error is smaller compared with the dry bundles, as more fibre fracture AE signals have been recorded because of the slower failure rate. All clustering algorithms produced similar results with relatively small errors.

The simplest clustering algorithm is the k-means. Algorithms like Forgy, ISODATA and SOM-LVQ are more complex and require increased computational power. For small and simple AE data sets, a simple and light clustering algorithm like k-means can quickly achieve efficient clustering results. Therefore, it can be impractical to use complex and computationally expensive clustering algorithms on small and simple AE datasets, or whenever quick clustering results are required.

Table 9.4: Error percentage between the approximate number of filaments and the number of the identified fibre fracture AE signals for each clustering algorithm

Fibre Bundle	Error between the number of filaments and the number of fibre fracture signals identified with k-means (%)	Error between the number of filaments and the number of fibre fracture signals identified with Forgy (%)	Error between the number of filaments and the number of fibre fracture signals identified with ISODATA (%)	Error between the number of filaments and the number of fibre fracture signals identified with SOM-LVQ (%)
As received 2	7.14	5.14	7.14	7
As received 3	5.42	4.42	5.42	5.42
As received 4	19.85	16.71	19.85	19.85
As received 5	12.14	10.71	12.14	12.14
As received 6	15.14	12	15.14	15
As received 7	13.57	12.57	18.28	17.85
As received 8	12.85	12.42	12.85	12.85
As receive d 9	9.85	3.71	0.28	0.14
As received 10	7	4.57	7	7
Average	**11.44**	**9.13**	**10.93**	**10.8**
Lubricated 1	5.42	3.42	4.42	4.42
Lubricated 2	2.85	10.14	8.71	8.57
Lubricated 3	1.71	1.71	1.71	1.71
Lubricated 4	2.42	4.14	2.42	2.28
Lubricated 5	4.85	9.14	9.57	9.57
Lubricated 6	3	2.71	2.57	2.42
Lubricated 7	1.71	2.71	2	2
Lubricated 8	0.17	3.42	2.71	2.71
Lubricated 9	1	1	1	1
Lubricated 10	1.71	2.57	1.71	1.71
Average	**2.48**	**4.09**	**3.68**	**3.63**

9.2.3 Acoustic Emission signal characteristics

Statistical analysis on the AE signals recorded during the tests was conducted to obtain the key characteristics of the fibre fracture and noise AE waveforms. The main differences between the noise and fibre fracture signals were observed among the Counts, Duration, Energy and Amplitude of the AE signals. Table 9.5 presents the range, the average and statistical median of the key signal features for fibre fracture AE signals from tests on dry and lubricated fibre bundles. Table 9.6 presents the main signal features for the noise signals.

The fibre fracture signals exhibit higher average energy, duration and amplitude compared with noise signals which have low energy, duration and amplitude values. Due to the low amplitude, selected threshold and frequency, the counts of the noise signals are lower compared to the fibre fracture signals.

The lubricant has a damping effect on the AE signals as it is retained between the filaments. Thus fibre fracture AE signals have lower amplitude, duration and energy values compared with those detected from the tests on the dry bundles. The damping effect of the lubrication is also seen on the characteristics of the noise signals which have lower energy values compared to the noise that is generated from dry bundles.

By conducting statistical analysis on the AE signals the key features of noise and fibre fracture signals were identified. As it can be seen from Tables 9.5 and 9.6, the key differences observed are related to signal duration and energy. Noise signals have low average energy and duration values compared with the fibre fracture waveforms. The identification of the noise signal features helped in determining suitable filters for removing noise signals.

A duration filter of 150μs and an energy filter of 4 or 5 (10μVolt-sec/count) can be used to effectively remove the noise signals. The use of filter above these values can remove or limit the acquisition of AE signals to those that are associated with actual damage events only.

Table 9.5: Signal characteristics for fibre fracture AE signals

Fibre fracture signals from dry bundles	Range	Average	Median
Counts	37-832	147	119
Duration (μs)	485-12606	2695	2196
Amplitude (dB)	65-99	90	90
Energy (10μVolt-sec/count)	17-3851	432	330
Fibre fracture signals from lubricated bundles	Range	Average	Median
Counts	39-124	64	62
Duration (μs)	649-2219	1602	1672
Amplitude (dB)	71-99	85	85
Energy (10μVolt-sec/count)	29-814	257	245

Table 9.6: Signal characteristics for noise signals

Noise signals from dry bundles	Range	Average	Median
Counts	1-114	7	2
Duration (μs)	0-2446	187	80
Amplitude (dB)	40-68	43	80
Energy (10μVolt-sec/count)	0-452	4	10
Noise signals from lubricated bundles	Range	Average	Median
Counts	1-56	11	6
Duration (μs)	0-1607	179.15	92.5
Amplitude (dB)	40-77	49	47
Energy (10μVolt-sec/count)	0-188	5	0

9.2.4 Fast Fourier Transform on Acoustic Emission signals from fibre bundles

To obtain further information regarding the frequency content of the AE signals, spectral analysis based on Fast Fourier Transform (FFT) was conducted on AE signals acquired using a custom-built AE system that continuously records AE signals for a time window of 5s. The recorded waveforms consisted of 5 million points. The high length of the recorded signals results in increased accuracy. Due to the increased length of the recorded signals, the power spectrum of the AE waveform can be determined reliably.

FFT analysis has been carried out on both fibre fracture and noise AE signals. Initial tests on fibre bundles with few filaments have been carried out to obtain the FFT spectrum from single fibre fractures. Furthermore, FFT analysis has been carried out on fibre fracture and noise signals recorded during the tests on small fibre bundles.

A single fibre fracture AE signal within a 5s time window is shown in Figure 9.15. Due to the high duration of the total acquisition time, the waveform of the fibre fracture related AE signal is not clearly visualised (Figure 9.15 a). Therefore, the overall recorded AE signal needs to be magnified in the time axis at the point where the peak is observed, in order to visualise the AE waveform shown in Figure 9.15 b). The frequency spectrum of the recorded signal is shown in Figure 9.16. A clear major peak is observed in the obtained power spectrum at 230kHz. Further spectral analysis has been carried out on several single fibre fracture signals and distinctive peaks in the resulting frequency spectra were identified around 235kHz and within the range of 225-240kHz.

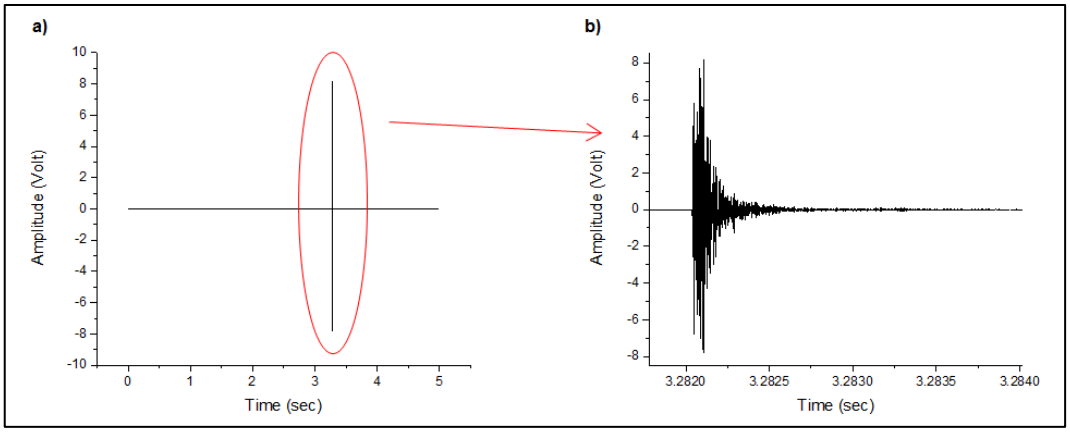

Figure 9.15: a) Single fibre fracture signal and b) AE waveform.

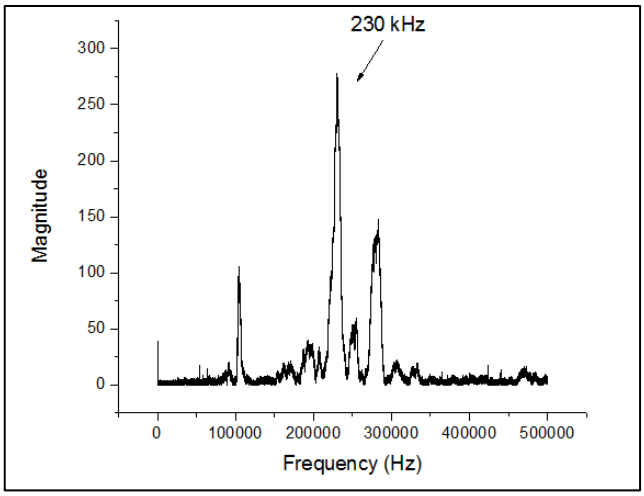

Figure 9.16: FFT spectrum of a single fibre fracture signal.

The high number of fibres in the dry and lubricated fibre bundles results in the custom DAQ system to record multiple filaments failing within the time window of 5s. A multiple fibre fracture AE signal recorded during the tests on dry E-glass fibre bundles is shown in Figure 9.17 a). Similarly to Figure 9.15, the recorded AE plot needs to be magnified in the time axis in order to visualise the waveform in Figure 9.17 b). As shown in Figure 9.18, the FFT of the recorded fibre fracture associated AE signal has generated a clear frequency spectrum with a distinctive peak at 238kHz. The implication of this frequency is to identify fibre breaks in

GFRPs using FFT. However, the frequency may differ in this case, due to attenuation and wave interaction phenomena that take place during wave propagation in FRPs.

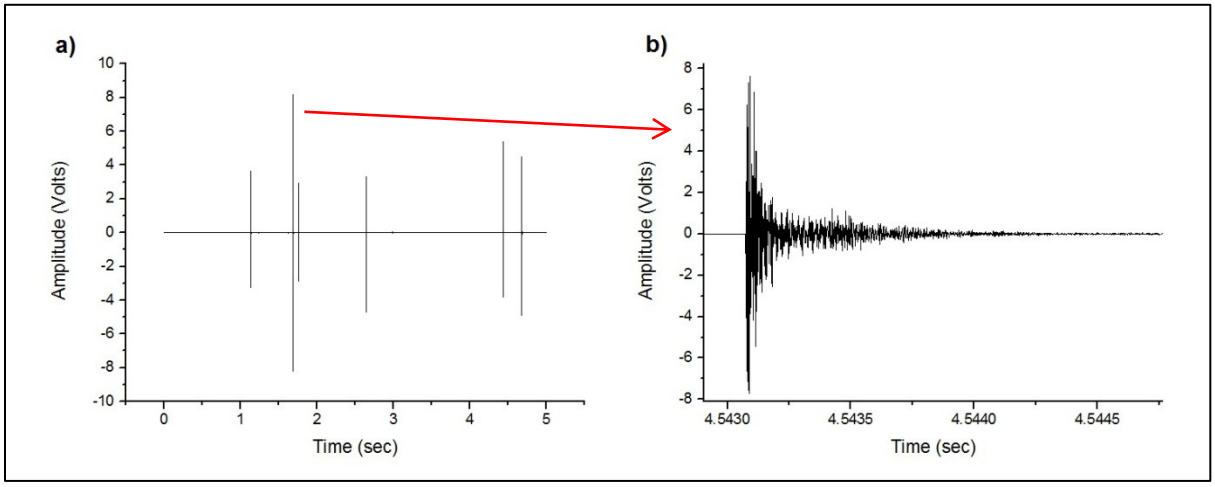

Figure 9.17: a) Multiple fibre fracture AE signal and b) AE waveform.

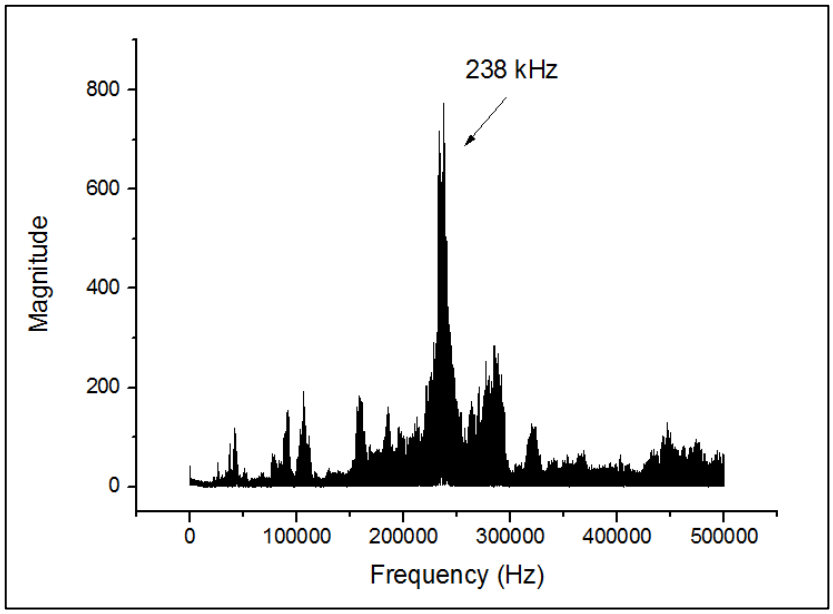

Figure 9.18: FFT from multiple fibre fractures.

FFT analysis was also carried out on fibre fracture signals recorded during the lubricated fibre bundle tests. The damping effect of the lubricant on the fibre fracture AE signals is expected to affect the frequency distribution of the recorded signals. Indeed, as it can be seen in Figure 9.19 the power spectrum from the lubricated bundles has some differences when compared with those obtained during the tests on the dry bundles. The power spectrum from the lubricated bundle tests is not clear and multiple peaks are observed. Similarly to the dry bundles, the major peak is identified on 223kHz. However, multiple secondary peaks are observed mainly around 100, 190 and 280kHz. Further spectral analysis on fibre fracture AE signals from the lubricated bundles resulted in similar frequency spectra with multiple secondary peaks, while major peaks were identified within the range of 220-235kHz. The differences in the spectral frequency distribution arise from the damping effect of the lubricant on the AE signals. The lubricant limits fibre recoil and supresses the resonance of the fibres during failure.

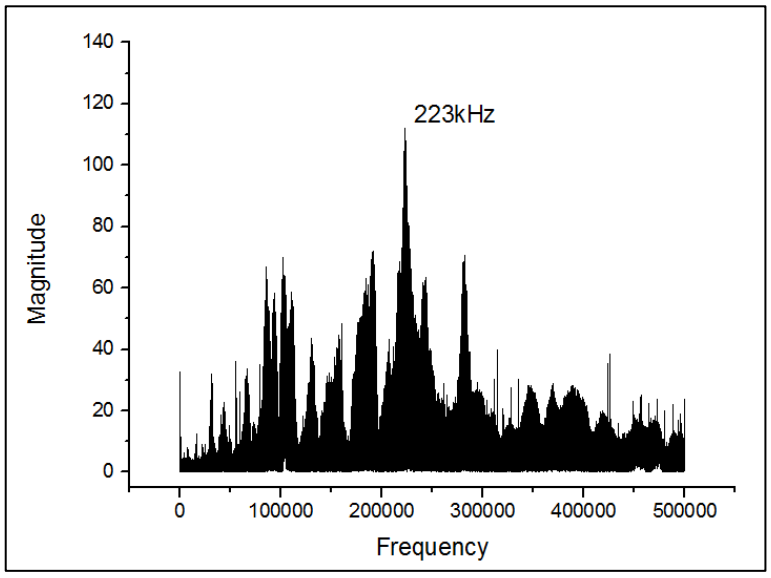

Figure 9.19: FFT from fibre fracture on lubricated fibre bundles.

During testing, unwanted noise signals were also recorded as a result of friction. Noise signals are in general continuous waveforms with a wide frequency response. A continuous low amplitude noise signal as a result of fibre friction during the tests is shown in Figure 9.20. From Figure 9.21 it can be seen that the power spectrum of the noise signal is not clear and no distinctive peaks were observed. Henceforth, unlike fibre fracture AE signals, noise signals are continuous waveforms with a flat frequency response over the entire frequency range.

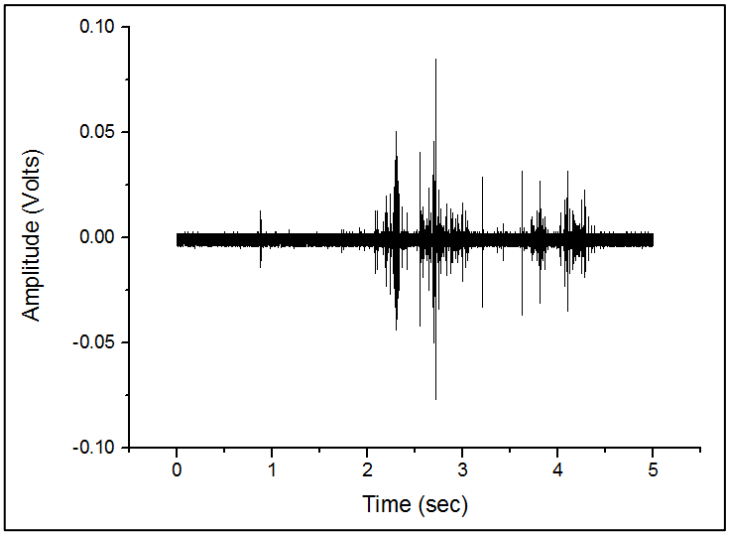

Figure 9.20: Continuous AE noise signal.

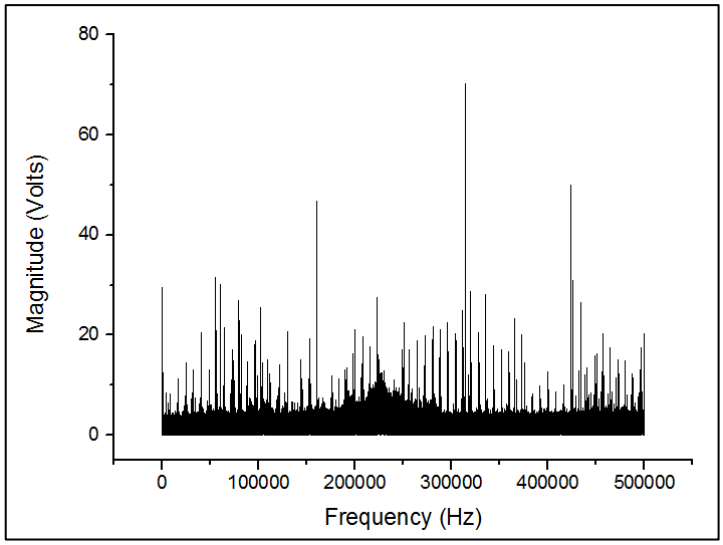

Figure 9.21: FFT from noise signal.

9.3 Mechanical tests on Glass Fibre Reinforced composites

9.3.1 Introduction

This section summarises the main results arising from the mechanical tests on glass fibre reinforced composite samples using tensile tests and AE testing. The results from the glass fibre bundle tests reported in the previous section have been used to establish an effective analysis methodology for the AE data collected from the more complicated composite samples, which involve multiple damage mechanisms like fibre fracture, matrix cracking, delamination, and debonding. Both void free and composite samples were subjected to tensile and bending tests to assess the effect of voids on the generation and evolution of AE signals during damage propagation. To further improve the effectiveness of AE in continuously monitoring damage initiation and subsequent evolution, data clustering was carried out to group the AE signals arising from the different damage mechanisms into separate clusters. Various clustering algorithms were tested and their results analysed.

9.3.2 Evaluation of tensile strength on vinyl-ester GFRP plates

Tensile tests were carried out on void free samples and on composite samples with high void content. Test specimens for each type of composite plate were tested in both wrap (0^o) and fill (90^o) directions.

Resin Infusion samples:

The samples made using resin infusion were tested along the warp and the fill direction. The stress-strain plots for the resin infusion samples tested in the warp and fill direction are given in Figures 9.22 and 9.23 respectively. The maximum strength and modulus of elasticity for each sample are listed in Table 9.7. The difference between the average strength and modulus of elasticity for the warp and fill direction are shown in Figures 9.24 and 9.25.

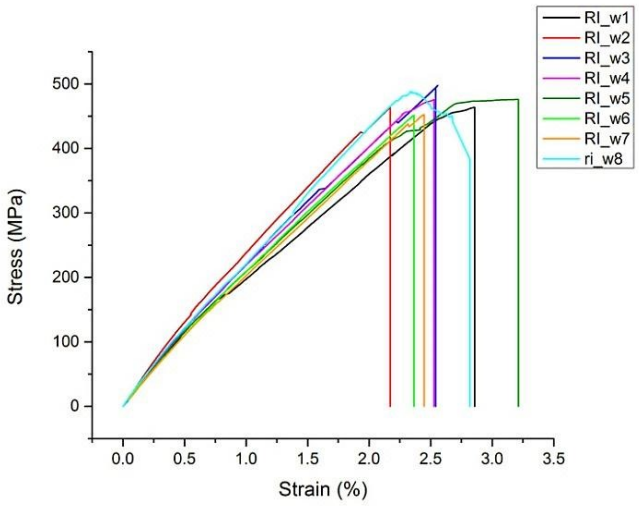

Figure 9.22: Stress-Strain plots for resin infusion samples tested in the warp direction.

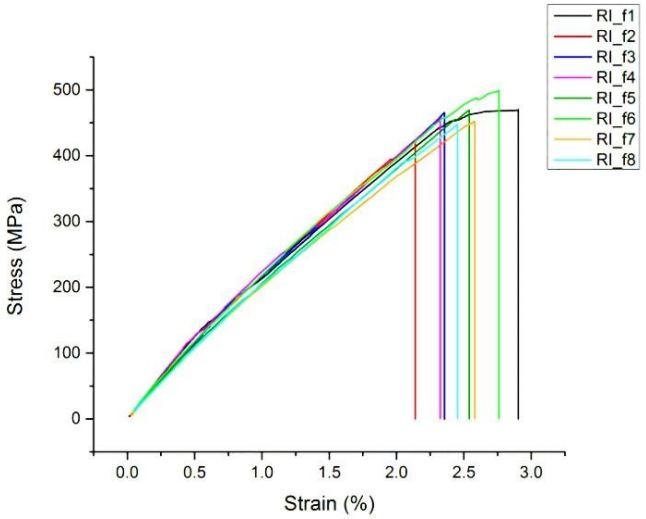

Figure 9.23: Stress-Strain plots for resin infusion samples tested in the fill direction.

Table 9.7: Main mechanical properties of the composite samples made with resin infusion

Sample	Maximum strength (MPa)	Young's modulus E (GPa)
RI_w1	463.91	24.70
RI_w2	463.8	31.98
RI_w3	497.61	25.91
RI _w4	476.04	26.80
RI _w5	476.03	25.24
RI _w6	450.53	23.90
RI _w7	452.4	25.15
RI _w8	487.88	29.76
Average	**471.025 ±15.45**	**26.68 ±2.6**
RI _f1	470.12	26.34
RI _f2	423.05	25.67
RI _f3	465.49	23.34
RI _f4	458.47	27.56
RI _f5	469.39	24.061
RI _f6	499.36	26.06
RI _f7	452.4	23.17
RI _f8	447.29	22.86
Average	**460.69 ±20.47**	**24.88 ±1.6**

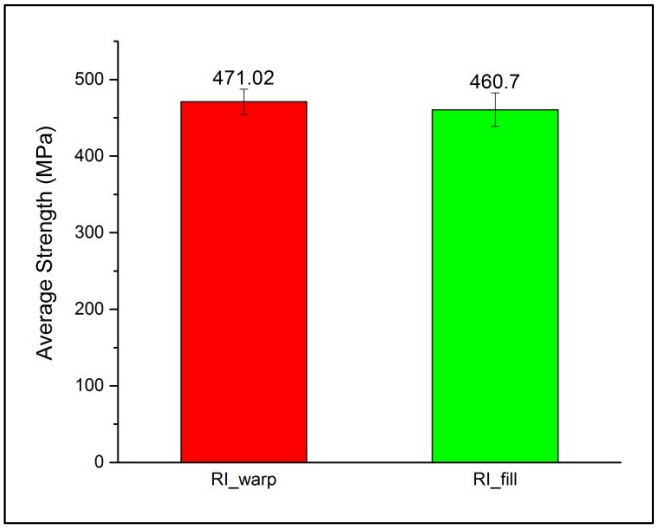

Figure 9.24: Comparison of average strength for the resin infusion samples loaded in the warp and fill direction.

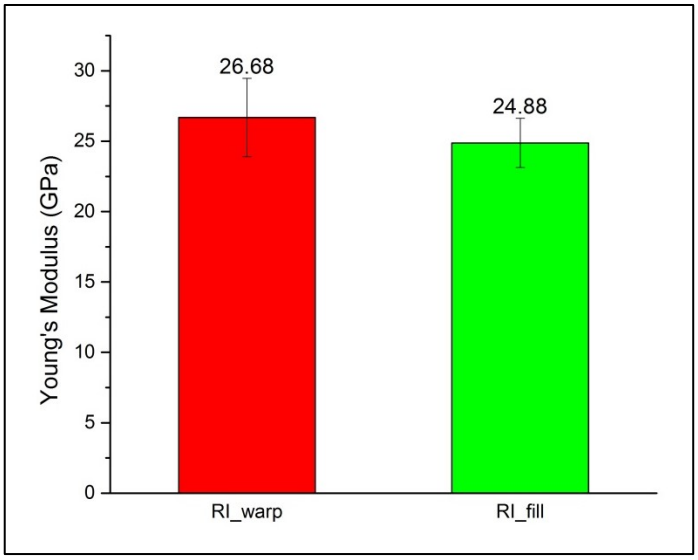

Figure 9.25: Comparison of E for the resin infusion samples loaded in the warp and fill direction.

The samples exhibited a linear increment of applied load until rupture. The samples loaded in the warp direction exhibited 2.2% higher strength and 6.74% higher modulus of elasticity compared with the samples loaded in the fill direction of the plate. This is due to the higher fibre fraction along the warp direction. The presence of gaps between the fibre tows on the fill side of the fabric resulted in reduced fibre fraction and reduced strength along the fill direction. The strain to failure ranges between 2.2-3% for both samples tested in the warp and fill direction.

First batch of Shipyard samples:

The first batch of the shipyard samples were tested along the warp and the fill direction. The stress-strain plots for the resin infusion samples tested in the warp and fill direction are given in Figures 9.26 and 9.27 respectively. The maximum strength and modulus of elasticity for each sample are listed in Table 9.8. The difference between the average strength and modulus of elasticity for the warp and fill direction are shown in Figures 9.28 and 9.29.

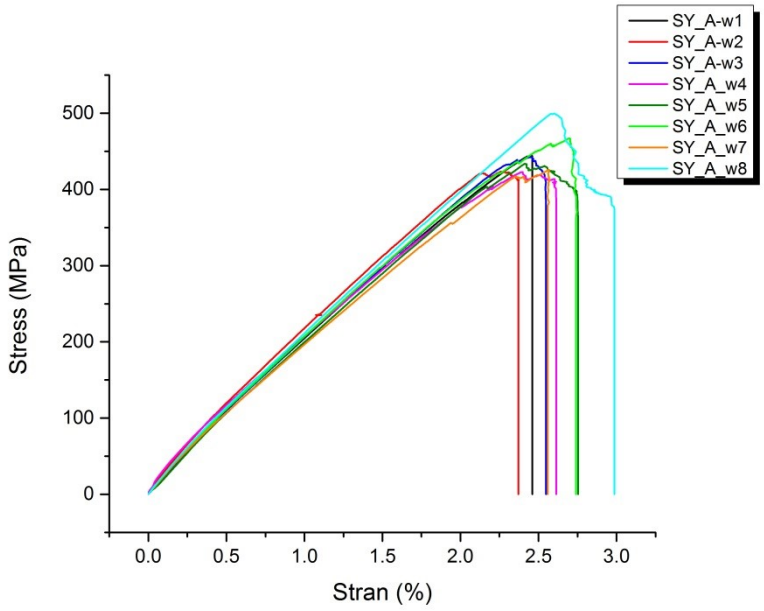

Figure 9.26: Stress-Strain plots for the Shipyard_A samples tested in the warp direction.

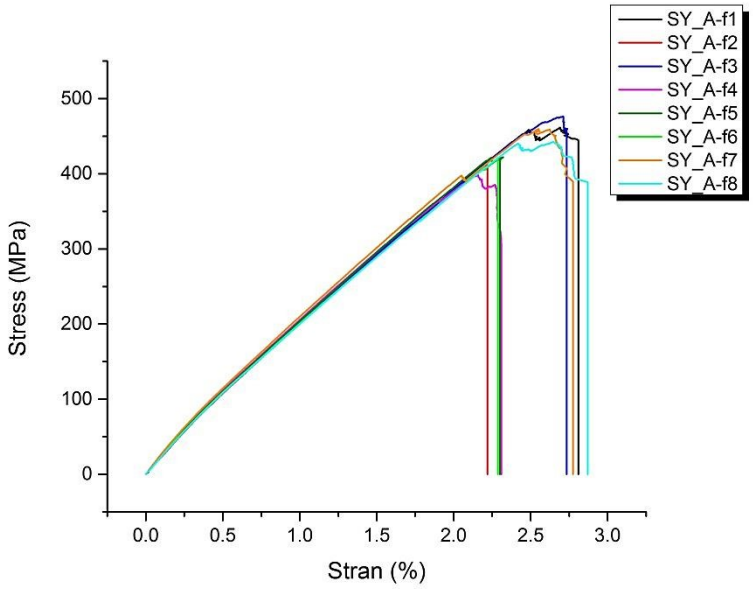

Figure 9.27: Stress-Strain plots for the Shipyard_A samples tested in the fill direction.

Table 9.8: Main mechanical properties of the Shipyard_A composite samples

Sample	Maximum strength (MPa)	Young's modulus E (GPa)
SY_A-w1	444.88	24.61
SY_A-w2	423.62	28.98
SY_A-w3	442.58	23.73
SY_A-w4	422.78	36.30
SY_A-w5	433.76	22.86
SY_A-w6	467.27	24.76
SY_A-w7	425.72	24.1
SY_A-w8	499.76	25.76
Average	**445.04 ±24.87**	**26.4 ±4.12**
SY_A -f1	461.49	24.72
SY_A -f2	411.87	23.008
SY_A -f3	476.39	24.70
SY_A -f4	398.36	25.97
SY_A -f5	422.2	25.15
SY_A-f6	419.68	27.15
SY_A-f7	459.76	27.07
SY_A -f8	442.67	23.93
Average	**436.55 ±25.84**	**25.21 ±1.36**

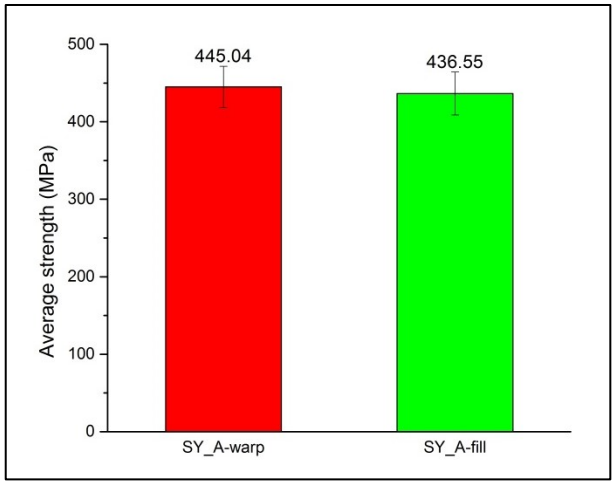

Figure 9.28: Comparison of average strength for the Shipyard_A samples loaded in the warp and fill direction.

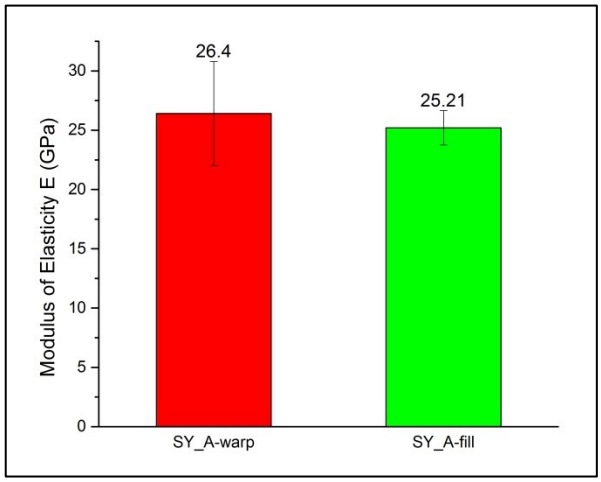

Figure 9.29: Comparison of E for the Shipyard_A samples loaded in the warp and fill direction.

Tested samples exhibit a linear increase in applied load until rupture occurs. In addition, the samples loaded in the warp direction exhibit 1.9% higher strength and 4.5% higher modulus of elasticity compared with the samples loaded in the fill direction of the plate. Similarly to the resin infusion samples, the slightly reduced strength and elasticity modulus of the fill

samples compared with the warp result from the lower higher fibre fraction along the fill direction. The strain to failure ranges between 2.2% and 3% for both samples tested in the warp and fill direction.

Second batch of Shipyard samples:

The second batch of the shipyard samples were tested along the warp and fill direction. The stress-strain plots for the resin infusion samples tested in the warp and fill direction are given in Figures 9.30 and 9.31 respectively. The maximum strength and modulus of elasticity for each sample are listed in Table 9.9. The difference between the average strength and modulus of elasticity for the warp and fill direction are shown in Figures 9.32 and 9.33.

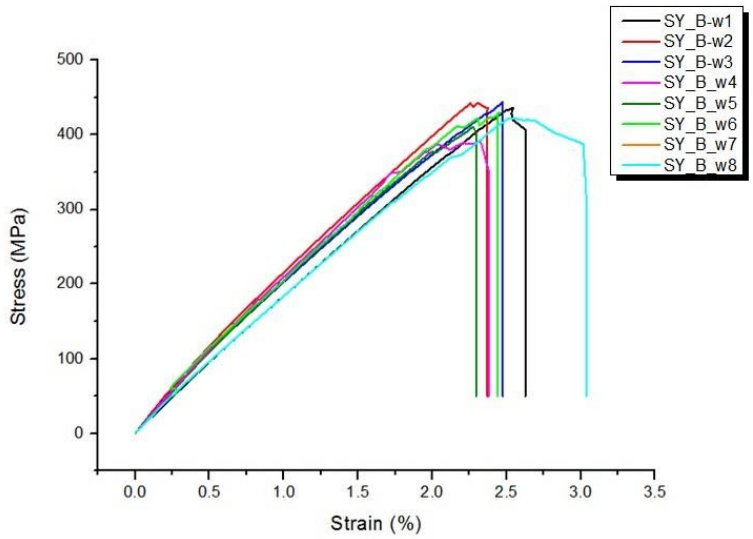

Figure 9.30: Stress-Strain plots for the Shipyard_B samples tested in the warp direction.

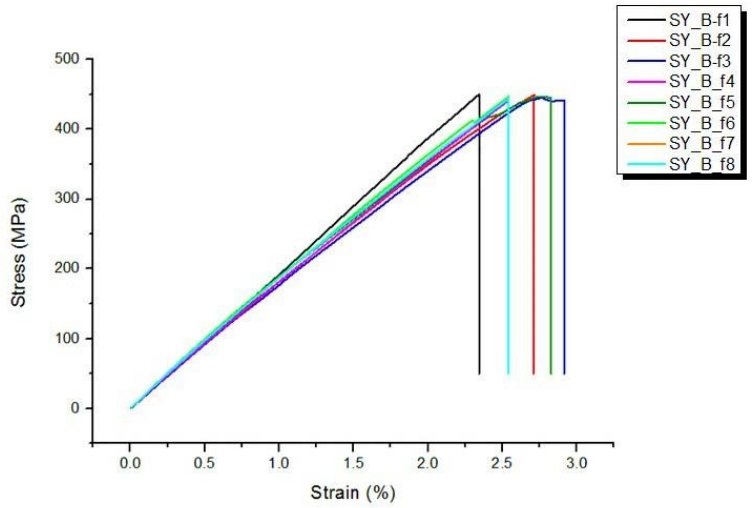

Figure 9.31: Stress-Strain plots for the Shipyard_B samples tested in the fill direction.

Table 9.9: Main mechanical properties of the Shipyard_B composite samples

Sample	Maximum strength (MPa)	Young's modulus E (GPa)
SY_B -w2	436.07	19.76
SY_B -w3	442.99	25.75
SY_B -w4	444.51	23.49
SY_B -w5	410.45	22.42
SY_B -w6	391.23	25.27
SY_B -w7	429.23	22.47
SY_B -w8	422.35	20.77
Average	**425.26 ±17.74**	**22.85 ±2.03**
SY_B -f2	488.61	20.36
SY_B -f3	449.57	20.09
SY_B -f4	445.44	18.93
SY_B -f5	446.76	20.52
SY_B -f6	442.11	19.36
SY_B -f7	447.46	20.65
SY_B -f8	444.92	20.28
Average	**452.12 ±15.05**	**20.03 ±0.6**

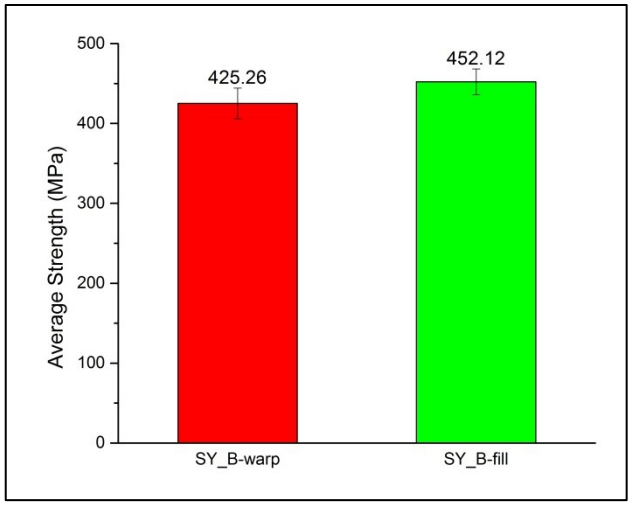

Figure 9.32: Comparison of average strength for the Shipyard_B samples loaded in the warp and fill direction.

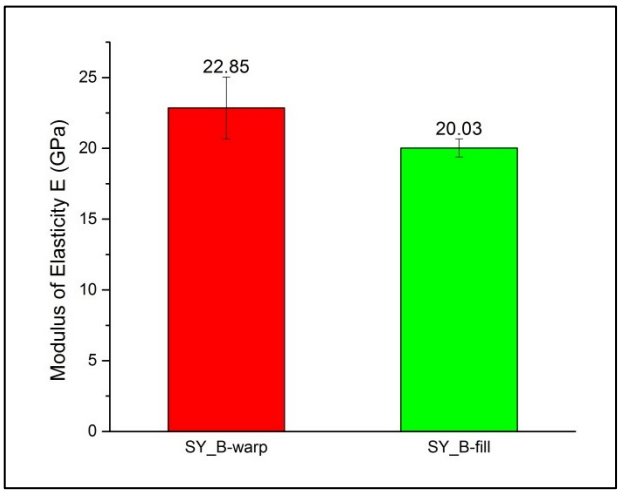

Figure 9.33: Comparison of E for the Shipyard_B samples loaded in the warp and fill direction.

The samples exhibited a linear increase in the applied load until the sample ruptured. The samples loaded in the warp direction exhibited 5.9% lower strength and 12.34% higher modulus of elasticity compared with the samples loaded in the fill direction of the plate. Similarly to the other types of samples, the higher fibre fraction in the weft direction leads to increased modulus of elasticity. However, errors in the stacking sequence and increased void

formation between the fibre tows along the warp direction resulted in decreased strength for the warp samples in comparison with those tested in the fill direction. Strain to failure ranged between 2.2-3% for both samples tested in the warp and fill direction.

Comparison of tensile properties:

A comparison between the maximum tensile strength and modulus of elasticity for the different types of composite plates is shown on Figures 9.34 and 9.35 respectively. It can be seen that in the warp direction the composite samples manufactured with resin infusion sustained 9.71% higher stress compared with the Shipyard_B samples and 5.5% higher stress compared to the Shipyard_A batch. Similar results were obtained in the fill direction were the samples made using resin infusion sustained 1.8% higher stress compared with Shipyard_B samples and 5.24% higher stress compared with Shipyard_A batch.

In the warp direction, the resin infusion samples exhibited 14.35% and 1.2% higher elasticity modulus compared with the Shipyard B and A batches respectively. Likewise, in the fill direction the resin infusion samples exhibited 19.5% and 1.67% higher elasticity modulus compared with the Shipyard B and A batches respectively.

The glass fibre composite plates made using resin infusion exhibited superior tensile properties compared with the shipyard plates. The improved performance of the resin infusion plates resulted from the higher fibre fraction and suppression of void formation to levels below 1%.

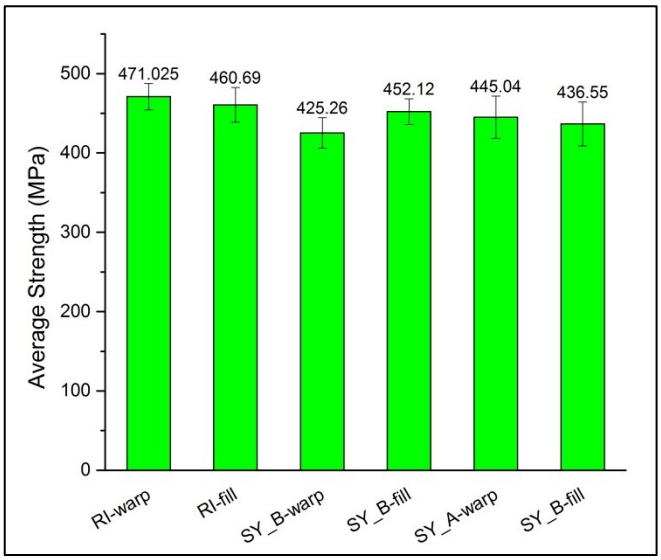

Figure 9.34: Comparison between the tensile strength for the different types of composites tested in the warp and fill directions.

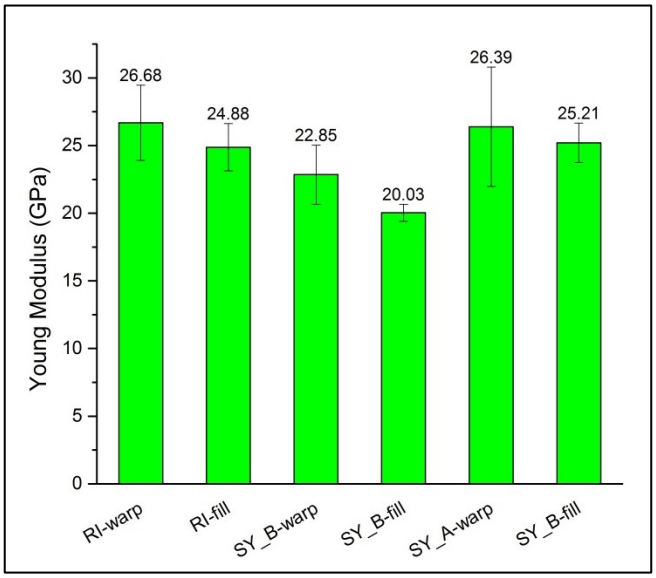

Figure 9.35: Comparison between the modulus of elasticity E for the different types of composites tested in the warp and fill directions.

9.3.3 Bending tests on vinyl-ester GFRP plates

Three-point bending tests were performed on void free glass fibre vinyl-ester samples and on composite samples with high void content. The flexural stress-deflection plots for the glass fibre vinyl-ester samples made using resin infusion are shown in Figure 9.36. The main flexural properties for these types of samples are listed in Table 9.10, where variations in the maximum strength are observed. These variation were caused by gaps between the fibre tows in the glass fibre fabric, which resulted in resin-rich areas. These gaps can be located at different positions. Since the samples are sectioned from a larger GFRP plate, the exact location of the gaps and resin-rich areas for each of the tested samples could not be controlled. A major drop in the applied load was observed after the maximum load had been reached. At this point as major damage event such as delamination had occurred in the material which could not any longer sustain high loads. The stress intensity in front of the damage zone was reduced and further loading was required to continue damage growth. Stress redistribution took place and load recovered to a second peak load lower than the previously attained maximum. Further damage progression is indicated by subsequent load drops.

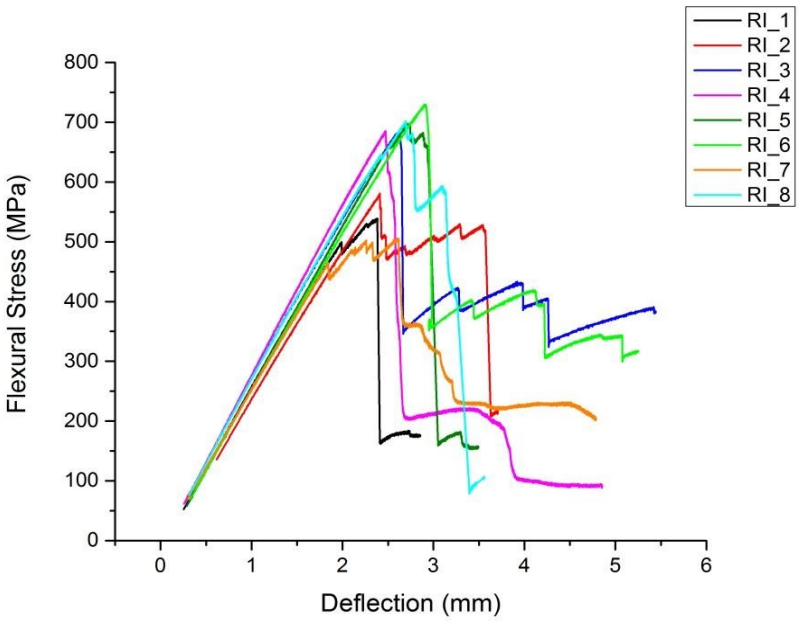

Figure 9.36: Flexural stress displacement plots for resin infusion samples.

Table 9.10: Main flexural properties of the composite samples made with resin infusion

Sample	Maximum strength (MPa)	Flexural modulus of elasticity E_B (GPa)
RI_1	539.29	30.061
RI_2	580.88	27.1
RI_3	682.39	31.2
RI_4	685.69	32.38
RI_5	698.44	31.01
RI_6	729.82	29.7
RI_7	599.68	28.18
RI_8	701.62	31.2993
Average	**652.22 ±64.45**	**30.12 ±1.64**

The first batch of shipyard samples with void content of approximately 9.6%, were subjected to three-point bending tests. The flexural stress-deflection plots are shown in Figure 9.37. The main flexural properties are listed in Table 9.11. Variations in the maximum strength are observed as a result of gaps and void formation between the fibre tows in the sample.

Similarly to the previous type of samples, a major drop in the applied load is observed indicating major cracking. Subsequent load drops indicate damage progression.

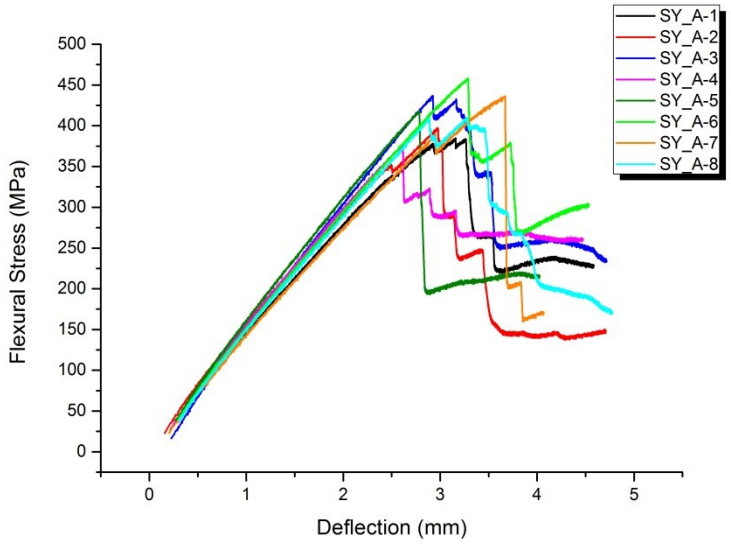

Figure 9.37: Flexural stress displacement plots for the Shipyard_A samples.

Table 9.11: Main flexural properties of the Shipyard_A samples

Sample	Maximum strength (MPa)	Flexural modulus of elasticity E_B (GPa)
SY_A-1	385.1	15.05
SY_A-2	397.51	15.16
SY_A-3	436.94	17.78
SY_A-4	376.73	16.53
SY_A-5	418.62	17.22
SY_A-6	458.11	15.86
SY_A-7	436.46	14.76
SY_A-8	533.15	16.002
Average	**430.33 ±46.84**	**16.048 ±1**

The second batch of shipyard samples with void content of approximately 6.6%, were subjected to three-point bending tests. The flexural stress-deflection plots are shown in Figure 9.38. The main flexural properties are listed in Table 9.12. Like in the previous type of

samples a major drop in the applied load is observed indicating major cracking, while subsequent load drops indicate damage progression until the end of the test. Variations in the maximum strength are also observed as a result of gaps and void formation between the fibre tows in the sample.

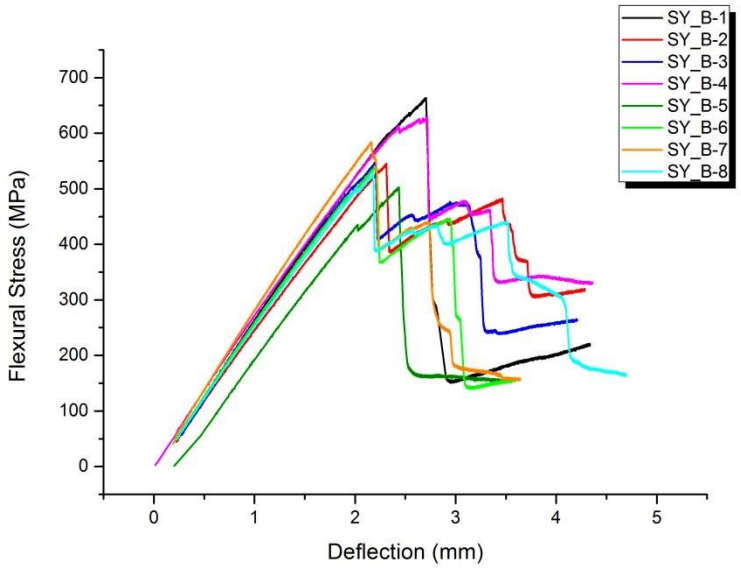

Figure 9.38: Flexural stress displacement plots for Shipyard_B samples.

Table 9.12: Main flexural properties of the Shipyard_B composite samples

Sample	Maximum strength (MPa)	Flexural modulus of elasticity E_B (GPa)
SY_B-1	663.68	28.63
SY_B-2	545.36	26.27
SY_B-3	548.9	28.32
SY_B-4	628.22	27.62
SY_B-5	503.37	26.61
SY_B-6	538.62	28.13
SY_B-7	584.37	31.02
SY_B-8	527.56	27.2
Average	**567.51 ±50.74**	**27.97 ±1.38**

Comparison of flexural properties:

A comparison between the flexural strength and modulus of elasticity for the different types of vinyl-ester samples is shown in Figures 9.39 and 9.40 respectively. Severe mechanical degradation occurred in both types of the Shipyard samples, due to their non-symmetrical structure and their high void content. The void free samples made with resin infusion could sustain 13% higher flexural strength and exhibited 7% higher flexural elasticity modulus compared with the second batch of Shipyard samples with a void content of 6.6%. The samples made using resin infusion could sustain 34% higher flexural strength and exhibited 46.7% higher flexural elasticity modulus compared with the Shipyard_A samples with a void content of 9.6%. It can be seen that a void content of approximately 6% decreased the flexural strength and flexural elasticity modulus by 13% and 7% respectively. A further increase in the void content up to 10% reduced the flexural strength by 34%, while the flexural modulus of elasticity was reduced by 46.7%. Similar results have been reported in previous studies [34, 35]. It can be safely concluded that the glass fibre composite plates made with resin infusion were superior to both the heavily voided samples made using vacuum bagging. The improved performance of the resin infusion plates resulted from a combination of higher fibre fraction, symmetrical lay-up, and low void content (>1%).

High void content and errors in the stacking sequence had great impact on the flexural properties and caused severe structural degradation under bending loading conditions. However, the presence voids even at high levels did not greatly affect the tensile properties. The stacking sequence errors had minor effect on the tensile strength of composite plates.

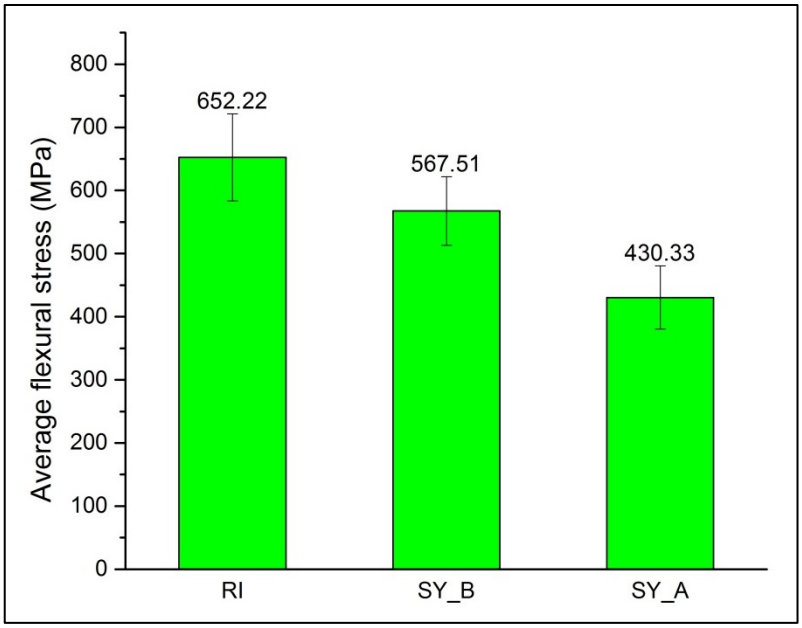

Figure 9.39: Comparison between the flexural strength for the different types of vinyl-ester plates.

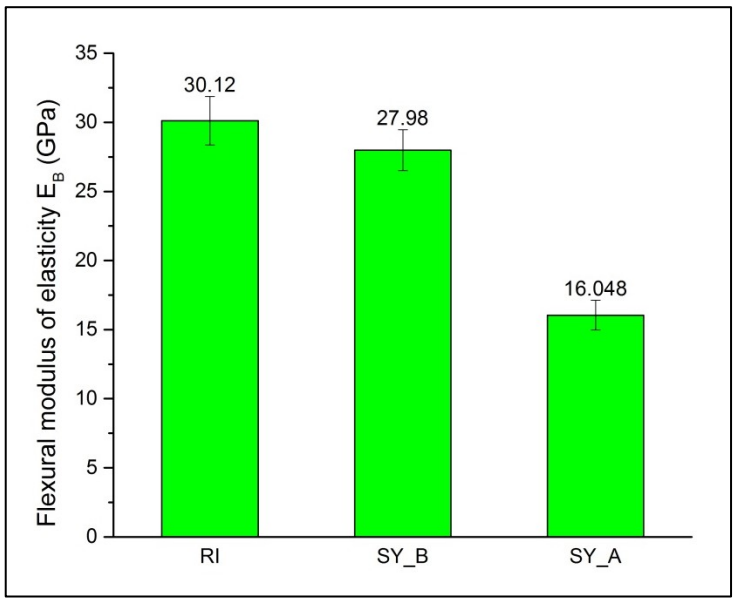

Figure 9.40: Comparison between the flexural modulus of elasticity E_B for the different types of vinyl-ester plates.

9.3.4 Bending tests on epoxy GFRP pre-preg plates cured in the autoclave

Additional three-point bending tests were carried out on defect free glass fibre epoxy samples and samples with drilled holes where 1.5mm bolts were placed after drilling. The flexural stress-deflection plots for the samples without any holes being drilled on them are shown in Figure 9.41. The main flexural properties are listed in Table 9.13. A major drop in the applied load is observed around 2.5mm, after the maximum load has been reached. At this point major damage occurred in the material. After the first load drop, stress redistribution takes place and the load recovers to a second peak load lower than the previously attained maximum, while a second major drop is observed prior to failure.

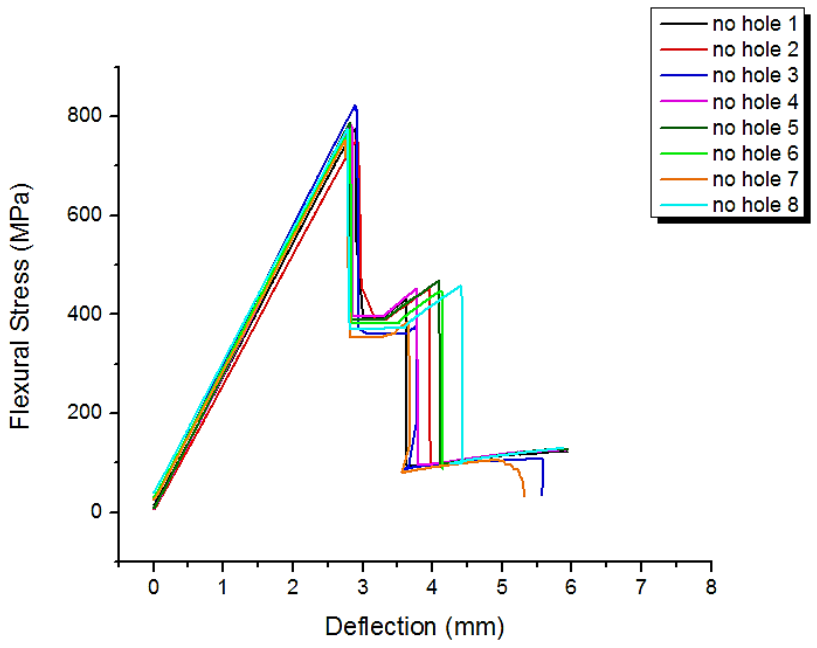

Figure 9.41: Flexural stress displacement plots for glass fibre epoxy samples without holes

Table 9.13: Main flexural properties of the glass fibre epoxy samples without hole

Sample	Maximum strength (MPa)	Flexural modulus of elasticity E_B (GPa)
no hole_1	773.88	25.088
no hole_2	753.58	24.91
no hole_3	822.98	26.40
no hole_4	783.42	26.51
no hole_5	787.24	26.42
no hole_6	772.88	25.56
no hole_7	752.05	25.01
no hole_8	774.45	26.07
Average	**777.56 ±20.8**	**25.75 ±0.64**

The drilled holes in the glass fibre epoxy samples are stress concentration points and their effect is considered for the calculation of the flexural stress. The maximum stress σ_{max} at the edge of the hole is calculated since this is the area where damage will initiate from.

For a rectangular plate with hole the average stress σ_{avg} is calculated according to the following expression [197]:

$$\sigma_{avg} = \frac{6M}{(b-d)h^2}$$

Where:

- $M = \frac{FL}{4}$ is the bending moment.

Therefore:

$$\sigma_{avg} = \frac{3FL}{2(b-d)h^2}$$

Where:

- F is the applied load
- L is the support span
- b is the width of the sample
- d is the diameter of the hole
- and h is the thickness of the sample

The maximum stress σ_{max} at the edge of the hole is:

$$\sigma_{max} = K_c \, \sigma_{avg}$$

K_c is the stress concentration factor

As shown in Figure 9.42, and according to the geometry of the sample, the stress concentration factor K_c is 2.15.

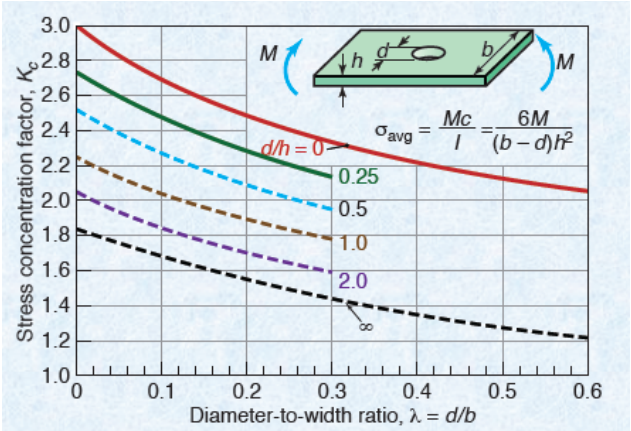

Figure 9.42: Stress concentration factors for rectangular plate with central hole under bending [197].

The maximum flexural stress σ_{max}-deflection plots for the samples with the hole are shown in Figure 9.43 while the main flexural properties are listed in Table 9.14. A sharp drop in the load is observed at 2.5mm after the maximum load has been reached. At this point catastrophic fracture occurred in the material. The presence of holes caused severe structural degradation since high stress concentration is introduced at their edges. Therefore, damage will initiate from these areas resulting in accelerated damage propagation. In addition to structural degradation, the presence of holes also reduced the flexural modulus of elasticity by 9.7% compared with the defect-free epoxy samples.

Damage may also have occurred by the bolts placed in the holes. As the sample was bent during loading, the head of the screw and supporting nut were pressed against the compressive and tensile face of the sample causing limited surface damage. However, the effect of the bolts on the performance of the material was minor compared with the effect of the holes. The structural degradation was predominantly controlled by the holes since they resulted in high stress concentration.

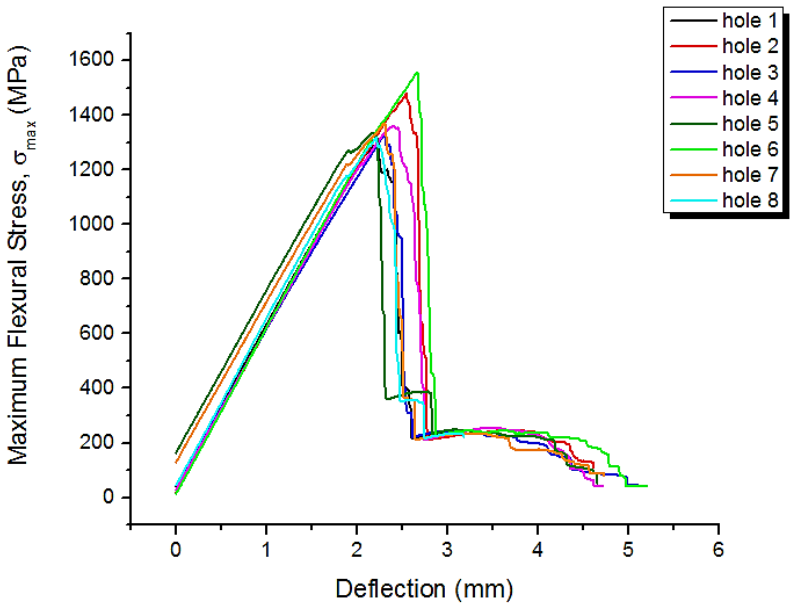

Figure 9.42: Maximum flexural stress σ_{max} at the edges of the hole.

Table 9.14: Main flexural properties of the glass fibre epoxy samples with hole.

Sample	Maximum flexural strength σ_{max} (MPa)	Flexural modulus of elasticity E_B (GPa)
hole_1	1297.30	23.28
hole_2	1479.08	23.460
hole_3	1327.93	21.943
hole_4	1359.73	23.6
hole_5	1334.27	23.34
hole_6	1557.22	23.41
hole_7	1369.68	23.07
hole_8	1315.95	23.92
Average	**1380.15 ±84.76**	**23.25 ±0.55**

9.4 Analysis of AE data recorded during the mechanical tests

AE testing was carried out during mechanical tests to record the AE signals generated arising from damage initiation and propagation. The efficiency of the AE technique in monitoring damage initiation and evolution, and its ability to discriminate between the different failure mechanisms are discussed in this section.

9.4.1 Analysis of AE data recorded during the tensile tests on vinyl-ester GFRP plates

Conventional monitoring of damage growth in materials and structures is commonly carried out by examining the evolution of the cumulative number of AE hits recorded. An alternative and more effective way in monitoring damage growth is the examination of the cumulative energy evolution during loading. Damage events like fibre fracture, matrix cracking and delamination result in generation of AE signals with high energy content, causing a sharp increase in the evolution of the cumulative AE energy plot. The use of energy in monitoring

the damage evolution in composite materials is also discussed in several studies [182, 187, 188, 198-202]. AE energy is the energy of the signal detected by the sensor. Strain energy is the elastic energy which is accumulated in the material before failure and is released in the form of stress waves. However, the plastic energy is absorbed by the material and is not released when failure occurs. AE is based on the detection of the elastic stress waves that are generated from localised sources releasing elastic strain energy during damage propagation.

Typical cumulative AE hits and cumulative energy plots with the stress-strain curve are shown in Figure 9.44. The tensile stress increases linearly with cumulative AE hits and AE energy increasing gradually with applied load. The cumulative hits evolution exhibits a smooth increase until failure. Prior to rupture the cumulative hits still increase smoothly but more steeply due to the increased generation of AE signals. It is clear that the cumulative hits plot cannot provide sufficient indication of damage growth. Therefore, the use of cumulative hits is not an effective methodology for monitoring damage evolution since the presence of unwanted noise signals can mask the evolution of the damage related AE signals.

The cumulative energy plot starts to increase linearly at around 150s up to 350s, indicating the point of damage initiation and slow damage growth. However, after 350s a sharp increase in the cumulative AE plot is observed indicating major cracking and rapid damage evolution with increasing load. Beyond 500s rupture is imminent as damage has developed considerably. Rupture is observed at the maximum load and identified as a steep and abrupt increase in the cumulative energy at 550s. Thus, using the evolution of cumulative energy is an effective method in motoring damage initiation and damage growth.

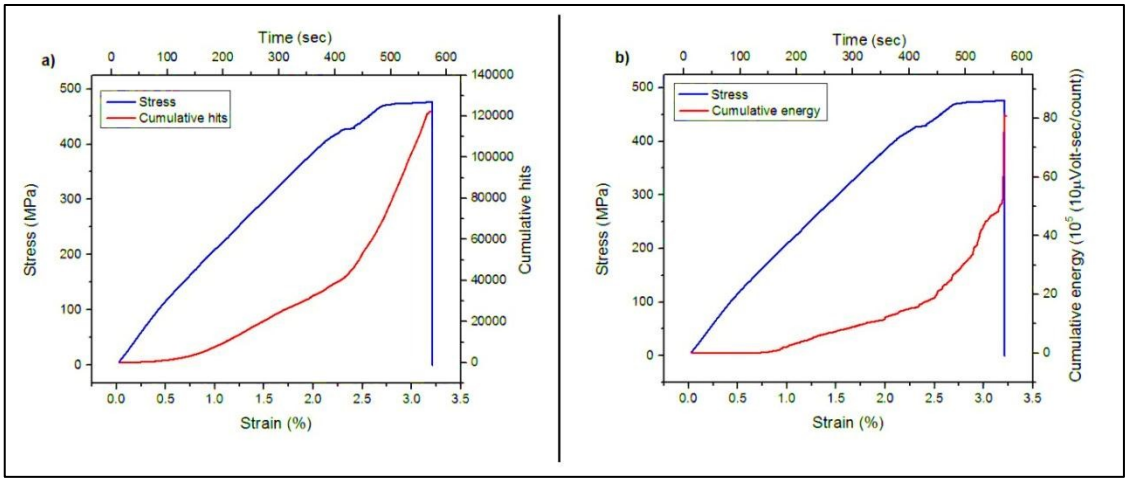

Figure 9.44: Stress-strain with a) cumulative AE hits and b) cumulative energy.

Figure 9.45 illustrates the evolution of the AE cumulative energy with increasing load for the samples made using resin infusion along the warp and fill directions. In the warp direction, the cumulative energy starts to increase at 200s. AE activity increases slowly until 320s. This slow and steady increase indicates low and steady damage growth rate. Beyond 320s, prior to rupture, abrupt and steep increase is observed in the cumulative AE energy graph indicating major and rapid damage evolution in the material.

In the fill direction the cumulative energy starts to increase earlier but steeper, at 100s, compared with the samples tested along the warp direction. The initial steep increase in the cumulative energy indicates the point of damage initiation and steady damage growth until 350s. Prior to rupture, sudden increase in the cumulative AE energy indicates rapid damage progression.

The cumulative energy plots for both samples increase steadily. Sudden increase in the cumulative energy is observed whenever major damage and cracking events occur with increasing load. The sudden and steep increase in the cumulative energy does not only

indicate major cracking and rapid damage growth, but provides warning of imminent rupture.

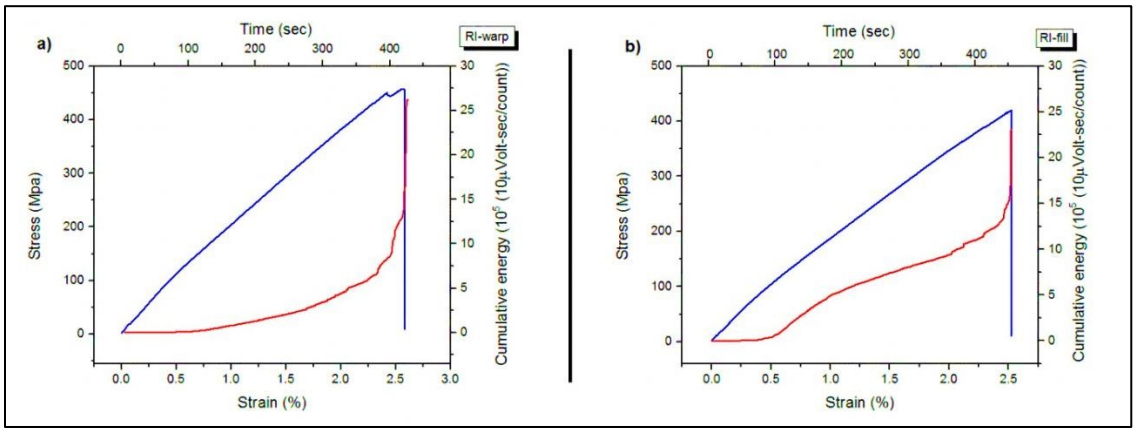

Figure 9.45: Typical stress-strain and cumulative AE energy evolution for a resin infusion sample tested in a) warp and b) fill direction.

The steep and sudden increase in the energy graph whenever major cracking occurred could also be visually observed in the videos recorded during the tests. Figure 9.46 shows a typical cumulative energy plot and corresponding images isolated from the videos where major damage is clearly visible. The images show the damage progression at certain times on the recorded video and are linked to the cumulative energy plot. Visible damage progression occurred whenever a sudden increase in the cumulative energy was observed.

Initial damage is observed at 320s. This damage event is related to the initial steep increase in the cumulative AE energy plot at the same exact time. As damage grows at 390s, a sharp increase in the cumulative AE energy is also observed. More damage zones are created which in turn generate high energy AE signals. Damage growth results in further increase in the cumulative energy until final rupture occurs.

The presence of defects such as voids results in multiple damage zones causing early damage growth and more rapid evolution compared to a defect free test piece. The generation of multiple damage zones in the material provides an easy cracking path. The main damage mode prior to rupture is longitudinal matrix cracking combined with rapid fibre breakage, and interface failure between the 0^{o} and 90^{o} fibre layers. This accelerates uncontrollable damage growth in the surviving areas of material, which cannot sustain further loading eventually resulting in final failure.

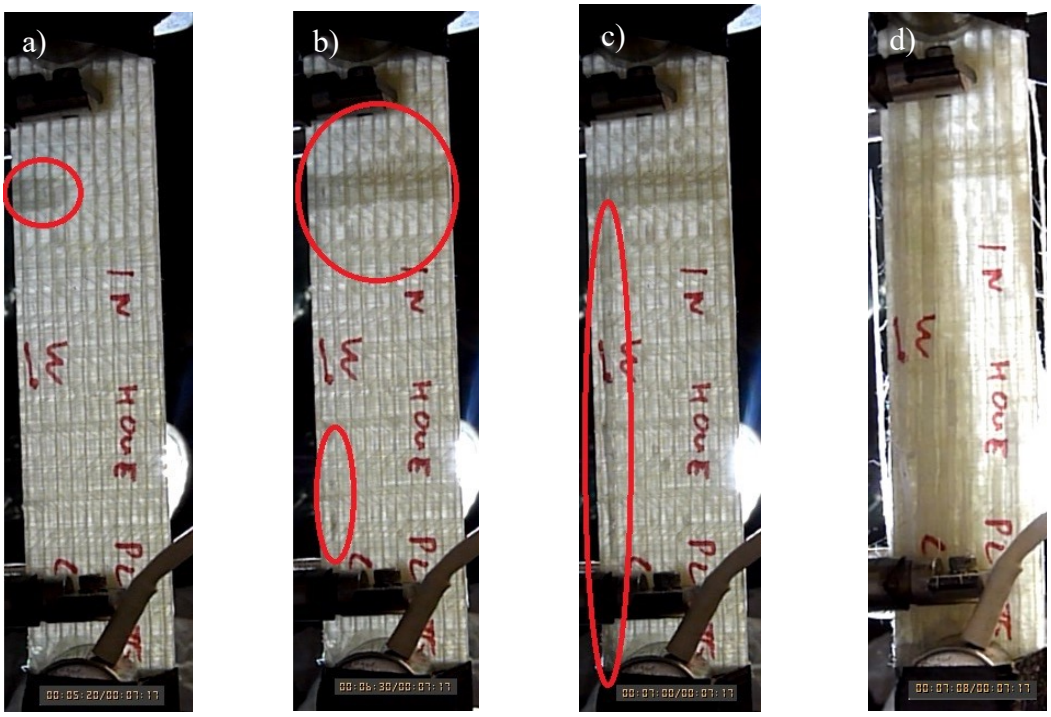

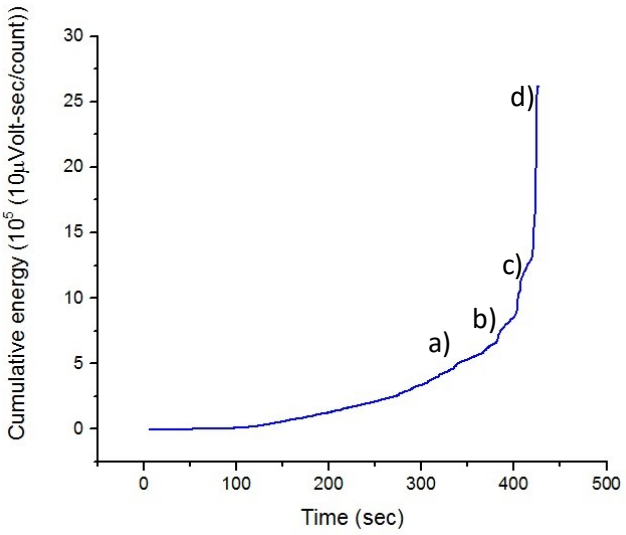

Figure 9.46: Damage at a) 5.20 min, b) 6.30 min, c) 7.00 and d) failure, and cumulative energy.

Major damage events consist of a mixture of different failure modes such as matrix cracking, rapid fibre breakage and longitudinal matrix cracking. However, other failure modes such as fibre matrix interfacial decohesion and fibre fracture can also take place before any damage becomes visible. Non-visible damage evolution can generate AE signals with high energy. Such AE signals can be used to monitor damage growth even at the initial stages of damage evolution.

Figure 9.47 illustrates the evolution of the AE cumulative energy and load for the Shipyard_B samples. It can be clearly seen that in the warp direction the cumulative energy starts to gradually increase at 150s until 420s. After 420s a steep increase is observed in the cumulative energy until rupture occurs. In the fill direction the cumulative energy evolution starts to gradually increase earlier, at 100s until 350s. After 350s a sudden increase in the cumulative energy is observed indicating rapid damage growth prior to rupture. Similarly to

the samples made with resin infusion, the second batch of the shipyard samples exhibit steady damage growth for both fill and wrap direction. However, damage initiates earlier and evolves faster compared with the resin infusion samples.

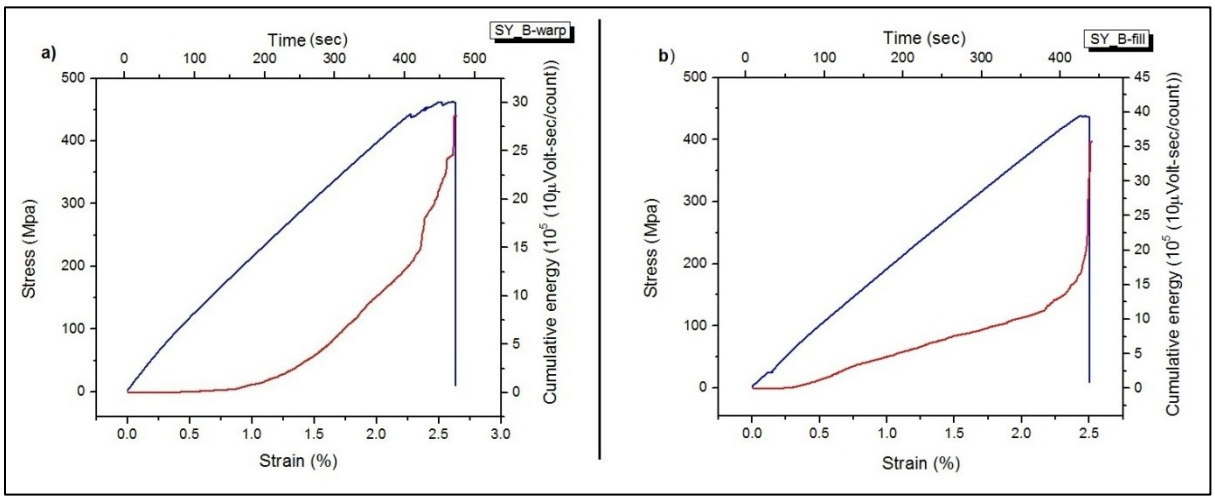

Figure 9.47: Typical stress-strain and cumulative AE energy evolution for a Shipyard_B sample tested in a) warp and b) fill direction.

The evolution of the AE cumulative energy and load for the Shipyard_A samples in both warp and fill direction is presented in Figure 9.48. For both warp and fill samples the cumulative energy starts to increase steadily at 100s. This slow and steady increase indicates slow and steady damage growth. Similarly to the previous type of samples, prior to rupture a sudden and steep increase is observed in the cumulative energy. However, damage grows at a faster rate in the fill samples prior to failure as steeper and more sudden rises in the cumulative energy are observed compared with the warp direction. The high void content in the Shipyard_A batch causes significant structural degradation resulting in early damage initiation and growth. As a result, the cumulative energy plots for both warp and fill direction exhibit similar evolution and gradual increase with increasing load until failure.

Shipyard_A samples exhibit gradual damage growth. However, due to their highest void content, they also exhibit earlier damage initiation compared to both resin infusion and Shipyard_B samples.

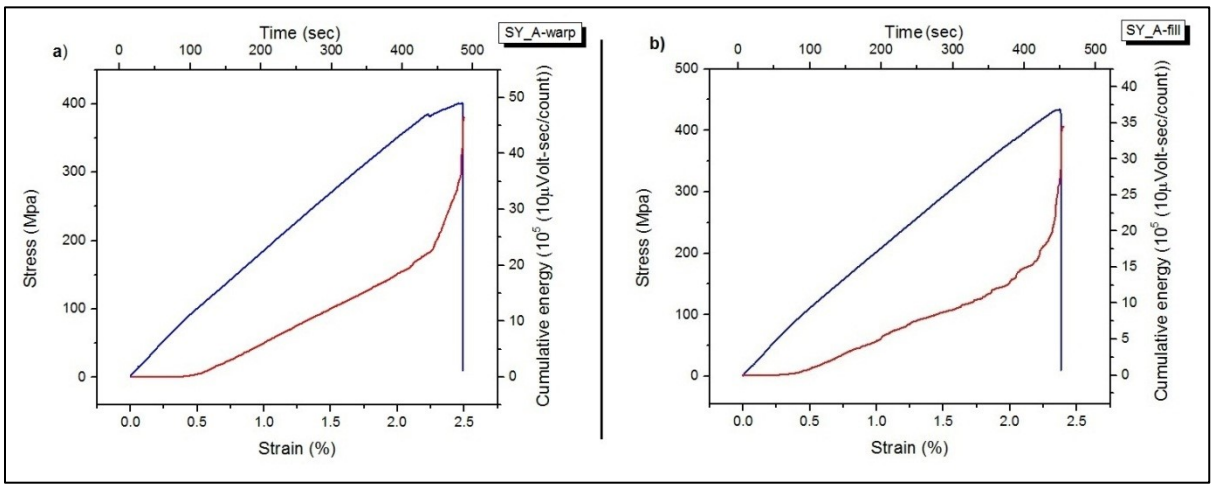

Figure 9.48: Typical stress-strain and cumulative AE energy evolution for a Shipyard_A sample tested in a) warp and b) fill direction.

Figure 9.49 presents the cumulative energy graphs for the different types of composite samples tested along the warp and fill direction. Damage initiates earlier in the fill direction for all the samples due to the lower fibre content parallel to the loading direction. The samples made using resin infusion exhibit damage initiation later together with slower propagation in comparison with the Shipyard samples. It can be safely concluded that the superior strength of the low void content of the samples made using resin infusion result in a slow damage evolution rate. On the other hand both of the Shipyard samples with high void content, exhibit earlier damage initiation and faster damage growth, since their cumulative energy graphs increase more rapidly during the stage of steady damage growth. From Figure 9.49 it can be seen that the heavily voided Shipyard_A samples exhibit earlier damage initiation and significant propagation rate compared with the rest of the samples.

The total cumulative energy for the samples made with resin infusion was the lowest compared with those from the Shnipyard_A samples exhibiting higher energy values at failure. Due to the lack of voids, damage evolution was slow and a reduced amount of high energy AE signals was generated. The generation of damage zones was initially required to produce damage growth with further loading. Prior to failure rapid damage growth occurred on the previously generated damage zones causing a steep increase in the cumulative AE energy graph. This is a key reason why the cumulative energy of the void free samples exhibited slow evolution up to the point of imminent rupture where energy increased more sharply compared with both Shipyard sample types. The presence of voids caused early failure and rapid damage evolution generating high energy AE signals. Therefore, the cumulative energy of the voided samples exhibited a rapid increase during the steady damage growth stage. Prior to rupture severe structural degradation already occurred and less extended major cracking events are therefore required to cause the catastrophic failure of the sample.

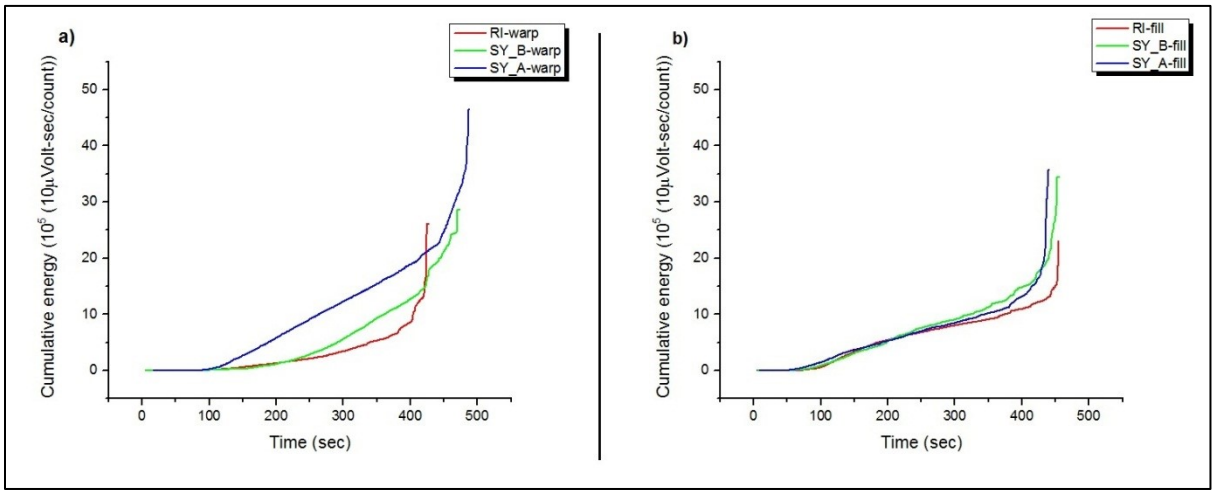

Figure 9.49: Comparison between the cumulative energy of the different types of samples for the warp and fill direction.

9.4.2 Analysis of AE data recorded during the bending tests on vinyl-ester GFRP plates

To further investigate the capability of AE testing in monitoring damage growth under bending conditions, AE testing was carried out during the bending tests of the composite samples. The evolution of the cumulative energy and applied flexural stress for the vinyl-ester composites are shown in Figure 9.50 a-c. From these graphs it is clear that the evolution of the cumulative energy is silent at the early stages of loading, while significant and sharp AE energy accumulation starts around the peak load.

The cumulative energy for the sample made with resin infusion starts to increase at 2.5mm after an initial silent stage, while the AE energy for the Shipyard_B and A samples increases at 1.5mm and 1mm respectively. In comparison with the voided plates, the energy accumulation in the void-free samples occurs at a later stage, indicating later damage initiation. All tested samples exhibit sharp rise in the cumulative energy occurring simultaneously with sudden load drops. Sudden drops are caused by major damage events such as delamination and cracking resulting in generation of high energy AE signals accompanied with a dramatic increase in the cumulative energy. After the first load drop, stress redistribution takes place and load recovers until the next drop. Subsequent drops in the applied load are followed by simultaneous sharp increases in the cumulative energy indicating further damage growth.

As it can be seen in Figure 9.50a, the cumulative energy for the void free sample made with resin infusion starts to increase at 2.5mm after an initial silent stage. During this stage the accumulation of AE energy is negligible since no damage occurs. The initial increase in the cumulative energy indicates damage initiation. After 3mm sharp rises are observed in the

cumulative energy graphs occurring simultaneously with sudden drops in the load. This may indicate that a major damage event such as delamination may have occurred. The applied load then recovers and cumulative energy increases steadily up to a displacement of 3.2mm were a sharp increase is observed in the cumulative energy. This indicates further damage growth and possibly the activation of other damage modes like transverse cracking and fibre fracture.

The effect of voids on damage initiation and evolution is observed in the cumulative energy measured for the voided samples (Figure 9.50b and 9.50c). For the Shipyard_B samples with a void content of 6 % earlier damage initiation occurs as the AE energy accumulation starts at 1.5mm and increases gradually until 2.2mm. After 2.2mm sharp increase is observed in the cumulative energy indicating damage growth occurring at an earlier stage compared with the void-free composite samples. In the Shipyard_A samples with a void content of 10%, the cumulative energy starts to increase at an early stage. Rapid increase starts after a displacement of 1mm. Delamination and major damage events are identified as subsequent dramatic increases in the cumulative energy. Due to the severe structural degradation caused by the high void content, the heavily voided composite samples experience earlier damage initiation and higher damage growth in comparison with the rest of the vinyl-ester composites.

Void-free samples exhibit a more gradual increase in the cumulative AE energy. For these samples a longer initial silent stage is observed with the AE energy accumulation remaining negligible up to the highest deflection point. This is explained by the fact that the void-free samples exhibit superior structural integrity in comparison with voided samples.

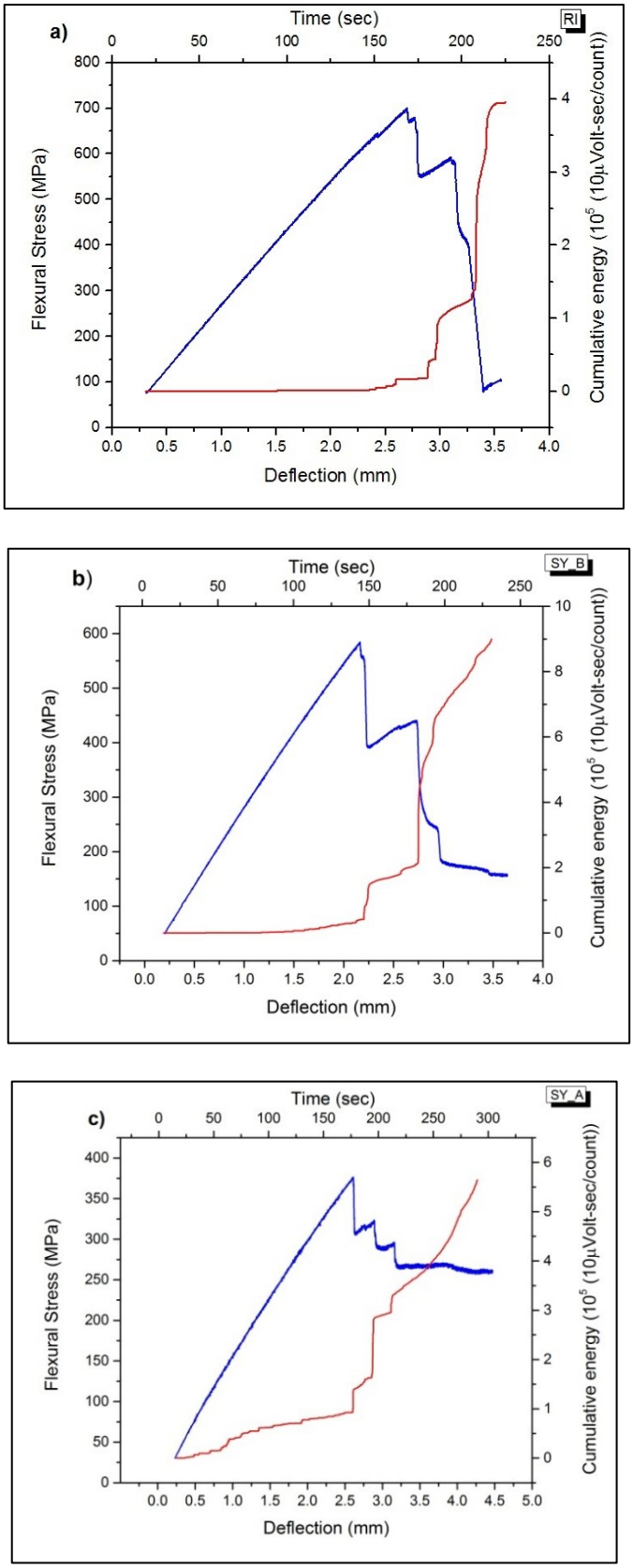

Figure 9.50: Flexural stress and cumulative AE energy for a) resin-infusion, b) Shipyard_B and c) Shipyard_A samples.

9.4.3 Analysis of AE data recorded during the bending tests on epoxy GFRP pre-preg plates cured in the autoclave

AE testing was also performed on both structurally sound and drilled glass fibre epoxy samples made with pre-preg preforms under three-point bending. The evolution of the cumulative energy and applied flexural stress for the epoxy samples without holes and for the drilled samples are shown in Figure 9.51a and 9.5b respectively. From these graphs, it is clear that there is no evolution in the cumulative energy at the early stages of loading. No damage related AE activity is generated until the peak load is reached. At this point significant AE energy accumulation is observed. Similarly to the vinyl-ester samples sharp drops in the applied load occur simultaneously with dramatic increases in the cumulative AE energy.

For the structurally sound sample without holes, major damage occurs suddenly causing sharp increase in the cumulative energy at 3mm after a silent stage of low AE activity. No damage occurs until the defect-free sample reaches its maximum strength. At the maximum stress the material cannot sustain further loading and fails suddenly giving rise to highly energetic AE signals. A subsequent drop in the flexural stress and a sharp increase in the AE energy indicate damage growth of the previously generated damage zone.

The glass fibre epoxy composites made with glass fibre pre-pregs exhibit superior strength compared to the vinyl-ester samples. The superior structural integrity of the epoxy samples results in damage initiation only after the peak load has been reached. No damage occurs at the early stages of loading.

For the epoxy samples with holes, damage initiation is observed at 2mm since a small increase is observed on the cumulative energy graph. After the damage initiation a dramatic increase in the cumulative energy occurs earlier at 2.5 mm indicating a serious damage event. The total cumulative energy for the drilled samples is significantly higher compared with the defect free epoxy composites exhibiting lower AE energy accumulation at failure. The drilled region causes early damage initiation and evolution resulting in increased AE activity. As the sample was bent during testing, the head of the screw and supporting nut were pressed against the compressive and tensile face of the sample causing limited compressive surface damage. This minor damage is related to the slow and steady increase in the cumulative energy that occurs after the major drop in the applied load.

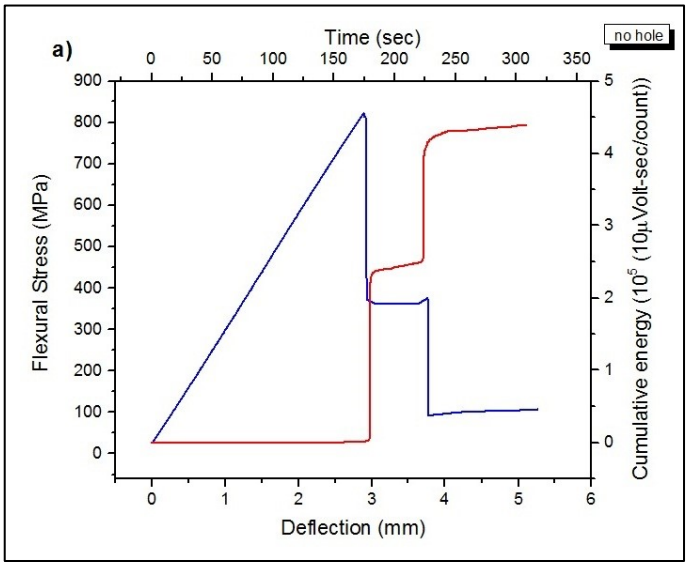

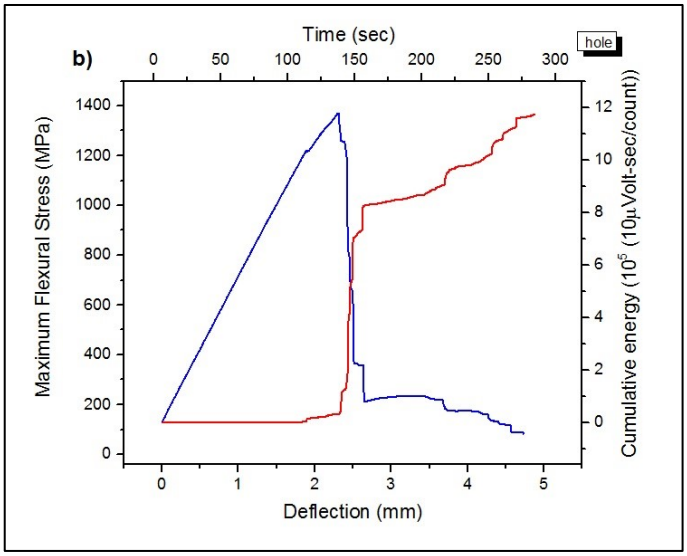

Figure 9.51: Flexural stress and cumulative AE energy for a) defect-free and b) drilled epoxy sample.

From the AE results discussed above it can be seen that when failure occurs in the material high energy AE signals are generated causing a steep increase in the cumulative energy evolution graph. By examining the energy evolution it is possible to assess if damage initiation has occurred and monitor damage growth. These sudden and sharp increases in the cumulative energy become more distinctive when damage has grown significantly prior to failure. As a result it can be safely concluded that imminent failure can be predicted by examining the AE energy accumulation. In general, cumulative energy is a useful AE signal feature for evaluating damage growth. However, additional AE signal features such as risetime, duration counts and counts to peak can also provide useful information.

9.5 Analysis of acoustic emission data using automated data clustering algorithms

9.5.1 Introduction

In this chapter data clustering is carried out using the K-means, Forgy, ISODATA and LVQ algorithms. The clustering method is based on multi-parameter analysis of AE signals collected from tensile and bending tests on glass fibre reinforced composite samples. The effectiveness and performance of the clustering algorithms has been assessed, while clustering results are compared to the manual filtering of the recorded AE signals.

9.5.2 Evaluation of the performance of commonly applied clustering algorithms

Data clustering was performed to group the AE signals generated from the different damage modes into separate clusters. Key AE signal parameters are used to cluster the AE signals based on different features. Before the clustering algorithms are run the signal parameters to be included in the clustering process must be defined. In this work the automated clustering method is based on the analysis of duration, risetime, counts, counts to peak and energy of individual AE signals recorded. The analysis of these signal features has been considered in several other studies [119, 152, 178-186].

Before the clustering procedure starts the number of the resulting clusters must be known in advance. Each one of the resulting clusters must be assigned to a certain failure mode in order to monitor the evolution of the different types of damage and ascertain the characteristics of

their key AE signal features. In addition to the damage-related clusters, noise signals are included in the clustering process and are grouped into a separate cluster. In many studies though, noise is not taken into consideration in the clustering methodology and the monitoring process of structural degradation is not effective since increased amounts of noise signals can be contained within the failure-related clusters. During AE testing a large volume of unwanted noise signals can be recorded having a seriously adverse effect in subsequent analysis. Noise signals must be initially identified and separated from the damage-related signals. Herewith, four clusters are expected arising from fibre fracture, matrix cracking, interface failure, and noise respectively.

To reduce the amount of noise, front-end filters are commonly applied during the acquisition. However the use of filters cannot eliminate completely noise signals in the measurement, while the detection of damage-related signals can be reduced in cases where over-filtering is applied. By grouping the noise signals into clusters it is possible to obtain their main signal features and establish a post-acquisition filtering methodology that can eliminate them improving the quality of the results obtained.

To perform effective clustering analysis, an appropriate algorithm has to be selected. The effectiveness of different clustering algorithms in grouping the various types of AE signals into clusters, can be compared under control testing conditions. Herewith, for direct comparison the data clustering algorithms have been applied on AE signals recorded during the tensile testing of a composite sample made using resin infusion. The clustering results consist of the cumulative hits and cumulative energy evolution for each cluster. The clustering results for k-means, Forgy, ISODATA and LVQ are shown in Figures 9.52-9.55.

The number of hits, total energy, cumulative hits percentage and energy percentage for each cluster and algorithm are shown in Table 9.15.

The k-means, Forgy and ISODATA algorithms have generated clustering results which primarily consist of one large cluster and three significantly smaller groups of AE signals. As seen from the energy evolution plots, large clusters such as the #1 and #2 consist of low energy signals since their overall energy is small. However, clusters with far fewer hits consist of high energy AE signals, which increase dramatically the corresponding cumulative energy. These highly energetic signals are related to major damage events. The large cluster containing low energy signals is related to general noise, friction and echoes. The low overall AE energy of the unwanted noise signals has been reported by Doan et al. [202]. From Table 9.15, it can be seen that the large cluster has the lowest energy content and occupies the greatest part of the original AE dataset. Consequently, the original datasets primarily consist of unwanted noise signals, which needed to be identified and separated from the damage related signals.

The k-means algorithm clustering results show that the low energy noise signals makes up 43.22% of the entire dataset. Low energy levels have been assigned to clusters #2 and #3 which are responsible for the 1.45% and 9.98% respectively of the total energy and can be related to different failure modes. High energy accumulation representing 87.63% of the overall energy has been assigned only to cluster #4. This becomes active towards the end of the test and is related to signals arising from major damage events. Due to the large differences in the cumulative energy between the damage-related clusters it can be concluded that the clustering results of the k-means are not entirely satisfactory for monitoring damage

growth. Improved clustering results for complicated AE data can be achieved using algorithms with additional features that result in a better control over the clustering process.

Forgy improves clustering results as it separates the noise signals more effectively resulting in a more balanced energy distribution between the different damage related clusters. It is clear that the cluster #4 has the highest energy, but the clusters #2 and #3 exhibit significantly higher energy accumulation compared to the k-means. Therefore, improved monitoring of the evolution of the different damage modes can be achieved using the Forgy algorithm. However, as it can be seen in Table 9.15, the noise cluster occupies the 80.53% of the overall AE dataset. This large cluster can contain significant amount of useful signals, which have been assigned to the noise-related cluster. As a result significant information related to the monitoring of the true damage growth will be eventually lost if the noise-related cluster is filtered out. Due to the false allocation of damage-related signals to the noise cluster, it can be safely concluded that the use of the Forgy algorithm cannot greatly improve the effectiveness of AE testing in monitoring damage evolution in GFRP materials under load.

The clustering results can be further refined by using ISODATA as it separates noise signals more effectively and results in improved energy distribution between the damage related clusters in comparison with k-means and Forgy. As seen from Table 9.15, cluster #4 has the highest energy, but clusters #2 and #3 exhibit considerably higher energy accumulation compared with Forgy, representing 13.48% and 21.88% of the overall AE energy respectively. The noise signals have been separated more efficiently as they represent 67.85% of the dataset and 1.34% of the overall AE energy. Compared to Forgy, the smaller size of the noise cluster indicates that less useful signals have been assigned to the noise cluster and therefore limited loss of damage-related signals will occur if the noise cluster is filtered out.

From the cumulative energy evolution plots for the different types of clusters shown in Figure 9.54, it can be seen that low energy AE signals have been assigned to the noise cluster only, while the damage-related clusters consist of high energy signals that increase sharply. The use of the ISODATA algorithm can greatly improve the effectiveness of AE testing during continuous evaluation of the structural degradation in composite materials. The ISODATA performs best in comparison with the other algorithms considered and is used to effectively monitor the evolution of the different damage modes. Despite the satisfactory clustering results of this algorithm, the clusters can have similar signal features and a clear differentiation between them can often be difficult and complicated. Furthermore some of the damage-related clusters can consist of mixed damage modes occurring simultaneously and generating AE signals with similar features.

The LVQ algorithm has also been considered in the clustering process but it performed poorly leading to ineffective clustering. From Table 9.15 it can be seen that it assigns the 97.75% of the signals to one cluster only while other clusters consist of very few signals. This happens because the LVQ has a weighting factor, which assigns AE signals to the largest group in the dataset. Since the original dataset consists of high amounts of noise, high amounts of damage-related AE signals will be assigned to the noise cluster. Despite the large discrepancies in the cluster size, all the clusters have similar energy content. Therefore it can be seen that the monitoring of damage growth and the discrimination between the noise and the different failure modes is unrealistic and even impossible with such clustering results.

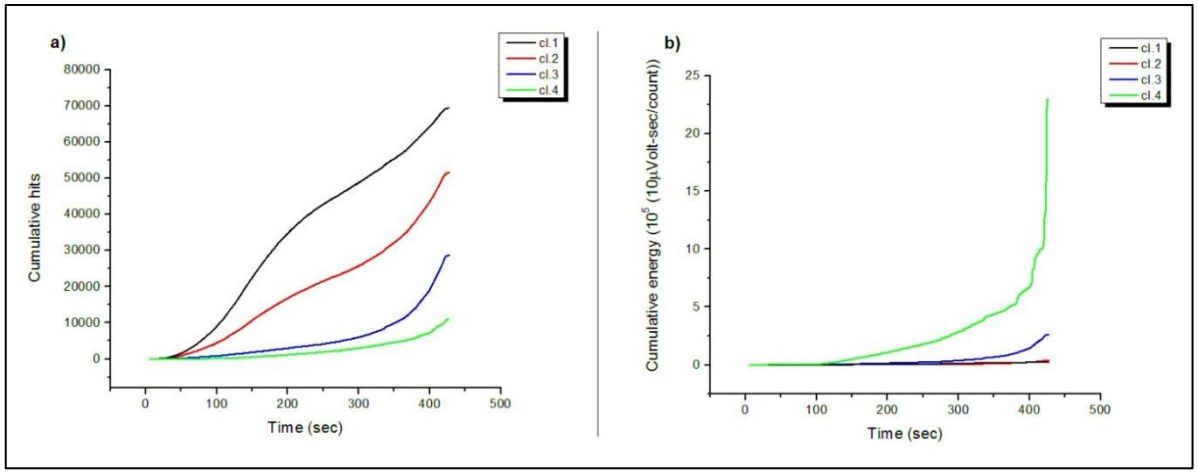

Figure 9.52: k-means clustering results

a) Cumulative hits and b) cumulative energy for the different clusters

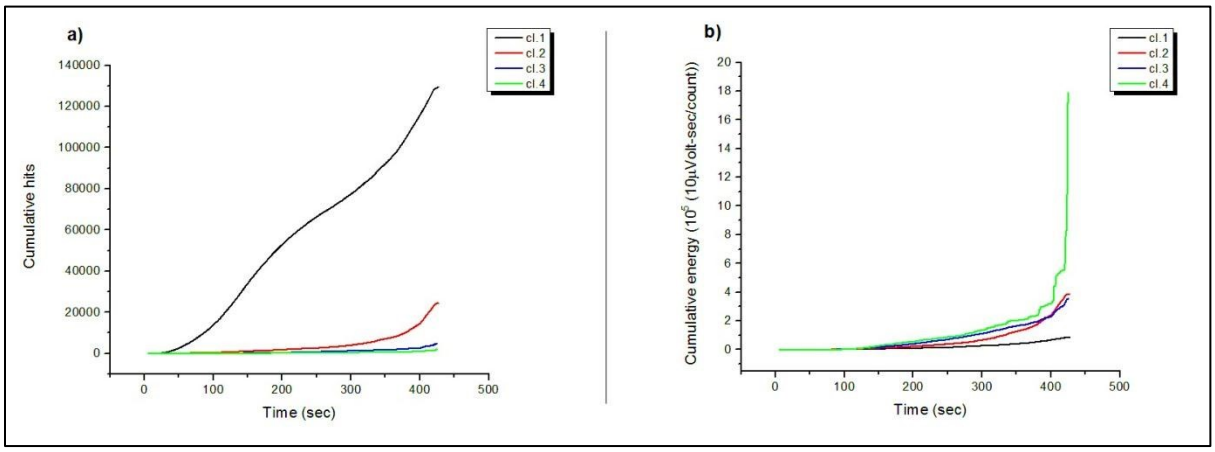

Figure 9.53: Forgy clustering results

a) Cumulative hits and b) cumulative energy for the different clusters.

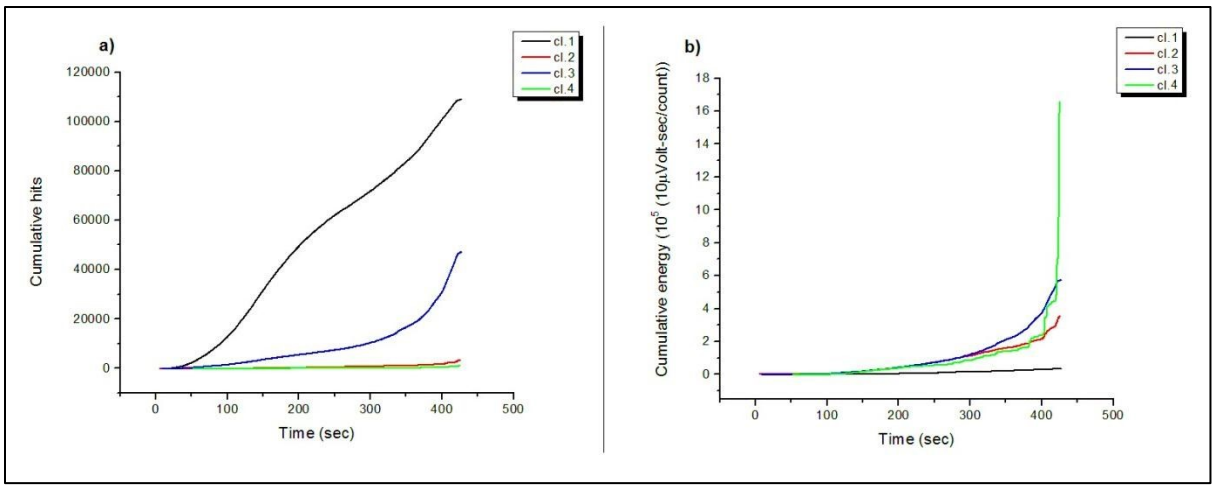

Figure 9.54: ISODATA clustering results

a) Cumulative hits and b) cumulative energy for the different clusters.

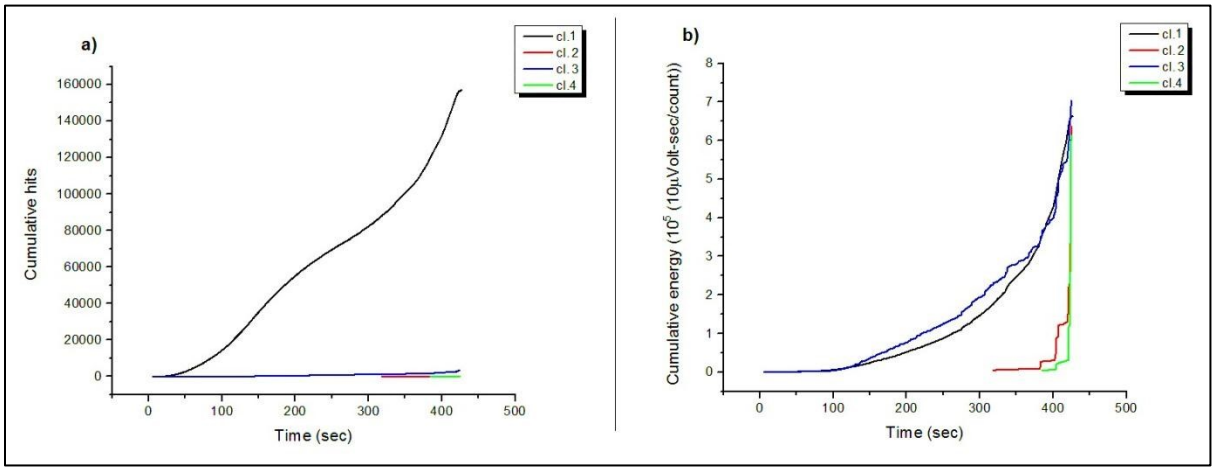

Figure 9.55: LVQ clustering results

a) Cumulative hits and b) cumulative energy for the different clusters

Table 9.15: Cumulative AE hits and energy for the different clusters and for each clustering algorithm

K-means				
Cluster	Cumulative hits	Cumulative energy 10^5 (10μ Volt-sec/count)	Cumulative hits percentage	Energy percentage
Cluster 1	69459	0.246	43.22 %	0.94 %
Cluster 2	51551	0.380	32.1 %	1.45 %
Cluster 3	28638	2.610	17.82 %	9.98 %
Cluster 4	11038	22.928	6.86 %	87.63 %
Total	**160686**	**26.164**	**100 %**	**100 %**
Forgy				
Cluster	Cumulative hits	Cumulative energy 10^5 (10μ Volt-sec/count)	Cumulative hits percentage	Energy percentage
Cluster 1	129413	0.8571	80.53 %	3.27 %
Cluster 2	24437	3.867	15.21 %	14.78 %
Cluster 3	4796	3.557	2.98 %	13.6 %
Cluster 4	2040	17.884	1.28 %	68.35 %
Total	**160686**	**26.164**	**100 %**	**100 %**
ISODATA				
Cluster	Cumulative hits	Cumulative energy 10^5 (10μ Volt-sec/count)	Cumulative hits percentage	Energy percentage
Cluster 1	109041	0.351	67.85 %	1.34 %
Cluster 2	47118	3.528	29.33 %	13.48 %
Cluster 3	3337	5.724	2.08 %	21.88 %
Cluster 4	1190	16.561	0.74 %	63.3 %
Total	**160686**	**26.164**	**100 %**	**100 %**
LVQ				
Cluster	Cumulative hits	Cumulative energy 10^5 (10μ Volt-sec/count)	Cumulative hits percentage	Energy percentage
Cluster 1	157071	6.626	97.75 %	25.32 %
Cluster 2	133	6.374	0.083 %	24.36 %
Cluster 3	3409	7.035	2.12 %	26.89 %
Cluster 4	73	6.129	0.047 %	23.43 %
Total	**160686**	**26.164**	**100 %**	**100 %**

9.5.3 Automated data clustering on AE signals recorded during the tensile tests on vinyl-ester GFRP plates

The clustering results from the tensile tests on void free samples are shown in Figure 9.56. As it was discussed in section 9.5.2, cluster #1 is associated with unwanted AE noise activity. This cluster has the largest size and also exhibits the lowest energy accumulation. In contrast, cluster #4 has the smallest size but has the highest energy content and exhibits sharp increases in the cumulative energy plot when major damage initiates and propagates in the material. This class is associated with major cracking generating high energy AE signals prior to failure. Since this class is more active prior to failure, it can consist of mixed damage modes such as matrix cracking, longitudinal matrix splitting and fibre fracture. As shown in Figure 9.46, major damage events such as matrix cracking, longitudinal matrix cracking and fibre fracture have been visually observed during the analysis of videos recorded. Therefore, it can be clearly concluded that cluster #4 is related to these damage modes.

Cluster #2 has relatively low number of AE cumulative hits and energy content. The cumulative energy plot increases gradually until rupture. This cluster is associated with fibre fracture occurring during the tests. The composite coupons consist of thousands of fibres. However, due to rapid and multiple fibre fracture happening simultaneously, it is not possible for the AE system to record every fibre fracture event. In addition, according to an analysis that has been presented by Kempf et al. [187], low amounts of fibre breakage compared with the interface failure signals indicates minor load transfer from the matrix to the fibres and a weak interface. Interfacial debonding leads to crack propagation and localised damage. Multiple interfacial failure and cracking indicates local stress relaxation and damage growth.

Nonetheless, a significant load transfer to the fibres is maintained, resulting in fibre fracture events [187].

Cluster #3 shows increased AE activity compared with clusters #2 and #4. Increased generation of these signals is observed at around 400s prior to failure. This cluster can be mostly associated to fibre/matrix interfacial failure between the fibres of the fabric perpendicular to the loading direction. Similar cluster evolution and cluster identification have been reported by Kempf et al. [187], while clusters associated with missed damage modes have also been reported in past studies [203]. Clusters #1, #2, #3 and #4 will hereafter be referred as noise, fibre fracture, interface failure and matrix cracking respectively. By examining the overall evolution of the different clusters it is possible to assess the failure behaviour of the material and to determine when failure is imminent during loading.

Representative clustering results, which have been obtained from the analysis of AE data obtained from the void-free and highly voided samples tested, are shown in Figures 9.56-9.58. For all types of composite samples tested in tension, it can be seen that damage initiates by fibre/matrix interfacial failure followed by fibre failure and matrix cracking. All clusters exhibit parallel evolution but differences in the cumulative energy recorded can indicate variations in the failure behaviour of the glass fibre composite plates tested in tension. The highest energy accumulation is observed for the matrix cracking-related cluster which is more active prior to failure. When increased AE activity is generated from this cluster, significant structural degradation has already occurred in the material and imminent failure is indicated by accelerated steep increase in AE energy accumulation in the matrix cracking cluster.

For the void free samples the AE cluster which is associated with interface failure has higher energy accumulation compared with fibre fracture signals. Therefore, interface failure is the main damage mechanism that is most active under loading. At the same time, fibre fracture takes place as the structural integrity of the sample gradually deteriorates until critical matrix cracking occurs. For the Shipyard_B samples the cumulative energy for the matrix cracking-related cluster starts to increase rapidly from an early stage. Energy accumulation for the fibre breakage cluster is much higher compared with the resin infusion sample. Due to the structural degradation caused by the high void content, early damage initiation and rapid damage growth are observed. Damage starts with matrix cracking at the early stages of loading, and rapidly results in increased fibre fracture events. Compared to the resin infusion sample, matrix cracking and fibre breakage are the main damage mechanisms, while interface debonding shows low activity. For the Shipyard_A samples which suffer from the highest void content compared with the rest of the samples, damage initiates at an early stage with matrix cracking. The cumulative energy for the matrix cracking cluster starts to increase rapidly until failure. The rapid matrix cracking is followed by fibre breakage and interface failure growing rapidly until failure. By examining the energy evolution of the resulting clusters in Figure 9.58 it can be seen that fibre fracture and interface debonding have similar energy accumulation. Therefore, interface failure and fibre fracture are both active under increasing load. Due to severe structural degradation that is caused by the high void content, the sample cannot sustain high loads and damage initiates at low loads. It can then be concluded that in comparison with the rest of the test samples, all expected damage modes are active in the heavily voided Shipyard_A samples during the mechanical testing.

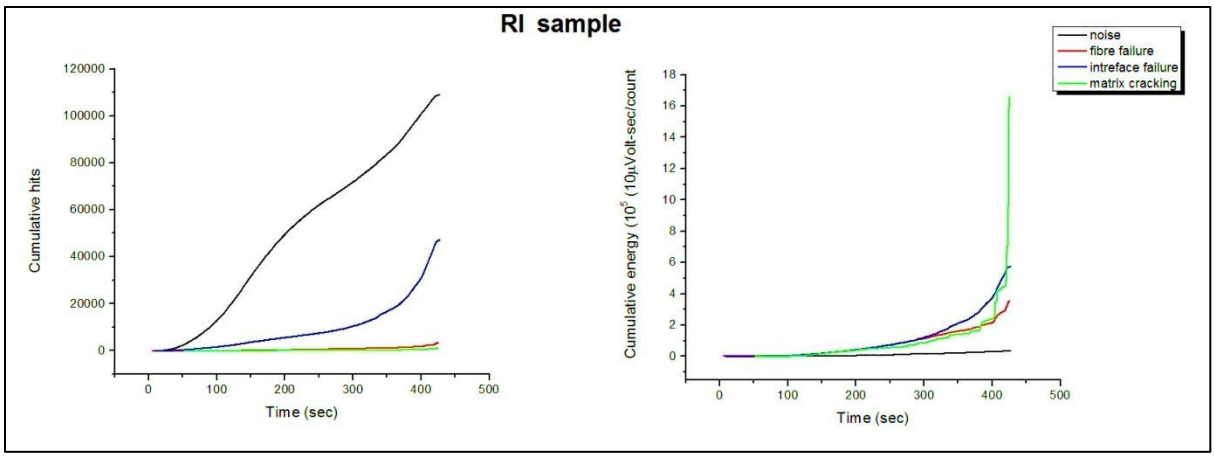

Figure 9.56: Cumulative hits and cumulative energy evolution of the AE clusters for a resin infusion sample.

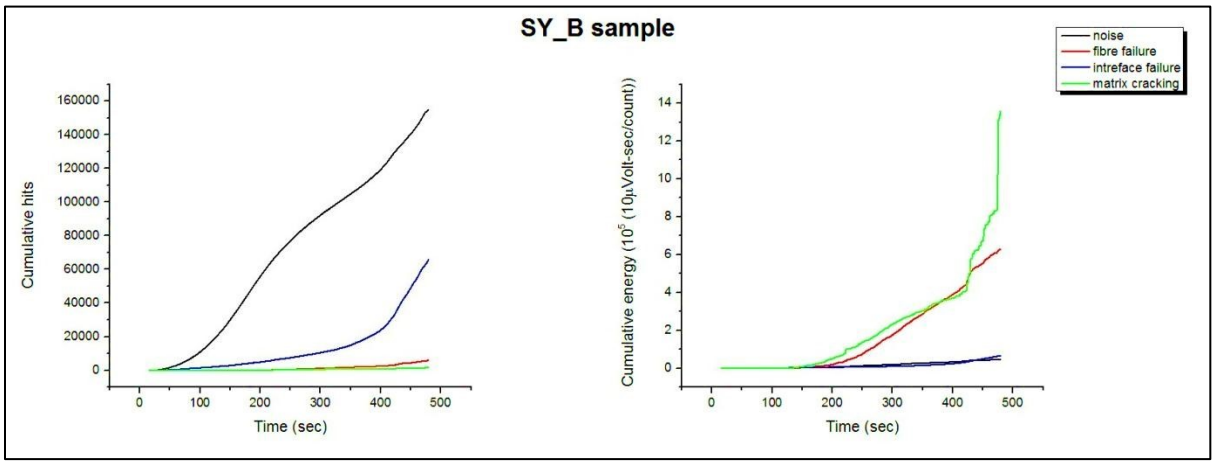

Figure 9.57: Cumulative hits and cumulative energy evolution of the AE clusters for a Shipyard_B sample

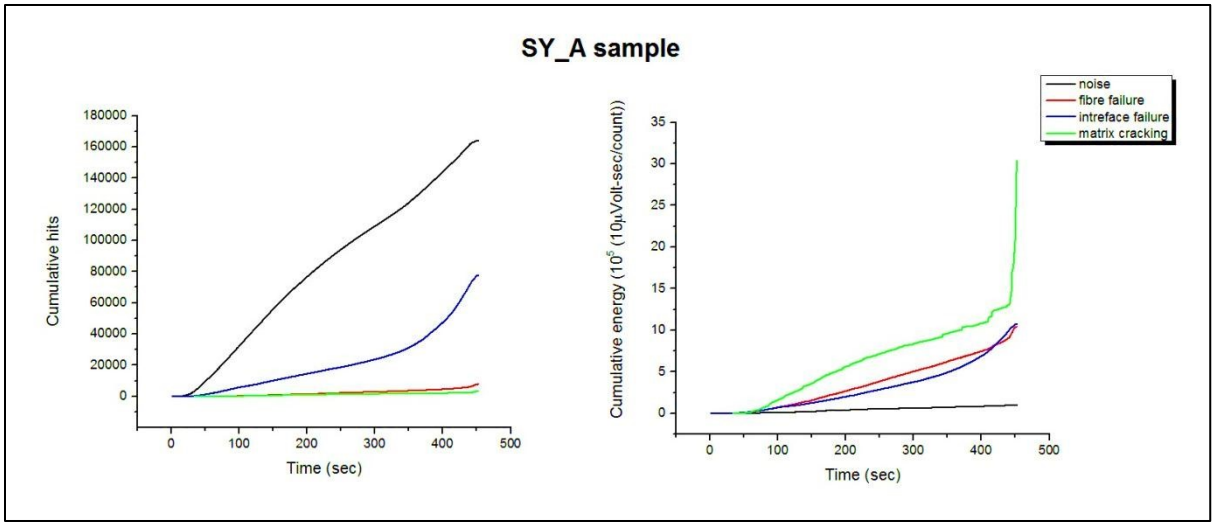

Figure 9.58: Cumulative hits and cumulative energy evolution of the AE clusters for a Shipyard_A sample

The statistical characteristics of the key signal features for each cluster are shown in Table 9.16. It can be seen that the cluster #1 which is associated with unwanted noise signals exhibits mainly low energy, duration and rise time values. By determining the characteristics of the noise signals it is possible to apply suitable filters during the acquisition in order to limit unwanted signals and improve the efficiency of the AE monitoring. The interfacial failure (cluster #3) signals exhibit relatively higher energy, duration and risetime signals in comparison with the noise-related cluster. The identification of fibre-matrix interfacial failure signals can be useful during acquisition as their increased generation can indicate the subsequent evolution of more severe failure modes like fibre fracture and matrix cracking.

In contrast to clusters #1 and #3, clusters related with fibre fracture and matrix cracking exhibit considerably higher AE energy, duration, and risetime values, due to the high strain energy released during major damage. The key difference between cluster #4 and cluster #2 is mainly observed on the considerably higher counts and counts to peak values of the cluster #4 AE signals. The determination of the AE signal characteristics associated with major

damage events can provide evidence of damage growth and imminent rupture when increased generation of such AE signals occurs.

The amplitude of the recorded signals has also been considered for the statistical analysis of the resulting clusters as it is a commonly used feature in conducting multi-parametric signal analysis. However, as it can be observed from Table 9.16, all clusters have a similar amplitude range and high amplitude signals are also present in the AE noise-related cluster. The amplitude of the signal is sensitive to the distance between the sensor and the source since the effect of attenuation on the recorded signal is reduced as the distance between the source and AE sensor decreases. This behaviour has been also reported in previous studies [204, 205]. Constructive signal interferences can result in higher amplitude values, while destructive interferences can lead to the detection of AE signals with lower amplitude. Consequently it can be concluded that the amplitude is not an entirely reliable signal feature in discriminating between the different types of damage. Signal features such as the energy, risetime, duration, counts and counts to peak have more distinctive statistical characteristics and their combined use can provide sufficient information in discriminating between the different damage modes.

Table 9.16: Statistical analysis of the clusters signal characteristics for the tensile tests

Cluster 1: Noise				
	Average	Minimum	Maximum	Median
Risetime (µs)	8	0	120	3
Counts to Peak	2	1	20	2
Counts	6	1	51	4
Energy (10µ Volt-sec/count)	0	0	115	0
Duration (µs)	32	0	120	22
Amplitude (dB)	46	40	79	45
Cluster 2: Fibre failure				
	Average	Minimum	Maximum	Median
Risetime (µs)	268	0	2213	70
Counts to Peak	32	1	356	14
Counts	145	29	565	133
Energy (10µ Volt-sec/count)	106	6	843	72
Duration (µs)	1497	584	2551	1422
Amplitude (dB)	78	47	99	79
Cluster 3: Fibre/matrix interfacial failure				
	Average	Minimum	Maximum	Median
Risetime (µs)	58	0	767	24
Counts to Peak	8	1	82	6
Counts	36	1	168	33
Energy (10µ Volt-sec/count)	10	0	348	4
Duration (µs)	316	121	1323	252
Amplitude (dB)	60	40	99	58
Cluster 4: matrix cracking				
	Average	Minimum	Maximum	Median
Risetime (µs)	1361	0	24741	56.5
Counts to Peak	213	1	5897	13
Counts	667	143	6712	368
Energy (10µ Volt-sec/count)	778	30	28148	328
Duration (µs)	5305	2552	25000	3491
Amplitude (dB)	89	53	99	91

To further understand data clustering and distribution of the AE signals for each of the resulting clusters, scatter graphs have been generated for the main signal features. Figure 9.59a) shows a typical scatter distribution for the duration against risetime of the AE signals, while the AE energy versus duration are shown in Figure 9.59b).

By examining both the scatter distribution and Table 9.16, a noticeable overlap between the main signal features is observed for all the clusters. During rapid failure high amounts of AE waves are simultaneously generated from multiple sources. As the waves propagate in the material, constructive and destructive interference, reflections, scattering and attenuation influence the characteristics of the recorded AE signals. The similarity of the signal features can lead to overlaps that can obscure the boundaries between clusters. Nonetheless, despite the presence of overlaps it can be seen that the clustering method applied in this work has effectively identified and separated the different types of AE signals into clusters, providing additional information on the main AE signal characteristics of the different types of failure.

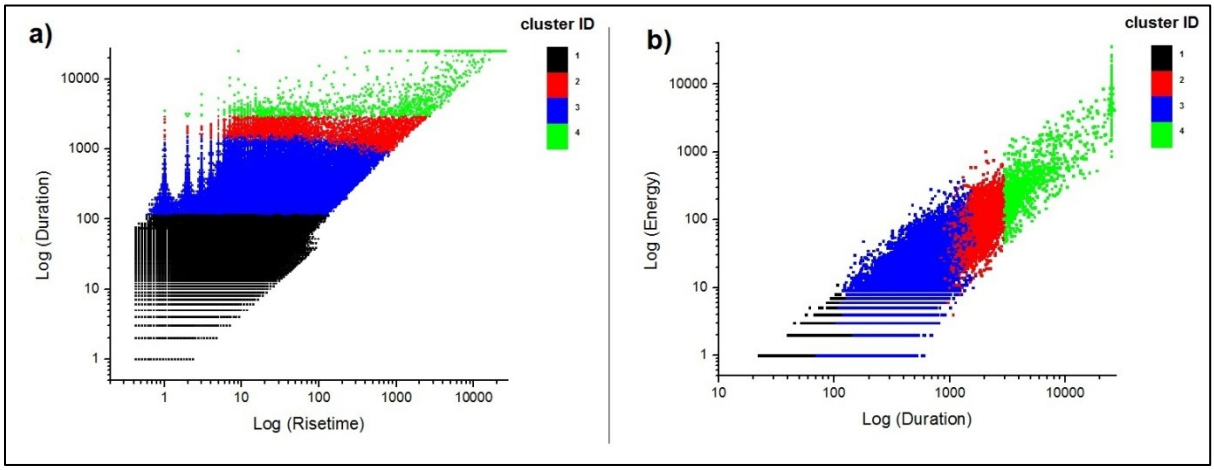

Figure 9.59: a) Duration-Risetime and b) Energy-Duration scatter distribution.

9.5.4 Automated data clustering on AE signals recorded during the bending tests on vinyl-ester GFRP plates

Automated data clustering has been also performed on the AE data recorded during bending testing. The effectiveness of each clustering algorithm in grouping into clusters the different types of AE signals has been assessed by following the same procedure discussed in the section 9.5.2. Similarly to the tensile tests, the k-means and LVQ have poor performance as they result in limited noise separation and inadequate cluster separation. Improved clustering results have been obtained by using the Forgy and ISODATA. Forgy generates similar clustering results to ISODATA, but it leads to slightly improved noise separation assigning more AE events to the damage-related clusters. Forgy exhibits the best performance in comparison with the other algorithms, and has been used to group into separate clusters the AE signals recorded during the bending tests.

Representative clustering results obtained from the analysis of the AE data from void-free and highly voided samples are shown in Figures 9.60-9.62. Similarly to the clustering results acquired from the tensile tests, four clusters have been generated. The largest cluster exhibits low energy accumulation related to general noise and echo-related AE signals. The smaller clusters consist of high energy AE signals which are related to damage events. In bending tests, the main damage mechanisms that are expected to be active are delamination, matrix cracking and fibre failure. According to Ullah et al. [206], damage in fabric-reinforced composite materials starts with transverse matrix micro-cracking. The matrix cracking is followed by delamination and ultimately fibre fracture that leads to ply fracture. The first ply fracture can be followed by subsequent delamination and ply fracture on the next layers.

Limited damage is often observed on the top layer due to the compressive stresses on the top of the bending sample [206].

The clustering results from the bending tests on the void free samples show that damage initiates with transverse matrix micro-cracking which is active until rupture occurs. This cluster has the largest size, exhibiting relatively low energy accumulation. The matrix cracking cluster consists of major matrix cracking AE events occurring after delamination and causing a sharp increase in the cumulative energy prior to failure. Matrix micro-cracking is followed by delamination which has the highest energy accumulation. The delamination-related cluster has the smallest size since individual delamination events cause severe and sudden damage growth resulting in the generation of highly energetic AE signals. Delamination is followed by fibre failure becoming more active after delamination has occurred. Compared with delamination, the fibre failure cluster is larger due to increased activity taking place within the reinforcement layers.

Delamination is the main and most energetic failure mechanism as it causes severe structural degradation, resulting in subsequent activation of fibre failure. Fibre failure and matrix cracking grow in parallel with delamination, while a sharp increase in the AE energy at 180s for all the clusters indicate accelerated damage growth and imminent failure which occurs at 220s.

Similar failure behaviour and damage growth patterns are also observed in the shipyard samples. Delamination is the main and most energetic damage mode followed by fibre fracture and matrix cracking. From the cluster evolution graphs in Figures 9.61 and 9.62 it can be seen that delamination is more prominent and exhibits higher cumulative energy

values in comparison with the samples made with resin infusion. Damage initiates with delamination, growing rapidly under loading followed by sudden matrix cracking and fibre failure. The presence of voids between the reinforcing layers and gaps between the fibre tows cause early delamination under bending loading conditions which in turn activates matrix cracking and fibre failure. This is more prominent for the heavily voided Shipyard_A samples where delamination initiates at an early stage of loading and grows rapidly until failure.

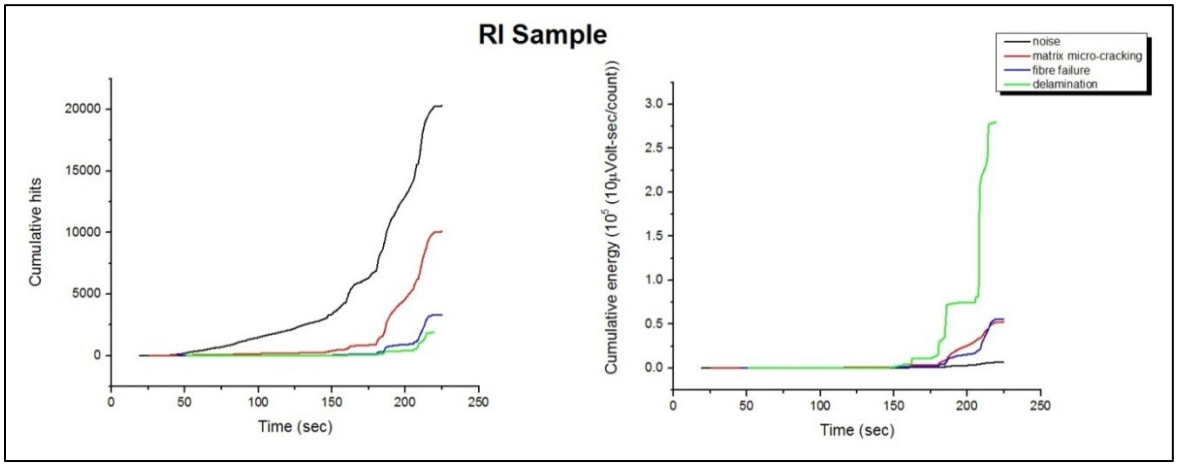

Figure 9.60: Cumulative hits and cumulative energy evolution of the AE clusters for a resin infusion sample subjected in bending tests.

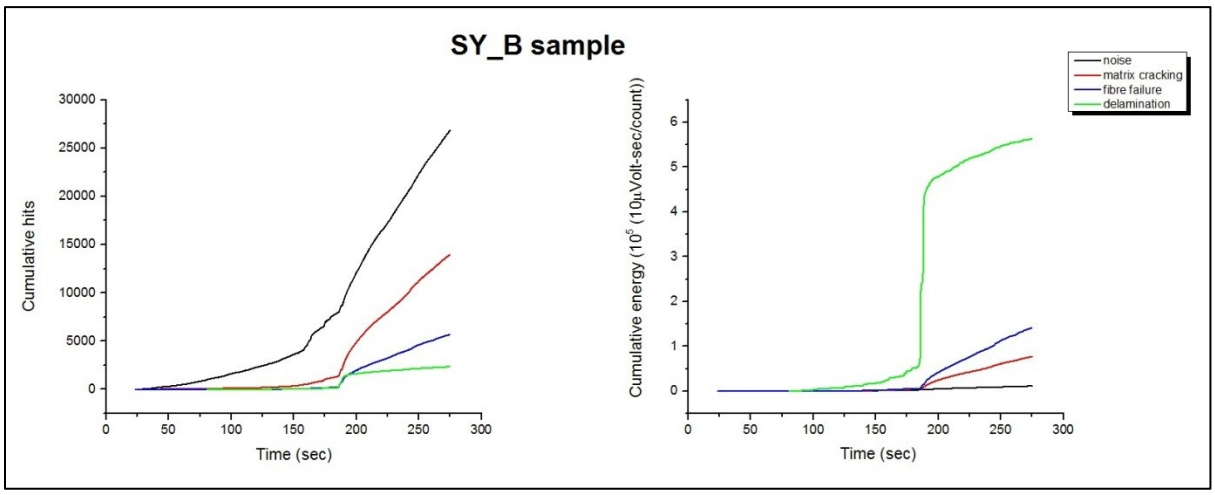

Figure 9.61: Cumulative hits and cumulative energy evolution of the AE clusters for a Shipyard_B sample subjected in bending tests.

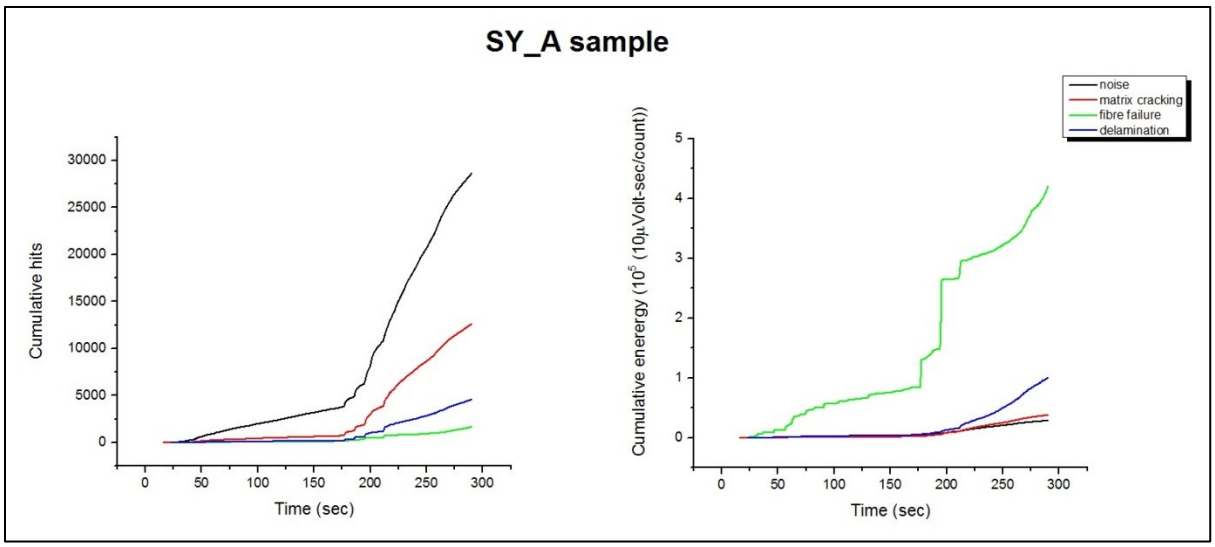

Figure 9.62: Cumulative hits and cumulative energy evolution of the AE clusters for a Shipyard_A sample subjected in bending tests.

Due to the limitation of the testing method applied in this study, the microstructural examination of step-by-step damage progression was not possible. However, the fractured specimens after bending testing were examined with optical microscope and stereoscope. Typical high magnification section images from fractured samples are shown in Figures 9.63 and 9.64. The presence of delamination, matrix cracking, transverse matrix micro-cracking and fibre fracture can be clearly observed from these pictures. The delaminated areas cannot be clearly seen in the high magnification images taken with an optical microscope since the mounting resin has filled the gaps of the damaged areas. However, delamination is clearly visible in Figure 9.64 which is taken using the stereoscope.

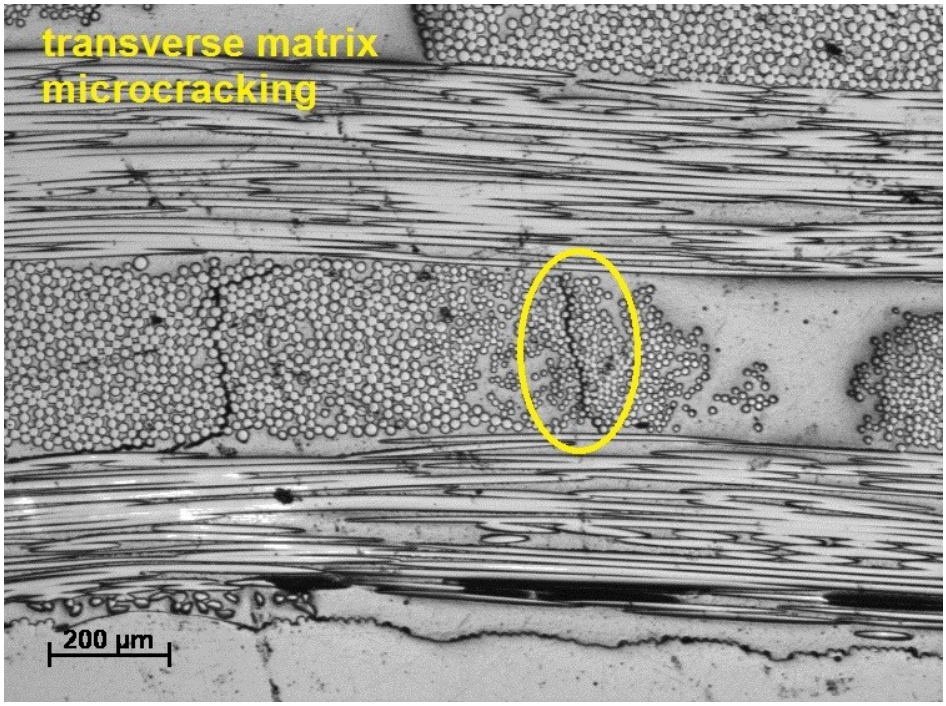
transverse matrix
microcracking
200 µm

a)

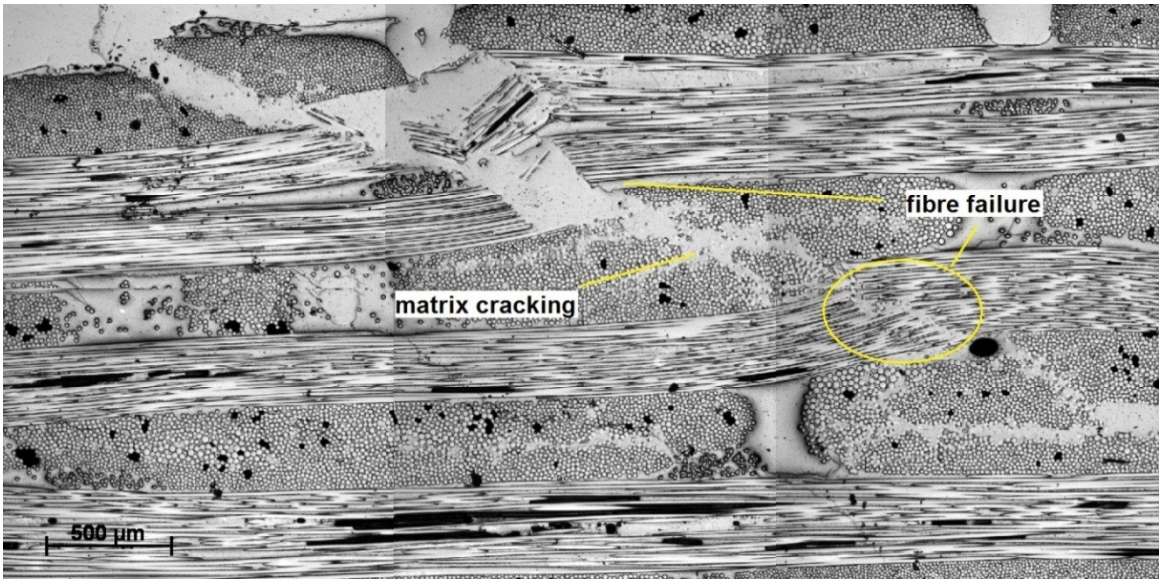
fibre failure
matrix cracking
500 µm

b)

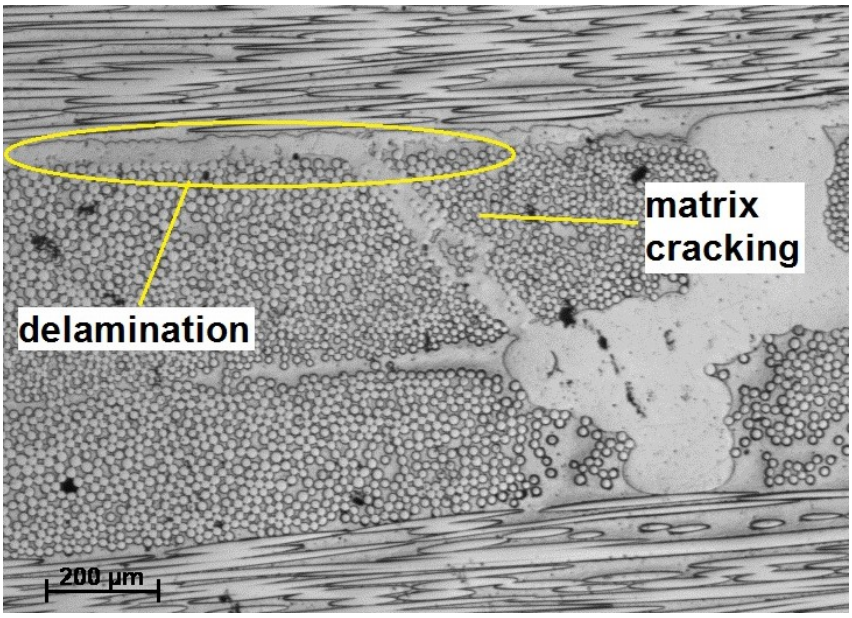

c)

Figure 9.63: High magnification micro-section images of a composite sample after failure

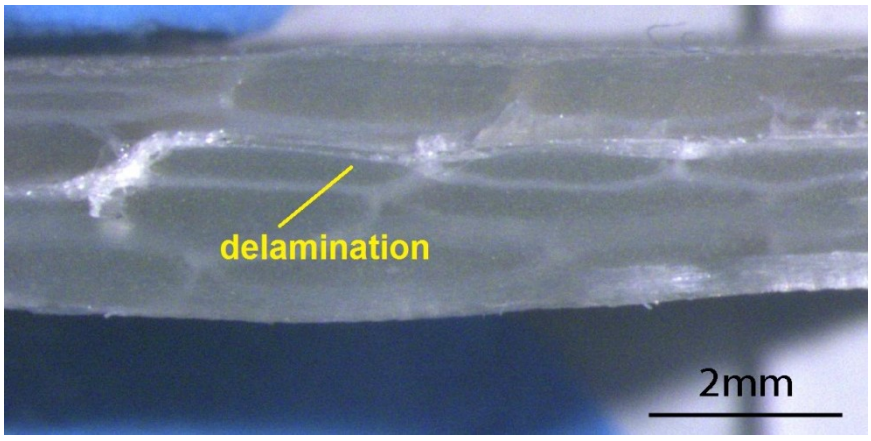

Figure 9.64: Side section image of a composite sample after failure

By analysing the signal features of the clusters it is possible to obtain the key AE signal characteristics of noise and different damage modes that are active during bending. The statistical characteristics of the key signal features for each cluster are shown on Table 9.17.

Similarly to the tensile tests, cluster #1 is associated with general noise signals caused by friction and echoes.

The matrix cracking AE signals have relatively higher energy, duration and risetime compared with the noise-related cluster. The early identification of these signals before any significant damage occurs during acquisition has vital importance, since their increased generation can give indication of imminent delamination. The cluster related with fibre fracture and matrix cracking exhibit considerably higher AE energy, duration, and risetime values. The identification of the signal characteristics associated with major damage events can provide evidence of active damage progression and fibre fracture within the reinforcement layers after delamination has occurred. The signals related with delamination exhibit significantly higher AE energy, duration and risetime values compared with fibre fracture and matrix cracking signals. The most distinctive characteristics of the delamination-related signals have considerably high duration and risetime values. The identification of the delamination-related AE signal characteristics can provide sufficient evidence of severe damage growth and give additional indication of imminent failure.

The amplitude of the AE signals has also been considered for the statistical analysis, but extensive overlap and similar amplitude range are present between the different damage-related clusters. Therefore, as for the tensile tests, the amplitude cannot be part of the multi-parametric analysis applied in this study. Comparing Tables 9.16 and 9.17 it can be seen that differences in the signal characteristics between the tensile and bending tests are present. These differences are caused by the different failure behaviour and damage evolution under the different loading configurations tested in this work.

The key differences are mainly observed on the higher risetime, counts, energy and duration values for the fibre fracture AE signals produced under tension, in comparison with fibre fracture events under bending. In addition, the matrix cracking related cluster under tension exhibits higher risetime, energy counts and duration values compared to the respective cluster under bending conditions. In the bending tests, highly energetic AE signals in the bending tests are mainly produced by delamination events and they also have the highest duration, risetime and counts values in comparison to the rest of the failure modes.

Table 9.17: Statistical analysis of the clusters signal characteristics for the bending tests

Cluster 1: Noise				
	Average	Minimum	Maximum	Median
Risetime (μs)	12	0	152	7
Counts to Peak	3	1	21	2
Counts	7	1	35	5
Energy (10μ Volt-sec/count)	0	0	48	0
Duration (μs)	51	0	191	43
Amplitude (dB)	46	40	43	45
Cluster 2: Matrix cracking				
	Average	Minimum	Maximum	Median
Risetime (μs)	43	0	337	23
Counts to Peak	7	1	45	5
Counts	32	1	92	31
Energy (10μ Volt-sec/count)	5	0	51	4
Duration (μs)	235	94	486	223
Amplitude (dB)	58	40	80	57
Cluster 3: Fibre failure				
	Average	Minimum	Maximum	Median
Risetime (μs)	157	0	596	134
Counts to Peak	17	1	86	13
Counts	64	7	166	62
Energy	17	1	233	11

(10μ Volt-sec/count)				
Duration (μs)	547	314	981	516
Amplitude (dB)	63	42	93	62
Cluster 4: Delamination				
	Average	Minimum	Maximum	Median
Risetime (μs)	922	0	24780	519
Counts to Peak	125	1	4797	52
Counts	316	23	5885	141
Energy (10μ Volt-sec/count)	149	3	9762	32
Duration (μs)	2228	533	25000	1186
Amplitude (dB)	68	48	99	66

9.5.5 Automated data clustering on AE signals recorded during the bending tests on epoxy GFRP pre-preg plates

In addition to the vinyl-ester composite samples, further automated data clustering analysis has been performed on defect free and on drilled glass fibre epoxy samples. Similarly to the bending tests on vinyl-ester samples, the AE data clustering analysis has been carried using Forgy since it performs better for this type of test. Representative clustering results obtained from the analysis on the AE data of the defect-free and drilled epoxy samples are shown in Figures 9.65 and 9.66.

The clustering results from the bending tests on the defect-free epoxy samples indicate that increased matrix cracking activity takes place until failure. Matrix cracking is followed by delamination which is the main damage mode generating high energy AE signals. Delamination occurs rapidly under increasing load followed by increased fibre fracture activity until rupture. For the drilled epoxy samples, the presence of the hole causes a

reduction in the load bearing capability of the sample. Fibre fracture is the main damage mechanism in this case. Compared with the structurally sound epoxy samples, fibre fracture occurs from the early stages of loading and grows rapidly until failure. In addition to fibre failure, delamination takes place, growing in parallel to fibre failure and matrix cracking.

Delamination is the main damage mode under bending loading for all types of composite samples subjected to bending testing. However, the presence of defects can cause the early activation of additional damage modes that cause structural degradation and result in rapid delamination growth until rupture. The increased generation of delamination-related AE signals can indicate severe structural degradation, while imminent failure can be indicated by the subsequent generation of fibre failure and matrix cracking related AE signals

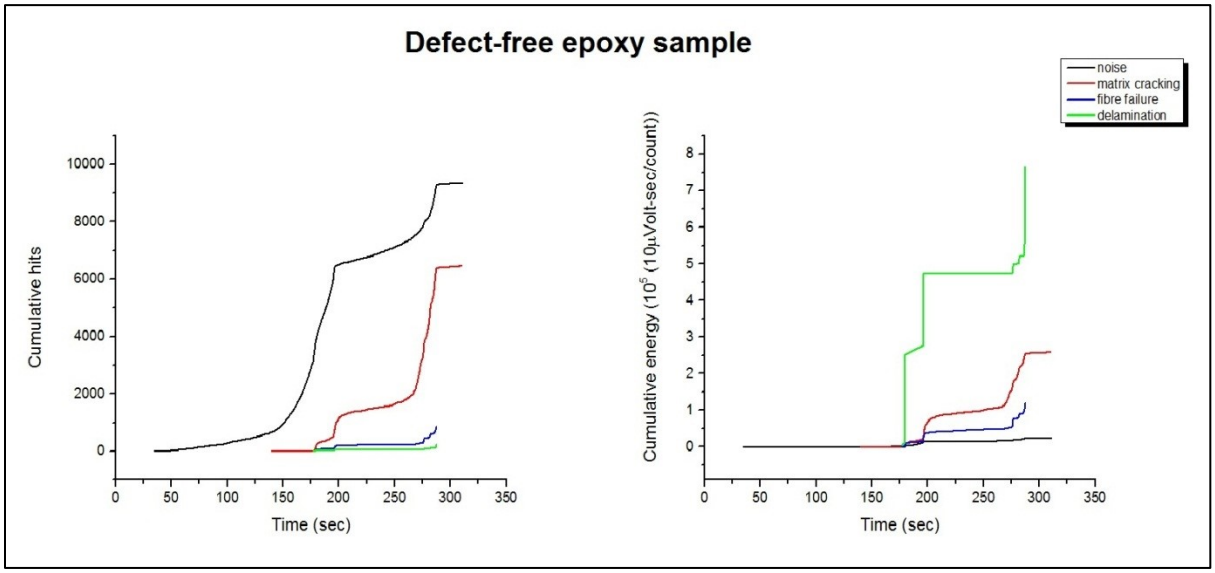

Figure 9.65: Cumulative hits and cumulative energy evolution of the AE clusters for a defect-free epoxy sample subjected in bending tests

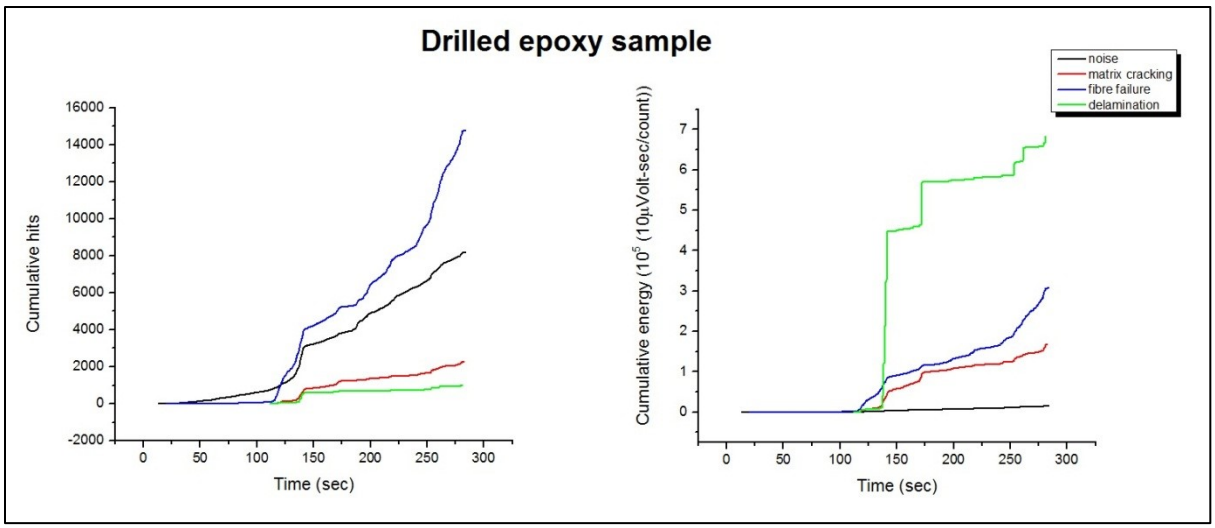

Figure 9.66: Cumulative hits and cumulative energy evolution of the AE clusters for a drilled epoxy sample subjected in bending tests

9.5.6 Acoustic emission noise signal characteristics and filtering

By determining the key characteristics of the noise signals it is possible to apply suitable filters during the acquisition to limit the recording of unwanted signals and improve the efficiency of the AE testing in continuously monitoring damage evolution and detecting structural failure. The key features of the noise AE signals are shown in Tables 9.16 and 9.17. It can be seen that the noise AE signals have predominantly low energy, duration and risetime values, while similar noise signal features have been determined for the tensile and bending tests. During acquisition a duration filter of 150μs is commonly applied to limit the recording of noise signals. In addition, an amplitude filter up to 45-50dB is commonly applied to remove any low amplitude noise-related signals. However, damage-related signals can also have low amplitude, while the amplitude of AE noise can often extend up to 80dB. As a result a manual filtering methodology is not always accurate since it can remove a substantial amount of damage related signals.

In this study a manual filtering method has been tested to remove the noise from the original dataset, and the filtering results are compared to the data clustering. A duration filter of 150μsec was used as low duration signals are commonly associated with noise. To further remove noise signals after filtering with duration, a PAC energy filter of 2 was used in order to reject signals with PAC energy smaller than 1. AE signals with energy values of 0 and 1 are related to unwanted AE activity, and do not usually represent actual damage events. In addition to manual filtering, noise signals can be effectively removed from the original dataset by simply deleting or hiding the noise-related cluster after data clustering. The cumulative hits evolution curves after the manual data filtering method has been applied and after removing the noise cluster, are plotted with the cumulative hits of the original dataset shown in Figure 9.67. In Figure 9.68 the cumulative hits evolution curves are plotted with the cumulative energy to evaluate the effectiveness of the filtering methods.

In general both filtering methods result in a significant noise reduction, since the shape of the cumulative hits profiles for both is similar to that of the cumulative energy (Figure 9.68). This indicates an accelerated increase in the generation of highly energetic damage-related AE signals whenever damage growth occurs, particularly prior to failure. The display of the cumulative energy profile after filtering has been considered, but the filtering has no or minor effect on the cumulative energy profile since only low energy signals are removed.

It can be seen that no significant difference between the resulting hits evolution profiles is observed after filtering, but the manual filtering method removes more AE hits in comparison with the filtering of the noise cluster. Therefore, the manual filtering method can lead to over-filtering and damage-related AE signals can be eventually lost. The removal of the noise cluster can limit (or supress) over-filtering and less damage related signals are lost. The

remaining damage-related clusters can be used to effectively monitor the evolution of the different types of failure. Therefore, by using the noise signal features in Tables 9.16 and 9.17, a filtering method can be established to effectively remove noise and supress any over-filtering effects, increasing the effectiveness of the AE testing in continuously monitoring structural degradation.

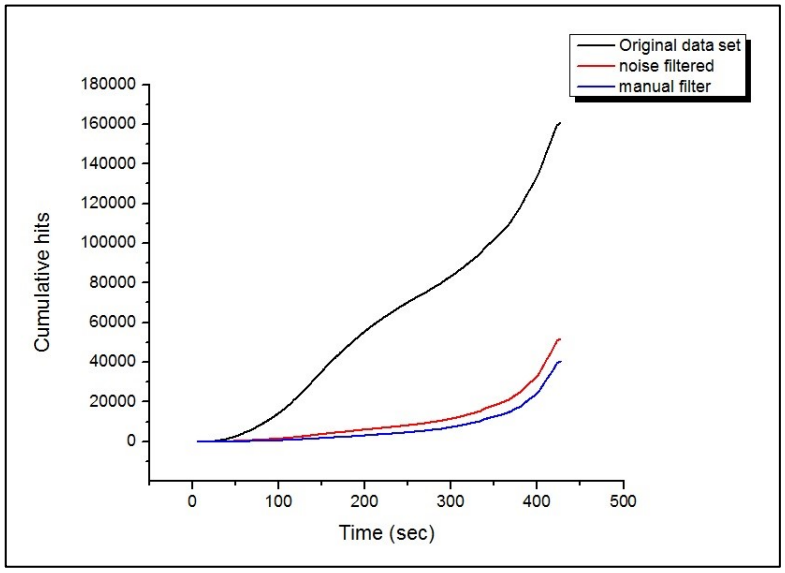

Figure 9.67: Cumulative hits evolution for the original and for the filtered AE data

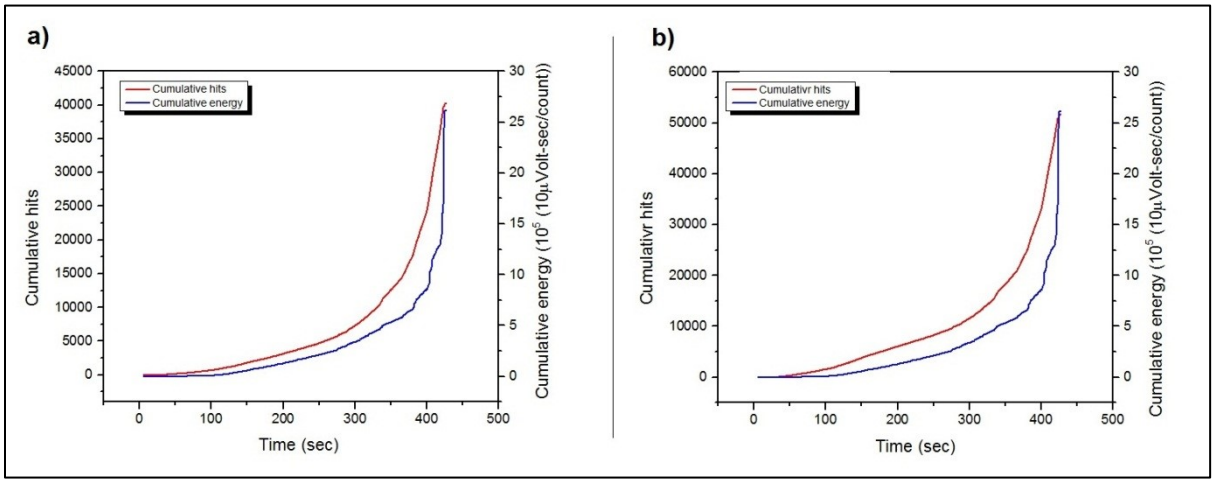

Figure 9.68: Cumulative energy and hits evolution for a) for the manual filtering method and b) after the noise cluster has been removed

9.6 Bending tests on hybrid composite/steel joints

9.6.1 Introduction

This section presents the main results arising from the bending tests on the different types of composite to steel hybrid joints. Composite-to-steel hybrid joints are components with complex structure. Their mechanical performance under bending conditions was assessed. AE testing was carried out during bending to detect damage initiation and growth. Typical load-displacement and load-strain plots followed by AE data analysis are presented for each type of joint. Damage progression during testing was recorded using a video camera, while images were taken from the failed joints to investigate the type of failure.

9.6.2 Joint A.1

The load-displacement and strain in different positions for the one of the joint types (Joint A.1) is shown in Figure 9.69, while the AE energy evolution is shown in Figure 9.70. It can be seen that the strain along the joint increases gradually with the load until failure. The highest strain is introduced at the weak point on both tensile and compressive face, (Strain 5 and 2 respectively). High strain is introduced along the balsa wood section in the tensile and compressive face (Strain 5 and 4 respectively). Low strain is introduced to the steel insert due to its superior strength and rigidity in comparison with the balsa wood (Strain 1). High strains at the weak point introduce high stress to the balsa wood resulting in balsa wood fracture.

Balsa wood fracture is the main type of failure in the composite to steel joints, as seen in Figure 9.71.

Figure 9.70 illustrates the load–displacement plot for the A.1 joint plotted with the AE cumulative energy curves for each AE channel. The cumulative energy evolution curves exhibit differences for each channel because each sensor is placed at a different location on the sample. Therefore, the recorded AE activity of each sensor will vary when compared with the other sensors. Despite some minor differences in the recorded AE activity of each sensor, all channels have similar trend and indicate damage initiation and progression until rupture. This behaviour is observed for all the joints tested in bending. The AE cumulative plot increases as the slope of the load curve starts to drop. Damage initiation is indicated as a sharp increase in the energy accumulation graphs at 8.5mm. The subsequent gradual increase in the cumulative energy evolution indicates damage progression until rupture which is identified as a sudden and sharp increase in the cumulative energy at 16.5mm.

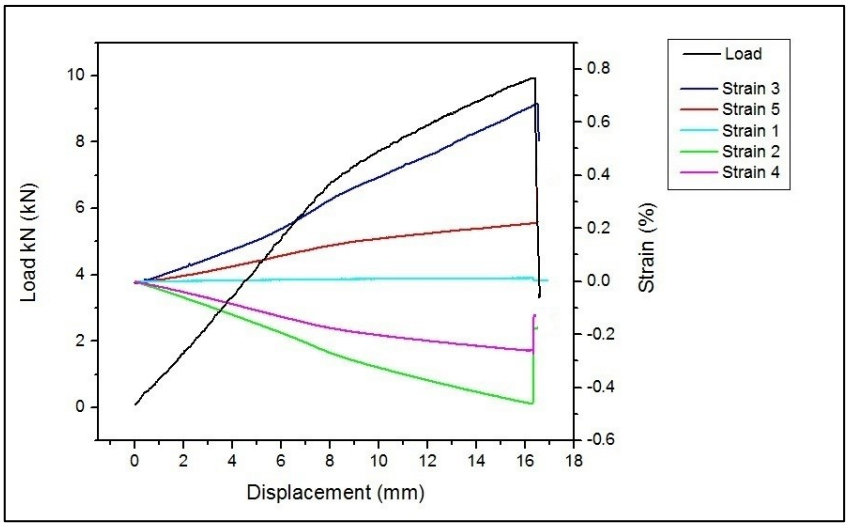

Figure 9.69: Load-displacement plot and strain at different positions of the A.1 joint.

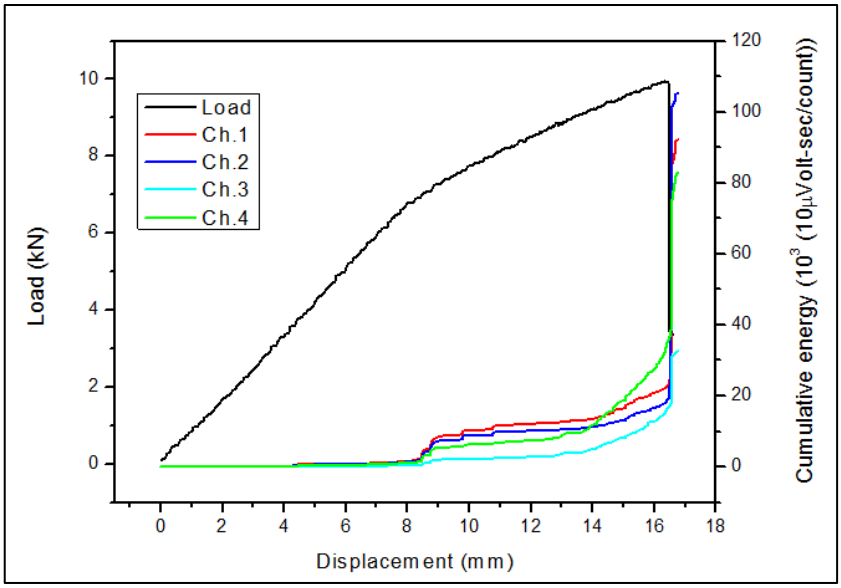

Figure 9.70 Load-deflection curve and AE cumulative energy for the A.1 joint.

Figure 9.71: Balsa wood failure in A.1 joint.

9.6.3 Joint A.2

The load-displacement and strain in different positions for the type of joint reinforced with 4 layers of glass fibre preforms on top and on the bottom of the weak point (Joint A.2) is shown in Figure 9.72, while AE energy evolution is shown in Figure 9.73. Strain evolution is similar

to the previously discussed type of joint. Load with displacement increase linearly until rupture. The additional reinforcement glass fibre preform layers increase the strength and rigidity of the joint, failing at higher load compared with the main type of joint. However, the deflection at failure is lower compared with the initial unreinforced joint. In this type of joints, balsa wood failure is the main damage mechanism, but failure in the interface between the balsa wood and insert is also observed in Figure 9.74.

Figure 9.73 shows the load-displacement plot for the A2 joint plotted with the AE cumulative energy curves for each channel. A sharp increase in the cumulative energy evolution at 9mm indicates damage initiation. The cumulative energy evolution plots then increase gradually until rupture which is identified as a sudden and sharp increase in the cumulative energy evolution profiles at 11mm.

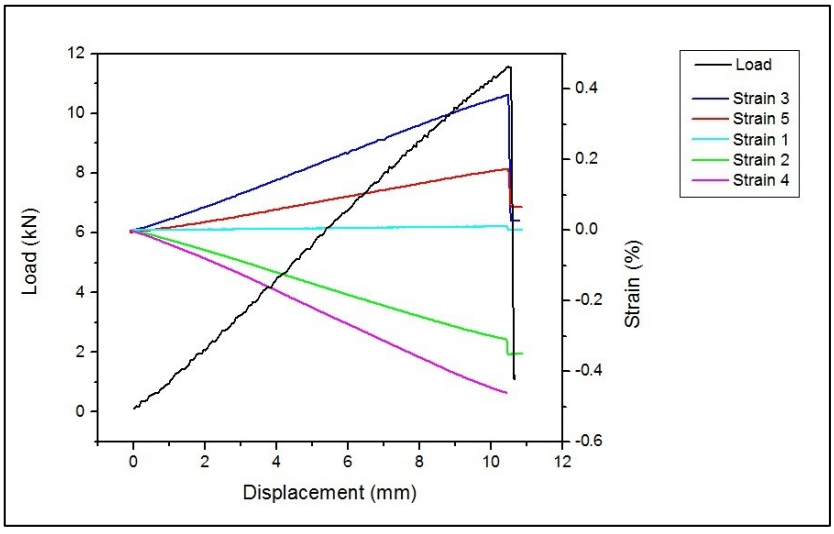

Figure 9.72: Load-displacement plot and strain at different positions of the A.2 joint.

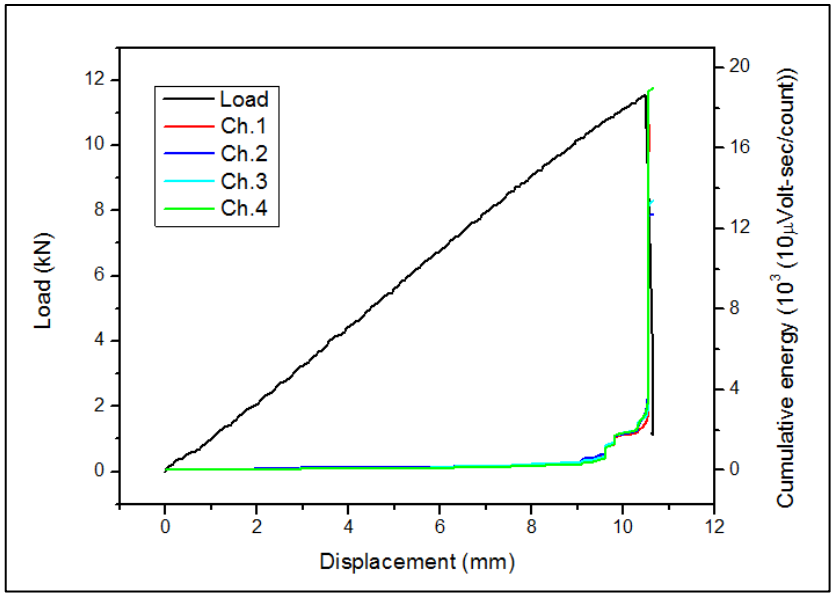

Figure 9.73: Load-deflection curve and AE cumulative energy for the A.2 joint.

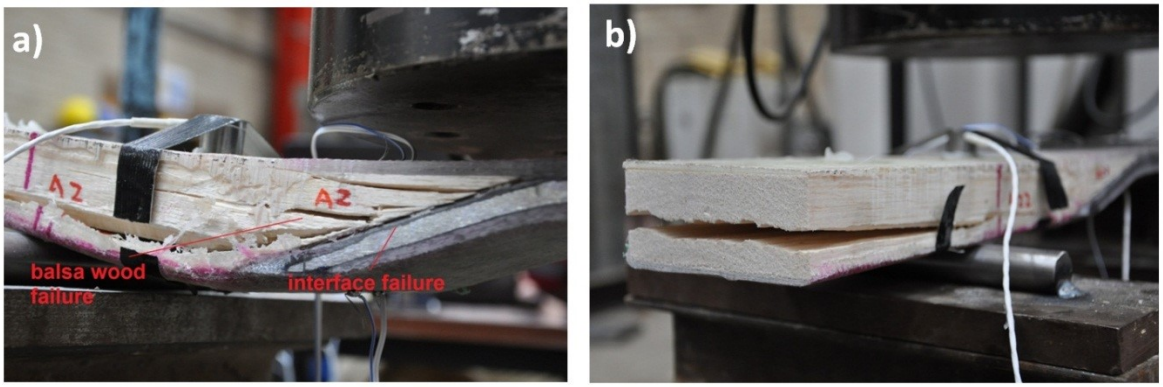

Figure 9.74: Balsa wood fracture and interfacial failure in A.2 joint.

9.6.4 Joint A.3

The load-displacement and strain plots at different positions for the type of joint where epoxy-based adhesive was applied on the steel insert and balsa wood is shown in Figure 9.75 (Joint A.3). The AE energy evolution is shown in Figure 9.76. Similar load-displacement and strain evolution to the previous types of joints is observed. The Joint A.3 fails at loads similar

to the main joint type while strain levels at failure are relatively lower. The brittle nature of the epoxy adhesive has resulted in sudden interface failure between the balsa wood core, steel insert and composite skin at high loads. Interface failure is the predominant damage mechanism for this type of joints as observed from Figure 9.77 with no further balsa wood cracking.

Figure 9.76 shows the load-displacement for the A31 joint plotted with the AE cumulative energy curves of each channel. Due to the brittle interface, damage initiation occurs suddenly at 11mm and rapidly grows until failure of the interface associated with a sudden increase in cumulative energy. Damage initiation and growth occur more rapidly compared with the other types of joints due to the brittle epoxy adhesive.

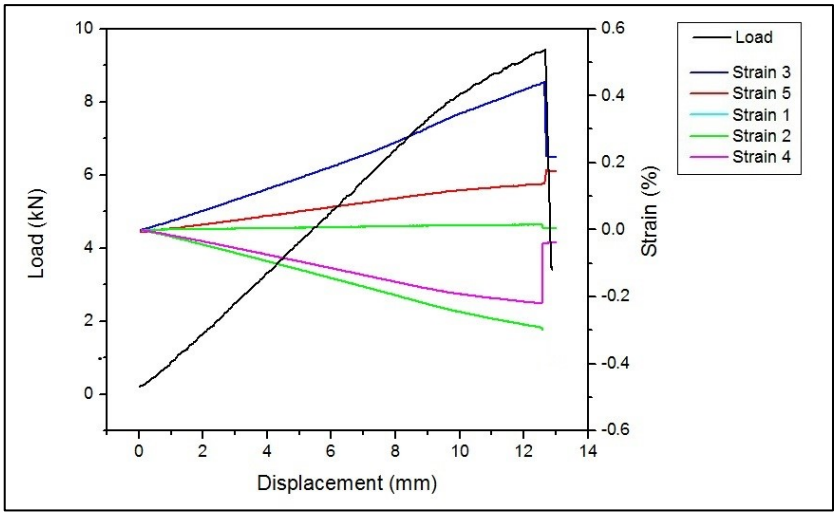

Figure 9.75: Load-displacement plot and strain at different positions of the A.3 joint.

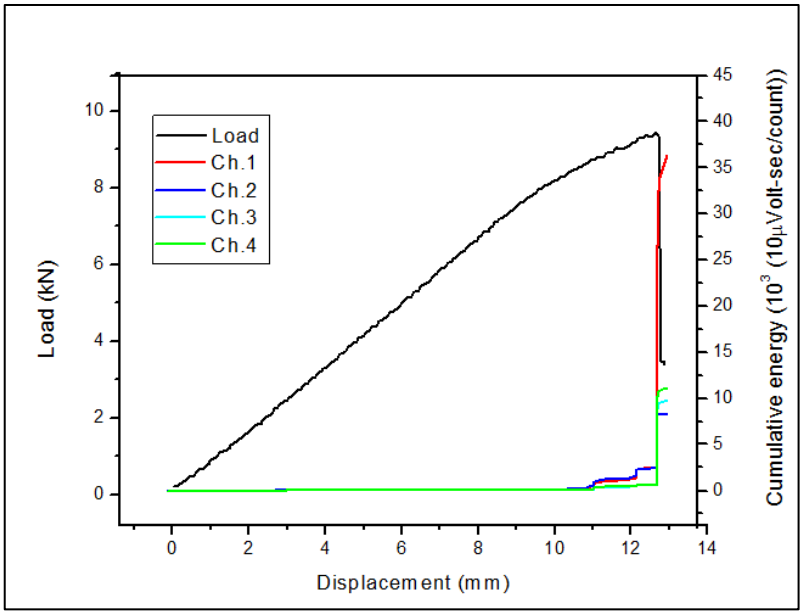

Figure 9.76: Load-deflection curve and AE cumulative energy for the A.3 joint.

Figure 9.77: Interfacial failure in A.3 joint.

9.6.5 Joint B.1

The load-displacement and strain plots at different positions for the main type of joint with a bolt placed on it (Joint B.1), are given in Figure 9.78, while the AE energy evolution is shown in Figure 9.79. The bolt was placed 120mm from the weak point on the steel insert as

shown in Figure 9.80. The joint with the bolt exhibited similar load-displacement and strain evolution to the main type of joints (A.1 joint) with the highest strains to be sustained in the weakest point (Strain 3 and 2) and on the balsa wood core (Strain 5 and 4). Limited strain is introduced at the midpoint of the steel insert. As seen in Figure 9.81, this type of joints fails due to interfacial and balsa wood failure.

Figure 9.79 shows the load-displacement curve for the B12 joint plotted together with the AE cumulative energy curves for each channel. A minor increase in the cumulative energy evolution plots at 5 mm indicates damage initiation subsequently growing slowly until a second more rapid increase in the cumulative energy at 9mm. The increase in energy accumulation at this stage indicates accelerating damage growth until rupture, which is identified as sharp increase in the cumulative energy curves at 10mm.

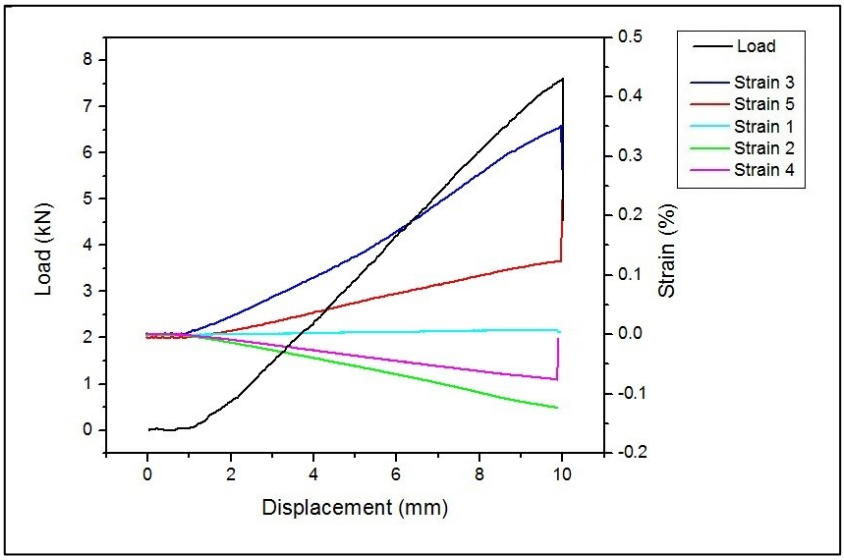

Figure 9.78: Load-displacement plot and strain at different positions of the B.1 joint.

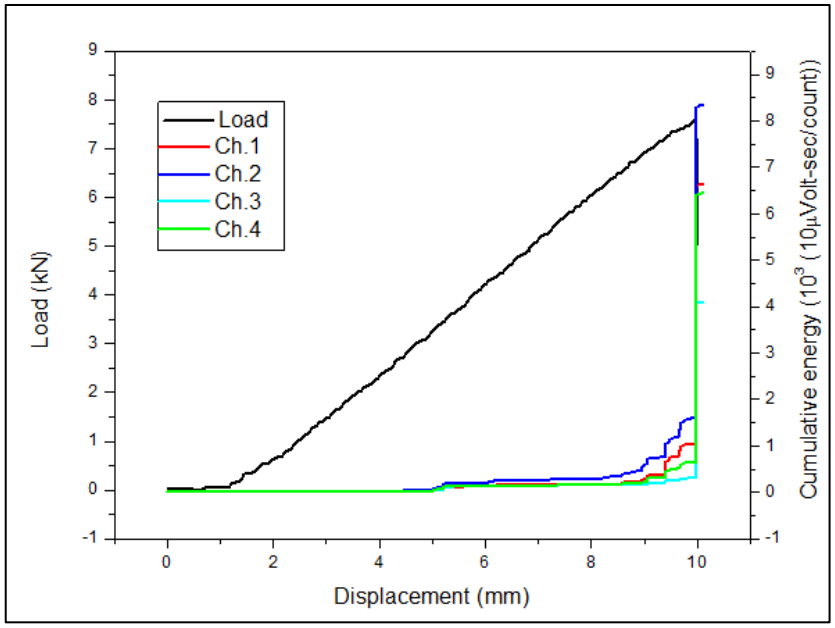

Figure 9.79: Load-deflection curve and AE cumulative energy for the B.1 joint.

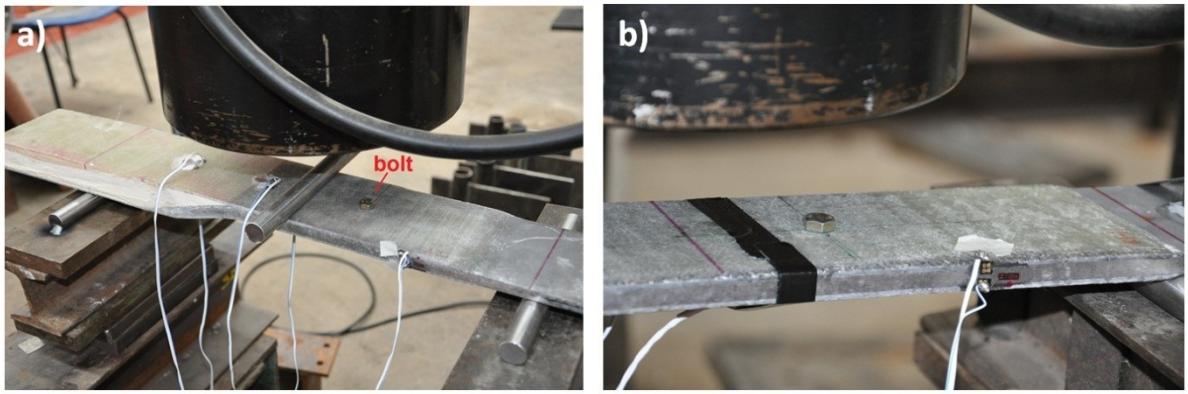

Figure 9.80: Position of the bolt on the composite/steel joints.

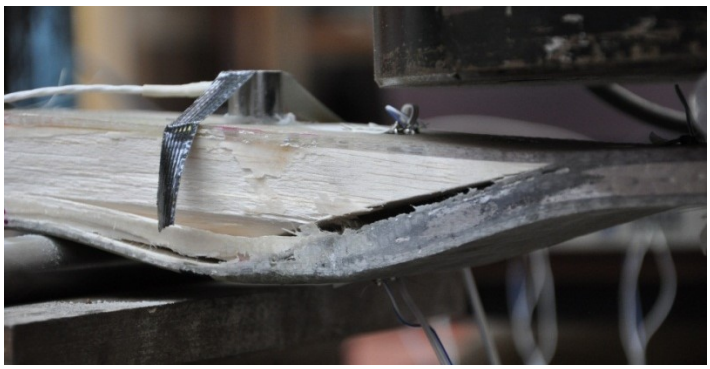

Figure 9.81: Balsa wood fracture and interfacial failure in A.3 joint.

9.6.6 Joint B.2

The load-displacement plot and strain in different positions for the reinforced joint with a bolt present (Joint B.2), is given in Figure 9.82, while the AE energy evolution is shown in Figure 9.83. It can be seen that the load-displacement curve exhibits an almost linear response until rupture. Furthermore, the strain evolution is similar to the previously discussed type of joint (B.1). The additional reinforcement glass fibre preform layers increase the strength and rigidity of the joint, as it fails at slightly higher loads. As observed from Figure 9.84, balsa wood cracking and interface failure between the steel insert and balsa wood core are the primary damage mechanisms occurring in this joint type.

Figure 9.83 presents the load-displacement curve for the B.2 joint plotted with AE cumulative energy curves for each channel. An increase in the energy accumulation at 3mm indicates the damage initiation. The gradual increase in the cumulative energy indicates steady damage growth until rupture identified as sharp increase in the cumulative energy at 10mm.

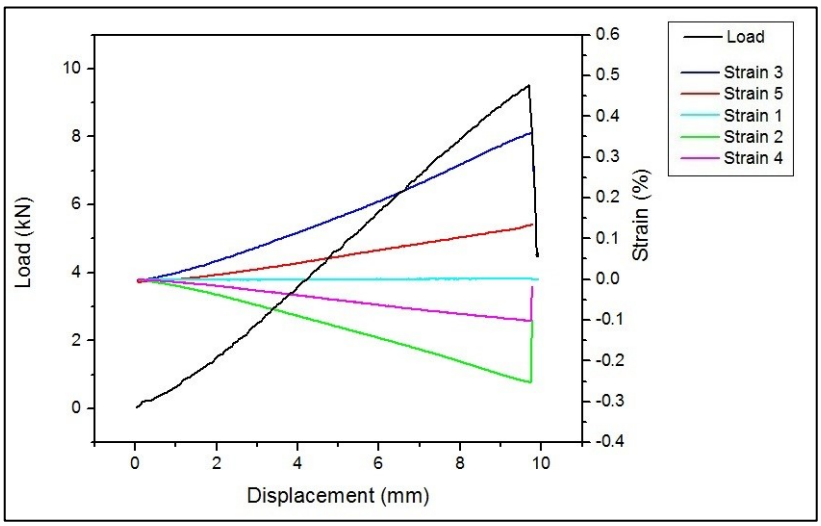

Figure 9.82: Load-displacement plot and strain at different positions of the B.2 joint.

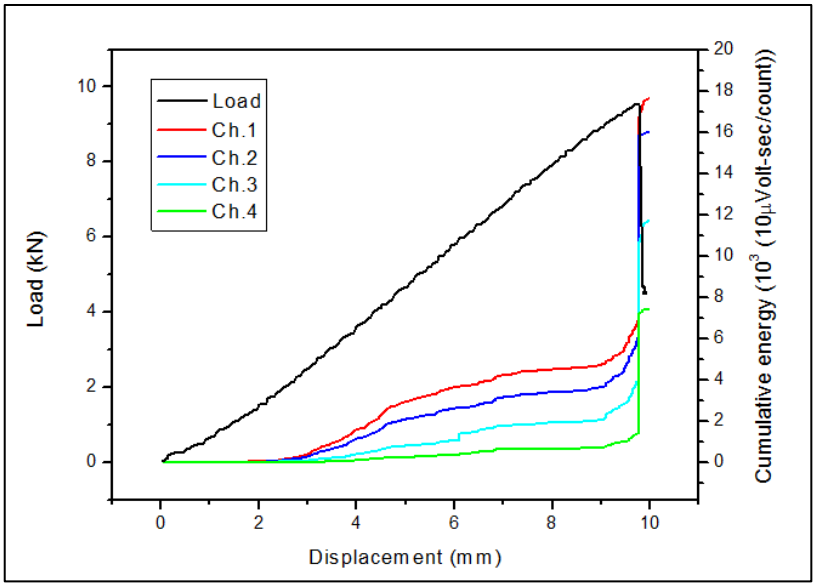

Figure 9.83: Load-deflection curve and AE cumulative energy for the B.2 joint.

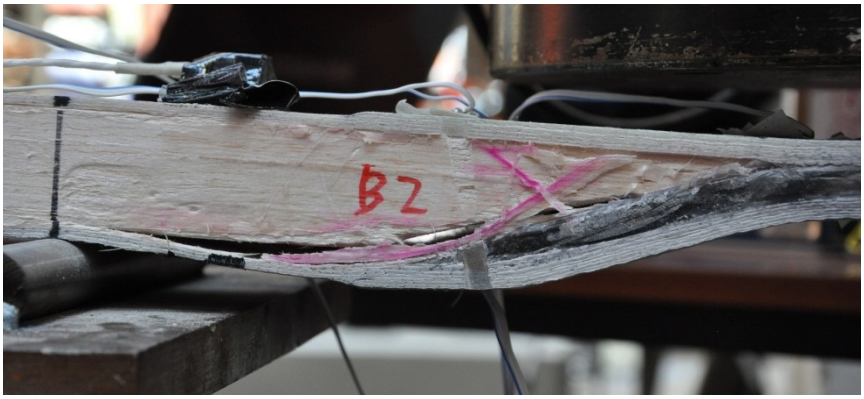

Figure 9.84: Balsa wood fracture and interfacial failure in B.2 joint.

9.6.7 Joint B.3

A bolt has been placed on the joint type were adhesive was applied on the steel insert and balsa wood (Joint B.3). The load-displacement curve and strain evolution for this joint are given in Figure 9.85, while the while the AE energy evolution is shown in Figure 9.86. Similarly to the previously discussed types of joints, high strains are sustained by the weak

point and balsa wood area on both compressive and tensile faces of the joint. During bending low strains are sustained by the rigid and stiff steel insert. The brittle nature of the epoxy adhesive results in sudden interface failure between the balsa wood core the steel insert at high loads. Interface failure is the main damage mechanism for this type of joints as observed in Figure 9.87.

Figure 9.86 shows the load-displacement curve for the B.3 joint plotted with the AE cumulative energy curves for each channel. The AE cumulative plot start to increase as the slope of the load curve starts to drop. A minor increase in the cumulative energy evolution plots at 7mm indicates damage initiation growing at low rate until a second and more steep increase in the energy accumulation is observed at 12mm. The increase in energy accumulation at this stage indicates further and accelerated damage growth until the joint's rupture identified as a sharp increase in the cumulative energy curves at 14mm.

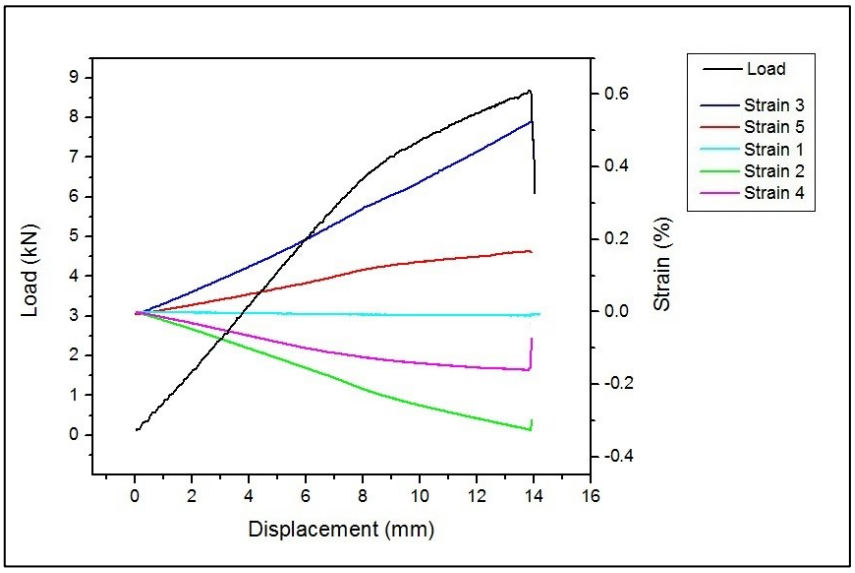

Figure 9.85: Load-displacement plot and strain at different positions of the B.3 joint.

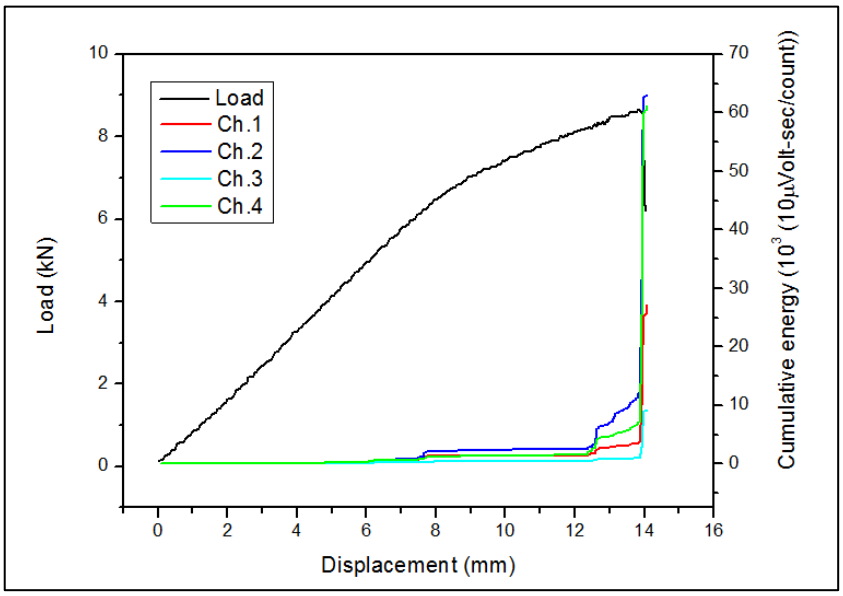

Figure 9.86: Load-deflection curve and AE cumulative energy for the B.3 joint.

Figure 9.87: Interfacial failure in B.3 joint.

9.6.8 Comparison of bending properties for the different types of joints

It can be concluded that all the joints have similar failure behaviour. The main types of damage modes at rupture is balsa wood cracking often combined with interfacial failure. The

joints were adhesive was used to bond the steel insert to the balsa wood core, experience predominantly interfacial failure. The presence of bolts has no significant effect on the bending properties of the joint since the bolted area as it is located away from the weak point. However, the presence of the bolt could have greater effect under cyclic loading conditions. The performance of the main joint design can be significantly improved by reinforcing the weak point. The presence of reinforcement increases the flexural strength and the rigidity of the joints as shown in Figure 9.88. The bending deflection at failure is relatively lower compared with the main design.

Analysis on the AE signals has shown AE signals with high energy are generated during failure mainly within peak frequency range of 100-200kHz, as shown in Figure 9.89. These signals are associated with balsa wood fracture since this is the main damage mechanism in the type of joints tested in this study. AE signals within the peak frequency range of 100-200kHz are associated with balsa wood cracking during the joint failure. Further bending tests on pure balsa wood samples have shown that balsa wood failure generates AE signals within the same peak-frequency range. Similar results have been also reported by Brunner et al. [207].

AE is an effective method of monitoring damage initiation and damage growth under loading and particularly prior to failure. It can be used to continuously monitor structural degradation of composite materials and FRC maritime components and structures in the field. In addition the characteristics of the AE signals can give indication of the type of failure that it is active during damage growth.

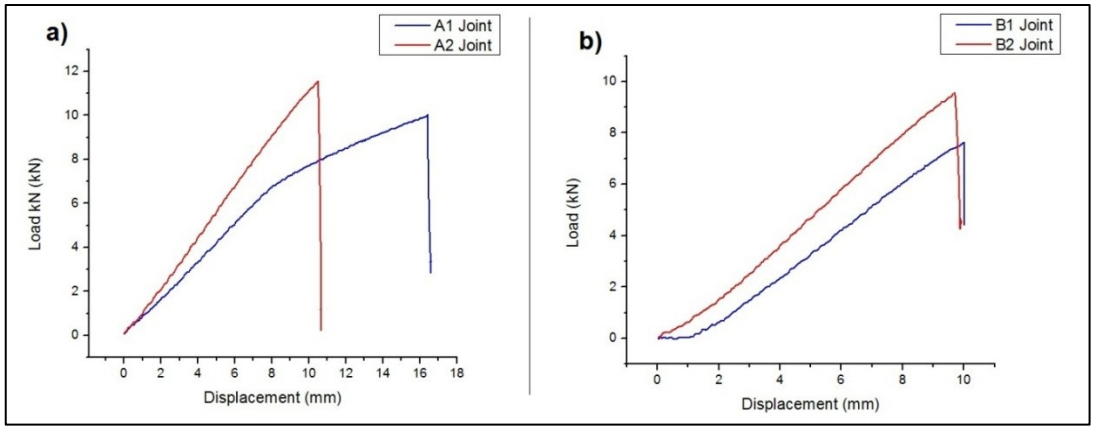

Figure 9.88: Effect of reinforcement on the bending properties of the a) Type A and b) Type B Joints

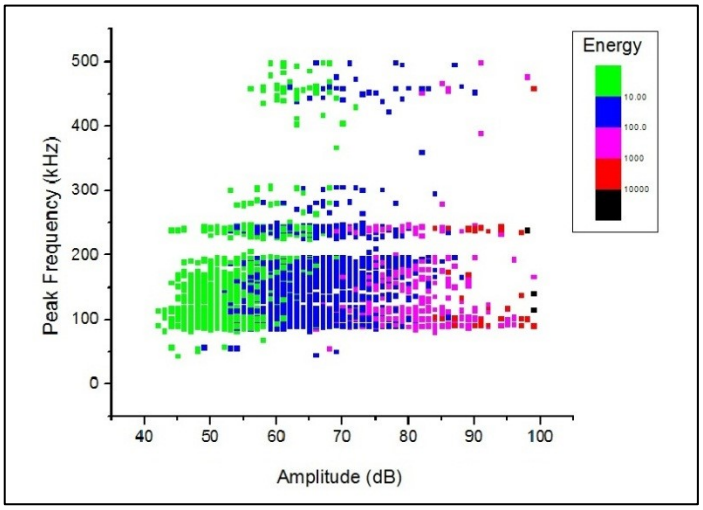

Figure 9.89: Frequency vs amplitude of distribution of AE signals

9.7 Applicability of AE testing on maritime structures

Structural degradation in critical structures and components needs to be monitored, since undetected damage can compromise the structural integrity of the structure and lead to catastrophic failure. The current study has highlighted that AE is a method which can be applied to effectively monitor damage initiation and growth in FRC structures. The structural integrity of maritime components and vessels can be assessed using AE testing methods. This can be achieved by establishing an AE testing methodology capable of detecting and analysing damage-related AE signals when a vessel is in-service. To increase the efficiency of the AE DAQ system in monitoring structural degradation it would be necessary to arrange the AE sensors on a grid along the vessel. In this way it becomes possible to detect failure from multiple areas with limited signal loss. However, due to the increased costs of AE sensors and acquisition equipment, an optimum number of AE sensors and an appropriate positioning grid must be established by further research and experimental work. The positioning of the AE sensors will depend on the geometry and size of the structure, material and type of application. The arrangement of AE sensors in a grid leads in the localisation of the damage events since the AE sources will be always located in a position between AE sensors.

A large part of the overall recorded AE signals is noise. During the operation of a vessel, naturally occurring events such as environmental noise, friction, vibrations from the engine room, wave slams, or even people simply walking on the deck, can give rise to unwanted AE noise signals that can mask out potential damage-related events. To eliminate the recording of unwanted AE noise signals when a vessel is in-service appropriate filters must be applied. The identification of the noise signal features presented in a previous section can result in the

use of potential filters that can be applied during operation of an AE system in the field. To eliminate noise signals multi-parametric filtering must be applied. For example, a duration filter of 150μs combined with an energy filter of 2 10μVolt-sec/count, can reduce by a significant percentage noise pick-up. However, due to the complexity of the in-service operation and different environmental conditions under which structural components are found, further research is necessary in order to establish an effective filtering methodology. By applying slightly higher high-pass filters some AE signals will be inevitably lost. Nonetheless the continuous monitoring of structural degradation will not be adversely affected, since serious damage related AE events with high energy and distinctive signal characteristics can still be recorded.

By examining the AE evolution and distribution of the AE signals it can become possible to identify active structural degradation and predict imminent failure. Automated data clustering can lead to the effective monitoring of the different damage modes, and increase the effectiveness of the AE system in assessing the severity of damage growth. Due to large variations in the cyclic loading conditions, preliminary research and tests on actual in-service structures are necessary in order to assess the extent of damage growth and determine the remaining service life of a component. Monitoring at local positions can be carried out in critical load bearing structures where high stress concentration can cause crack initiation and growth [208].

To increase the flexibility of the AE system, the recorded data can be automatically updated and stored to an online server for remote operation and monitoring assessment, removing the need of having dedicated personnel on board. This will allow the CM engineers to gain remote access to the AE data.

Due to physical limitations arising from the AE sensors capabilities as well as the AE system electronics and acquisition parameters, a limited amount of damage-related AE events occurring simultaneously under rapid failure conditions will not be recorded. Simultaneous signals generated by multiple sources can cause complex wave interactions such as wave reflections and constructive and destructive interference phenomena. These interactions can significantly affect the final AE wave that will reach the sensors and generate the AE signal. As a result the recorded AE signal can differ significantly from the original mechanical wave. Moreover, load needs to be applied on the material in order to produce AE activity. Therefore the presence of defect of a damage zone such an area of delamination, will remain unnoticed unless sufficient amount of load is applied that can cause further damage growth and generate AE events.

Nonetheless, despite certain limitations AE is a promising and cost-effective technique and it has great potentials in continuously monitoring structural degradation in maritime components and structures in the field. The application of AE testing can offer significant advantages over conventional NDT methods. AE can be carried out during service and monitor damage initiation and evolution. Instead of inspecting the whole structure in order to detect the faulty or failed areas, maintenance engineers can gather data from the AE system and focus their attention directly to damaged locations for additional inspection and further repairs. As a result the demand for frequent inspection can be limited. Thus maintenance downtime, resource and effort requirements can be reduced, resulting thus in lower operational cost, higher availability, increased reliability and improved profitability.

CHAPTER 10

CONCLUSIONS AND FUTURE WORK

10.1 Conclusions

This research study has investigated the applicability of the AE technique in continuously monitoring damage evolution in FRC components which can potentially be used in the construction of maritime vessels. Tensile and three-point bending tests were carried out on different types of samples, including bundles (tensile only), composite plate coupons and composite to steel joints. Damage initiation and propagation during these tests were monitored using AE, supplemented in some cases with video image recording, to establish effective parametrisation of data acquisition and define appropriate signal processing tools for reliable analysis of the results obtained.

To increase confidence in the applicability of AE in monitoring FRC components and assess the factors that influence the quality of the AE signals recorded, initial tests were limited to simple testing configurations based on the use of E-glass fibre bundles. In this way, it was possible to simplify AE acquisition parametrisation and subsequent data processing. Tests on fibre bundles consisting of few filaments have shown that AE events with high duration energy and amplitude are representative of individual filament failures. Such signals are recorded whenever a fibre breaks. The number of such AE events can be used to estimate the number of filaments in the fibre bundle and monitor damage propagation until final failure of the remaining filaments in the bundle occurs. Tensile tests were also carried out on as received and lubricated E-glass fibre bundles consisting of approximately 700 filaments. Friction and inter-fibre interactions induce surface damage to the fibres leading to an early failure giving rise to unwanted AE activity such as echoes and noise that need to be identified and filtered out. The lubrication reduces significantly inter-fibre friction and as a result, the bundle fails at higher load and strain. Furthermore, the failure of the lubricated fibre bundles

is slower, enabling the AE acquisition system prior to failure to detect more effectively fibre failure-related AE signals.

Further to the initial fibre bundle tensile tests, several unsupervised algorithms have been used to identify and separate the unwanted noise signals from the fibre fracture AE signals. Due to the simplicity and small size of the AE data set, all clustering algorithms exhibited similar performance when applied on AE datasets obtained from simple glass fibre bundle tests. Despite a small experimental error, all clustering algorithms can effectively identify and separate noise from the fibre fracture-related AE signals. Hence, gradual failure of the bundle can be monitored effectively.

The analysis of the AE data obtained during the mechanical tests on glass fibre composite samples has shown that damage initiation and growth can be monitored using AE cumulative energy as one of the key parameter indicators. Damage events such as fibre failure, matrix cracking and delamination generate highly energetic AE signals which cause a sudden increase in the cumulative energy evolution. Therefore, damage initiation and subsequent evolution are identified by sharp increase in the cumulative energy plots. In contrast to cumulative energy, the use of cumulative number of hits is not an effective methodology in monitoring damage evolution since the presence of low energy noise signals can mask the evolution of the damage related AE signals.

The presence of voids can have detrimental effects on the mechanical performance of FRCs. The effect of voids on the failure characteristics of glass fibre composites has been assessed by analysing the AE signals recorded during mechanical testing. It has been shown that damage initiates earlier and propagates faster in the voided composite samples in comparison

with the void-free samples which exhibit superior mechanical strength. The AE energy accumulation starts to increase at an early stage of loading until rupture. Steep increase in the AE energy is associated with rapid damage growth. Drilled holes on FRC panels for bolted connections also cause early damage initiation and subsequent rapid damage growth.

The effectiveness of AE in continuously monitoring damage evolution and detecting structural failure can be improved by distinguishing between the different damage mechanisms that are active in a material undergoing loading. Automated data clustering has been carried out in order to group the AE signals generated from the different failure mechanisms into separate clusters. Data clustering has been carried out using commonly applied clustering algorithms including k-means, Forgy, ISODATA and SOM-LVQ. It has been shown that for the tensile tests ISODATA is the most efficient algorithm as it effectively separates the noise signals. It also results to improved energy distribution between the damage-related clusters in comparison with other common clustering algorithms. For the bending tests Forgy and ISODATA perform reasonably well, but Forgy is preferred as it leads to slightly larger damage-related clusters, making monitoring of the damage mechanics under bending conditions clearer. Data clustering results have shown that the largest percentage of the original AE dataset consists of low energy noise signals containing the lowest fraction of the overall AE energy captured. In contrast, the damage-related clusters are far smaller in size and contain the high energy AE signals and hence the majority of the energy measured during tests. By analysing the signal features of the clusters it is possible to obtain the key AE signal characteristics of noise and different damage modes active in a composite material. The main features of the noise signals have been identified in order to establish a filtering methodology capable of eliminating unwanted noise signals during acquisition. Furthermore, knowledge on the damage-related signal characteristics results in

the discrimination between the types of damage mechanisms that are active under load. Monitoring of damage growth can be carried out by inspecting the evolution of different failure modes. This can improve the effectiveness of AE testing in continuously monitoring structural degradation, and increase understanding on the failure behaviour of FRC materials.

Despite the effective clustering results obtained, the resulting clusters can have similar signal features and a clear differentiation between them can often be difficult and complicated. In addition, some of the damage-related clusters can consist of mixed damage modes occurring simultaneously and generating AE signals with similar features. Therefore further research is required in order to clearly discriminate between the different damage mechanisms in FRC materials.

Flexural tests on hybrid composite to steel joints has shown that damage initiation and propagation have been effectively identified using AE, demonstrating the suitability of the technique. Different manufacturing setups such as the presence of reinforcement and use of adhesive between the balsa wood core and steel insert, can affect the strength and the failure behaviour of the joints. The differences in the failure behaviour are not easily observed visually due to the complexity of the structure. However, the failure behaviour of the different types of joint can be determined by examining the AE energy evolution, since damage events have been identified by sudden increases in the AE energy accumulation. After initial failure accelerated and sharp increase in the cumulative energy can indicate imminent failure. This can be particularly useful in the field where sufficient indication of structural degradation before it becomes critical can avert the occurrence of sudden catastrophic failure.

AE has great potential as a means of continuously monitoring structural degradation in maritime vessels and structures manufactured from FRCs in the field. However, the effective widespread application of the AE technique will require further research proving its suitability in quantifying damage in actual structures. The effect of variability in the loading conditions during maritime operations can complicate further the structural health evaluation of FRC maritime vessels and structures.

10.2 Recommendations for future work

The current study has highlighted the main aspects of AE testing in monitoring damage evolution in FRCs and components. The data processing and automated data clustering methodologies proposed in this work can be effectively used to monitor damage evolution and assess the structural integrity in FRC materials and maritime components.

However, significant amount of further research still needs to be carried out. Step-loading tests can be beneficial in gaining further understanding on the quality of the monitoring results during damage evolution. Moreover, fatigue loading using AE testing could also add significant value to this research since fatigue testing could be closer related to the damage evolution monitoring in the field, where complex loading conditions can render AE analysis very challenging.

The analysis of the AE data presented in this study can be used as a basis for the fundamental understanding of the AE testing and its application in SHM of FRC materials. However, additional research on the data clustering needs to be carried out using supervised algorithms

to automatically classify the detected signals into clusters during the acquisition of the AE signals.

Further research can be carried out to develop an AE system capable of detecting structural degradation in maritime structures in the field. This would require extensive research, as the optimum positioning of the AE sensors, an appropriate filtering methodology and an effective technique in analysing the recorded signals must initially established. Prolonged exposure to in-service conditions can cause serious environmental degradation. Therefore, the effectiveness of AE in monitoring damage growth in environmentally eroded FRC components needs to be assessed in order to lay the foundations for the development of an AE system working effectively and consistently through all the service life of a maritime structure. The use of such system will increase the safety of FRC maritime structures and it would decrease the maintenance costs since the position and the extent of damage will be known before the scheduled maintenance of the vessel.

Nonetheless the usefulness of the present work is obvious and it is hoped that these can be used by researchers following up this work.

APPENDIX

A.1 Automated data clustering algorithms

This section presents the main principles and steps of commonly used unsupervised clustering algorithms.

A.1.1 K-Means

The k-means is an iterative algorithm proposed by McQueen in 1967 [209]. It is widely used for data clustering. The k-means aims to minimise the squared distance error function between a data point X_l and a cluster centre k_j for each cluster k according to: [210, 211].

$$J = \sum_{j=1}^{m} \sum_{l=1}^{n} \left\| X_l - k_j \right\|^2 \qquad \text{Equation A.1}$$

$$X_l \in C_j$$

Where:

- C_j is the group of data points that compose the cluster
- m is the number of clusters and is a user defined parameter.
- n is the total number of data points
- $\left\| X_l^{(k)} - k_j \right\| = \sqrt{\sum_{i=1}^{n} \left(X_{l_i} - k_{j_i} \right)^2}$ Equation A.2

The above expression is the Euclidean distance between a data point $X_l = (X_{l_1}, X_{l_2}, X_{l_3}, \ldots, X_{l_n})$ and the corresponding cluster centre $k_l = (k_{l_1}, k_{l_2}, k_{l_3}, \ldots, k_{l_n})$ in a Euclidean n-dimensional space. The Euclidian distance between each data point and the cluster centre is widely used with the k-means algorithm [209-215].

The k-means algorithm can be described as follows [209-215]:

1. The algorithm starts by randomly selecting the cluster centres Y_i for each cluster C_j.

2. The algorithm assigns each data point to the cluster C_j in accordance with the criterion of minimum squared distance.

3. When all data points have been assigned to a cluster C_j, the algorithm moves the cluster centres in order to minimise the squared distance error and get a better classification.

4. If the cluster centre co-ordinates remain unchanged, then the algorithm has converged and the procedure is terminated. Otherwise, the algorithm returns to step 2 and repeats the same processes until convergence occurs, or until the number of iterations defined by the user has been exceeded.

A.1.2 Forgy

The Forgy algorithm is a pattern recognition technique proposed by Forgy in 1965 [211, 216, 217]. Forgy's algorithm is a modified variant of k-means equipped with additional functions, which cause the creation of new clusters and deletes the small clusters from the clustering process. These additional functions result in a better control of the clustering and produce more accurate results. Along with k-means, Forgy is an iterative algorithm aiming primarily to minimise the squared distance error function (Euclidean distance) between a data point and a cluster centre for a given number of clusters [218-220].

According to Dubes and Jain (1975) [220], the Forgy algorithm can be described as follows:

1. The algorithm starts by randomly selecting the cluster centres for each cluster.

2. The algorithm assigns each data point to the closest cluster according to the criterion of minimum squared distance

3. The algorithm recalculates the cluster centres in order to represent the mean sample of all the data points by minimising the squared distance criterion between the data points and the cluster centres. The first three steps of the Forgy algorithm are identical to k-means.

4. If a data point is adequately separated from the existing structure, it cannot be assigned to any cluster and a new cluster that is centred at this point is created. When all new clusters have been created, the algorithm repeats the steps 3 and 4 until two

successive iterations through all the data points lead to the same clustering results, or until the number of iterations defined by the user for steps 3 and 4 has been exceeded.

A new cluster is created if:

$$\left| d_{k_0}(i) - \bar{d}(i) \right| \leq \left| \bar{d}(i) \right| T_F \qquad \text{Equation A.3}$$

Where:

- d_{k_0} is the distance between the data point i and the nearest cluster centre k_0.
- $\bar{d}(i)$ is the average distance between a data point i all the cluster centres n.

The average distance can be expressed as:

$$\bar{d}(i) = \left(\frac{1}{n}\right) \sum_{k=1}^{n} d_k\ (i) \qquad \text{Equation A.4}$$

  - d_k is the distance between a data point i and the corresponding cluster centre k.

- T_F is a user defined parameter in the range between 0 and 1. This parameter controls the generation of new clusters. By increasing the value of T_F more clusters will be generated

5. The algorithm compares the number of points N_k in each cluster k to a user defined threshold limit that indicates the minimum acceptable number of points M in a single cluster. If the number of data points in an existing cluster N_k is smaller than the threshold limit, the cluster is deleted and corresponding data points are omitted from the clustering process being regarded as outliers.

6. The algorithm returns to step 2 and repeats the same process until the cluster centres remain unchanged, or until the number of iterations defined by the user has been exceeded.

A.1.3 ISODATA

ISODATA (Iterative Self-Organising Data Analysis Technique) is an unsupervised data clustering algorithm proposed by Ball and Hall in 1965 [221]. ISODATA is a k-means based algorithm and incorporates several functions which control the clustering process by merging and splitting clusters [218, 222-225]. These additional features offer a better control on the clustering compared to Forgy and k-means.

According to the descriptions given by Tou and Gonzalez (1974) [222], the steps of ISODATA can be comprehensively summarised as follows:

1. Before the algorithm starts the following input parameters must be specified by the user:
    - The initial number of clusters, **m**
    - The Desired number of clusters, **K**
    - The minimum number of data points assigned in a single cluster, $\boldsymbol{\theta_n}$
    - The standard deviation parameter for all the clusters, $\boldsymbol{\theta_s}$
    - The merging parameter which indicates the maximum allowable distance between the cluster centres, $\boldsymbol{\theta_c}$
    - The maximum number of pairs of clusters that can be merged, **L**
    - The number of iterations to be performed by the k-means function of the algorithm, $\mathbf{I_{k-m}}$ [218].
    - The maximum number of iterations that control the splitting and the merging steps, **I**. According to the Noesis software user manual [218], the k-means function will be performed as many times as the number **I** indicates.

2. The algorithm stars by randomly selecting the m initial cluster centres. Like k-means and Forgy, ISODATA is an iterative algorithm, which assigns each data point to the nearest cluster centre, by aiming to minimise the squared distance error function (Euclidean distance) between a data point and the corresponding cluster centre. This step is executed as many times as the I_{k-m} parameter indicates, or if an initial convergence occurs. This step is actually the k-means algorithm.

3. Clusters with fewer than $\boldsymbol{\theta_n}$ data points are deleted and the corresponding data points are treated as outliers and they are omitted from the clustering process.

4. The algorithm updates the cluster centres k_j according to:

$$\boldsymbol{k_j = \frac{1}{n_j} \sum_{x \in C_i} X} \ , \qquad \boldsymbol{j = 1, 2, 3, \ldots, n_c} \qquad \text{Equation A.5}$$

Where:

- K_j is a cluster centre
- C_j is the corresponding cluster
- n_j is the number of data points in a cluster C_j
- x (x_1, x_2, x_3,…, x_n) is a data point vector
- n_c is the number of clusters

5. The algorithm calculates the average distance $\bar{d}_j$ of data points in a cluster C_j from the corresponding cluster centre according to:

$$\bar{d}_j = \frac{1}{n_j} \sum_{x \in C_j} d_j \ , \qquad j = 1,2,3, \ldots, n_c \qquad \text{Equation A.6}$$

Where:

- n_j is the number of data points in a cluster C_j
- n_c is the number of clusters
- d_j is the distance between a data point x and the corresponding cluster centre k_j. The distance is defined according to:

$$d_j = \|x - k_j\|$$ Equation A.7

6. The algorithm calculates the overall distance $\bar{d}$ of the data points from their respective cluster centres according to:

$$\bar{\boldsymbol{d}} = \frac{\mathbf{1}}{\boldsymbol{N}} \sum_{\boldsymbol{j=1}}^{\boldsymbol{n_c}} \boldsymbol{n_j}\, \overline{\boldsymbol{d_j}}$$ Equation A.8

Where:

- N the total number of data points
- n_c is the number of clusters
- $\overline{d_j}$ is the average distance mentioned above

7. In this step the algorithm determines if it will proceed to the subsequent splitting or merging steps.

Therefore:

- If the maximum number of iterations I is reached, or if the last iteration is being executed, then the algorithm sets the merging parameter which indicates the maximum allowable distance between the cluster centres, θ_c=0 and moves to step 11.
- If $n_c \leq K/2$, (K is the desired number of clusters) the algorithm moves to step 8 for splitting.

- If $n_c \geq K/2$ or if the current iteration, in which the algorithm is in, is even-numbered, then the algorithm moves to step 11, or else it moves to step 8.

8. The algorithm calculates the standard deviation σ_j (σ_{1j}, σ_{2j}, σ_{3j},… σ_{nj}) for each cluster according to:

$$\sigma_{ij} = \sqrt{\frac{1}{n_j}\sum_{x \in C_j}\left(x_{li} - k_{ji}\right)^2} \qquad \text{Equation A.9}$$

$$i = 1,2,3,\ldots n \quad , \quad j = 1,2,3,\ldots, n_c$$

σ_{ij} represents the standard deviation of the data points σ_j assigned in a cluster C_j, along with a coordinate axis I, which represents the i^{th} dimension feature of a data point, cluster centre and a standard deviation vector.

Therefore:

- x_{li}, represents i^{th} feature of the l^{th} data point in a cluster C_j
- k_{ij} represents the i^{th} feature of the cluster centre k_j
- n_j is the number of data points in a cluster C_j
- n_c is the number of clusters

9. The algorithm finds the maximum standard deviation σ_{jmax} of each cluster C_j.

10. The algorithm compares each σ_{jmax} to the standard deviation parameter θ_s.

If $\sigma_{jmax} > \theta_s$, the current cluster C_j is split

only if $\bar{d}_j > \bar{d}$, and $n_j > (2\theta_n + 1)$

or $n_c \leq K/2$

A cluster C_j is split in two clusters (C_j^+ and C_j^-) and two new cluster centres k_j^+ and k_j^- are created, one of each side of the initial cluster centre k_j.

$$\boldsymbol{k_j^+ = k_j + \gamma_j} \qquad \text{Equation A.10}$$

$$\boldsymbol{k_j^+ = k_j - \gamma_j} \qquad \text{Equation A.11}$$

The γ_j parameter is related to the maximum standard deviation $\sigma_{j\,max}$ according to:

$$\boldsymbol{\gamma_j = k\sigma_{jmax}} \qquad \text{Equation A.12}$$

- k is a parameter ranging from 0 to 1.

The key requirement of selecting the value of γ_j parameter is that it should provide a small detectable distance difference between a random data point and the two new cluster centres. This distance must not be too large, as it can radically modify the existing cluster structure.

After splitting, the algorithm returns to step 2 and repeats the same process. If no further splitting occurs the algorithm proceeds to step 11.

11. The algorithm calculates in pairs the distances between all the cluster centres according to:

$$\boldsymbol{d_{ij} = \|k_i - k_j\|}, \quad \boldsymbol{i = 1, 2, \ldots, n_c - 1}, \quad \boldsymbol{j = i + 1} \qquad \text{Equation A.13}$$

12. The algorithm calculates all the d_{ij} distances against the θ_c input parameter, which indicates the maximum allowable distance between the cluster centres. Those pairs of distances that are less than θ_c are sorted in a list in an ascending distance order:

$$d_{i_1 j_1} < d_{i_2 j_2} < \cdots < d_{i_L j_L} \qquad \text{Equation A.14}$$

Where L, is the maximum number of clusters that can be lumped.

13. In this step, the algorithm is merging two clusters in one according to:

$$k_l^* = \frac{1}{N_{i_l} + N_{j_l}} \left[N_{i_l}(k_{i_l}) + N_{j_l}(k_{j_l}) \right] \qquad \text{Equation A.15}$$

Where

- k_l^*, is the new cluster centre,
- k_{i_l} and k_{j_l} are the pair of clusters that are about to be merged
- N_{i_l} is the number of data points assigned in the cluster centre k_i
- N_{j_l} is the number of data points assigned in the cluster centre k_j

The first pair of clusters in the list is merged first. For each iterative step, a cluster can be merged only once. Consequently the next pair of clusters is merged only if neither of the two cluster centres has been used for merging during the same iteration.

After the merging is completed, the old pair of clusters is deleted and a new cluster centre is created. The merging process results in the new cluster centre being representative of the true average point of the initial cluster centres.

14. If the maximum number of iterations I is reached the algorithm terminates. Otherwise, the algorithm returns to step 2 and repeats the same process until I is reached. If convergence occurs in less iterations, the algorithm stops [218]

A.1.4 SOM-LVQ

The LVQ (Learning Vector Quantization) neural network is a data clustering algorithm introduced by Kohonen and is similar to the Kohonen's SOM (Self Organising Map). The SOM and LVQ algorithms can be used together for optimised clustering results. When these two algorithms are used together the clustering process consists of an unsupervised SOM stage and a supervised LVQ stage [226-230].

A.1.4.1 SOM algorithm fundamentals

The Kohonen's Self-Organising Map (SOM) is an artificial neural network used for data processing and clustering applications. The SOM is implemented for the visualisation of high-dimensional data on a low-dimensional map, while it retains the information and metric relationships between the elements of the displayed data set [227]. As it can be seen in Figure A.1, SOM consists of an input layer and an output grid layer of neurons, or nodes [227, 229]. The input layer represents the original input data, while the output nodes represent the data that are organised in a map or grid. Each neuron is connected to all the elements of the data set that compose the input layer [230]. The algorithm organises the input data vectors into a feature map where neurons with similar features are closer to each other, while neurons with dissimilar features are placed far from each other. Consequently, the SOM is actually a clustering diagram and a similarity graph as well [228].

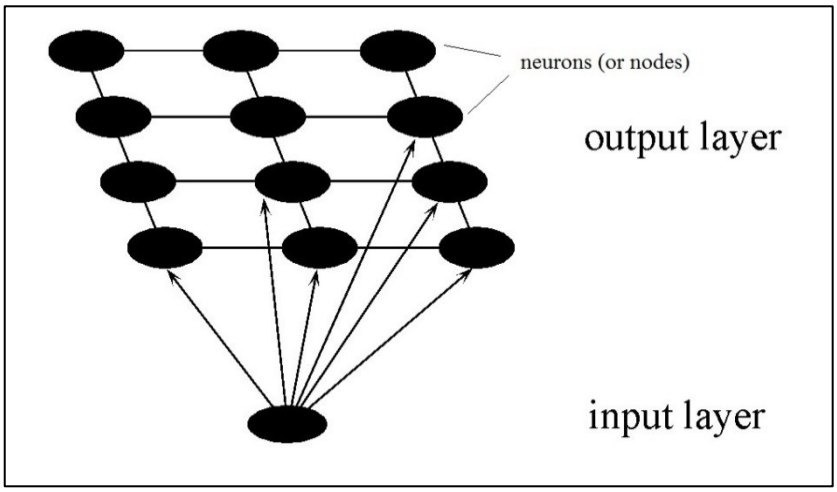

Figure A.1: Self-Organised Map structure.

The SOM algorithm recursively arranges the input data space in an array of neurons. Most frequently, the array is a two dimensional grid. Every neuron in the map is associated to a weight vector m_i. Before the processing starts, the weight vectors are initialised randomly as starting points. The weight vectors obtain their map-order values as the map is being ordered, showing thereafter the algorithm's self-organising effect.

The input vectors are then connected to all the neurons in the grid. The distance between the input vectors, x_i, and weight vectors, m_i, is measured using the Euclidean distance. The minimum distance defines the winning vector, m_c, of the neuron c that is closest to an input vector, x_i, providing a good approximation of the original input data.

The winning vectors are defined as follows [226]:

$$\|x_i - m_c\| = \min\{\|x_i - m_i\|\} \quad \text{Equation A.16}$$

$$\|x_i - m_c\| < \|x_i - m_i\| \quad \text{Equation A.17}$$

During the construction of the map the learning process takes place. The values of the neurons that are close to the winning vector up to a certain distance range will be recursively assigned in the iterations of the algorithm, according to [226]:

$$m_i(t+1) = m_i(t) + h_{ci}(t)\,[x(t) - m_i(t)] \quad \text{Equation A.18}$$

Where:

- t = 0,1,2,3, … is the discrete-time coordinate and increases as the algorithm is executed
- h_{ci} (t) is the neighbouring function and expresses the smoothing effect on the weight vectors m_i of the neurons around the winning vector m_c, and refers to the number of the neighbouring neurons, N_c, around the winning vector node C.

The number of neurons, N_c, can be defined as $N_c = N_c(t)$ and it is a decreasing function of time.

The neighbourhood function can be simply expressed as:

$$h_{ci}(t) = \alpha(t) \qquad \text{Equation A.19}$$

Where:

- $\alpha(t) \in [0,1]$ is the learning rate factor and decreases with the regression steps.

The h_{ci} (t) function can be also expressed as follows:

$$h_{ci} = \alpha(t) \exp\left(-\frac{\|r_c - r_i\|^2}{2\sigma^2(t)}\right) \qquad \text{Equation A.20}$$

Where:

- r_c is the location of the winning vectors in the grid
- r_i is the location of the weight vectors in the grid

- $\sigma(t)$ defines the width of the N_c (t) and it is decreasing with time
- $\|r_c - r_i\|$ is the average width of the neighbouring function and defines the stiffness of the grid.

If the neurons belong to the group of the neighbourhood around the winning vector, the neighbouring function can be simplified to $h_{ci}(t) = \alpha(t)$. In the opposite case, the neighbouring function will be $h_{ci}(t) = 0$.

Special caution is required when the size of the neuron's neighbourhood $N_c(t)$ is defined. If the map ordering starts with a small N_c, the map will not be ordered globally. Improper ordering of the network can be avoided if the ordering starts with a wide $N_c(t)$. The initial range of the $N_c(t)$ can extend up to the half size of the network. As the ordering takes place, the initial width will decrease with time. Adequate ordering takes place after the first 1000 iterations and N_c radius can shrink gradually to one unit [226].

During the initial ordering iterations the learning rate factor, $\alpha(t)$, carries high values that are close to 1 gradually reducing with time as the ordering takes place. The ordering of the map takes place in the first phase of the algorithm, as the remaining iterations are required for the fine adjustments of the map. During the refinement of the network the learning rate factor $\alpha(t)$ will get values below 0.2. The number of iterations for the refinement phase must be reasonably high and can extend up to 500 times the number of neurons in the grid. The SOM algorithm requires therefore a very high number of iterations in order to achieve a proper network ordering. However, because the algorithm is very light, proper map ordering can be achieved with relatively little computational effort [226].

A.1.4.2 The Batch SOM algorithm

The version of the SOM algorithm as it was described in the previous section, can be replaced by a batch version of the algorithm which is faster and does not require any specification of the learning rate factor α(t) [226, 227].

Examining the convergence behaviour of the sequence

$$m_i(t+1) = m_i(t) + h_{ci}(t)\,[x(t) - m_i(t)] \qquad \text{Equation A.21}$$

It is required that for $t \to \infty$,

$$m_i(t+1) = m_i(t), \qquad \text{Equation A.22}$$

even if $h_{ci}(t) \neq 0$

Therefore, the convergence limit of the weight vectors sequence m_i^* is approximated as follows [227]:

$$m_i^* = \frac{\sum_t h_{ci} x(t)}{\sum_t h_{ci}} \qquad \text{Equation A.23}$$

If the neighbouring function, h_{ci}, is defined in terms of the neighbourhood set N_c, a simpler expression for the m_i* arises [227]:

$$m_i^* = \frac{\sum_{x(t)\in U_i} x(t)}{n(U_i)} \qquad \text{Equation A.24}$$

Where:

- U_i is the union of the Voronoi sets V_i that belong to the neighbouring set N_c.
- n is the number of data that belong to the Voronoi union U_i

The Voroinoi set V_i is a domain of values in the input data x_i that lie closest to the winning vectors and they are able to update the weight vectors, and henceforth the ordering of the map [19,20].

The Batch-SOM algorithm then is summarised as follows [227]:

1. The algorithm starts by initialising the values of the m_i* vectors (the initialisation is usually preformed randomly)
2. The algorithm assigns the input data x_i to the closest vector m_i* according to the Euclidean distance metric.
3. The algorithm computes the mean input vectors $\overline{x_1}$ in each Voronoi set closest the m_i* and updates the weight vectors.
4. The algorithm repeats the steps 2-3 until the map ordering is considered as steady.

Another expression for the m_i* is obtained when the mean of the input data $\bar{x}_i$ in a Voronoi set V_j and a neighbouring function h_{ji} are weighted by the number n_j of samples in the V_j [227].

$$m_i^* = \frac{\sum_j n_j h_{ji} \overline{x_j}}{\sum_j n_j h_{ji} \overline{x_j}} \qquad \text{Equation A.25}$$

The sum over j is taken for all the input data in the network. In the case were the neighbourhood set N_i is used instead of the h_{ji} [227]:

$$m_i^* = \frac{\sum_{j \in N_i} n_j \overline{x_j}}{\sum_{j \in N_i} n_j} \qquad \text{Equation A.26}$$

The algorithm can be very effective and produce satisfactory results if the initial vectors are roughly ordered. Improper ordering can lead to poor ordering results, which will not be representative of the initial dataset structure. The shrinking of the neighbouring set N_j, takes place as the map ordering takes place during the iterations of the steps 2 and 3. In the end, N_i may contain only one neuron and the last remaining iterative steps of the Batch-SOM algorithm are equivalent to the k-means algorithm and approximates the density function of the input data x_i [226].

A.1.4.3 LVQ algorithm fundamentals

The Self Organising Map algorithm is used to arrange the input data x(t) into a grid. The fine tuning of the map ordering is then achieved with the Learning Vector Quantization (LVQ) algorithm [229, 230]. The LVQ uses the initial values that have been previously obtained by the SOM. In the next steps the algorithm uses the class labels of the input data x(t) to fine tune the ordering of the weight vectors m_i on the grid, by defining the winning vectors m_c [228].

The LVQ algorithm defines the winning vectors m_c according to [226-228, 230, 231]:

- $m_c(t+1) = m_c(t) + a(t)[x(t) - m_c(t)]$ Equation A.27

  If the input vector x(t) and the winning vector $m_c(t)$ belong to the same class.

- $m_c(t+1) = m_c(t) - a(t)[x(t) - m_c(t)]$ Equation A.28

  If the input vector x(t) and the winning vector $m_c(t)$ belong to different classes.

The learning rate factor a(t) ($0 < a(t) < 1$) should start with a very small value around 0.01-0.02 and over time, will gradually decrease to zero [228, 231]. After the winning vectors have been redefined, the weight vectors are updated according to:

$$m_i(t+1) = m_i(t) \quad for\ i \neq c$$ Equation A.29

Where:

- c: is the class label index.

The minus sign in equation $m_c(t+1) = m_c(t) - a(t)[x(t) - m_c(t)]$, defines the optimised corrections for the class in which the winning vector m_c was initially defined. The probability function of the sample data in which a winning vector m_c belongs, is subtracted from the probability function of a neighbouring and overlapping class. The difference between the probability functions of two neighbouring classes drops to zero at the class borders leaving behind a zone with very few weight vectors mi. Such zones are also known as Bayesian borders and divide the map into separate class regions. Therefore, the LVQ algorithm tends to arrange the network by placing the weight vectors away from the class borders [231].

A.1.4.4 Batch LVQ algorithm

The Batch LVQ is similar to the basic LVQ algorithm and can be simply described in a compact form [226, 227]:

$$m_c(t+1) = m_c(t) + a(t)s(t)\delta_{ci}[x(t) - m_c(t)] \quad \text{Equation A.30}$$

Where:

- s(t) = 1 if x(t) and the corresponding winning vector m_c belong to the same class
- s(t) = -1 if x(t) and the corresponding winning vector m_c belong to different classes.
- δ_{ci} is the Kronecker's delta

$$\delta_{ci} = 1 \; for \; c = i$$

$$\delta_{ci} = 0 \; for \; c \neq i$$

The class labels are defined dynamically. The steps of the Batch-LVQ are briefly described as follows [226, 227]:

1. The algorithm starts by accepting the initial values of the weight vectors obtained from the SOM algorithm.

2. The algorithm uses the class labels to assign the input data x(t) to the corresponding winning vectors.

3. The algorithm determines the labels of the neurons according to the population of the input data with the same label.

4. The algorithm determines whether the input data x(t) and the winning vectors $m_c(t)$ belong to the same class by multiplying the input data with the corresponding s(t) factor.

5. For each neuron in the network the algorithm determines the new value of the reference weight vectors according to:

$$m_i^* = \frac{\sum_{t'} s(t')x(t')}{\sum_{t'} s(t')}$$ Equation A.31

The above formula is applied for the indices t' of the input data that are assigned under a corresponding node i

6. The steps 3-5 are repeated until the ordering of the map is considered steady.

A.2 Fast Fourier Transform

One of the most common signal processing technique is the Fast Fourier Transform (FFT) algorithm which generates the frequency spectrum of a continuous signal. The FFT is a variant of the Discrete Fourier Transform (DFT), but it is equipped with clever algorithms to perform the same function as the DFT in considerably less time. The FFT converts a continuous time signal x(t) from the time domain into its frequency domain representation according to the following expression [232]:

$$S_x(\omega) = \int_{-\infty}^{\infty} x(t)e^{-i\pi\omega t}\, d(t)$$ Equation A.32

Where:

- $S_x(f)$ is the frequency domain representation of the signal
- x(t) is the time domain representation of the signal
- $i = \sqrt{-1}$

The FFT process is fully reversible and the frequency domain representation can be converted back to its time domain representation according to:

$$x(t) = \int_{-\infty}^{\infty} S_x(\omega) e^{i\pi\omega t} d(\omega)$$ Equation A.33

The time domain representation is a record of the changes to a signals parameter such as the voltage or amplitude over time. An example of the time domain representation is the waveform of the recorded signal. The frequency domain is the representation of a signal with respect to its frequency. The frequency domain representation is also known as the frequency spectrum of the signal, and each peak on the spectrum represents a component frequency of the signal [232]. In general, signal processing on the frequency domain generates compact and more detailed information, while it demands less complex mathematical and algorithmic operations compared to a time domain analysis.

The FFT algorithm can be described as follows [233]:

1. The initial input data for the algorithm are the input signal x(t) and the sampling frequency f_s. The sampling frequency is determined from the DAQ system, while other parameters such as the length L of the signal and the signal's time vector t are obtained directly from the input signal.

2. The length L of the FFT must be a power of two ($L=2^n$). If the length L of FFT is not a power of two, then the length is padded with zeros up to the next power of two, in order to improve the performance of the algorithm.

3. Next, then algorithm performs a DFT to convert the input signal to the frequency domain. The frequency domain representation is in essence a graph of the signal's magnitude versus the frequency.

4. Then the magnitude axis of the frequency domain is normalised by dividing the magnitude values with the total length L of the FFT.

   The FFT power spectrum contains sufficient information up to the first half of its frequency range, which is known as the Nyquist frequency. The Nyquist frequency f_N, is the half of the sampling rate ($f_N = f_s/2$) of the recorded signal. The second half of the FFT spectrum above the Nyquist frequency is symmetrical to the first half. Therefore, the FFT power spectrum can be plotted up to the Nyquist frequency. By increasing the sampling rate, more peaks can appear at higher frequencies in the FFT spectrum, indicating the possible presence of defects or different failure modes. In contrast, decreasing the sampling rate will remove peaks at higher frequencies that can be associated with defects or different failure modes.

5. The algorithm plots the FFT power spectrum until the Nyquist frequency.

The FFT algorithm can be summarised in the flowchart shown in Figure A.2.

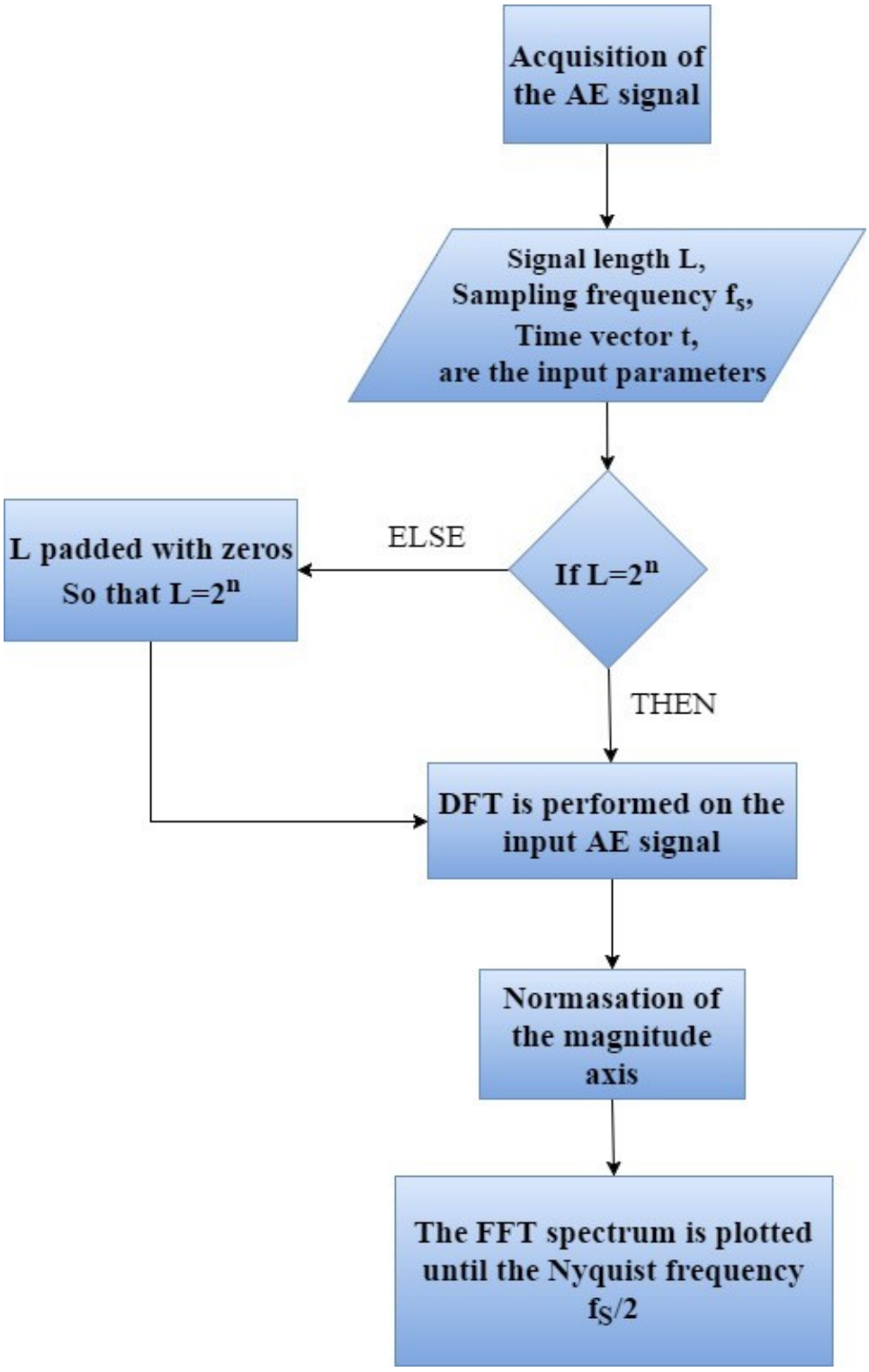

Figure A.2: FFT algorithm flow chart

BIBLIOGRAPHY

1. Hull, D. and T.W. Clyne., *An Introduction to Composite Materials*. 1996: Cambridge University Press.
2. *ASM Handbook, Vol 21*. 2001: ASM International.
3. Beltsios K, *Science and Technology of Composite Materials*. 2008, University of Ioannina.
4. G Papanikolaou and D. Mouzakis, *Composite Materials*. 2007, Klidarithmos Publications: Athens.
5. Gay, D., *Composite materials: design and applications*. 2003: CRC press.
6. *Airbus S.A.S, Innovation*.
7. *A350 XWB*.
8. *The Boeing Company , Boeing 787 Dreamliner*. available on www.boeing.com website.
9. Jacob, A., *Built in Italy: the Lamborghini Avendator.* Reinforced Plastics, 2013. **57**(5): p. 29-31.
10. Thornton, P.H., J.J. Harwood, and P. Beardmore, *Fiber-reinforced plastic composites for energy absorption purposes.* Composites Science and Technology, 1985. **24**(4): p. 275-298.
11. Thornton, P.H. and R.A. Jeryan, *Crash energy management in composite automotive structures.* International Journal of Impact Engineering, 1988. **7**(2): p. 167-180.
12. Mamalis, A.G., et al., *Crashworthy capability of composite material structures.* Composite Structures, 1997. **37**(2): p. 109-134.
13. Park, C.-K., C.-D. Kan, and W.T. Hollowell, *Evaluation of crashworthiness of a carbon-fibre-reinforced polymer (CFRP) ladder frame in a body-on-frame vehicle.* International Journal of Crashworthiness, 2014. **19**(1): p. 27-41.
14. Chalmers, D.W., *The Potential for the use of composite materials in marine structures.* Marine Structures, 1994. **7**(2–5): p. 441-456.
15. Grabovac, I., *Bonded composite solution to ship reinforcement.* Composites Part A: Applied Science and Manufacturing, 2003. **34**(9): p. 847-854.
16. Critchfield, M.O., T.D. Judy, and A.D. Kurzweil, *Low-cost design and fabrication of composite ship structures.* Marine structures, 1994. **7**(2): p. 475-494.
17. Slater, J.E., *Selection of a blast-resistant GRP composite panel design for naval ship structures.* Marine Structures, 1994. **7**(2–5): p. 417-440.
18. Mouritz, A.P., et al., *Review of advanced composite structures for naval ships and submarines.* Composite Structures, 2001. **53**(1): p. 21-42.
19. Smith, C.S., *Design of marine structures in composite materials*. 1990, Elsevier Science: London.
20. Hayman, B., A. Echtermeyer, and D. McGeorge. *Use of fibre composites in naval ships*. in *WARSHIP-INTERNATIONAL SYMPOSIUM THEN CONFERENCE-*. 2001.
21. Hentinen, M., M. Hildebrand, and M. Visuri, *Adhesively bonded joints between FRP sandwich and metal.* Different concepts and their strength behaviour. Espoo, 1997.
22. Cao, J. and J.L. Grenestedt, *Design and testing of joints for composite sandwich/steel hybrid ship hulls.* Composites Part A: Applied Science and Manufacturing, 2004. **35**(9): p. 1091-1105.
23. Kabche, J.-P., et al., *Experimental characterization of hybrid composite-to-metal bolted joints under flexural loading.* Composites Part B: Engineering, 2007. **38**(1): p. 66-78.
24. Boyd, S.W., et al., *Optimisation of steel–composite connections for structural marine applications.* Composites Part B: Engineering, 2008. **39**(5): p. 891-906.
25. Boyd, S., et al., *Integrity of hybrid steel-to-composite joints for marine application.* Proceedings of the Institution of Mechanical Engineers, Part M: Journal of Engineering for the Maritime Environment, 2004. **218**(4): p. 235-246.

26. Antão, P. and C. Guedes Soares, *Causal factors in accidents of high-speed craft and conventional ocean-going vessels.* Reliability Engineering & System Safety, 2008. **93**(9): p. 1292-1304.
27. Graziano, A., A.P. Teixeira, and C. Guedes Soares, *Classification of human errors in grounding and collision accidents using the TRACEr taxonomy.* Safety Science, 2016. **86**: p. 245-257.
28. Guedes Soares, C., E. Bitner-Gregersen, and P. Antao. *Analysis of the frequency of ship accidents under severe North Atlantic weather conditions*. in *Proceedings of the Conference on Design and Operation for Abnormal Conditions II, RINA, London*. 2001.
29. Summerscales, J., *Manufacturing defects in fibre-reinforced plastics composites.* INSIGHT, 1994. **36**(12): p. 936-942.
30. Croft, K., et al., *Experimental study of the effect of automated fiber placement induced defects on performance of composite laminates.* Composites Part A: Applied Science and Manufacturing, 2011. **42**(5): p. 484-491.
31. Tavares, S.S., V. Michaud, and J.A.E. Månson, *Through thickness air permeability of prepregs during cure.* Composites Part A: Applied Science and Manufacturing, 2009. **40**(10): p. 1587-1596.
32. Afendi, M., W.M. Banks, and D. Kirkwood, *Bubble free resin for infusion process.* Composites Part A: Applied Science and Manufacturing, 2005. **36**(6): p. 739-746.
33. Grunenfelder, L.K. and S.R. Nutt, *Void formation in composite prepregs – Effect of dissolved moisture.* Composites Science and Technology, 2010. **70**(16): p. 2304-2309.
34. Liu, L., et al., *Effects of cure cycles on void content and mechanical properties of composite laminates.* Composite Structures, 2006. **73**(3): p. 303-309.
35. Ghiorse, S., *Effect of void content on the mechanical properties of carbon/epoxy laminates.* SAMPE quarterly, 1993. **24**(2): p. 54-59.
36. Bowles, K.J. and S. Frimpong, *Void Effects on the Interlaminar Shear Strength of Unidirectional Graphite-Fiber-Reinforced Composites.* Journal of Composite Materials, 1992. **26**(10): p. 1487-1509.
37. Surya D. Pandita, Mayorkinos Papaelias, and Gerard F. Fernando, *Report on MOSAIC FP7 project deliverable 2.2*. Novemeber 2013, School of Metallurgy and Materials, University of Birmingham.
38. Kapadia, A., *Best Practice Guide on Non-Destructive Testing of Composite Materials*. National Composites Network.
39. Smith, R., *Composite defects and their detection.* Materials Science and Engineering, 2009. **3**: p. 103-143.
40. Sohn, H., et al., *A review of structural health monitoring literature: 1996-2001*. 2004: Los Alamos National Laboratory Los Alamos, NM.
41. Balageas, D., et al., *Structural health monitoring for composite structures.* OFFICE NATIONAL D ETUDES ET DE RECHERCHES AEROSPATIALES ONERA-PUBLICATIONS-TP, 2001(214).
42. Dupont, M., et al., *Permanent monitoring of damaging impacts by a piezoelectric sensor based integrated system.* Structural Health Montoring 2000, 1999: p. 561-570.
43. Majumder, M., et al., *Fibre Bragg gratings in structural health monitoring—Present status and applications.* Sensors and Actuators A: Physical, 2008. **147**(1): p. 150-164.
44. Pollock, A.A., *Acoustic Emission Inspection*. 2003, Physical Acoustics Corporation, MISTRAS Holdings Group.
45. Pollock, A.A., *Back to Basics: Loading and Stress in Acoustic Emission Testing*. 2004, American Society for Nondestructive Testing, Inc.
46. Okoroafor, E.U. and R. Hill., *Relating acoustic emission signal parameters to the strength of fibres used in the manufacture of polymeric composites.* Ultrasonics, 1995. **33** (2).
47. Bagherpour, S., *Chapter 6, Fibre Reinforced Polyester Composites*, INTECH, Editor. 2012.
48. Jones, R.M., *Mechanics of composite materials*. 1998: CRC press.

49. *The making of carbon fiber, Online source: http://www.compositesworld.com/blog/post/the-making-of-carbon-fiber , Composites World, Gardner Business Media, Inc*.
50. *Composite Materials Handbook*.
51. Beardmore, P. and C.F. Johnson, *The potential for composites in structural automotive applications.* Composites Science and Technology, 1986. **26**(4): p. 251-281.
52. *Historical pricing, Online source: http://www.plasticsnews.com/resin/thermosets/historical-pricing*.
53. Smith, R., *Composite Defects and Their Detection.* Materials Science and Engineering, 1997. **3**: p. 10-14.
54. *Hand Lay-up, Online source: https://www.wacker.com/cms/en/industries/pl_composites/pl_comp_appl/handlayup.jsp*.
55. *Spray-Up, Online source: http://www.nuplex.com/composites/processes/spray-up*.
56. *Resin transfer moulding, Online source: http://www.nuplex.com/composites/processes/resin-transfer-moulding*.
57. R. Singh and G. Soni, *Composites Manufacturing, Manufacturing Processes II Notes*, in *ME 338 Manufacturing Processes II Notes*. Department of Mechanical Engineering, Indian Institute of Technology, Bombay.
58. Bai, Y. and W.-L. Jin, *Chapter 2 - Marine Composite Materials and Structure*, in *Marine Structural Design (Second Edition)*, Y. Bai and W.-L. Jin, Editors. 2016, Butterworth-Heinemann: Oxford. p. 19-37.
59. Smith, C., F. Eng, and D. Chalmers, *Design of ship superstructures in fibre-reinforced plastic.* Naval Architect, 1987.
60. Høyning, B. and J. Taby. *Warship design: the potential for composites in frigate superstructures*. in *RINA conference "Lightweight Construction Latest Developments", London*. 2000.
61. High Strength Structural Steel for Marine Applications, Online source: http://www.aasteel.com/ah-36-dh-36-eh-36-40.html.
62. *Mechanical Properties of Carbon Fibre Composite Materials, Fibre / Epoxy resin, Online Source: http://www.performance-composites.com/carbonfibre/mechanicalproperties_2.asp*.
63. Tanimoto, T. and S. Amijima, *Progressive Nature of Fatigue Damage of Glass Fiber Reinforced Plastics.* Journal of Composite Materials, 1975. **9**(4): p. 380-390.
64. Allah, M.H.A., et al., *Effect of fibre volume fraction on the fatigue behaviour of GRP pultruded rod composites.* Composites Science and Technology, 1996. **56**(1): p. 23-29.
65. Brunbauer, J. and G. Pinter, *Effects of mean stress and fibre volume content on the fatigue-induced damage mechanisms in CFRP.* International Journal of Fatigue, 2015. **75**: p. 28-38.
66. Chen, N.-Z. and C. Guedes Soares, *Reliability assessment for ultimate longitudinal strength of ship hulls in composite materials.* Probabilistic Engineering Mechanics, 2007. **22**(4): p. 330-342.
67. Chen, N.-Z., H.-H. Sun, and C. Guedes Soares, *Reliability analysis of a ship hull in composite material.* Composite Structures, 2003. **62**(1): p. 59-66.
68. Hassoon, O.H., M. Tarfaoui, and A. El Moumen, *Progressive damage modeling in laminate composites under slamming impact water for naval applications.* Composite Structures, 2017. **167**: p. 178-190.
69. Shah Khan, M.Z. and G. Simpson, *Mechanical properties of a glass reinforced plastic naval composite material under increasing compressive strain rates.* Materials Letters, 2000. **45**(3–4): p. 167-174.
70. Gargano, A., et al., *Comparative assessment of the explosive blast performance of carbon and glass fibre-polymer composites used in naval ship structures.* Composite Structures, 2017. **171**: p. 306-316.
71. Harboe-Hansen, H., *Norway's new Skjold class FPBs.* The Naval Architect, 1996.
72. Foxwell, D., *Skjold class comes in from the cold.* Jane's Navy International, 1999: p. 14-20.

73. Storman, K., *The Skjold class fast patrol boat.* Naval Forces, 1999. **5**: p. 38-43.
74. Brown, D., *Design considerations for MCMV (1) : 31-8.* Naval Forces.
75. Hepburn, R.D., G. Magliulo, and T. Wright, *The US Navy's new coastal minehunter (MHC): design, material, and construction facilities.* Naval Engineers Journal, 1991. **103**(3): p. 60-73.
76. Trimming, M., *Monocoque GRP minehunters*, in *International Symposium on Mine Warfare Vessels and Systems*. 1984: LOndon, June 1984
77. Molland, A. and S. Turnock, *The design and construction of model ship propeller blades in hybrid composite materials.* Composites Manufacturing, 1991. **2**(1): p. 39-47.
78. Pegg, R. and H. Reyes, *Progress in naval composites.* Advanced Materials & Procesees 1987. **131**(3): p. 35-&.
79. Wilhelmi, G.F., W.M. Appleman, and F.T.C. Loo, *Composite shafting for naval propulsion systems.* Naval Engineers Journal, 1986. **98**(4): p. 129-136.
80. Smith Jr, L.E. and M. Smith, *Shipbuilding and Ship Design Perspectives on Applications of Composite Materials: Capability Drivers and Technical Issues.* Society for the Advancement of Material and Process Engineering(USA), 1992: p. 63-77.
81. Davies, P., *6 - Behavior of marine composite materials under deep submergence*, in *Marine Applications of Advanced Fibre-Reinforced Composites*, J.G.-J. Summerscales, Editor. 2016, Woodhead Publishing. p. 125-145.
82. Caplan, I.L., *Marine Composites-The US Navy Experience, Lessons Learned Along the Way.* Nist Special Publication SP, 1995: p. 91-114.
83. Ritter, G.W., *Composites-to-Metal: Engineered Bonded Systems*. EWI, Tech Brief – Composites-Metal Engineered Bonded Systems.
84. Matthews, F.L., P.F. Kilty, and E.W. Godwin, *A review of the strength of joints in fibre-reinforced plastics. Part 2. Adhesively bonded joints.* Composites, 1982. **13**(1): p. 29-37.
85. Anyfantis, K.N. and N.G. Tsouvalis, *Experimental Parametric Study of Single-Lap Adhesive Joints Between Dissimilar Materials*, in *ECCM 15 - 15th European ConferenceOon Composite Materials* 2012: Venice, Italy , 24-28 June.
86. Ikegami, K., et al., *Strength of adhesively bonded scarf joints between glass fibre-reinforced plastics and metals.* International Journal of Adhesion and Adhesives, 1990. **10**(3): p. 199-206.
87. *Redux bonding technology*. July 2003, Hexcel Corporation.
88. Melograna, J.D. and J.L. Grenestedt, *Improving joints between composites and steel using perforations.* Composites Part A: Applied Science and Manufacturing, 2002. **33**(9): p. 1253-1261.
89. Glen Smith, T.H., and Sami Rizkalla, *Bond Characteristics and Qualifications of Adhesives for Marine Applications and Steel Pipe Repair.*
90. Melograna, J.D. and J.L. Grenestedt, *Adhesion of stainless steel to fiber reinforced vinyl ester composite.* Journal of composites technology & research, 2002. **24**(4): p. 254-260.
91. Madenci, E., A. Barut, and I. Guven, *5 - Stress analysis of bolted composite joints under multiaxial loading*, in *Composite Joints and Connections*, P. Camanho and L. Tong, Editors. 2011, Woodhead Publishing. p. 186-207.
92. Ebnesajjad, S., *Handbook of Adhesives and Surface Preparation*. 2011, Oxford: William Andrew Publishing. 107-134.
93. Menon, B., R.A. Pike, and J.P. Wightman, *Metal alkoxide primers in the adhesive bonding of mild steel.* Journal of Adhesion Science and Technology, 1991. **5**(10): p. 883-892.
94. Matsumura, H., T. Tanaka, and M. Atsuta, *Effect of acidic primers on bonding between stainless steel and auto-polymerizing methacrylic resins.* Journal of Dentistry, 1997. **25**(3–4): p. 285-290.
95. Ochoa-Putman, C. and U.K. Vaidya, *Mechanisms of interfacial adhesion in metal–polymer composites – Effect of chemical treatment.* Composites Part A: Applied Science and Manufacturing, 2011. **42**(8): p. 906-915.

96. Wisnom, M.R., *Size effects in the testing of fibre-composite materials.* Composites Science and Technology, 1999. **59**(13): p. 1937-1957.
97. Guild, F.J., P.J. Davy, and P.J. Hogg, *A model for unidirectional composites in longitudinal tension and compression.* Composites Science and Technology, 1989. **36**(1): p. 7-26.
98. Hsiao, H.M. and I.M. Daniel, *Effect of fiber waviness on stiffness and strength reduction of unidirectional composites under compressive loading.* Composites Science and Technology, 1996. **56**(5): p. 581-593.
99. Hsiao, H.M. and I.M. Daniel, *Elastic properties of composites with fiber waviness.* Composites Part A: Applied Science and Manufacturing, 1996. **27**(10): p. 931-941.
100. Adams, D.O.H. and M. Hyer, *Effects of layer waviness on the compression strength of thermoplastic composite laminates.* Journal of Reinforced Plastics and Composites, 1993. **12**(4): p. 414-429.
101. Wisnom, M.R. and J. Atkinson, *Fibre waviness generation and measurement and its effect on compressive strength.* Journal of reinforced plastics and composites, 2000. **19**(2): p. 96-110.
102. Wisnom, M.R., *Analysis of Shear Instability in Compression Due to Fibre Waviness.* Journal of Reinforced Plastics and Composites, 1993. **12**(11): p. 1171-1189.
103. Wisnom, M.R., *The Effect of Fibre Waviness on the Relationship between Compressive and Flexural Strengths of Unidirectional Composites.* Journal of Composite Materials, 1994. **28**(1): p. 66-76.
104. Lemanski, S.L. and M.P.F. Sutcliffe, *Compressive failure of finite size unidirectional composite laminates with a region of fibre waviness.* Composites Part A: Applied Science and Manufacturing, 2012. **43**(3): p. 435-444.
105. Guo, Z.X., et al., *Analysis of interfacial defects in solid-state consolidated composites.* Composites, 1994. **25**(7): p. 563-569.
106. de Almeida, S.F.M. and Z.d.S.N. Neto, *Effect of void content on the strength of composite laminates.* Composite Structures, 1994. **28**(2): p. 139-148.
107. Zhu, H.-y., et al., *Influence of voids on interlaminar shear strength of carbon/epoxy fabric laminates.* Transactions of Nonferrous Metals Society of China, 2009. **19, Supplement 2**(0): p. s470-s475.
108. Zhan-Sheng, G., et al., *Critical Void Content for Thermoset Composite Laminates.* Journal of Composite Materials, 2006. **43**(17): p. 1775-1790.
109. Huang, H. and R. Talreja, *Effects of void geometry on elastic properties of unidirectional fiber reinforced composites.* Composites Science and Technology, 2005. **65**(13): p. 1964-1981.
110. Brouwer, W.D., E.C.F.C. van Herpt, and M. Labordus, *Vacuum injection moulding for large structural applications.* Composites Part A: Applied Science and Manufacturing, 2003. **34**(6): p. 551-558.
111. Jinlian, H., L. Yi, and S. Xueming, *Study on void formation in multi-layer woven fabrics.* Composites Part A: Applied Science and Manufacturing, 2004. **35**(5): p. 595-603.
112. Patel, N. and L.J. Lee, *Effects of fiber mat architecture on void formation and removal in liquid composite molding.* Polymer Composites, 1995. **16**(5): p. 386-399.
113. Patel, N., V. Rohatgi, and L.J. Lee, *Micro scale flow behavior and void formation mechanism during impregnation through a unidirectional stitched fiberglass mat.* Polymer Engineering & Science, 1995. **35**(10): p. 837-851.
114. Olivier, P., J.P. Cottu, and B. Ferret, *Effects of cure cycle pressure and voids on some mechanical properties of carbon/epoxy laminates.* Composites, 1995. **26**(7): p. 509-515.
115. Wood, J.R. and M.G. Bader, *Void control for polymer-matrix composites (1): Theoretical and experimental methods for determining the growth and collapse of gas bubbles.* Composites Manufacturing, 1994. **5**(3): p. 139-147.
116. Wood, J.R. and M.G. Bader, *Void control for polymer-matrix composites (2): Experimental evaluation of a diffusion model for the growth and collapse of gas bubbles.* Composites Manufacturing, 1994. **5**(3): p. 149-158.

117. Whitney, J.M. and R.J. Nuismer, *Stress Fracture Criteria for Laminated Composites Containing Stress Concentrations.* Journal of Composite Materials, 1974. **8**(3): p. 253-265.
118. Persson, E., I. Eriksson, and L. Zackrisson, *Effects of hole machining defects on strength and fatigue life of composite laminates.* Composites Part A: Applied Science and Manufacturing, 1997. **28**(2): p. 141-151.
119. Godin, N., S. Huguet, and R. Gaertner, *Influence of hydrolytic ageing on the acoustic emission signatures of damage mechanisms occurring during tensile tests on a polyester composite: Application of a Kohonen's map.* Composite Structures, 2006. **72**(1): p. 79-85.
120. Kumar, B.G., R.P. Singh, and T. Nakamura, *Degradation of Carbon Fiber-Reinforced Epoxy Composites by Ultraviolet Radiation and Condensation.* Journal of Composite Materials, 2002. **36**(24): p. 2713-2733.
121. Correia, J., et al. *Durability of glass fibre reinforced polyester (GFRP) pultruded profiles used in civil engineering applications*. in *Proceedings of the 3rd International Conference on Composites in Construction*. 2005.
122. Shokrieh, M.M. and A. Bayat, *Effects of Ultraviolet Radiation on Mechanical Properties of Glass/Polyester Composites.* Journal of Composite Materials, 2007. **41**(20): p. 2443-2455.
123. Fouad, Y., M. El-Meniawi, and A. Afifi, *Erosion behaviour of epoxy based unidirectionl (GFRP) composite materials.* Alexandria Engineering Journal, 2011. **50**(1): p. 29-34.
124. Shyr, T.-W. and Y.-H. Pan, *Impact resistance and damage characteristics of composite laminates.* Composite Structures, 2003. **62**(2): p. 193-203.
125. Geubelle, P.H. and J.S. Baylor, *Impact-induced delamination of composites: a 2D simulation.* Composites Part B: Engineering, 1998. **29**(5): p. 589-602.
126. Mouritz, A.P. and R.S. Thomson, *Compression, flexure and shear properties of a sandwich composite containing defects.* Composite Structures, 1999. **44**(4): p. 263-278.
127. Zhang, Z.Y. and M.O.W. Richardson, *Low velocity impact induced damage evaluation and its effect on the residual flexural properties of pultruded GRP composites.* Composite Structures, 2007. **81**(2): p. 195-201.
128. Kim, J.-K. and M.-L. Sham, *Impact and delamination failure of woven-fabric composites.* Composites Science and Technology, 2000. **60**(5): p. 745-761.
129. Cantwell, W.J. and J. Morton, *The significance of damage and defects and their detection in composite materials: A review.* The Journal of Strain Analysis for Engineering Design, 1992. **27**(1): p. 29-42.
130. Beaumont, P., *Fracture mechanisms in fibrous composites.* Fracture Mechanics—Current Status, Future ProspectsUniversity of Cambridge, 1979.
131. Bishop, S.M., *The significance of defects on the failure of fibre composites*. 1981, AGARAD SMP subcommittee on defects.
132. Gillespie Jr, J.W. and R.B. Pipes, *Compressive strength of composite laminates with interlaminar defects.* Composite Structures, 1984. **2**(1): p. 49-69.
133. Peck, S.O. and G.S. Springer, *The behavior of delaminations in composite plates—analytical and experimental results.* Journal of composite materials, 1991. **25**(7): p. 907-929.
134. Yeh, M.K. and C.M. Tan, *Buckling of Elliptically Delaminated Composite Plates.* Journal of Composite Materials, 1994. **28**(1): p. 36-52.
135. Liu, D., *Impact-induced delamination—a view of bending stiffness mismatching.* Journal of composite materials, 1988. **22**(7): p. 674-692.
136. *Fundamentals of Ultrasonic Imaging and Flaw Detection (Online source: http://www.ni.com/white-paper/3368/en/)*. 2010, National Instruments.
137. Cantwell, W.J.M., J., *The significance of damage and defects and their detection in composite materials: A review.* The Journal of Strain Analysis for Engineering Design, 1992. **27**(1): p. 29-42.
138. Ray, B.C., S.T. Hasan, and D.W. Clegg, *Evaluation of Defects in FRP Composites by NDT Techniques.* Journal of Reinforced Plastics and Composites, 2007. **26**(12): p. 1187-1192.

139. Hopkins, D., G. Neau, and L. Le Ber, *Advanced phased-array technologies for ultrasonic inspection of complex composite parts.*
140. *Phased Array Ultrasonic Testing (PAUT)*. Online source: http://www.nde.com/phased_array_technology.htm.
141. Garnier, C., et al., *The detection of aeronautical defects in situ on composite structures using Non Destructive Testing.* Composite Structures, 2011. **93**(5): p. 1328-1336.
142. Wong, B.S., et al., *Thermographic evaluation of defects in composite materials.* Insight, 1999. **41**(8): p. 504-509.
143. Montanini, R. and F. Freni, *Non-destructive evaluation of thick glass fiber-reinforced composites by means of optically excited lock-in thermography.* Composites Part A: Applied Science and Manufacturing, 2012. **43**(11): p. 2075-2082.
144. Bai, W. and B. Wong, *Evaluation of defects in composite plates under convective environments using lock-in thermography.* Measurement Science and Technology, 2001. **12**(2): p. 142-150.
145. Li, Y., et al., *Low-velocity impact damage characterization of carbon fiber reinforced polymer (CFRP) using infrared thermography.* Infrared Physics & Technology, 2016. **76**: p. 91-102.
146. Heuer, H. and M.H. Schulze, *Eddy current testing of carbon fiber materials by high resolution directional sensors.* Smart Materials, Structures and NDT in Aerospace, NDT in Canada, 2011. **2011**.
147. Lee, L.J. and Y.J. Fan, *Bending and vibration analysis of composite sandwich plates.* Computers & Structures, 1996. **60**(1): p. 103-112.
148. Shi, G. and K.Y. Lam, *Finite element vibration analisys of composite beams based on higher-order beam theory.* Journal of Sound and Vibration, 1999. **219**(4): p. 707-721.
149. Shu, D. and C.N. Della, *Free vibration analysis of composite beams with two non-overlapping delaminations.* International Journal of Mechanical Sciences, 2004. **46**(4): p. 509-526.
150. Udd, E. *Structural Health Monitoring Using FBGs for Aerospace and Composite Manufacturing.* in *Optical Fiber Sensors*. 2006. Cancun: Optical Society of America.
151. Kim, S.-W., et al., *Structural performance tests of down scaled composite wind turbine blade using embedded fiber Bragg grating sensors.* International Journal Aeronautical and Space Sciences, 2011. **12**(4): p. 346-353.
152. De Oliveira, R. and A.T. Marques, *Health monitoring of FRP using acoustic emission and artificial neural networks.* Computers & Structures, 2008. **86**(3–5): p. 367-373.
153. Williams, R.V., *Acoustic Emission*. 1980: Adam Hilger Ltd.
154. Muravin, B., *Acoustic Emission Wave Propagation and Source Location*.
155. Hamstad, M., *Acoustic emission signals generated by monopole (pencil lead break) versus dipole sources: finite element modeling and experiments.* Journal of Acoustic Emission, 2007. **25**: p. 92-106.
156. *Chapter 10: Acoustic Emission Testing*, in *Handbook of Nondestructive Evaluation*. 2003, The MacGraw-Hill Companies.
157. Short, D. and J. Summerscales, *Amplitude distribution acoustic emission signatures of unidirectional fibre composite hybrid materials.* Composites, 1984. **15**(3): p. 200-206.
158. Ito, K. and M. Enoki, *Acquisition and analysis of continuous acoustic emission waveform for classification of damage sources in ceramic fiber mat.* Materials Transactions, 2007. **48**(6): p. 1221-1226.
159. *Acoustic Emission Testing Fundamentals - Equipment - Data Analysis (Overview)*. Vallen - Systeme GmbH.
160. Shiotani, T., *Parameter Analysis*, in *Acoustic Emission Testing: Basics for Research - Applications in Civil Engineering*, C. Grosse and M. Ohtsu, Editors. 2008, Springer Berlin Heidelberg: Berlin, Heidelberg. p. 41-51.
161. *PCI Based AE System User's Manual, Physical Acoustic's Corporation*. Mistras Group INC.

162. Anastassopoulos, A.A., Philippidis, T.P., *Clustering Methodology for the evaluation of Acoustic Emission from Composites.* Journal of Acoustic Emission, 1995. **13**(1/2): p. 11-22.
163. Anastassopoulos, A.A., Philippidis, T.P., *Pattern recognition analysis of AE from composites*
164. Philippidis, T.P., V.N. Nikolaidis, and A.A. Anastassopoulos, *Damage characterization of carbon/carbon laminates using neural network techniques on AE signals.* NDT & E International, 1998. **31**(5): p. 329-340.
165. Aggelis, A.S.P.a.D.G., *Damage Assessment in Fibrous Composites Using Acoustic Emission*, in *Acoustic Emission*, D.W. Sikorski, Editor. 2012, InTech. p. 279-294.
166. Aggelis, D.G., Barkoula, N. M., Matikas, T. E., Paipetis, A. S., *Acoustic structural health monitoring of composite materials : Damage identification and evaluation in cross ply laminates using acoustic emission and ultrasonics.* Composites Science and Technology, 2012. **72**(10): p. 1127-1133.
167. Kappatos, V. and E. Dermatas, *Feature Selection for Robust Localization of Acoustic Emission Sources in Ship-Hull Structures.* Research in Nondestructive Evaluation, 2010. **21**(2): p. 127-140.
168. Kappatos, V. and E. Dermatas, *Neural localization of acoustic emission sources in ship hulls.* Journal of Marine Science and Technology, 2009. **14**(2): p. 248-255.
169. Kappatos, A.V. and S.E. Dermatas, *Feature Extraction for Crack Detection in Rain Conditions.* Journal of Nondestructive Evaluation, 2007. **26**(2): p. 57-70.
170. Kappatos, V. and E. Dermatas, *Crack detection in noisy environment including raining conditions.* Aircraft Engineering and Aerospace Technology, 2007. **79**(2): p. 163-169.
171. *Acoustic Emission Sensors Specification*. 2012, Vallen - Systeme GmbH.
172. *Acoustic emission sensors*. Online source: www.fujicera.co.jp/product/e/05/index.html.
173. Grosse, C., *Hsu-Nielsen source*. 2002: Online source: www.ndt.net/ndtaz/content.php?id=474.
174. Arumugam, V., Kumar, S.C., Santulli, C., Sarasini, F., Stanley, A., *A Global Method for the Identification of Failure Modes in Fiberglass Using Acoustic Emission.* Journal of Testing and Evaluation, 2011. **39**(5): p. 1-13.
175. Bussiba, A., Kupiec, M., Ifergane, S., Piat, R., Böhlke, T., *Damage evolution and fracture events sequence in various composites by acoustic emission technique.* Composites Science and Technology, 2008. **68**(5): p. 1144-1155.
176. Okafor, A.C., N. Singh, and N. Singh, *Acoustic Emission Detection and Prediction of Fatigue Crack Propagation in Composite Patch Repairs Using Neural Networks.* AIP Conference Proceedings, 2007. **894**(1): p. 1532-1539.
177. Naderi, M., A. Kahirdeh, and M.M. Khonsari, *Dissipated thermal energy and damage evolution of Glass/Epoxy using infrared thermography and acoustic emission.* Composites Part B: Engineering, 2012. **43**(3): p. 1613-1620.
178. Godin, N., S. Huguet, and R. Gaertner, *Integration of the Kohonen's self-organising map and k-means algorithm for the segmentation of the AE data collected during tensile tests on cross-ply composites.* NDT & E International, 2005. **38**(4): p. 299-309.
179. Godin, N., et al., *Clustering of acoustic emission signals collected during tensile tests on unidirectional glass/polyester composite using supervised and unsupervised classifiers.* NDT & E International, 2004. **37**(4): p. 253-264.
180. Huguet, S., et al., *Use of acoustic emission to identify damage modes in glass fibre reinforced polyester.* Composites Science and Technology, 2002. **62**(10–11): p. 1433-1444.
181. Moevus, M., et al., *Analysis of damage mechanisms and associated acoustic emission in two SiCf/[Si–B–C] composites exhibiting different tensile behaviours. Part II: Unsupervised acoustic emission data clustering.* Composites Science and Technology, 2008. **68**(6): p. 1258-1265.

182. Crivelli, D., M. Guagliano, and A. Monici, *Development of an artificial neural network processing technique for the analysis of damage evolution in pultruded composites with acoustic emission.* Composites Part B: Engineering, 2014. **56**: p. 948-959.
183. Gutkin, R., et al., *On acoustic emission for failure investigation in CFRP: Pattern recognition and peak frequency analyses.* Mechanical Systems and Signal Processing, 2011. **25**(4): p. 1393-1407.
184. Kostopoulos, V., T. Loutas, and K. Dassios, *Fracture behavior and damage mechanisms identification of SiC/glass ceramic composites using AE monitoring.* Composites Science and Technology, 2007. **67**(7–8): p. 1740-1746.
185. Marec, A., J.H. Thomas, and R. El Guerjouma, *Damage characterization of polymer-based composite materials: Multivariable analysis and wavelet transform for clustering acoustic emission data.* Mechanical Systems and Signal Processing, 2008. **22**(6): p. 1441-1464.
186. Monti, A., et al., *Mechanical behaviour and damage mechanisms analysis of a flax-fibre reinforced composite by acoustic emission.* Composites Part A: Applied Science and Manufacturing, 2016. **90**: p. 100-110.
187. Kempf, M., O. Skrabala, and V. Altstädt, *Acoustic emission analysis for characterisation of damage mechanisms in fibre reinforced thermosetting polyurethane and epoxy.* Composites Part B: Engineering, 2014. **56**(0): p. 477-483.
188. Njuhovic, E., et al., *Identification of failure mechanisms of metallised glass fibre reinforced composites under tensile loading using acoustic emission analysis.* Composites Part B: Engineering, 2015. **81**: p. 1-13.
189. Kotsidis, E.A., Kouloukouras, I.G., Tsouvalis, N.G., *Composite materials manufacturing and characterization.* Project MOSAIC (Materials On board: Steel Advancement and Integrated Composites), Deliverable D2.2, NTUA-TR-WP2-1-v0NTUA-TR-WP2-1-v0, 2007.
190. ASTM D 3039/D 3039M-08, *Standard Test Method for Tensile Properties of Polymer Matrix Composite Materials*.
191. ASTM D 790-07, *Standard Test Methods for Flexural Properties of Unreinforced and Reinforced Plastics and Electrical Insulating Materials*
192. Pandita, S.D., Angelopoulos, N., Papaelias, M., Fernando, G. F., *MOSAIC Deliverable 3.4, Report with the Composite-to-Steel Joints test Results.* June 2014.
193. Surya D. Pandita, Mayorkinos Papaelias, and Gerard F. Fernando, *Report on MOSAIC FP7 project deliverable 2.2*. January 2014, School of Metallurgy and Materials, University of Birmingham.
194. R'Mili, M., M. Moevus, and N. Godin, *Statistical fracture of E-glass fibres using a bundle tensile test and acoustic emission monitoring.* Composites Science and Technology, 2008. **68**(7–8): p. 1800-1808.
195. Okoroafor, E.U. and R. Hill, *Weibull statistics of fibre bundle failure using mechanical and acoustic emission testing: the influence of interfibre friction.* Composites, 1995. **26**(10): p. 699-705.
196. Amir Refahi Oskouei and M. Ahmadi, *Fracture Strength Distribution in E-Glass Fiber Using Acoustic Emission.* Journal of Composite Materials, 2010. **44**(6): p. 693-705.
197. Schmid S.R. Hamrock, B.J., Jacobson Bo O., *Chapter 6: Failure Prediction for Static Loading, Fundamentals of Machine Elements 3rd ed.* 2014, CRC Press, Taylor & Francis Group.
198. Liu, P.F., et al., *A study on the failure mechanisms of carbon fiber/epoxy composite laminates using acoustic emission.* Materials & Design, 2012. **37**(0): p. 228-235.
199. Refahi Oskouei, A., et al., *An integrated approach based on acoustic emission and mechanical information to evaluate the delamination fracture toughness at mode I in composite laminate.* Materials & Design, 2011. **32**(3): p. 1444-1455.
200. Suresh Kumar, C., et al., *Failure strength prediction of glass/epoxy composite laminates from acoustic emission parameters using artificial neural network.* Applied Acoustics, 2017. **115**: p. 32-41.

201. Vieille, B., et al., *A fracture mechanics approach using Acoustic Emission Technique to investigate damage evolution in woven-ply thermoplastic structures at temperatures higher than glass transition temperature.* Composites Part B: Engineering.
202. Doan, D.D., et al., *An unsupervised pattern recognition approach for AE data originating from fatigue tests on polymer–composite materials.* Mechanical Systems and Signal Processing, 2015. **64–65**: p. 465-478.
203. Jerzy Schmidt, I.B.a.K.O., *Acoustic Emission Behavior of Failure Precesses of Glass-Fiber Laminates Under Complex State of Loading.* Acoustic Emission, 2005. **23**: p. 173-180.
204. Asamene, K., L. Hudson, and M. Sundaresan, *Influence of attenuation on acoustic emission signals in carbon fiber reinforced polymer panels.* Ultrasonics, 2015. **59**: p. 86-93.
205. Maillet, E., et al., *Feasibility and limitations of damage identification in composite materials using acoustic emission.* Composites Part A: Applied Science and Manufacturing, 2015. **75**: p. 77-83.
206. Ullah, H., A.R. Harland, and V.V. Silberschmidt, *Damage modelling in woven-fabric CFRP laminates under large-deflection bending.* Computational Materials Science, 2012. **64**: p. 130-135.
207. Brunner, A.J., T. Tannert, and T. Vallee, *Waveform analysis of acoustic emission monitoring of tensile tests on welded wood-joints.* Journal of Acoustic EMISSION, 2010. **28**: p. 59-68.
208. Anastasopoulos, A., et al., *Acoustic emission monitoring for detecting structural defects in vessels and offshore structures.* Ships and Offshore Structures, 2009. **4**(4): p. 363-372.
209. MacQueen, J. *Some methods for classification and analysis of multivariate observations*. in *Proceedings of the Fifth Berkeley Symposium on Mathematical Statistics and Probability, Volume 1: Statistics*. 1967. Berkeley, Calif.: University of California Press.
210. Li, Y. and H. Wu, *A Clustering Method Based on K-Means Algorithm.* Physics Procedia, 2012. **25**(0): p. 1104-1109.
211. Jain, A.K., *Data clustering: 50 years beyond K-means.* Pattern Recognition Letters, 2010. **31**(8): p. 651-666.
212. Niknam, T., et al., *An efficient hybrid algorithm based on modified imperialist competitive algorithm and K-means for data clustering.* Engineering Applications of Artificial Intelligence, 2011. **24**(2): p. 306-317.
213. Ng, M.K., *A note on constrained k-means algorithms.* Pattern Recognition, 2000. **33**(3): p. 515-519.
214. Krishna, K. and M.N. Murty, *Genetic K-means algorithm.* IEEE Transactions on Systems Man and Cybernetics Part B-Cybernetics, 1999. **29**(3): p. 433-439.
215. Likas, A., N. Vlassis, and J. J. Verbeek, *The global k-means clustering algorithm.* Pattern Recognition, 2003. **36**(2): p. 451-461.
216. Anderberg, M.R., *Cluster analysis for applications*. 1970: Academic Press, NY.
217. Steinley, D., *K-means clustering: A half-century synthesis.* British Journal of Mathematical and Statistical Psychology, 2006. **59**(1): p. 1-34.
218. *Noesis Manual Rev.5, Copyright © 1999-2008, Enviroacoustics S.A., Athens, Greece*.
219. Anastasopoulos, A., *Pattern recognition techniques for acoustic emission based condition assessment of unfired pressure vessels.* J. of Acoustic Emission, 2005. **23**: p. 318-330.
220. Dubes, R. and A.K. Jain, *Clustering techniques: The user's dilemma.* Pattern Recognition, 1976. **8**(4): p. 247-260.
221. Ball, G.H. and D.J. Hall, *ISODATA, a novel method of data analysis and pattern classification*. 1965, DTIC Document.
222. Tou, J.T. and R.C. Gonzalez, *Pattern recognition principles.* 1974.
223. Hua, G., S. Guang-Da, and D. Cheng. *Fuzzy and ISODATA classification of face contours*. in *Machine Learning and Cybernetics, 2004. Proceedings of 2004 International Conference on*. 2004.

224. Dhodhi, M.K., et al., *D-ISODATA: a distributed algorithm for unsupervised classification of remotely sensed data on network of workstations.* J. Parallel Distrib. Comput., 1999. **59**(2): p. 280-301.
225. Therrien, C.W., *Decision Estimation and Classification, An Introduction to Pattern recognition and Related Topics* 1989: John Wiley & Sons, Inc.
226. Kohonen, T., *Self-Organising Maps*. Third ed. 2001: Springer -Verlag Berlin Heidelberg New York.
227. Kohonen, T., *The self-organizing map.* Neurocomputing, 1998. **21**: p. 1-6.
228. Kohonen, T., *The self-organizing map.* Proceedings of the IEEE, 1990. **78**(9): p. 1464-1480.
229. Hämäläinen, T., et al., *Mapping of SOM and LVQ algorithms on a tree shape parallel computer system.* Parallel Computing, 1997. **23**(3): p. 271-289.
230. Bullinaria, J.A., *Learning Vector Quantization (LVQ), Introduction to neural computation : Guest Lecture 2.* © John A Bullinaria, 2007.
231. Kohonen, T. *Improved versions of learning vector quantization*. in *Neural Networks, 1990., 1990 IJCNN International Joint Conference on*. 1990.
232. *The Fundamentals of Signal Analysis*. Agilent technologies.
233. *Fast Fourier Transform (FFT)*. On line source: http://uk.mathworks.com/help/matlab/math/fast-fourier-transform-fft.html#responsive_offcanvas.